Quasi-Periodic Pulsations in Solar Flares and the Earth's Ionosphere

Astrophysics Research Group
Supervisor: Prof. Peter T. Gallagher

Laura A. Hayes B.A. (Mod.)
Trinity College Dublin, 2019

School of Physics
University of Dublin
Trinity College

Declaration

I declare that this thesis has not been submitted as an exercise for a degree at this or any other university and it is entirely my own work.

I agree to deposit this thesis in the University's open access institutional repository or allow the library to do so on my behalf, subject to Irish Copyright Legislation and Trinity College Library conditions of use and acknowledgement.

Name: Laura A. Hayes

Signature: .... **Date:** ....

Summary

Solar flares are the most powerful and energetic physical phenomena in our solar system, releasing radiation across the whole electromagnetic spectrum with total energies reaching on the order of 10^{25} J in a matter of minutes. On Earth, the conditions of the terrestrial ionosphere are significantly affected by the enhanced radiation of such events.

A key observational feature of the emission generated in solar flares is the presence of pronounced pulsations and oscillatory signatures known as *quasi-periodic pulsations* (QPPs). The presence of such QPPs in solar flare emission places important constraints on the interpretation and understanding of fundamental processes that operate in flares. To date, the characteristics and origins of QPPs remain unclear. In this thesis we aim to further our current understanding of the QPP phenomena, in both solar flaring emissions and the geophysical impacts QPPs have on the Earth's terrestrial ionosphere.

The first two investigations in this thesis examine the recently identified temporal fine structure QPPs that are observed in the soft X-ray emissions from solar flares. We present a multi-wavelength investigation of QPPs observed during both the impulsive and decay phases of an X-class solar flare. Unlike previous investigations, we focus on the QPPs evident in the soft X-ray time derivative, and compare this variability with observations at other wavelengths including hard X-ray and microwave observations. The soft X-ray thermal pulsations are found to follow the structure of the non-thermal emission in the impulsive phase of the flare, but then tend towards longer timescales later in the event. This analysis provides new insights into the prevalence of soft X-ray QPPs in solar flaring emission and highlights that these extended fine structure QPPs can persist during both phases of a solar flare, with a potentially different dominant QPP driver in each.

Following this, a second investigation into the nature of extended soft X-ray QPPs that is observed to exist throughout an entire large solar eruptive X-class flare is presented. This study focuses on relating the soft X-ray QPPs to the spatial length scales and eruptive dynamics of the flaring event. We find that there are two regimes of QPPs, an impulsive regime of shorter periods QPPs ($\sim$65 s) that is associated with the extremely fast CME eruption, and an extended decay phase QPP regime with longer periods QPPs ($\sim$150-160 s) associated with co-existing sunward moving features observed in EUV.

We also present the first observational evidence of the geoeffectiveness of QPPs in solar flares. Through the remote sensing of the Earth's lower ionosphere using Very Low Frequency (VLF) radio wave measurements, together with X-ray and EUV observations, we report the detection of pulsations in the ionospheric electron density that are synchronized with solar flare QPPs. It is found that over the period of a pulsation ($\sim$20 mins), the electron density can vary by up to an order of magnitude. We use these observations, together with the electron continuity equation, to estimate the effective recombination coefficient of the lower ionosphere during the flaring event.

Finally we explore some preliminary avenues of future work that build upon the results of this thesis, and discuss the new and exciting directions for the study of the QPP phenomena.

Acknowledgements

First and foremost I would like to sincerely thank my supervisor Peter Gallagher. Your guidance, motivation, and enthusiasm has made these four years very enjoyable. I would like to particularly acknowledge your invaluable support and encouragement throughout my PhD and for always pushing me in the right direction.

Secondly, I would like to thank Brian Dennis for your insights and attention to detail you provided throughout my PhD. Your passion for the subject is contagious! I fondly remember my trips to Goddard to work with you. I would also like to sincerely thank Jack Ireland and Andy Inglis for the help and support throughout the four years of my PhD. I am hugely grateful to have worked with you both.

A big thank you to Danny Ryan, for your friendship and guidance over the years. And for the many (many) pints in different cities we bumped into each other in.

To the astrophysics group at Trinity, both the old gang and the new gang. The 'office' has been an institution in itself and I am very lucky to have colleagues that I would also consider to be close friends.

To my PhD sista Aoife McCloskey - here we are now at the end. We pulled ourselves through with endless dancing and random laughs. From all our 'winging-it' outreach talks and workshops, its always been an inspiration to work with you.

On a personal note, I would like to sincerely thank my family for the continuous love and support. Its so nice to return home and forget about the bubble of the PhD for a while. To my parents, Fergus and Loraine, your motivation and constant stream of encouragement throughout my PhD has made it possible. Thank you for everything.

And finally to Colin, my partner in crime and rock in life. Thank you for for the love, the laughs, the support, and your general amazing attitude towards life. You can always reel me back from times of stress. A special thank you for putting up with me while writing this thesis!

List of Publications

1. **Hayes, L.A.**, Gallagher, P.T., Dennis, B.R., Ireland, J., Inglis, A.R. and Ryan, D.F., 2016. Quasi-Periodic Pulsations during the Impulsive and Decay phases of an X-class Flare. *Astrophysical Journal Letters*, 827(2), p.L30.

2. **Hayes, L.A.**, Gallagher, P.T., McCauley, J., Dennis, B.R., Ireland, J. and Inglis, A., 2017. Pulsations in the Earth's Lower Ionosphere Synchronized With Solar Flare Emission. *Journal of Geophysical Research: Space Physics*, 122(10), pp.9841-9847.

3. **Hayes, L.A.**, Gallagher, P.T., Dennis, B.R., Ireland, J. and Inglis, A., Morosan, D. 2019. Persistent Quasi-Periodic Pulsations During a Large X-Class Solar Flare. *in review Astrophysical Journal*

4. Dennis, B.R., Tolbert, A.K., Inglis, A., Ireland, J., Wang, T., Holman, G.D., **Hayes, L.A.** and Gallagher, P.T., 2017. Detection and Interpretation of Long-lived X-Ray Quasi-periodic Pulsations in the X-class Solar Flare on 2013 May 14. *Astrophysical Journal*, 836(1), p.84.

5. Inglis, A.R., Ireland, J., Dennis, B.R., **Hayes, L.** and Gallagher, P., 2016. A Large-scale Search for Evidence of Quasi-periodic Pulsations in Solar Flares. *Astrophysical Journal*, 833(2), p.284.

6. Ireland, J., Inglis, A.R., Shih, A.Y., Christe, S., Mumford, S.J., **Hayes, L.A.**, Thompson, B.J. and Hughitt, V.K., 2019. AWARE: An algorithm for the automated characterization of EUV waves in the solar atmosphere. *in review Solar Physics arXiv preprint arXiv:1804.07325.*

7. Morosan, D.A., Carley, E.P., **Hayes, L.A.**, Murray, S.A., Zucca, P., McCauley, J., Kilpua, E. and Gallagher P.T., 2019. Multiple Regions of Shock Accelerated Particles in the Solar Corona. *accepted Nature Astronomy*
8. Carley, E.P., **Hayes, L.A.**, Murray, S.A., Morosan, D.A., Shelley, W., Vilmer, N. and Gallagher, P.T., 2019. Modulation of a loss-cone instability due to a magnetohydrodynamic sausage mode oscillation in the solar corona. *in review*
9. Broomhall, A-M., **Hayes, L.A.**, Inglis, A.R., Kolotkov, D.T., McLaughlin, J.A., Mehta, T., Nakariakov, V.M., Notsu., Y., Pascoe, P.J., Pugh, C.E., Van Doorsselaere, T. 2018. A blueprint of state-of-the-art techniques for detecting quasi-periodic pulsations in solar and stellar flares. *in prep*

Contents

List of Figures

List of Tables

LIST OF TABLES

1

Introduction

We live in the presence of an active star, the Sun. Throughout history the Sun and its activity have been a focus of fascination and a source of religious, spiritual and scientific interest. The Neolithic passage tomb of Newgrange built in Ireland in ∼3200 BC reveals that even Stone Age civilisations had precise knowledge of the Sun's motion given the perfectly aligned chamber passages of the tomb that illuminate on the winter solstice. Historically the presence of aurora was not linked to solar activity, however the phenomena still inspired awe and was noted by society at the time. For example, Ulster Annals dating from 994 AD noted in Old Irish *'Tadbhsiu ingnadh aidchi feile Stefan, combo croderg in nemh'* which translates to English as *'An unusual appearance on St. Stephan's Eve, and the sky was blood-red'.* Dating the carbon-14 level in tree rings during this time has revealed these noted aurora were most likely related to an extreme solar storm that occurred (Hayakawa *et al.*, 2017).

The solar-terrestrial relationship was first suggested by Sabine *et al.* (1852) who recognised that geomagnetic disturbances and the appearance of aurora on Earth was correlated with times of high sunspot numbers observed on the solar disk. Several years later the first recorded solar flare observation was reported independently by R.C Carrington and R. Hodgson in 1859 (Carrington, 1859; Hodgson, 1859). During a routine sunspot survey, they saw what they reported as an 'exceedingly rare' event, a localized brightening in white light observations within a sunspot group. Seventeen hours later, a severe geomagnetic storm was recorded at Kew Observatory (Stewart, 1861) and other magnetometers around the world (Tsurutani *et al.*, 2003). Intense aurora became visible as far south as Cuba, and currents generated in the telegraph systems caused failures in both the US and Europe. It is recognised today that what Carrington observed was a *solar eruptive event*, a large solar flare followed by a coronal mass ejection (CME) that caused the subsequent geomagnetic storm. Known as the *Carrington event*, this observation provided one of the first example of the intimate solar-terrestrial connection and sparked 150 years of investigation into the solar flare phenomena and the Sun-Earth connection.

Today, modern ground- and space- based observations in multiple wavelengths have demonstrated the rich complexity of the Sun's atmosphere from where these dynamic events occur. Observations of explosive energy release from the Sun's atmosphere in the form of solar flares and CMEs have been directly linked to geomagnetic effects at Earth and to the adverse disruptions to our technological infrastructure. These effects include disruptions to our power grids, the Global Navigational Satellite Systems (GNSS) and high frequency radio communications. Solar flaring events are also known to damage satellites and can cause increased radiation exposure during polar flight routes.

Our understanding of solar flares has improved significantly over the past number of years, however several details remains elusive and our current understanding of the solar flaring phenomena and the coupled Sun-Earth system remain incomplete. This thesis aims to contribute to the continuing growth of understanding of solar flares and their effects on the Earth's atmosphere. In this Chapter we set the stage for the research undertaken in this thesis. We begin with an introduction to the solar atmosphere, the home to the Sun's dynamic activity and eruptive events. This is followed with an outline of our current understanding of solar flares and the phenomenon of quasi-periodic pulsations. We will then introduce the D-region of the Earth's ionosphere and its susceptibility to solar flare X-ray emissions. Finally, a thesis outline will be given.

1.1 The Solar Atmosphere

At the so called 'surface' of the Sun, known as the *photosphere*, visible wavelengths become optically thin and photons can readily escape into space. This is where the solar atmosphere begins, consisting of a highly structured ionized plasma that is threaded and modified by a complex and dynamic magnetic field. The

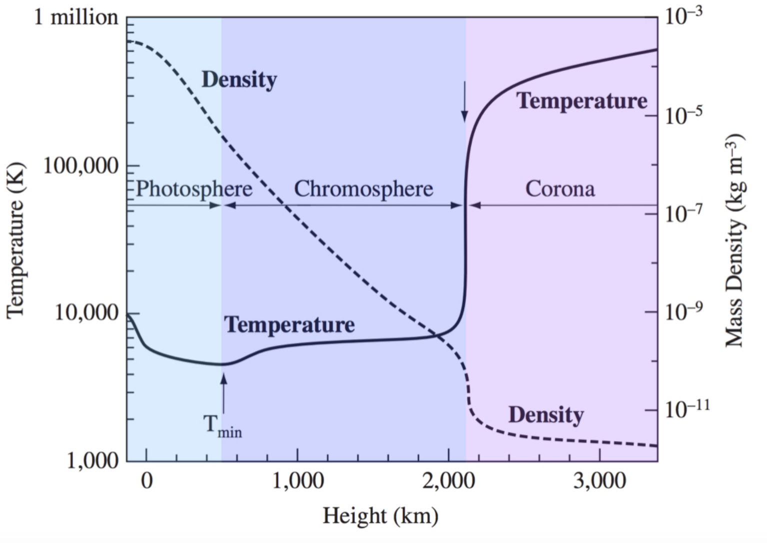

Figure 1.1: Schematic of the mean temperature and density structure of the (quiet) solar atmosphere with height. The temperature is marked with a filled line and the density with a dashed line. Adapted from Priest (2014).

solar atmosphere can be divided into broad constituent regions; beginning at the photosphere, and then extending out to the *chromosphere*, the *transition region*, and the *corona*. These regions are stratified depending on the thermodynamic conditions and physical properties that dominate. The density and temperature profiles for the different atmospheric regions (for a 1D quiet Sun) is shown in Figure 1.1, and the details of each of these regions are described below.

1.1.1 Photosphere

The photosphere is the visible 'surface' of the Sun consisting of a thin layer (~ 0.1 Mm thick) which forms the innermost region of the solar atmosphere. It is from this region that the bulk of solar energy is radiated in the form of visible light, to which human eyes have developed prime sensitivity through evolution. The distribution of photospheric radiation resembles that of a blackbody peaked at an effective temperature of 5778 K (Severino, 2017). The typical number density in the photosphere is $\sim 10^{17}$ cm^{-3}. The visible appearance of the photosphere shows granulation, representing the tops of underlying convection cells rising to the solar surface. The continuous motions of plasma in the photosphere acts to tangle and shear magnetic fields higher up in the atmosphere increasing the stored non-potential magnetic energy. The most notable features of the photosphere are sunspots, regions of concentrated magnetic field that have penetrated into the solar atmosphere from the underlying convection zone. An image of the Sun's photosphere observed at $\lambda = 4500$ Å from the Atmospheric Imaging Assembly (AIA) (Lemen *et al.*, 2011) on board the Solar Dynamics Observatory (SDO) is shown in Figure 1.2. An arrow points to a sunspot group. Sunspots appear as dark regions due to their relatively cooler temperature ($\sim$3000-4000 K) caused by the strong magnetic field which is on the order of kilogauss (compared to the tens of Gauss of the quiet photosphere) that suppresses convection. Sunspots play an important role as an indicator of solar activity as their structure and complexity determines the topology of magnetic *active regions*, the source of most solar flares and CMEs.

1.1.2 Chromosphere

The chromosphere is the region of the atmosphere that extends $\sim$2 Mm above the photosphere. It takes its name ('chrome' - Greek for colour) from the pink and red appearance observed during a solar eclipse from the dominant Hα (6563 Å) emission. The number densities in the chromosphere decrease when moving outward from the photosphere ranging from 10^{16} cm^{-3} at the top of the photosphere to 10^{11} cm^{-3} at the edge of the transition region. The temperature also continues to drop until a temperature minimum is reached at 4400 K at about 500 km above the photosphere. After this, the temperature begins to rise again reaching 20,000 K at the upper boundary. At these temperatures, the chromosphere is partially ionized.

The chromosphere is spectroscopically distinct from the underlying photosphere and is observable in ultraviolet (UV) emission lines and continua, as well as certain other lines such as Hα and Lyα (1216Å). Observations of the chromosphere show that it is very dynamic. In Hα, bright regions called *plages* are often observed in the vicinity of active regions, usually in uni-polar regions of magnetic flux that have emerged from the photosphere. The most prominent structures observed in chromospheric lines are *filaments*, which are structures of cool dense chromospheric material that are suspended at greater heights in the tenuous corona. When viewed in Hα these features appear dark, however when they are observed on the solar limb they appear as bright arcades and are termed *prominences*.

1.1.3 Transition Region

The transition region lies between the chromosphere and the corona, and demarcates an abrupt boundary where, over a region of ∼100 km, the coronal densities decrease by several orders of magnitude lower that the chromosphere and the temperature rises dramatically from 20,000 K to over 1 MK (Mariska, 1992). The extreme temperature results in prominent UV and extreme ultraviolet (EUV) emission from this region as the plasma is almost completely ionized.

Figure 1.2 (c) shows observations at $\lambda = 304$ Å which is sensitive to transition region plasma, demonstrating a complex environment.

The rapid rise of temperature in coronal plasmas compared to the underlying atmospheric layers appears to violate the laws of thermodynamics and constitutes the 'coronal heating problem'. To explain the dramatic increase in temperature a heating mechanism that can sustain the levels of the combined radiative and conductive losses in the corona is required. It is generally accepted that the ultimate source of energy to account for the high temperatures is connected to the conversion of free magnetic energy that is built up through convective motions in and below the photosphere. The main problem lies in the identification of how this energy is dissipated and converted into heat.

There are two main branches of theories proposed to resolve the issue of how the energy is dissipated. These are categorised by the timescales of the underlying plasma convective motions of the coronal magnetic field. Slow motions (slower than the Alfvén speed) can cause the build up of magnetic stresses in the field which can then be dissipated in the form of magnetic reconnection (e.g. nanoflares). This results in direct heating of the corona and is referred to as a direct current (DC) heating model. Alternatively, faster convective motions can generate magnetohydrodynamic (MHD) waves that can then propagate through the atmosphere and dissipate to heat the local coronal plasma. This is referred to as an alternating current (AC) heating model. To date, a consensus on a dominant mechanism has not been reached and the issue of coronal heating remains an outstanding problem in modern astrophysics. We refer the reader to comprehensive reviews on the topic by De Moortel & Browning (2015); Klimchuk (2006); Parnell & De Moortel (2012).

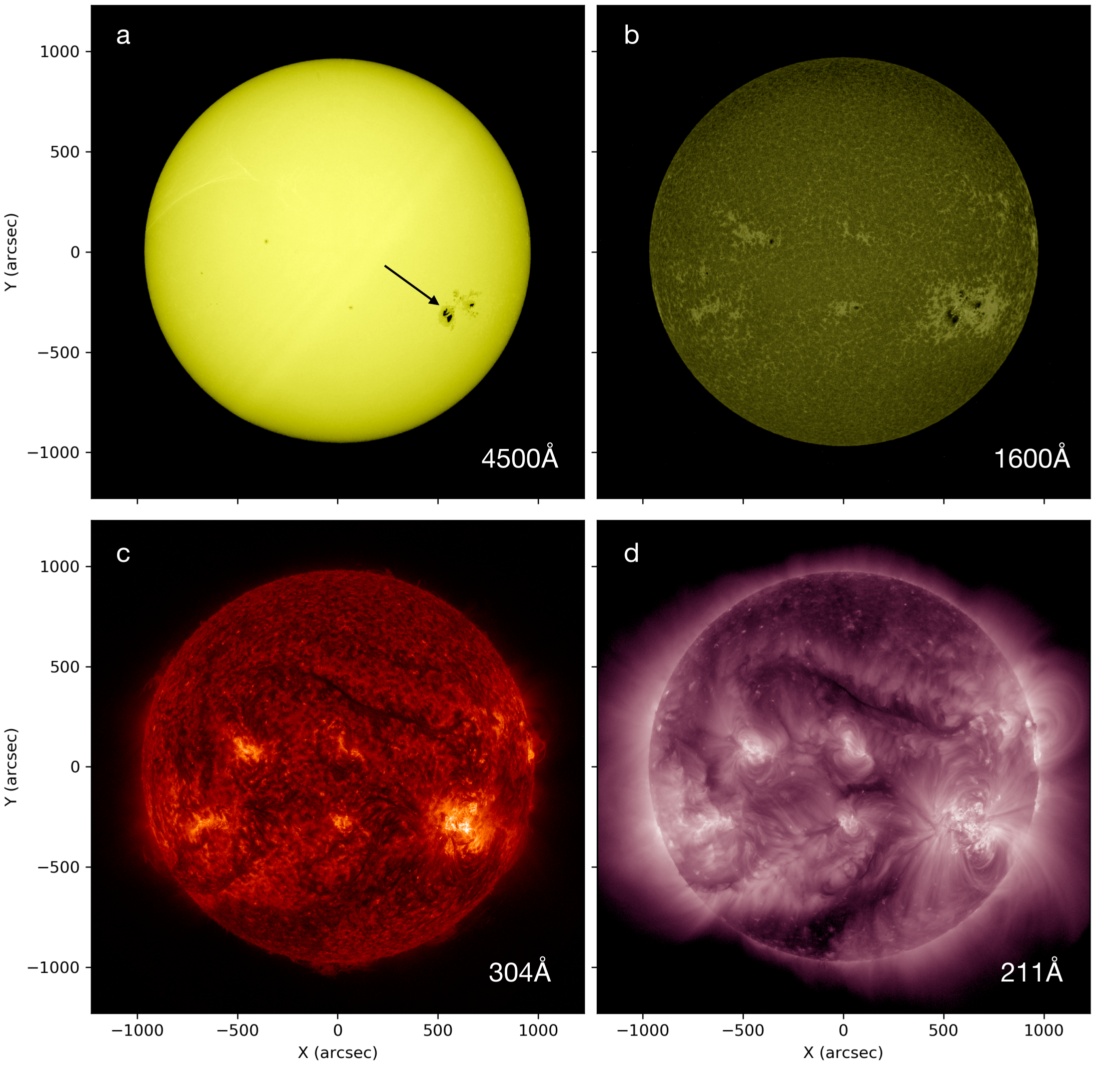

Figure 1.2: Images from the Atmospheric Imaging Assembly (AIA) on board the Solar Dynamics Observatory (SDO) demonstrating the different regions of the solar atmosphere. (a) The photosphere of the Sun observed in white light continuum observations from the 4500 Å channel of AIA. The arrow points to a sunspot group evident on disk. (b) The lower chromosphere observed in 1600 Å. The sunspot group can still clearly be seen with plage regions around it. (c) The 304 Å channel of AIA that is sensitive to both upper chromosphere and transition region. A bright active region can be observed around the region of the underlying sunspot groups. (d) The corona as observed in 211 Å. The extended nature of the emission and inhomogeneity can be observed, along with coronal loop structures.

1.1.4 Corona

The uppermost region of the solar atmosphere is the corona, an extremely hot and tenuous region, extending out above the transition region to several solar radii. The number density of the corona is typically on the order of 10^8 cm^{-3} but varies drastically over different regions of coronal structures, ranging from 10^6 cm^{-3} in quiet regions, and up to 10^{11} cm^{-3} in coronal flaring loops (Aschwanden, 2006). The temperature of the corona is $\sim$1 MK, but similar to the density structure, this can vary across different regions, reaching up to tens of MK in flaring loops.

The high temperature of the coronal plasma allows for the formation of emission features that belong to highly ionized heavy elements such as iron (Fe). This emission is primarily observed in EUV and X-ray wavelengths. The coronal plasma is magnetically dominated and coupled to the magnetic field ('frozen in'), causing the distribution of hot coronal plasma to trace out structures in the coronal magnetic field. Given the complexity of the magnetic field, the corona appears highly inhomogeneous and structured when observed in X-ray and EUV wavelengths, and consists of a combination of both 'open' and closed magnetic field configurations. Open field regions, which permanently exists at the poles, connect the solar atmosphere to interplanetary space to give rise to the fast solar wind. As heated coronal plasma escapes along these field lines, these regions have relatively low density and temperature and are observed as relatively dark regions in EUV, known as *coronal holes*. The most defining features of the corona are observed as bright active regions that are located around areas of intense magnetic field associated with underlying sunspots. These regions have a closed magnetic field configuration that act to confine hot plasma in coronal loops, giving an appearance of bright emission in X-ray and EUV as they are relatively hotter and more dense that the background.

1.1.5 Solar Magnetic Field and Active Regions

The solar magnetic field lies at the center of all solar activity and plays an integral role in the dynamics of the solar atmosphere. The magnetic field of the Sun is believed to be generated through a dynamo process. This process is believed to take place at $\sim$0.7 $R_\odot$ at the thin shear interface boundary between the solidly-rotating radiative zone and the differentially-rotating convective zone within the Sun's interior. This region interface is known as the *tachocline.* The complexity of the Sun's magnetic field is governed by the interchange between the poloidal and toroidal field components which give rises to a magnetic polarity flip that occurs every $\sim$11 years. This corresponds to the *solar cycle*, in which the solar magnetic field transitions from a poloidal state of minimal solar activity (solar minimum), through to a time of a toroidally stressed state of maximum solar activity (solar maximum) and back again. The solar cycle is characterized by the emergence rate of sunspots observed on disk, with a larger number of sunspots evident during times of maximum solar activity. Observations of the average number of sunspots hence acts as a indicator of the solar activity and can give historical accounts of the solar cycle. The numbering of the solar cycles began in the mid 19th century using compiled observations of the average number of sunspots. Cycle 1 refers to the 1755–1766 solar cycle. We are currently approaching solar minimum at the end of solar cycle 24.

The mechanism that creates the solar dynamo is unclear and is an active area of research (for a recent review see Charbonneau, 2010). The general paradigm of the Babcock model (Babcock, 1961) provides a schematic description of the processes that leads to the magnetic cycle. It begins with the Sun's magnetic field in a poloidal configuration that is aligned to the rotation axis. In the convective zone the gas pressure dominates the magnetic pressure (high-β condition, see Section 2.1) meaning that the motion of the magnetic field is determined by the motion of the plasma, i.e. the plasma will drag the magnetic field along with it as it moves. This condition combined with the differential rotation of the convective zone acts to force the magnetic field to deviate from its poloidal state, becoming wrapped up around the solar axis into a toroidal field state. This is known as the Ω-effect. As the field is continuously wound and stressed through this motion, regions of high magnetic density develop and twisted structures form flux-ropes. The internal pressure of the flux-ropes begins to increase until the gradient is large enough for the flux-ropes to become buoyant and rise up through the surface, forming sunspots of opposite polarity. A schematic view of this process is shown in Figure 1.3 adapted from Dikpati & Gilman (2009). The Coriolis force due to solar rotation, twists the loops back towards a north-south orientation regenerating the original poloidal field, known as the α effect, and hence completing the cycle, from a poloidal state to a toroidal one and back again.

Regions of concentrated flux emergence, such as in Figure 1.3 (d-f), form sunspot groups and complex magnetic field structures in the solar corona known as *active regions* (Fan, 2009). Sunspot groups typically exhibit a bi-polar nature, with a strongly concentrated leading magnetic polarity, followed by a more fragmented trailing group of opposite polarity. In this way, active regions are made

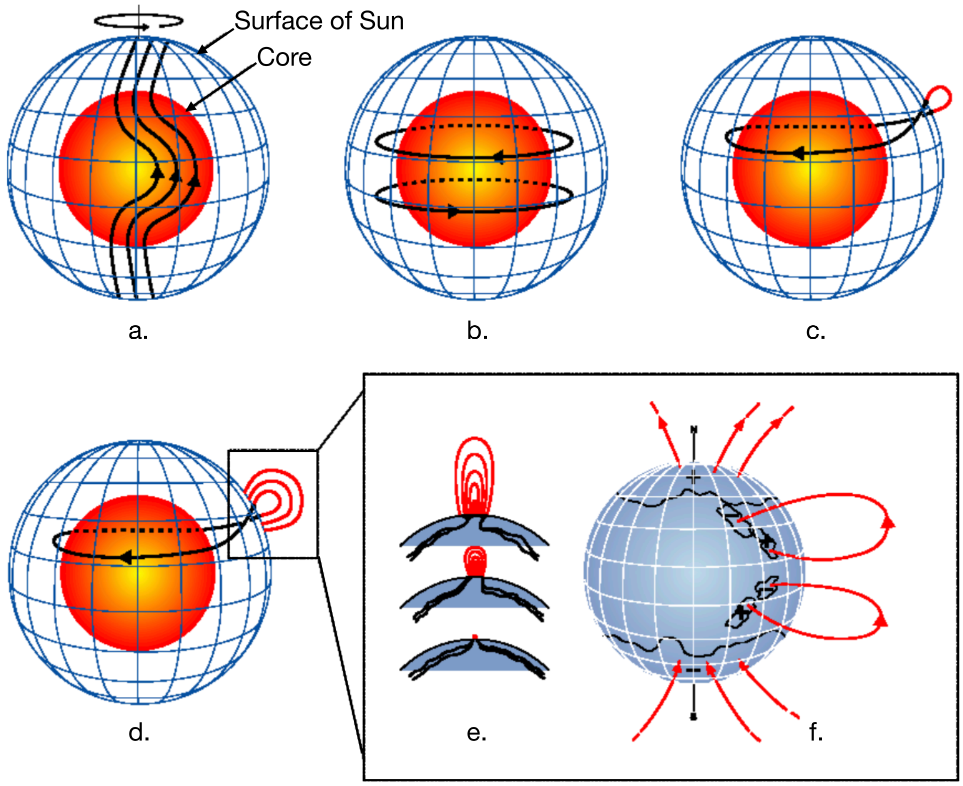

Figure 1.3: A schematic diagram of the solar dynamo process that results in flux emergence at the solar surface. (a) The poloidal field becomes sheared at the tachocline due to the differential rotation. (b) Toroidal field are then produced due to this shearing. (c) Regions of strong toroidal field become buoyant and rise up to the surface, twisting as they rise due to the rotational influence. Further flux emerges in (d) and (e) and expands outwards (f). Sunspots are formed at the base of the loops. Figure is adapted from Dikpati & Gilman (2009).

up of closed magnetic field structures in the form of coronal loops. The constant motion of the photospheric plasma, in which the magnetic footpoints of the coronal loops are anchored, causes the continual build up of non-potential magnetic energy, restructuring of the coronal magnetic magnetic field and triggering solar eruptive events.

1.2 Solar Flares

Solar flares are a sudden, powerful release of magnetic energy stored in the solar atmosphere. They are observed as an intense localized brightening, capable of releasing total energies on the order of 10^{25} J (10^{32} erg) in tens of minutes (Emslie *et al.*, 2004, 2012). Solar flares are the most energetic phenomena in our solar system. The central engine for this release is believed to be *magnetic reconnection*, a process in which sheared and stressed magnetic field lines reorganize themselves into a lower energy configuration (Priest & Forbes, 2002). During this process, stored magnetic energy is converted into both thermal and kinetic energy, accelerating particles to non-thermal velocities. This results in an enormous amount of both line and continuum emission from all layers of the solar atmosphere spanning the entire electromagnetic spectrum from radio to γ-rays (Fletcher *et al.*, 2011).

The magnitude of a solar flare is often characterized in terms of its associate GOES class, which ranks a flare based on the peak emission observed in the 1-8 Å channel of the X-ray sensor on-board the GOES satellite. GOES classes have a logarithmic scaling ranging from 10^{-4} to 10^{-8} Wm^{-2}, for which classes X, M, C, B and A are assigned. Within each class there is a linear scale from 1-9, except for the X-class range (largest flares) which can extend past an X10 classification. For example, a flare observed to have a peak flux of 2.2×10^{-4} Wm^{-2} is classified as an X2.2 flare. In the context of this classification, the largest flare of this solar cycle (cycle 24) was an X9.3 class solar flare. Estimates for the Carrington event place it as an X45±5 (Cliver & Dietrich, 2013). It should be noted however that not all solar flares have the same duration and hence the peak flux GOES classification is not necessarily the best proxy for classifying the energetics and total magnitude of a flaring event. However given that GOES soft X-ray observations are standardized in the same form since 1975, the GOES classification scheme offers the best modern systemic approach to characterize solar flare magnitudes.

1.2.1 Standard Flare Model

The standard framework for solar flares involving large scale magnetic reconnection is discussed in terms of the CSHKP model, a 2D model named after the scientists behind its principle development (Carmichael, 1964; Hirayama, 1974; Kopp & Pneuman, 1976; Sturrock, 1968). Although the intimate nature and mechanisms operating in flares are still unknown, this ‘standard model’ describes a widely accepted scenario of the fundamentals of flaring emission. Figure 1.4 displays a schematic overview of a flare eruption, illustrating the processes described by this model which are discussed in detail below.

Under the CSHKP framework, a rising magnetic flux rope, such as a rising filament, stretches out the magnetic field below forming a current sheet in the corona. Magnetic reconnection occurs between oppositely directed magnetic field lines in the current sheet above the loop apex, and the energy stored in the magnetic field is released, heating the local coronal plasma and accelerating particles to relativistic, non-thermal energies. The majority of the highly energetic particles spiral down along the newly reconnected closed magnetic field lines of the loop structure towards the chromosphere. The sudden increase in density at the chromosphere acts as a thick-target (Brown, 1971) for the accelerated electrons,

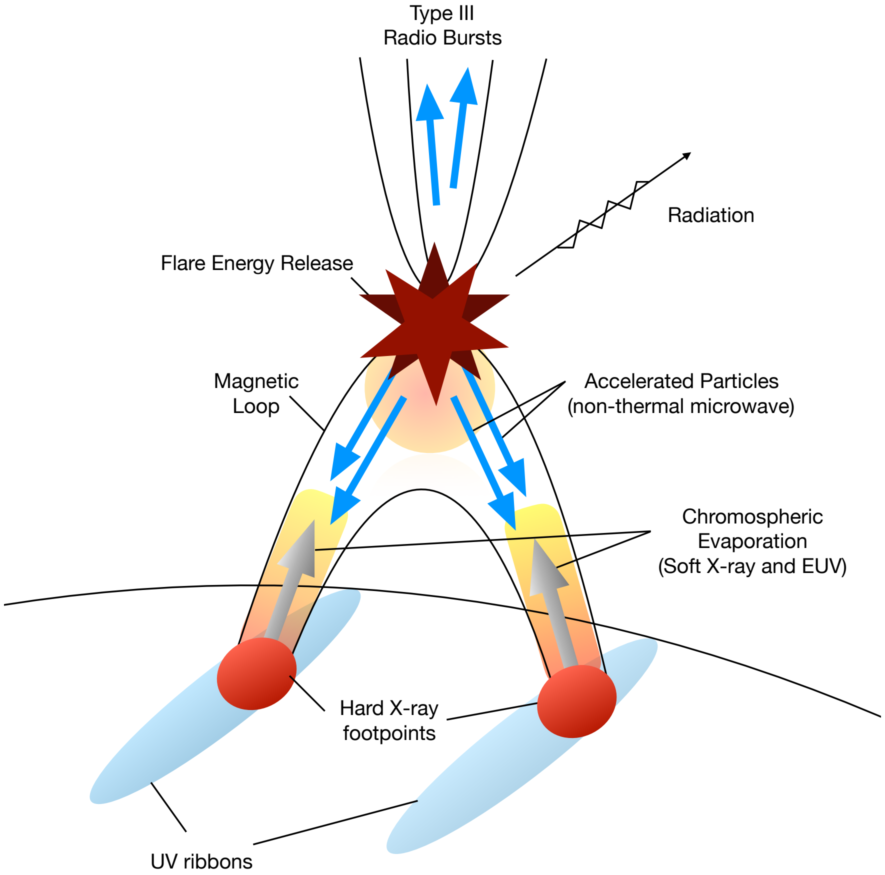

Figure 1.4: An illustration of the geometry and the associated flaring emissions as described by the standard flare model.

resulting in non-thermal bremsstrahlung emission, observed as hard X-ray footpoints. Accelerated ions also interact with the dense plasma, and excite nuclear reactions to produce γ-ray emission. As the precipitating accelerated particles lose their energy, mainly via Coulomb collisions, they rapidly heat the ambient plasma of the dense chromosphere. The efficient radiation process of the chromosphere however is much less than the rate of impulsive heating, resulting in the build up of pressure gradients. This imbalance drives mass up-flows of chromospheric plasma, observed as blue shifts in chromospheric lines with velocities on the order of 100s kms^{-1} (Milligan, 2015; Milligan *et al.*, 2006). This process is known as *coronal evaporation*, filling the coronal loops with hot plasma. This hot plasma (tens of MK) is the source of the soft X-ray and EUV emissions from flaring loops. Accelerated particles that are accelerated in an upward moving direction, have the opportunity to escape along open magnetic field lines and sometimes produce decimetric Type III radio bursts.

1.2.2 The Multi-wavelength Flare: Signatures and Timing

During the flare development, different physical processes dominate and the temporal evolution can be characterized by three main stages; the *pre-flare* phase, the *impulsive* phase and the *decay* (or gradual) phase (Benz, 2017; Fletcher *et al.*, 2011). In the pre-flare phase, initial signs of activity are observed as small-scale brightenings in EUV and soft X-ray as the flaring region slowly heats up. The abrupt flare onset occurs during the impulsive phase which is dominated by primary energy release with the bulk of this energy transferred to efficiently accelerating charged particles. This phase of flaring activity is characterized by hard X-ray, γ-ray, non-thermal microwave and in some cases white light continuum emission. These emissions all reflect the accelerations of highly energetic particles. Accompanying these are strong enhancement in chromospheric line and continuum emission, together with a rise in UV, EUV and soft X-ray intensity.

The morphology of solar flares can be either *compact* or *two-ribbon*; compact flares are characterized by a compact loop shape, whereas two-ribbon flares form an arcade of extended loops, so that the footpoints in the chromosphere are observed as extended UV brightenings, called *ribbons*. During the impulsive phase, brightenings in Hα and UV are also observed at the footpoints or in elongated ribbons at the footpoints of the flaring loop heated by the energetic electrons, or by thermal conduction.

Hard X-ray emission is generally observed as compact double-footpoint sources in the chromosphere located on either side of the magnetic polarity inversion line. These sources have a non-thermal power-law photon spectrum, suggesting the presence of an energetic population of non-thermal electrons that have precipitated into the chromosphere. In addition to the footpoint sources, coronal hard X-ray above-the-loop-top sources have also been observed (Masuda *et al.*, 1994). Similarly these sources display a non-thermal component in their energy spectrum which can be associated with thin-target emission of electrons propagating in a collisionless plasma of the corona. An example of hard X-ray observations from a solar flare is demonstrated in Figure 1.5 from Krucker & Battaglia (2013). The left panel shows the lightcurves of the hard X-ray (blue) emission from RHESSI (Lin *et al.*, 2002) and soft X-ray emission from the GOES X-ray sensor (shaded grey). The middle panel displays the flaring loop observed in EUV from the 193 Å channel of AIA, with hard X-ray contours (from RHESSI) overplotted on top. The hard X-ray (30-80 keV) contours are shown in blue and demonstrate two footpoint sources, slightly occulted over the limb, and a above-the-loop-top source. The soft X-ray (3-8 keV) contours in green are observed at the top of the loop which represents hot thermal plasma. The right hand panel demonstrates the energy spectra from both the footpoint and loop top sources, both of which exhibit a power-law shape.

Highly energetic accelerated electrons can also be magnetically trapped in the flaring loop due to the strong magnetic fields at the footpoint bases. Trapped electrons produce gyrosynchrotron emission as they propagate in the flaring loop, observed in microwave observations ($\geq$2 GHz). Eventually these electrons are scattered into the loss cone and can precipitate to the chromosphere. During the impulsive phase of a flare, hard X-ray and microwave emissions have extremely similar lightcurves, with bursts of emissions correlating well in both wavelength bands. This similarity is attributed to the fact that both emissions represent highly-energetic accelerated electrons that are produced during the energy release process. The electrons that precipitate to the chromosphere emit hard X-rays while those energetically trapped within the loop structure produce microwave gyrosynchrotron. The temporal relationship between the microwave and hard X-ray emissions suggests that a common source of energetic electrons is responsible for both emissions, however sometimes while the temporal relationship is the same, the spectral index variations of the both emissions can be different (White *et al.*, 2011).

In the context of X-ray emission from a flare, we talk about both 'soft' and 'hard' X-rays. Soft X-ray emission refers to thermal emission that takes the form of a Maxwellian distribution in energy, and typically dominates X-ray observations up-to ~20 keV. Hard X-ray emission on the other hand is associated with non-thermal bremsstrahlung and demonstrates a power-law energy distribution, dominating X-ray energies above ~20 keV. It is only the larger flares that have detectable hard X-ray emission above 100 keV. These two regimes are shown in an example X-ray photon spectrum shown in in Figure 1.6.

The main brightening in soft X-ray readily increases during the impulsive

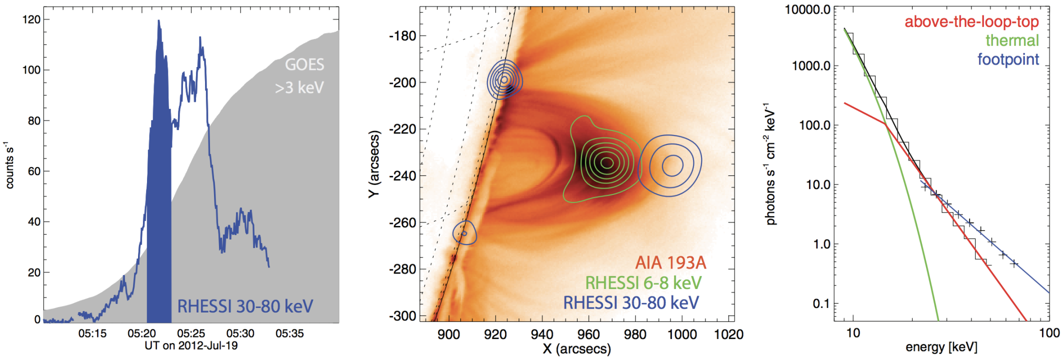

Figure 1.5: Summary of X-ray observations from an M7.7 solar flare from Krucker & Battaglia (2013). Left: Time-profile from both RHESSI 30-80 keV (blue) and GOES 1–8 Å (grey). The shaded blue region is the time interval of the main hard X-ray peak that used to construct the image in the middle panel. Middle: The hard X-ray footpoints and loop top source can be identified as the blue contours, whereas the soft X-ray source in the 6-8 keV energy range is shown as the green contours. These X-ray contours are overplotted on the EUV 193 Å channel image from AIA. Right: The imaging spectroscopy results of the source. Figure from Krucker & Battaglia (2013).

phase, reaching a peak that invariably lags that of hard X-ray, a manifestation of the so-called Neupert effect (Dennis & Zarro, 1993; Neupert, 1968). The Neupert effect is an empirical relationship that relates the flux of hard X-rays to the time-derivative of the soft X-ray flux[1] ($F_{hxr} \propto \dot{F}_{sxr}$), implying a causal relationship between energetic electrons and the heated plasma. An example of the Neupert effect observed during a flare is shown in Figure 1.7 from Dennis & Zarro (1993). The GOES soft X-ray time profile is shown in (a) and the numerical derivative of this lightcurve is shown in (b). The corresponding hard X-ray lightcurve from the Hard X-ray Burst Spectrometer (HXRBS) is shown in (c). The temporal relationship between the soft X-ray time derivative and the hard X-ray time profile is clearly evident. This relationship is attributed to the fact that the soft

---

[1] In the original paper, Neupert (1968) actually related the time integral of microwave emission to that of the soft X-ray emission.

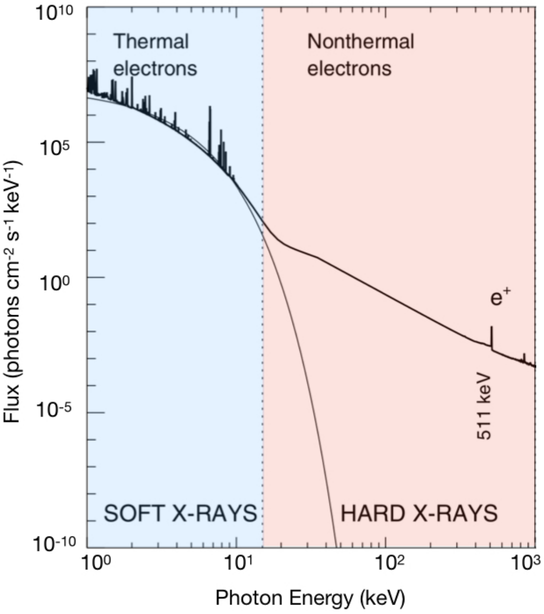

Figure 1.6: An example of a photon spectrum of a large solar flare, demonstrating both the soft X-ray (~1–10 keV) and hard X-ray (~10 keV–1 MeV) spectral regimes. Figure adapted from Aschwanden (2006).

X-ray emission originates from a plasma ($T \geq 10^7$ K) heated by the deposited energy from accelerated electrons, observed as hard X-rays.

The decay phase follows the rapid and energetic impulsive phase, and is identified by slowly decaying soft X-ray and EUV signatures as the coronal plasma gradually returns to its original state. Although continued energy release and heating events may continue into the decay phase, the emission associated with accelerated particles (e.g. hard X-rays) is generally no longer observed, and the physical process that dominates is that of cooling. It is during this time that the effects of the flare on the corona become apparent. Arcades of coronal flaring loops that result from the reconfiguration of the magnetic field during the impulsive phase are filled with flare heated plasma that emit in soft X-ray and EUV.

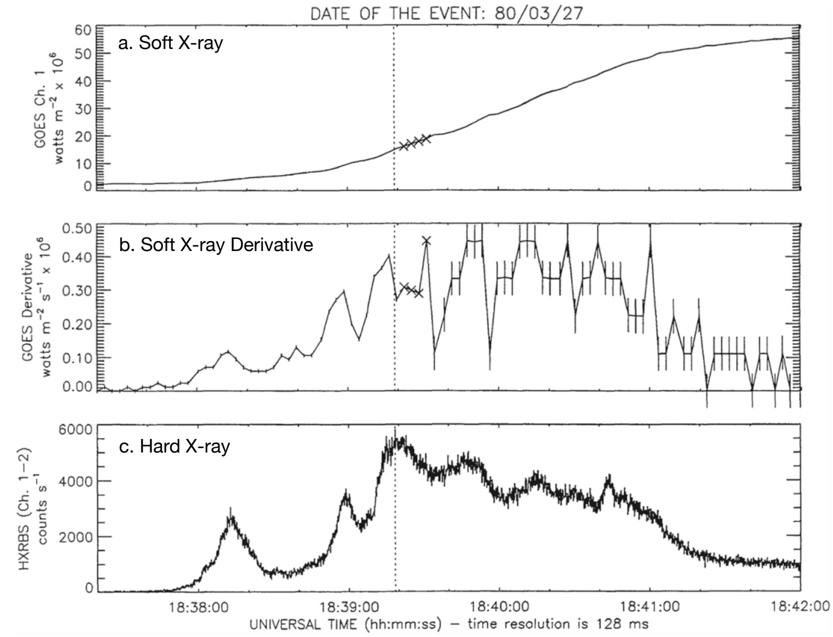

Figure 1.7: An example of the Neupert effect observed during the impulsive phase of a solar flare. The GOES 1-8 Å lightcurve is shown in (a), and its time derivative shown in (b). The corresponding hard X-ray observations in the energy range of 26-51 keV from the Hard X-ray Burst Spectrometer (HXRBS) on board the Solar Maximum Mission is plotted in (c). A correlation can be observed between the hard X-ray and the soft X-ray derivative. Figure from Dennis & Zarro (1993).

The emission and temperature of this plasma gradually falls throughout the decay phase due to the cooling processes that occur (e.g. Raftery *et al.*, 2009). During the early decay phase, thermal conduction is the dominant cooling mechanism given the high temperatures present. Later in the decay phase, as the temperature decreases, radiation as a cooling mechanism dominates (Culhane *et al.*, 1970; Raftery *et al.*, 2009; Vršnak *et al.*, 2006). A delay in the expected cooling times is observed in most flares, interpreted as some form of additional post flare heating mechanism (Cargill *et al.*, 1995; Ryan *et al.*, 2013).

Post-flare loops often exhibit a 'cusp-shaped' structure, and are observed to grow upwards and outwards as time proceeds (Gallagher *et al.*, 2002; Liu *et al.*, 2013), with the hottest plasma observed in the outermost loops. The cusp-structure is indicative of the shape of a magnetic field below a coronal current sheet following reconnection, and hence provides circumstantial evidence for continuous reconnection during this time (Fletcher *et al.*, 2011). The motion outwards is interpreted as the reconnecting site moving slowly upwards in the corona resulting in newly reconnected loops that are then filled with hot plasma. Further evidence for continued magnetic reconnection is the observation of supra-arcade downflows observed in EUV, suggestive of reconnection outflows (McKenzie & Hudson, 2001; Savage & McKenzie, 2011).

The standard flaring model outlined here provides a big-picture view of the solar flare phenomenon, and can successfully describe many of the observational features of solar flares. However the detailed physics of the energy release, particle acceleration, and heating processes are not fully understood and a unified view of fundamental flaring processes remains elusive. One important observational feature that is not taken into account in the standard flare model is that the emission associated with the energy release is often accompanied by a sequence of 'bursty' pulsations and oscillatory signals known as *quasi-periodic pulsations.*

1.3 Quasi-Periodic Pulsations

Solar flare emission is often accompanied by pronounced pulsations and oscillatory signatures known as quasi-periodic pulsations (QPPs). The definition of QPPs is loosely defined in the literature but is most often used to describe variations of flux as a function of time that appears to have a characteristic timescale or periodic component. The presence of QPPs is observed across a wide range of wavelengths from radio and microwaves to hard X-ray and γ-rays, encompassing all aspects of the flaring process. The typical characteristic timescales of QPPs range from seconds to several minutes, although both shorter (millisecond, Tan & Tan, 2012) and longer ($\sim$tens of minutes, Foullon *et al.*, 2010) periods are also found. There is growing evidence that the QPP phenomena is a common, if not intrinsic, feature of solar flares (Kupriyanova *et al.*, 2010; Simões *et al.*, 2015), and likewise well pronounced QPPs have been observed in stellar flares (e.g. Doyle *et al.*, 2018; Pugh *et al.*, 2016). A prominent example of QPPs observed in flaring emission is the 'seven-sisters flare' (Kane *et al.*, 1983) shown in Figure 1.8. Here QPPs are observed in both hard X-ray and radio observations, with a period of $\sim$8 s.

The scientific interest in QPPs has many motivations. The occurrence of QPPs in flaring emission places important constraints on the interpretation and understanding of the physical processes operating in flares such as magnetic energy release, particle acceleration and heating processes, and hence a full description of the QPP phenomena is required in order to work towards an integrated model of solar flares. Furthermore, the apparent similarity between solar and stellar QPPs (e.g. Cho *et al.*, 2016) indicates that a common underlying mechanism occurs in both, and hence the investigation of solar QPPs may aid in the development of the understanding of stellar flares. An example of QPPs detected in a large megaflare from M-dwarf star YM CMi observed in white light emissions from Anfinogentov *et al.* (2013) (see also Kowalski *et al.*, 2010) is shown in Figure 1.9. The work outlined in this thesis aims to further the current understanding of QPPs in solar flares through multi-wavelength observational studies of solar flare events.

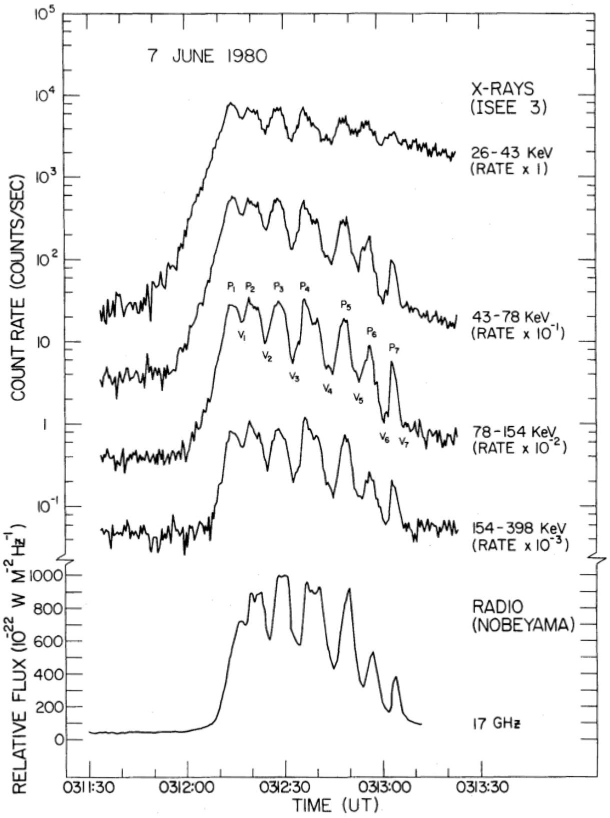

Figure 1.8: QPPs observed in radio and hard X-ray intensities from the famous 'seven-sisters' solar flare on June 7 1980. Note the several distinctive peaks in both wavelength bands, separated by ∼8 s, with some substructure observed within the larger peaks. Figure from Kane *et al.* (1983).

The nature of QPPs in flaring lightcurves has been an important topic in solar flare studies for several decades, and has been widely discussed in the literature (see Nakariakov & Melnikov, 2009; Van Doorsselaere *et al.*, 2016b, for recent comprehensive reviews). The presence of QPPs was first reported in early hard X-ray and microwave observations (e.g. Chiu, 1970; Parks & Winckler, 1969). Indeed, the most pronounced QPPs are often observed in these wavebands associated with flare accelerated non-thermal electrons, particularly during the impulsive phase of solar flares (e.g. Asai *et al.*, 2001; Fleishman *et al.*, 2008; Inglis *et al.*,

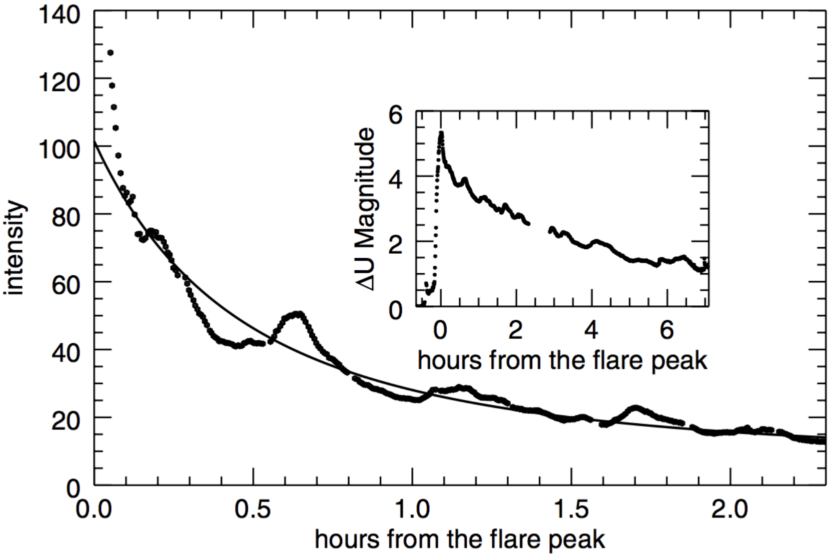

Figure 1.9: An example of QPPs detected in stellar flaring emission. This plot demonstrates a lightcurve of the white light emission from a megaflare observed from YZ CMi on January 16 2009. QPPs can clearly be identified throughout the decay phase of the flare. Figure from Anfinogentov *et al.* (2013).

2008). Modulation depths of the pulsations can sometimes reach up to 100% of the emission trends, and are often detectable by eye without any data-processing (i.e. such as detrending). In recent years however, studies have provided evidence of QPP signatures across the whole electromagnetic spectrum of flaring emission, such as γ-rays (Nakariakov *et al.*, 2010), chromospheric line emission (Brosius & Daw, 2015), and soft X-ray and EUV (Dolla *et al.*, 2012; Simões *et al.*, 2015). In particular, observations have demonstrated that QPPs can co-exist across different wavelengths spanning both non-thermal and thermal emissions. An example of this is shown in Figure 1.10 from a multi-wavelength study by Dolla *et al.* (2012).

QPPs are most often detected during the impulsive phase of solar flares, but have also been reported during both the pre-flare phase (Tan *et al.*, 2016) and into the decay phase (Simões *et al.*, 2015; Zimovets & Struminsky, 2010). The relationship between the phases of a solar flare and detection of QPP signatures remains unclear. QPPs can also be non-stationary, with both the amplitude and period varying in time (Dennis *et al.*, 2017; Nakariakov *et al.*, 2018b; Reznikova & Shibasaki, 2011). Several statistically significant periods have also been observed to co-exist in QPP events (Inglis & Nakariakov, 2009; Kolotkov *et al.*, 2015).

The exact nature and underlying physical mechanism for the generation of QPPs remains debated. Two main theories are currently being pursued as possible causes of QPP signatures. These are that the QPPs are driven by either magnetohydrodynamic (MHD) waves in the coronal flare site, or instead an intrinsic feature of the reconnection process which may be periodic or 'bursty'. A combination of these has also been suggested. To date, observations have not been able to permit an unambiguous choice between various QPP models, and it is quite likely that a number of non-exclusive mechanisms play a role. A comprehensive description of proposed mechanisms is detailed in a recent review by McLaughlin *et al.* (2018), and is discussed further in Chapter 2. Identifying the underpinning mechanism generating QPPs is important not only to develop a self-consistent model of flaring energy release, but also for the exploitation of QPP observations in coronal seismology - the inference of magnetic and other plasma properties from observed oscillatory behaviour in the solar corona (e.g. De Moortel & Nakariakov, 2012).

The difficulty in determining the true nature and governing mechanisms of QPPs is that the quasi-periodic signatures manifest at different wavelengths associated with physically different processes. For example, hard X-ray emission is associated with bremsstrahlung emission produced by accelerated electrons in-

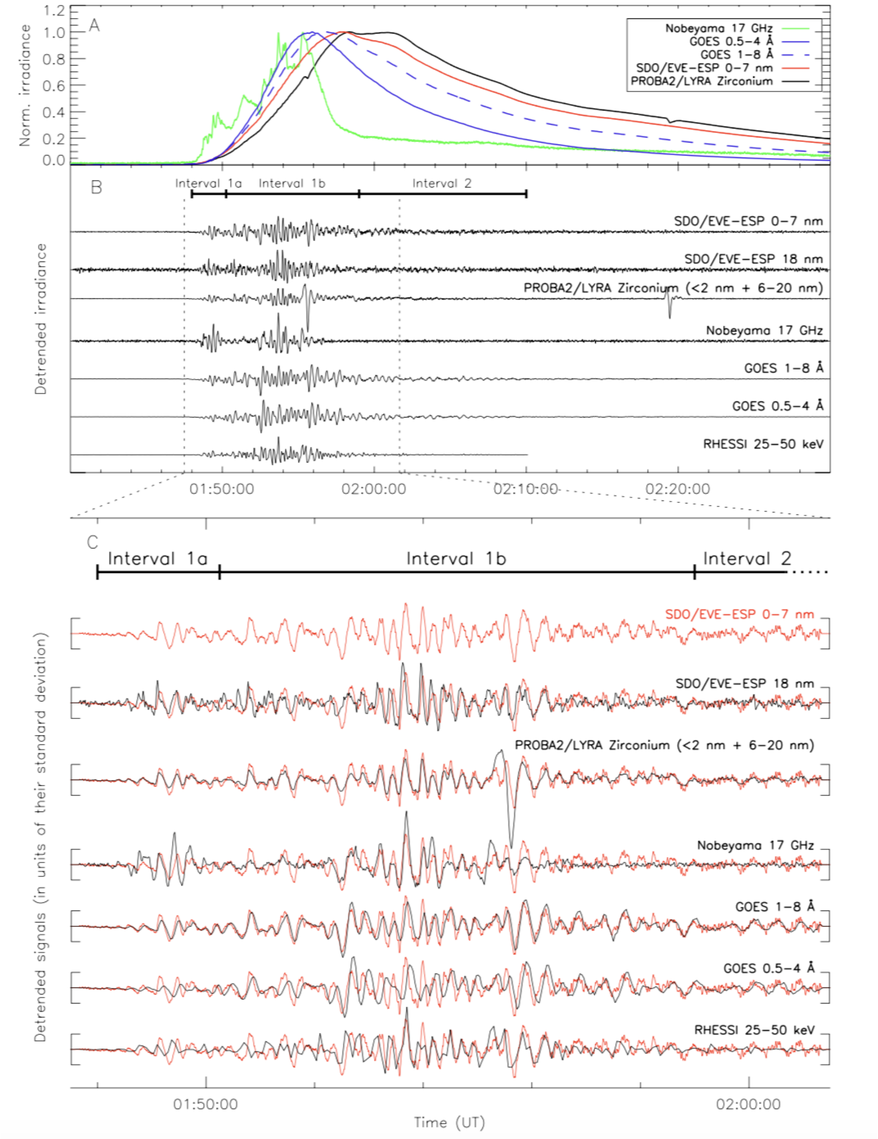

Figure 1.10: Detection of co-existent QPPs in both thermal and non-thermal emission. The top panel shows the lightcurves during the flare, with the subsequent panels displaying the detrended lightcues which highlight the quasi-periodic fluctuations across all channels. Figure from (Dolla *et al.*, 2012)

teracting with the dense layers of the chromosphere, and depends on the ambient density. Microwave emission on the other hand depends on the magnetic field strength and other plasma properties. QPPs at soft X-ray and EUV wavelengths depend on the thermal plasma properties and heating mechanisms. Hence a unified model to explain to generation of QPPs must be able to describe the variations of electron acceleration, plasma parameters, thermal processes and reconnection itself. Detailed multi-wavelength investigations into the presence of QPPs and their relationships with other flaring features is required to help constrain potential mechanism properties. This is the focus of the research presented in Chapters 4 and 5.

1.4 The Earth's Ionosphere

The ionized region of the Earth's atmosphere that exists between 60-1000 km in altitude above the Earth's surface is defined as the *ionosphere*. The ionosphere is formed through photoionization of neutral atmospheric constituents primarily by solar radiation and highly energetic particles that penetrate the upper atmosphere. The presence of free electrons and ions effectively makes this region of the upper atmosphere an electrical conductor affecting the propagation of all radio waves. In this way, the ionosphere plays a governing role in radio wave communications, permitting the reflection of radio waves over a broad range of frequencies.

The presence of the ionosphere was realized at the beginning of the 20th century following Marconi's famous trans-Atlantic experiment in which a radio signal was sent from Cornwall in the UK to St-Johns in Newfoundland. In order to explain how a radio signal could travel this distance around the curvature of the Earth, O. Heaviside and A. Kennelly both (independently) suggested in 1902 the presence of a conductive atmospheric layer from which the signal was reflected.

Experimentally, the existence of the ionosphere was later proven unambiguously by Appleton and Barnett (Appleton & Barnett, 1925) through radio phase measurements. In the years that followed, the known existence of the ionosphere enabled high-frequency world-wide communications to be established.

1.4.1 Ionospheric Regions

The ionosphere can be divided into four main ionized regions, namely the D, E, F1 and F2 in order of increasing altitude (Davies, 1990). These regions are historically defined by radio wave reflections at different altitudes, depending on the electron density present. The critical frequency, f_{crit} at which a wave will reflect depends on the electron density N_e ($f_{crit} \propto \sqrt{N_e}$), thus higher frequencies will penetrate further into the ionosphere and are reflected at regions of higher electron density. It was originally considered that the ionosphere consisted of distinct layers, however it is now clear that it is a continuous medium with several 'bumps' in the electron density profile resulting in the observed reflections. The structure of the ionosphere's vertical electron density profile as a function of altitude above the Earth's surface is shown in Figure 1.11. The different regions have a physically different ion chemistry and characteristics affecting radio communications in different ways. The Sun and solar activity both produce and maintain the ionosphere and drive the dynamics of its variability. The highly variable nature of the ionosphere is demonstrated in Figure 1.11, showing the electron density variations both as a result of the diurnal effect (day and night) and during different times of solar activity (solar max and min).

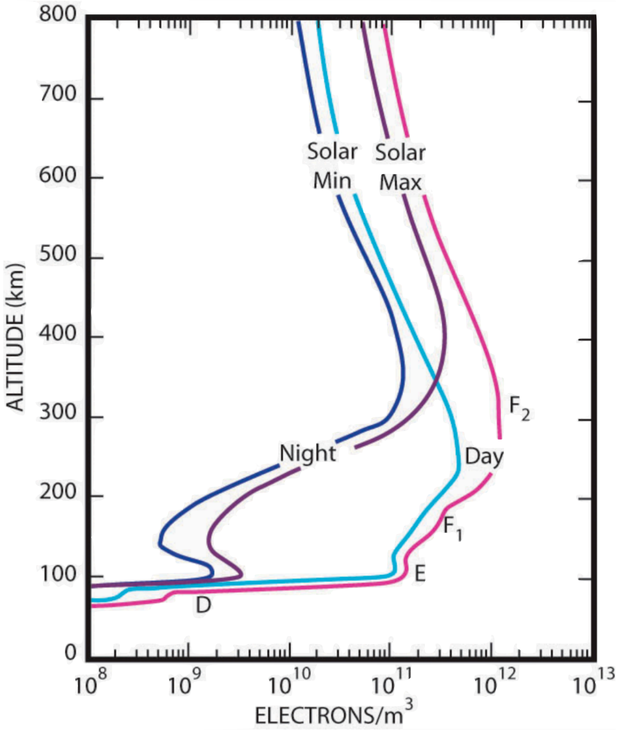

Figure 1.11: The electron density structure in the ionosphere, demonstrated for both night and day, and during solar minimum and solar maximum. Figure from Wiki University of Oulu, *Chapter 3: The ionosphere of the Earth*.

1.4.1.1 D-region

The D-region is the lowermost region of the ionosphere, extending in altitude from 60-100 km. It has a comparatively low electron density compared to the other ionospheric regions, on the order of $10^8 - 10^9$ m^{-3}. Ionization in the D-region is produced by both solar radiation and galactic cosmic rays. Solar Lyman-α (1216 Å) radiation is the primary source of ionization in the D-region, ionizing the minor constituent nitric oxide (NO), however X-rays ($\lambda < 10$ Å) acting on nitrogen (N_2) and oxygen (O_2) (Hargreaves, 1992) also can have a significant role in times of solar maximum, and particularly during solar flares (Grubor *et al.*, 2008). Given the high neutral density in the D-region, collisions are frequent and recombination processes dominate. The D-region varies both due to diurnal and seasonal effects, and almost disappears at night due to the various recombination processes. Negative ions are a distinguishing feature of the D-region, and the photochemistry of this small region of the ionosphere is the most complex, and least understood.

The D-region plays a significant role in radio wave communications. The high collisional rate in this region has the effect to absorb or attenuate radio waves, particularly mid frequency (MF; 300 kHz–3 MHz) and high frequency (HF; 3 MHz–30 MHz) portions of the radio spectrum. This has adverse effects on the radio wave communications that make use of these frequencies, with this effect more apparent during times of increased ionization (e.g. during a solar flare). At lower frequencies, such as VLF (3–30 kHz) the D-region acts as a reflector.

1.4.1.2 E-region

The E-region is located just above the D-region and extends 100-170 km in altitude, and has electron density values in the range of 10^{11} m^{-3}. The primary ionization source for this region is from solar soft X-ray ($\sim$10-100 Å) and EUV in the 1000-1500 Å wavelength range (Hargreaves, 1992). The neutral density in the E-region is much less than that of the D-region and far fewer collisions occur. At night the E-region becomes weaker but does not disappear. This is the region first discovered by Marconi in 1901.

1.4.1.3 F-region

The F-region has the highest electron density in the ionosphere extending 170-600 km in altitude. During the day, increased ionization splits the F-regions into a lower F1 (170-200 km) and upper F2 (300-600 km) region. Much of the ionization in the F-region comes from solar UV as well as part of EUV, typically in the wavelengths range of 100-1000 Å. The high electron density in spite of the low atmospheric neutral density at these altitudes means that recombination in this region is significantly reduced, and the F2-region exists during the night. Given the large electron densities in the F region, it acts as a reflector to HF radio waves, enabling HF communications.

Above the F-region (above 600 km) is the so-called *topside* ionosphere. The electron density decreases again due to the extremely low atmospheric density, and its dynamics here are controlled by the governing magnetic field of the Earth.

1.4.2 Solar Flare Effects on the Ionosphere

Solar flares have direct consequences on the ionosphere (Davies, 1990; Mitra, 1974; Tsurutani *et al.*, 2009). The enhancement of EUV and X-ray emission during a flare results in the rapid increase of ionization on the entire dayside ionosphere causing a *sudden ionospheric disturbance* (SID). While SIDs occur in all regions of the ionosphere, the effect on the D-region is the most apparent. In particular, X-rays with $\lambda <10$ Å penetrate down to D-region altitudes and dominate photoionization of all neutral constituents there, including N_2 and O_2. The altercation to the D-region electron density profile caused by the enhanced ionization leads to a series of effects on the propagation of radio waves over a large range of frequencies (Mitra, 1974). VLF (3–30 kHz) radio waves can experience an increase in signal strength, whereas adverse deleterious impacts are experienced at the higher end of the spectrum. HF radio waves, such as those used by HF radio communications, reflect at higher regions of the ionosphere such as the E and F regions, passing through the D-region as they travel. As a result of a SID, HF waves interact with the increased number of free electrons in the D-region and lose their energy due to the more frequent collisions that occur in this enhanced environment. The radio signals then become degraded, or in severe cases are completely absorbed, rendering the use of some frequencies unusable. This is known as a radio blackout. The onset of a SID is often abrupt, and is followed by a relatively slow recovery (Davies, 1990). Other solar flare effects include sudden frequency deviations of HF reflected signals, as well as an increase in the total electron content (TEC) caused by increased ionization in the upper F and E regions. This increase in TEC plays an important role in solar radio interferometric observations, causing the observations of radio sources to be misplaced due to refraction. This is a particular cause for concern for instruments like the LOw Frequency Array (LOFAR) which operates at low frequencies susceptible to ionospheric effects ($\sim$10–250 MHz).

A recent example of adverse solar flare effects on the ionosphere was during the devastating Caribbean hurricanes that occurred in September 2017. Coincidental to these events, an evolving active region on the Sun produced a number of large X-class flares that resulted in radio communication disruptions during a time of the major weather emergency (Redmon *et al.*, 2018). On the 6th of September, as communities were responding to hurricane Irma, the largest flare of this solar cycle - an X9.3 - erupted and caused a HF radio blackout. This blackout was reported to occur for up-to 8 hours, effecting emergency services that rely on HF communications. The French civil aviation also reported a 90-minute loss of communication with a cargo plane. A few days later, following storm Jose, further blackouts were experienced by another large solar flare on September 10 (X8.2). Our understanding of the solar-terrestrial relationship, particularly in response to dynamic solar flares, is a major focus of current space weather research.

1.4.3 The D-region as an X-ray Detector

The response of the D-region electron density to ionizing disturbances can be reliably probed through the observation of VLF (3–30 kHz) radio signals that propagate in the waveguide formed between the Earth's surface and the lower ionosphere. The D-region acts as a sharp reflective boundary to VLF radio waves, and the amplitude and phase of a received VLF signal inherently contains information about the D-region electron density and collisional frequency. In undisturbed conditions, the propagation of VLF signals is stable in both amplitude and phase, characterized by a predictable diurnal variation. During a flare however, the increased ionization at the upper boundary of the Earth-ionosphere waveguide, through which VLF waves reflect, is significantly altered and manifests as variations in received VLF signals. The variations are observed as sudden amplitude enhancements and phase advancements given that the increased electron density acts to make the upper waveguide boundary a sharper reflector and reduces the reflective height. Measurements of narrowband VLF signals that are transmitted by large navigational and communication transmitters located around the world can hence be used as a detector to sudden ionospheric disturbances caused by solar flares. These measurements, together with theoretical models of the VLF propagation and conductivity profile (Wait & Spies, 1964b) of the lower ionosphere can be used to estimate the variation of electron density with height and time in the D-region.

The direct measurement of the D-region electron density is a difficult task as its altitude is too high for balloons and too low for satellites, and the usual radio techniques for ionospheric measurement (e.g. ionosonde and incoherent scatter radar) do not work well given the comparatively low electron density. Rockets and radar measurements have been used, but they provide poor spatial and temporal resolutions and can't be used for continuous monitoring. In this way, VLF remote sensing of the D-region is a unique tool to probe this complex region and gain understanding of the dynamical processes. It has been utilized extensively in the study of solar flare effects on the D-region (Grubor *et al.*, 2008; McRae & Thomson, 2004; Palit *et al.*, 2013; Thomson *et al.*, 2005; Žigman *et al.*, 2007), and indeed in the study of other transient ionospheric disturbances at D-region altitudes from phenomena such as gamma ray bursts (Inan *et al.*, 1999), solar eclipses (Kumar *et al.*, 2016), meteor showers (Kaufmann *et al.*, 1989) and from terrestrial disturbances such as lightening strikes (Shao *et al.*, 2013), and even earthquakes (Parrot & Mogilevsky, 1989).

An observation of solar flaring signatures in VLF measurements is shown in Figure 1.12. The top panel shows the amplitude of a VLF signal that was received in Birr, Co. Offaly, Ireland from the large VLF transmitter (24 kHz) located in Culter, Maine, US. The bottom panel shows the GOES soft X-ray measurements. Clearly, during daytime, solar flares can readily be detected in VLF signal amplitude variations, reflecting the enhancement of the D-region electron density. The

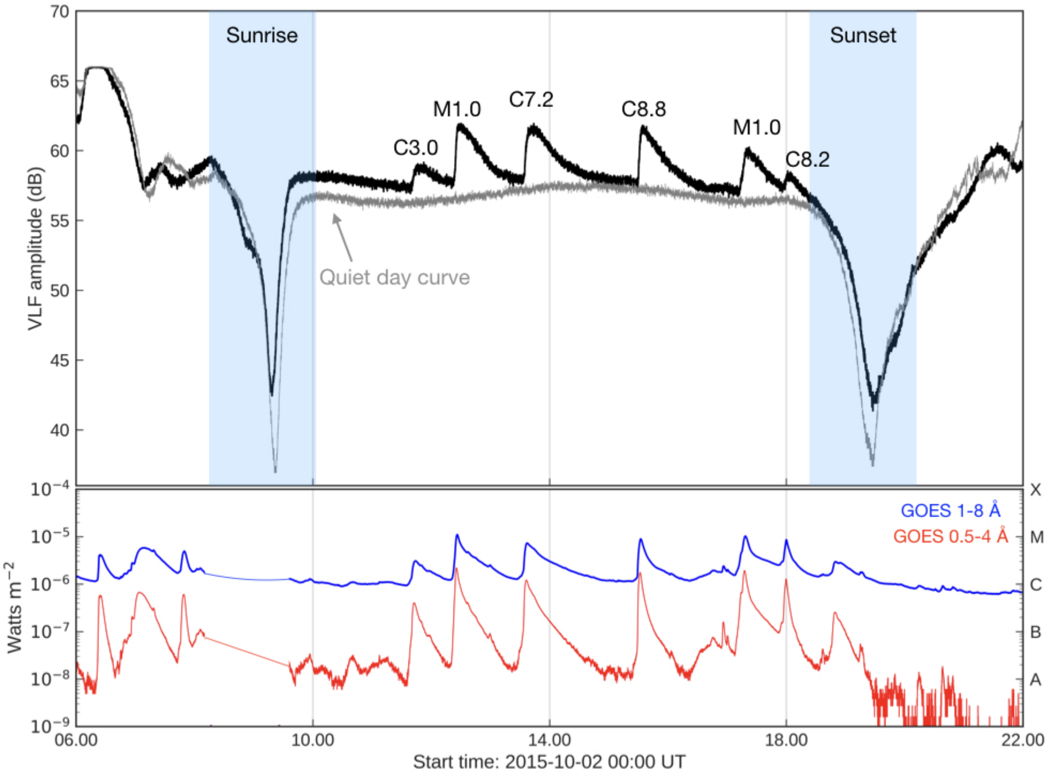

Figure 1.12: Example of VLF observations of solar flares during an active flaring day from April 2 2015. The top panel shows the VLF amplitude measurements from April 2 2015 (black) and from a quiet day with no solar flares on April 6 2015. The signal was received with a sudden ionospheric detection monitor (see Chapter 3). The bottom panel shows the GOES measurements of solar X-ray flux in both the 1–8 Å and 0.5–4 Å channels.

signal falls sharply before sunset, follows a diurnal pattern during the day, and then recovers fairly rapidly at sunset. The reason has to do with the formation of and detachment of negative ions and sunrise and sunset. The grey curve shows a solar quiet day, in which no solar flares occurred.

Now that it has become clear that QPPs are a common feature of solar flares, particularly in X-ray emission, the question arises as to whether quasi-periodic signatures can be detected in the terrestrial ionosphere. To date, no such studies have been performed.

1.5 Thesis Outline

The research presented in this thesis attempts to further the current understanding of the nature and characteristics of QPPs, both in solar flare emission and into the impact flaring QPPs have on the terrestrial ionosphere.

In Chapter 2, we present the relevant theoretical background for the research outlined in this thesis and provide an overview of the current proposed mechanisms of the generation of QPPs in solar flares. A description of the D-region electron density profile and VLF radio wave propagation is also detailed in this chapter. In Chapter 3 the different observational instruments that provided the data that is used in this thesis is described.

In Chapter 4 we present a multi-wavelength investigation of QPPs identified in the emissions of an X-class solar flare. In this study we focus on the recently identified temporal fine structure QPPs that are observed in the soft X-ray time derivative, and investigate the detailed characteristics of these QPPs during both the impulsive and decay phases of this solar flare and compare the variability with QPPs detected in the non-thermal emissions including hard X-ray and microwave observations. The results of this study are published in Hayes *et al.* (2016).

Building upon this, in Chapter 5 we perform a second investigative study into the nature of the fine structure QPPs observed in a large solar eruptive X-class flare. In this study we report extensive soft X-ray QPPs that are detected throughout the entire solar eruptive process, both during the impulsive phase and late into the decay phase, up to three hours after the peak of the flare. These observations provide one of the longest duration QPP events detected on these timescales (several tens of seconds). We relate the QPP features to the spatial features of the flare using spatially resolved observations from RHESSI and AIA. This investigation is currently in review as Hayes *et al.* (2019).

As outlined above, solar flares can significantly affect the conditions of the terrestrial ionosphere, but to date it was not known if the ionosphere was sensitive to solar flaring QPPs. In Chapter 6 we present the first detailed investigation into the relationship between long period X-ray QPPs and the lower ionospheric response. In this study we focus on VLF remote sensing of the ionospheric D-region, and present for the first time the detection of synchronized solar flaring QPPs and corresponding electron density variations of the lower ionosphere. This research is detailed in Chapter 6 and the results of this work has been published in Hayes *et al.* (2017).

Finally, in Chapter 7 we provide a summary and conclusion of the results in this thesis and explore future work directions.

2

Theoretical Background

In this Chapter the necessary formulation and theoretical basis that underpin the research performed in this thesis are introduced. We begin with an introduction to the magnetohydrodynamic description of the solar atmosphere and the associated waves and oscillatory behaviour that can be supported in such a magnetized plasma medium. These topics are then built upon to discuss the theories of magnetic reconnection, the process believed to be the primary driver of solar flare energy release. The different suggested QPP mechanisms are then discussed in detail. Finally an introduction to the propagation of VLF waves in the Earth-ionosphere waveguide is presented and a discussion about how this theory can be used to infer the electron density from VLF signal measurements.

2.1 Magnetohydrodynamics (MHD)

A well-established framework to describe the collective behaviour of plasma in the presence of a magnetic field is that of *magnetohydrodynamics* (MHD). MHD treats a plasma as an electrically conducting, magnetized, fluid that is expressed in terms of macroscopic parameters of density, velocity and pressure. Mathematically, MHD couples Maxwell's equations of electrodynamics with Navier-Stokes equations of fluid dynamics to describe the evolution of plasma and the interplay between the plasma motion and the magnetic field.

In describing a plasma in terms of MHD, a number of implicit assumptions are made; the plasma is treated as electrically neutral (i.e. equal number of ions and electrons), the characteristic speeds of the plasma are assumed non-relativistic (i.e. $\mathrm{v} \ll \mathrm{c}$), the characteristic timescales are much greater than the ion gyro-period and mean free path time, and similarly the characteristic length scales are much greater than the Larmor radius and mean free path length of the plasma. In this way MHD describes large-scale, highly ionized plasmas and hence works well in describing the plasma in the solar corona.

2.1.1 Maxwell's Equations

To begin, we examine Maxwell's equations, as they form the foundation of the electromagnetic contribution to the set of MHD equations describing a plasma.

Maxwell's equations form a closed set of equations that relate the electric field **E** to the magnetic field **B**, and are given below in the form of Ampère's law, the solenoid constraint, Faraday's law and Gauss's law, respectively:

$$\nabla \times \mathbf{B} = \mu_0 \mathbf{j}, \tag{2.1}$$

$$\nabla . \mathbf{B} = 0, \tag{2.2}$$

$$\nabla \times \mathbf{E} = -\frac{\partial \mathbf{B}}{\partial t}, \tag{2.3}$$

$$\nabla . \mathbf{E} = \frac{1}{\epsilon_0} \rho^c \tag{2.4}$$

Here, ϵ_0 is the permittivity of free space, μ_0 is the magnetic permeability, ρ^c is the electric charge density, and $\mathbf{j}$ the current density. For non-relativistic speeds, as in the case of MHD, the displacement current is negligible and hence is neglected from Ampère's law in Equation 2.1.

2.1.2 Fluid Equations

To describe the mass motions of the plasma, the appropriate fluid conservation equations are required. To begin, the mass continuity equation, expressed as

$$\frac{\partial \rho}{\partial t} + \nabla \cdot (\rho \mathbf{v}) = 0, \tag{2.5}$$

states that matter cannot be created nor destroyed. Here ρ is given as the plasma density, and $\mathbf{v}$ is the velocity of the plasma. For an incompressible fluid, ρ is constant, and the equation reduces to $\nabla \cdot \mathbf{v} = 0$. Following this, the conservation of momentum condition can be written in the form of Newton's Second Law

($\mathbf{F} = m\mathbf{a}$) applied to a fluid, described as

$$\rho \frac{D\mathbf{v}}{Dt} = -\nabla p + (\mathbf{j} \times \mathbf{B}) + \rho \mathbf{g} \tag{2.6}$$

Here $D/Dt = \partial/\partial t + (\mathbf{v}.\nabla)$ is the convective derivative, representing derivative in a velocity field, and p is the pressure. The terms on the right hand side of the equation represent the appropriate forces acting on the fluid. In static equilibrium, the terms on the right hand side of the equation sum to zero, as there is no acceleration. This results in a force balance relationship given by[1]:

$$\nabla \left(p + \frac{B^2}{2\mu_0} \right) = \frac{1}{\mu_0} (\mathbf{B}.\nabla)\mathbf{B} \tag{2.7}$$

The gravitational force ($\rho \mathbf{g}$) has been excluded as it is negligible compared to the gas pressure and magnetic effects. The term on the left hand size of Equation (2.7) represents the gradient of the total pressure, consisting of the gas (thermodynamic) pressure (p) and magnetic pressure (B^2/μ_0). The right hand term is the magnetic tension, a force acting to straighten curved magnetic field lines. In the case that the field lines do not vary significantly along their axis (i.e. straight) this tension term can be neglected and the equilibrium state of the plasma is determined by the gas and magnetic pressure only. The ratio of these two is called the plasma-β parameter:

$$\beta = \frac{p}{B^2/2\mu_0} \tag{2.8}$$

---

[1] after applying Ampère's law and the vector identity $\nabla(\frac{1}{2}\mathbf{B}.\mathbf{B}) = \mathbf{B} \times (\nabla \times \mathbf{B}) + (\mathbf{B}.\nabla)\mathbf{B}$

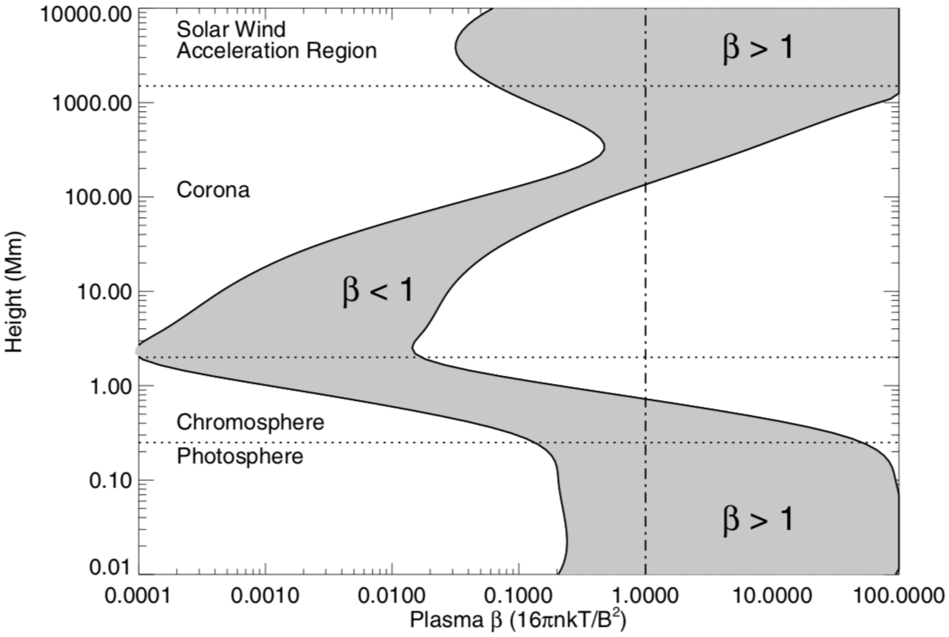

Figure 2.1: Plasma β as a function of height in the solar atmosphere. The values are shown in the shaded region for open and closed magnetic field lines for two assumed field strengths, 100 G and 2500 G. It can be seen that the magnetic pressure dominates in the lower corona ($\beta < 1$), whereas the gas pressure dominates the plasma in the photosphere ($\beta > 1$). Figure from Gary (2001).

This is an important expression, denoting whether a plasma is dominated by the gas pressure ($\beta < 1$) or by the magnetic pressure ($\beta > 1$). At the photosphere, $\beta \gg 1$, and the plasma motions dominate over the magnetic field, whereas in the corona $\beta \ll 1$ and the magnetic pressure dominates, and plasma follows along magnetic field lines. The variation of the plasma β value through the different layers of the solar atmosphere is shown in Figure 2.1.

An energy equation is also required to describe the system, and is given by

$$\frac{D}{Dt}\left(\frac{p}{\rho^{\gamma}}\right) = -\mathcal{L} \tag{2.9}$$

Here $\mathcal{L}$ is the total loss function and γ is the ratio of specific heats, usually taken as 5/3. However assuming that the fluid is described by an ideal gas $p = \rho RT$, then for adiabatic processes, $\mathcal{L} = 0$ (i.e. constant energy) this becomes:

$$\frac{\partial p}{\partial t} + (\mathbf{v}.\nabla)p = -\gamma p \nabla.\mathbf{v}. \tag{2.10}$$

2.1.3 Induction Equation

These fluid descriptions can then be combined with Maxwell's equations to provide a closed set of MHD equations linking $\mathbf{j}$, $\mathbf{B}$, and $\mathbf{v}$. This is achieved through the simplified generalized Ohm's law;

$$\mathbf{j} = \sigma \mathbf{E}' = \sigma(\mathbf{E} + \mathbf{v} \times \mathbf{B}), \tag{2.11}$$

where σ is the electrical conductivity of the plasma. A plasma moving with respect to a magnetic field at a velocity $\mathbf{v}$ is subject to an additional electric field component given by the Lorentz force $\mathbf{v}\times\mathbf{B}$. Ohm's law (Equation 2.11) can then be combined with Ampère's (Equation 2.1) and Faraday's (Equation 2.3) laws, together with the solenoid constraint (Equation 2.2) and a vector identity[1] to arrive at the *induction* equation:

$$\frac{\partial \mathbf{B}}{\partial t} = \nabla \times (\mathbf{v} \times \mathbf{B}) + \eta \nabla^2 \mathbf{B}, \tag{2.12}$$

where $\eta = 1/\mu_0 \sigma$ is the magnetic diffusivity term. This equation forms the basis for describing the magnetic behaviour of a plasma in MHD, and determines $\mathbf{B}$ once $\mathbf{v}$ is known. The first and second terms on the right hand side of Equa-

---

[1] $\nabla \times (\nabla \times \mathbf{B}) = \nabla(\nabla.\mathbf{B}) - \nabla^2 \mathbf{B}$

tion 2.12 are known as the magnetic advection and magnetic diffusion terms, respectively. The ratio of these two terms plays an important role in governing how a magnetic field will respond to the forces of plasma motion. This ratio is defined as the dimensionless magnetic Reynolds number R_m expressed as:

$$R_m = \frac{\nabla \times (\mathbf{v} \times \mathbf{B})}{\eta \nabla^2 \mathbf{B}} \approx \frac{vL}{\eta}. \tag{2.13}$$

Here L is given as the length scale over which $\mathbf{B}$ varies ($\nabla \sim 1/L$). The magnetic Reynolds number, R_m, is essentially a measure of the coupling strength between the plasma flow and the magnetic field. If $R_m \ll 1$, the diffusion term dominates in the induction equation, meaning that the magnetic field can 'leak' through the plasma, and diffuse away on timescales given by $t_d \approx L^2/\eta$. This term is important for the process of magnetic reconnection to occur, and suggests that the length scales of magnetic reconnection in the corona must be very small to account for the timescales we observe, such as in solar flares .

If $R_m \gg 1$ on the other hand, the advection term dominates, and field lines are constrained to move with the plasma (flow velocity). They move as though they are 'frozen into' the plasma (Alfvén, 1942). For typical coronal conditions above an active region, for which $T \approx 10^6$ K, $\eta \approx 1$ m^{2}s^{-1}, $L \approx 10^5$ m, $v \approx 10^4$ ms^{-1}, it is found that $R_m \approx 10^9$ (Priest & Forbes, 2000). Hence for the corona, the diffusion term is negligible, and the plasma acts close to a perfectly conducting medium. For a perfectly conducting fluid ($\sigma \to \infty$, and $\eta \to 0$), Equation 2.12 can be expressed as

$$\frac{\partial \mathbf{B}}{\partial t} = \nabla \times (\mathbf{v} \times \mathbf{B}) \tag{2.14}$$

This forms the basis of *ideal* MHD, in which the magnetic field is coupled to the plasma motion. For the case of most astrophysical plasmas $R_m \gg 1$, and this approximation to the induction equation can be made.

Thus the closed set of ideal MHD equations are then given by the mass (Equation 2.5), momentum (Equation 2.6), energy (Equation 2.10), and induction (Equation 2.14) equations, all being subject to the solenoid constraint (Equation 2.2).

2.1.4 MHD waves

A plasma is a compressive and elastic medium which can support a variety of different types of waves. In the solar corona, the observational evidence of MHD waves of various kinds is now abundant, and their presence provides a natural probe for the plasma properties, i.e. coronal seismology (e.g. De Moortel & Nakariakov, 2012; Nakariakov & Ofman, 2001).

MHD waves are driven by the different restoring forces that are experienced by a plasma when perturbed from an equilibrium position. From the momentum equation (Equation 2.6), these forces include a gas pressure, a magnetic pressure and a magnetic tension force that then result in the generation of sound waves, *magnetoacoustic* waves (both *fast* and *slow*) and *Alfvén* waves, respectively.

To understand the various waves and oscillations that exist in a coronal plasma, wave solutions to the MHD equations need to be sought and a *dispersion relation* determined. This can be achieved by considering a uniform plasma (constant ρ_0, p_0) in stationary equilibrium within a homogeneous magnetic field in the z direction, $\mathbf{B}_0 = (0, 0, B_z)$. A *small* perturbation is introduced into the system in the form

$$p(\mathbf{x},t) = p_0 + p_1(\mathbf{x},t), \tag{2.15}$$

$$\rho(\mathbf{x},t) = \rho_0 + \rho_1(\mathbf{x},t), \tag{2.16}$$

$$\mathbf{B}(\mathbf{x},t) = \mathbf{B}_0 + \mathbf{B}_1(\mathbf{x},t), \tag{2.17}$$

$$\mathbf{v}(\mathbf{x},t) = \mathbf{v}_1(\mathbf{x},t) \tag{2.18}$$

Here the subscripts are used to separate the background (p_0) from the perturbed quantities (p_1). These can then be substituted into the set of ideal MHD wave equations, namely Equations 2.2, 2.5, 2.6, 2.10, and 2.14. Neglecting the non-linear (quadratic) and gravitational terms, these equations then provide a set of linearized MHD equations in the form:

$$\nabla.\mathbf{B}_1 = 0, \tag{2.19}$$

$$\frac{\partial \rho_1}{\partial t} + \nabla.(\rho_0 \mathbf{v}_1) = 0, \tag{2.20}$$

$$\rho_0 \frac{\partial \mathbf{v}_1}{\partial t} = -\nabla p_1 + \frac{(\nabla \times \mathbf{B}_0)}{\mu_0} \times \mathbf{B}_1 + \frac{(\nabla \times \mathbf{B}_1)}{\mu_0} \times \mathbf{B}_0, \tag{2.21}$$

$$\frac{\partial p_1}{\partial t} + (\mathbf{v}_1.\nabla) p_0 = -\gamma p_0 \nabla.\mathbf{v}_1, \tag{2.22}$$

$$\frac{\partial \mathbf{B}_1}{\partial t} = \nabla \times (\mathbf{v}_1 \times \mathbf{B}_0) \tag{2.23}$$

In order to derive a dispersion relation, Fourier decomposition of these equations is then performed to search for wave solutions in the form of $Ae^{i(\mathbf{k.r}-\omega t)}$, where $\mathbf{k} = (k_x, k_y, k_z)$ is the wavenumber, ω is the angular frequency and A is a constant.

In a static equilibrium, the dispersion relations for MHD waves are found to be:

$$\omega^2 - v_A^2 k_z^2 = 0 \tag{2.24}$$

$$\omega^4 - k^2(c_S^2 + v_A^2)\omega^2 + k_z^2 k^2 c_S^2 v_A^2 = 0 \tag{2.25}$$

Here we have introduced two characteristic speeds, the sound speed $c_S = \sqrt{\gamma p_0/\rho_0}$ and the Alfvén speed $v_A = B_0/\sqrt{\mu_0 \rho_0}$. Equation 2.24 describes the Alfvén wave, an incompressible wave that is driven by the magnetic tension force and propagates parallel to the magnetic field (in z direction). The magnetoacoustic waves are described by Equation 2.25. This expression has a quadratic solution for ω^2 giving rise to both the *fast* and *slow* magnetoacoustic waves. The fast wave, unlike the Alfvén wave is not restricted to the magnetic field and can propagate in almost any direction given that the gas and magnetic pressure are in phase. The slow magnetoacoustic wave, however, is an ansiotropic one, with its propagation direction along the magnetic field with the gas and magnetic pressure out of phase.

2.1.5 MHD waves of a plasma cylinder

In coronal conditions, the plasma is dominated by the magnetic field ($\beta \ll 1$) which introduces significant structuring to the plasma medium. This modifies the dispersion relation described above, which is formulated for an unbound homogeneous medium. A common framework to describe MHD wave modes in coronal structures is that of a plasma cylinder stretched along the magnetic field. This model has proven to be an important building block of MHD wave theory in the

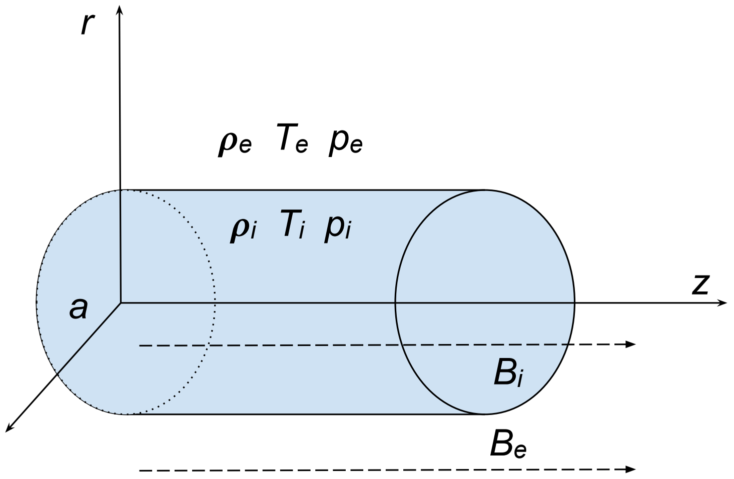

Figure 2.2: Schematic of the plasma cylinder model embedded in a magnetized plasma. Here ρ, T, p and B represent the density, temperature, pressure and magnetic field both inside (subscript i), and outside (subscript e) the cylinder.

solar atmosphere as it can reproduce the main properties of axially symmetric plasma structures such as coronal loops and filaments.

The formalism and determination of the different MHD wave modes and their dispersion relationships was developed by Edwin & Roberts (1983); Zajtsev & Stepanov (1975). In the model, a cylindrical tube of radius a that is filled with a plasma of uniform density ρ_i is considered. The magnetic field strength inside the cylinder is B_i (with only a z component), and has a gas pressure p_i. The external medium is also uniform, with a given density ρ_e, magnetic field strength B_e (also only with z component) and a gas pressure p_e. A visualization of this straight cylinder model is shown in Figure 2.2.

For the system to be in equilibrium, the total pressure (the gas pressure and magnetic pressure) must be balanced at the boundary,

$$p_i + \frac{B_i^2}{2\mu} = p_e + \frac{B_e^2}{2\mu} \tag{2.26}$$

The MHD equations can then be linearized with respect to a small perturbation from equilibrium for both inside and outside the cylinder. With the condition that the internal and external solutions of the MHD equations need to match at the boundary ($r = a$) by the continuity of the radial velocity component and total pressure, the classic dispersion relationship for the plasma cylinder can be derived as (Edwin & Roberts, 1983; Nakariakov & Verwichte, 2005)

$$\rho_e(\omega^2 - k_z^2 v_{Ae}^2)\kappa_i \frac{I'_m(\kappa_i a)}{I_m(\kappa_i a)} + \rho_i(k_z^2 v_{Ai}^2 - \omega^2)\kappa_e \frac{K'_m(\kappa_e a)}{K_m(\kappa_e a)} = 0 \tag{2.27}$$

Here, k_z is the longitudinal wavenumber, $I_m(x)$ and $K_m(x)$ are modified Bessel functions of order m, with $I'_m(x)$ and $K'_m(x)$ being their derivatives with respect to x. The functions κ_i and κ_e are the radial wavenumbers in the internal and external media respectively, and are defined by κ_α (with $\alpha = i, e$),

$$\kappa_\alpha^2 = \frac{(k_z^2 c_{S\alpha}^2 - \omega^2)(k_z^2 v_{A\alpha}^2 - \omega^2)}{(c_{S\alpha}^2 + v_{A\alpha}^2)(k_z^2 c_{T\alpha}^2 - \omega^2)} \tag{2.28}$$

Here, the characteristic speeds are defined as the sound speed, c_S, the Alfvén speed, v_A, and the tube speed, c_T, which is defined as

$$c_T = \frac{c_S v_A}{\sqrt{c_S^2 + v_A^2}} \tag{2.29}$$

Different solutions to the dispersion relations in Equation 2.27 correspond to

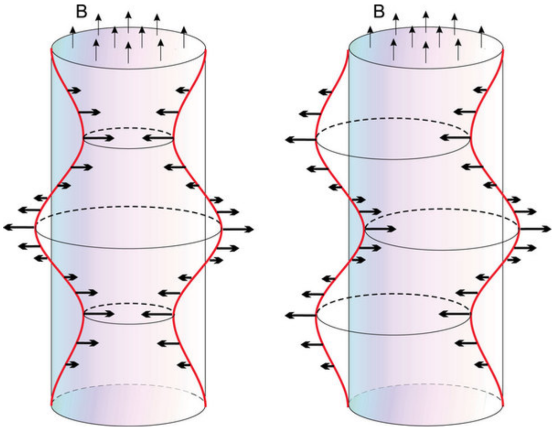

Figure 2.3: Visualization of the sausage (left) and kink (right) wave modes of a plasma cylinder. Figure from Morton *et al.* (2012)

waves, or MHD wave modes of the plasma cylinder. For modes that are confined or *trapped* to the tube (i.e. evanescent outside the cylinder) and guided by the cylinder, the condition $\kappa_e^2 > 0$ has to be fulfilled. On the other hand, modes with $\kappa_e^2 < 0$ are subject to move into the *leaky* regime, in which the wave energy can be radiated into the external medium.

The azimuthal number m determines the modal structure of the MHD wave. Solutions to $m = 0$ are called *sausage* modes, axis-symmetric expansions and contractions of the cylinder cross section, accompanied by plasma density and magnetic field variations. For $m = \pm 1$, we have the *kink* mode, which has anti-symmetric displacement, with little or no deformation of the cylinder cross section. Schematics of both the kink and sausage modes are demonstrated in Figure 2.4. Higher orders of m are referred to as *flute* or *ballooning* modes.

The solution to the dispersion relation under coronal conditions is shown in Figure 2.4. Two branches of phase speed solutions are evident, a slow-mode branch with characteristic speeds between c_{Ti} and c_{Si}, and a fast-mode branch that has speeds between v_{Ai} and v_{Ae}. The wave modes in these two branches are

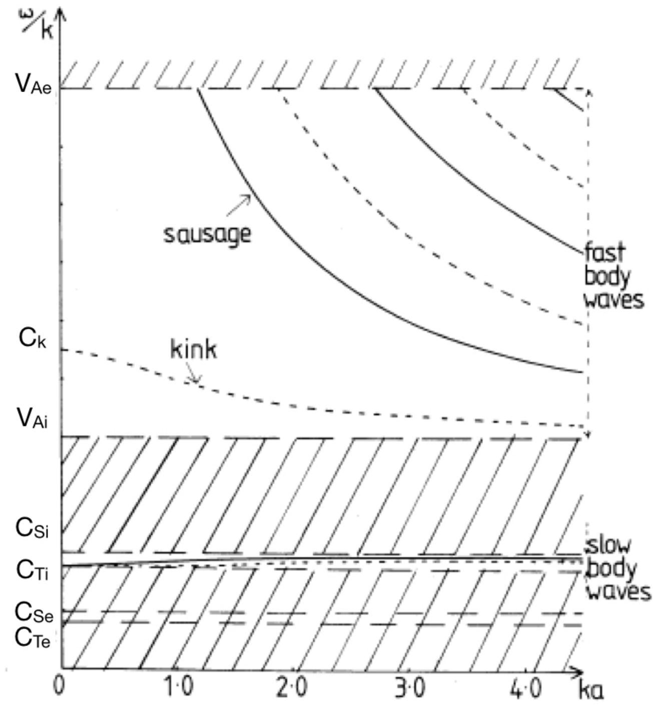

Figure 2.4: Dispersion relation for both fast and slow MHD waves of a cylindrical flux tube in coronal conditions ($c_{Se} < c_{Si} < v_{Ai} < v_{Ae}$), showing phase speed ω/k as a function of longitinal wavenumber k. The sausage mode is indicated by the solid lines, the kink modes the dashed lines. The different characteristic phase speeds are also marked on the phase speed axis, namely the Alfvén speed inside and outside tube (v_{Ai}, v_{Ae}), the sound speed (c_{Si}, c_{Se}), the tube speed (c_{Ti}, c_{Te}) and the kink speed c_k. Figure adapted from Edwin & Roberts (1983)

analogous to the fast and slow magnetoacoustic waves derived for an homogeneous plasma above. The sausage and kink modes are indicated by the solid and dashed lines respectively. The fast wave modes clearly demonstrate dispersion, with an associated cut-off at the external Alfvén speed, v_{Ae}, for the sausage mode in the long wavelength limit. The slow modes, or *longitudinal* modes, however are almost non-dispersive and propagate at the sound speed, c_{Si} moving towards the tube speed velocity, c_{Ti} in the long wavelength limit.

For each type of mode, m, there are an infinite number of wave harmonics available. The longest wavelength oscillation is known as the *global* mode, with a wavelength double the length of the plasma cylinder. In the corona, we discuss the cylinder in terms of a loop, with loop length L. The period of the global sausage mode is given by (Nakariakov & Verwichte, 2005)

$$P_{sausage} = \frac{2L}{c_p} \tag{2.30}$$

where c_p is the phase speed of the mode, which lies in the range of $v_{Ai} < c_p < v_{Ae}$. As mentioned above, the sausage mode is highly dispersive and is subject to a cut-off in the long-wavelength limit, and in the case of long thin loops, the sausage mode becomes leaky. In this way, the period of a sausage mode is generally shorter than the other wave modes such as the kink and slow magnetoacoustic, making them difficult to detect in spatially resolved observations. The first confident detection of a sausage mode in a coronal loop was demonstrated by Nakariakov *et al.* (2003) using microwave observations of a coronal flaring loop.

The period of the global kink mode is given by

$$P_{kink} = \frac{2L}{c_k}, \tag{2.31}$$

where c_k is the kink speed expressed as

$$c_k = \left(\frac{\rho_i v_{Ai}^2 + \rho_e v_{Ae}^2}{\rho_i + \rho_e}\right)^{1/2} \approx \left(\frac{2}{1 + \rho_e/\rho_i}\right)^{1/2} v_{Ai} \tag{2.32}$$

The approximation of the second expression can be made for a low-β plasma where the magnetic field inside and outside the loop is almost equal. Kink modes are commonly observed as transverse coronal loop oscillations in EUV observations. They have been extensively investigated since their first detection (Aschwanden *et al.*, 1999a; Nakariakov *et al.*, 1999), and are now observed to be present in a majority of active regions (Anfinogentov *et al.*, 2015).

The period of the global longitudinal mode is given by

$$P_{long} = \frac{2L}{c_{Te}} \tag{2.33}$$

In the case of a low-β plasma, as in the corona, the internal tube speed, c_{Te}, is close to the internal sound speed c_{Se}. The period is hence dependent on the temperature of the loop. Longitudinal oscillations in coronal loops are often observed in so-called SUMER oscillations (Wang *et al.*, 2002).

2.2 Magnetic Reconnection

The solar corona is filled with a highly conductive plasma that enables large amounts of magnetic energy to be stored in the magnetic field due the inefficiency to dissipate electric currents. One way this energy is believed to be released is through magnetic reconnection, a process that liberates the stored magnetic energy through the topological restructuring of a magnetic field. Magnetic reconnection is believed to play the central role in the energy release observed in solar flares and other dynamic solar activity.

The plasma of the solar corona can be described in terms of ideal MHD, in which the magnetic field is coupled to the plasma motions (‘frozen in’, $R_m \gg 1$), such that the diffusion term in the induction equation (Equation 2.12) can be

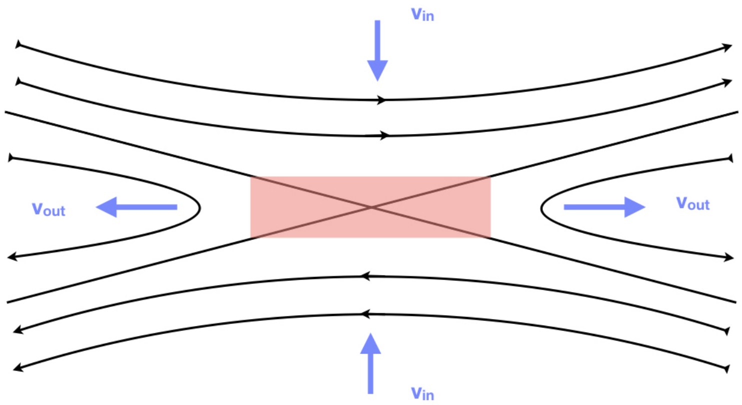

Figure 2.5: Simple 2D idealized model of magnetic reconnection driven by two oppositely directed inflows with velocity v_{in}. The diffusion region is marked by the red shaded region through which reconnection can occur to create oppositely directed outflows with velocities v_{out}

ignored. However, when regions of opposite polarity flux come together (e.g. a rising magnetic flux tube emerges into a region of existing flux), a boundary layer (current sheet) with a large current density is formed to separate the two regions. Across this boundary, large magnetic field gradients are established, and the magnetic field approaches zero at an 'X' point (or null point) to facilitate the continuous change in field from one polarity to the other. The large gradients over the small length scales of this boundary results in non-ideal MHD processes to occur allowing diffusion to take place. This occurs in the so-called diffusion region, illustrated by the red shaded area in Figure 2.5

A required balance of total (magnetic and gas) pressure across the diffusion region gives rise to a large gas pressure in the region (as $B = 0$). This pressure gradient causes the magnetic field to inflow into the diffusion region with a velocity, v_{in}, as shown in Figure 2.5. The magnetic field reconnects and exits the region with a velocity v_{out}. The highly pointed magnetic fields in the outflow

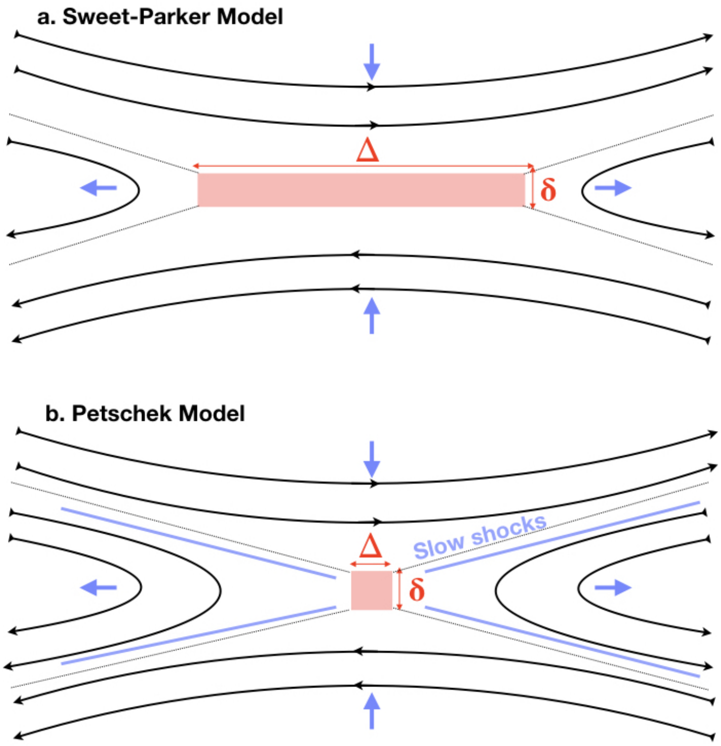

Figure 2.6: Diagram of the geometries of the Sweet-Parker (a) and Petschek (b) reconnection models. The red shaded region in both marks the diffusion region of the models. For the Sweet-Parker model, this is a long thin sheet with $\Delta >> \delta$, whereas for the Petschek model, the diffusion region is much more compact with $\Delta \sim \delta$. Slow mode shocks are considered in the Petschek model, marked as blue lines in (b).

region experience a magnetic tension force that ejects the outflows away at high speed, resulting in the basic conversion of magnetic to kinetic energy. The outflows, in turn, result in a lower pressure in the diffusion region which allows for continued inflows.

This idealized steady-state 2D reconnection process was first formulated in the Sweet-Parker model of reconnection (Parker, 1963; Sweet, 1958). In the Sweet-Parker model, the diffusion region is assumed to be much longer (length Δ) than it is wide (width δ), illustrated in Figure 2.6 (a). The continuity equation dictates that the density of the inflow region must equal that of the outflow regions such that

$$\rho_{in} v_{in} \Delta = \rho_{out} v_{out} \delta \tag{2.34}$$

This relationship then restricts the reconnection rate, M, which can then be defined as the ratio of the inflow and outflow velocities given by

$$M = \frac{v_{in}}{v_{out}} = \frac{1}{\sqrt{R_{mi}}}, \tag{2.35}$$

where R_{mi} is the magnetic Reynolds number at the Alfvén speed (also known as Lunquist number). Comparing this to coronal conditions ($R_{mi} \sim 10^8 - 10^{12}$) yields a reconnection timescale of $10^8 - 10^9$ s (years!), much longer than the typical timescale of flares which are on the order of $10^2 - 10^4$ s (Shibata & Magara, 2011), and is hence a major limitation to the Sweet-Parker model.

A much faster reconnection model was suggested by Petschek (1964), which involved reducing the diffusion region size so that the length and thickness have similar dimensions ($\Delta \sim \delta$), as shown in Figure 2.6 (b). Reconnection can now occur at a faster rate as the propagation time through the diffusion region is reduced given the smaller length scales. However, as the size of the diffusion region is reduced, the amount of plasma that can flow through is also reduced. It is found that much of the plasma turns around outside the diffusion region, and two slow mode shocks arise where flow speed changes from v_{in} to v_{out} abruptly. These shocks also act as a main site of the conversion of magnetic energy into heat and kinetic energy (in addition to the diffusion region). The estimated maximum reconnection rate in this scenario is found to be

$$M = \frac{\pi}{8\ln(R_{me})}, \tag{2.36}$$

providing values in the range of 0.01-0.02 for coronal conditions. This is a few orders of magnitude less than the Sweet-Parker model and provides a timescale that is comparable to solar flares. This mechanism seems to solve the issue of reconnection timescales, however Petschek reconnection with uniform resistivity cannot be reproduced in numerical simulations within the limits of high magnetic Reynolds numbers (Aschwanden, 2006; Priest & Forbes, 2002). Simulations of the Sweet-Parker model though have been successful (Biskamp, 1986).

While both the Sweet-Parker and Petschek mechanisms form the basis of many reconnection models, they are both steady-state and in 2D. Magnetic reconnection that occurs in flaring events in the corona is inherently time-dependent and in 3D. More realistic 2D time-dependent reconnection involving the tearing mode and coalescence instabilities have been considered, demonstrating that magnetic island formation could play a role in the fast reconnection rates (Kliem *et al.*, 2000). Indeed, 3D magnetic reconnection has also been explored, with magnetic topologies that are much more complex (see recent reviews Janvier, 2017; Pontin, 2011).

2.3 Quasi-Periodic Pulsation Mechanisms

In this section, the proposed mechanisms to explain the appearance of QPPs in flaring emissions is addressed. Two main theories have been pursued in recent years to describe the physical process responsible for QPPs. As discussed in a recent review by McLaughlin *et al.* (2018), these can be categorized into *oscillatory* or *self-oscillatory* processes according to the nature of the underpinning mechanism. In the oscillatory category, QPPs can be described by motions around an equilibrium - such as MHD oscillations in/near the flaring site. For the self-oscillatory category, on the other hand, QPPs are a result of some intrinsic property of the energy release such as a periodic or 'bursty' regime of magnetic release.

2.3.1 QPPs as signature of MHD wave modes

The first and most established explanation of QPP signatures considers that they are a direct signature of MHD wave modes excited in the flaring regions. Indeed, the observed periodicity of QPPs coincide with the expected timescales of various MHD waves modes in coronal conditions (Inglis *et al.*, 2009; Nakariakov & Melnikov, 2009; Pascoe & De Moortel, 2014; Pascoe *et al.*, 2009). MHD wave modes in flaring loops could periodically vary the macroscopic plasma parameters, which could either modulate the emission directly (Nakariakov & Melnikov, 2009; Nakariakov, 2007), or affect the dynamics of charged particles (Zaitsev & Stepanov, 2008). MHD waves can also play a role in the periodic modulation of flaring energy release. The period of QPPs would depend on the type of MHD wave mode (i.e. kink, sausage, longitudinal), and on the properties of the magnetic loop through which they propagate (e.g. loop length, magnetic field strength).

2.3.1.1 MHD waves in the flaring system

Modulation of thermal plasma

QPPs in the thermal emission, such as observed in soft X-ray and EUV, can be a direct result of density perturbations of the emitting plasma by compressive MHD wave modes. The emission intensity in these wavebands is proportional to the density squared, and hence perturbations in the plasma density can modulate the intensity of observed emissions. For example, with a background density ρ_0, and a density perturbation ρ_1 ($\rho_0 \gg \rho_1$) the modulated intensity is given by $I \propto (\rho_0 + \rho_1)^2 \approx \rho_0^2 + 2\rho_0\rho_1$ (Nakariakov, 2007). Thus a density perturbation is observed to be two times stronger in the emission intensity. Compressible modes, such as the sausage and longitudinal wave modes, can directly perturb the density of a coronal loop. The kink mode, when oscillating in the vertical polarization, acts as a 'sausage like' oscillation due to the conservation of magnetic flux, and can also cause small density perturbations (Aschwanden & Schrijver, 2011).

Modulation of gyrosynchrotron emission

QPPs are a common phenomenon in microwave observations associated with gyrosynchrotron emission. MHD wave modes can perturb the various source parameters that gyrosynchrotron emission depends on such as the energetic electron distribution, magnetic field strength and line of sight (LOS). Gyrosynchrotron emission from flares can occur in both optically thick and optically thin regimes, with the optically thin (thick) observed at frequencies higher (lower) than the gyrosynchrotron spectrum peak frequency. Dulk (1985) gives approximations for the gyrosynchrotron emissivity that can be used to illustrate the parametric dependencies on the different source parameters. For example, in the optically thin regime at a fixed frequency, the emission dependence on the magnetic field strength, B, and total number of non-thermal electrons, N, is given by $I_{thin} \propto NB^{0.9\delta-0.22}$. Here δ is the power law spectral index ($2 \leq \delta \leq 7$ for this to expression to be valid (Dulk, 1985)). Hence, the emission is very dependent on the magnetic field, and the emission increases with increasing magnetic field. In contrast, the dependence for the optically thick regime, $I_{thick} \propto B^{-0.5-0.09\delta}$, shows an anti-correlated dependence on the magnetic field, i.e. if the magnetic field increases, the emission would decrease. For a MHD wave mode that can perturb the magnetic field, i.e. the sausage mode, variations in the magnetic field would manifest as QPP signatures in the gyrosynchrotron emission, with anti-phase oscillations in the optically thin and thick parts of the spectrum. Similarly, the gyrosynchrotron emission has a dependence on angle of the LOS and the magnetic field, θ, given by $I_{thin} \propto (sin\theta)^{-0.43+0.65\delta}$ for the optically thin. Again the optically thin emission has a strong dependence on the angle, and hence also variations in the angle which could be caused by kink or torsional standing modes. Similarly, an anti-correlation between the optically thin and thick emission should be observed as the optically thick dependence is given by $I_{thick} \propto (sin\theta)^{-0.36-0.6\delta}$. Another possibility for MHD modes modulating gyrosynchrotron emission is through perturbation of the efficiency in the Razin suppression. This can be achieved through the modulation of the plasma density which can be caused by the slow magnetoacoustic wave in which the magnetic field remains constant (Nakariakov & Melnikov, 2006).

These mechanisms however cannot account for the large modulation depths (up to 100%) often observed in microwave observations of gyrosynchrotron emis-

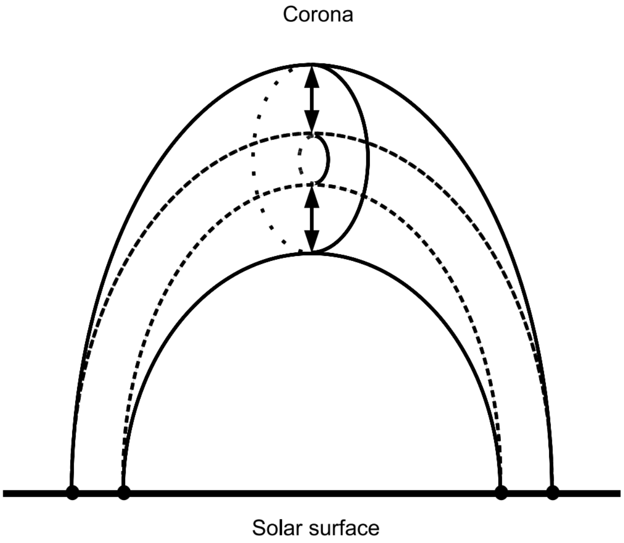

Figure 2.7: Cartoon of a global sausage mode in a coronal loop. This axis symmetric perturbation results in a variation of the loop minor axis, causing contractions (dashed line) and widenings (solid line) periodically. The magnetic field perturbations are a maximum at the loop apex and minimum at the footpoints. Figure from Pascoe *et al.* (2007).

sion. Moreover, it also cannot explain the simultaneous and coherent QPPs often observed in different wavebands. Hard X-ray emission is associated with footpoint sources generated by non-thermal bremsstrahlung of highly energetic particles that precipitate to the dense chromosphere, while gyrosynchrotron emission is produced by the same population of accelerated electron magnetically trapped in the loop legs.

2.3.1.2 Modulation of the electron precipitation rate

Simultaneous hard X-ray and microwave QPPs can be explained in terms of the modulation of non-thermal charged particle dynamics by MHD waves, such as the periodic variation of the electron precipitation rate. Flaring loops can act as magnetic traps confining a significant portion of accelerated electrons between two magnetic mirrors at the flaring loop footpoints. The dynamics of the non-thermal electrons is determined by the critical pitch angle θ_c which depend on the magnetic field at the loop top B_{top} and footpoints B_{foot},

$$sin^2\theta_c = \frac{B_{top}}{B_{foot}} \tag{2.37}$$

Non-thermal electrons with large enough pitch angles ($\theta > \theta_c$) are trapped and bounce between the magnetic mirrors, whereas electrons with a small pitch angle ($\theta < \theta_c$) escape the trap and precipitate towards the dense plasma layers at the footpoints resulting in hard X-ray emission. Periodic variations of the critical angle θ_c manifests as the periodic precipitation of non-thermal electrons, hence resulting in QPPs of hard X-ray emission at the footpoints. This scenario also simultaneously produces QPP signatures in gyrosynchrotron emission generated by the non thermal electrons that periodically fill the loop legs. The global sausage mode (see Figure 2.7) is a candidate for this effect, as it can effectively perturb B_{top} resulting in the periodic variation of θ_c from Equation 2.37.

2.3.1.3 Periodic triggering of energy release by external MHD oscillations

In addition to MHD waves affecting the physical conditions of the emitting plasma itself, they can also play a role in the periodic triggering of magnetic reconnection. A scenario was developed by Foullon *et al.* (2005) and Nakariakov *et al.* (2006), in which the interaction of a fast magnetoacoustic transverse wave (such as kink or sausage) from an external loop resulted in the periodic modulation of magnetic reconnection in a flaring site. In the model, illustrated in Figure 2.8, an oscillating loop is situated near a flaring site, and is linked to the flaring site via an evanescent or leaky part of the oscillation. This part of the oscillation, from the point of view of the flare, is a perpendicular fast magnetoacoustic wave with a small amplitude and a period prescribed by the external loop properties. As the wave approaches the magnetic X-point (null point), the wave amplitude experiences an amplification and the length scales rapidly decrease, leading to an increase in the current density (see McLaughlin & Hood, 2004). The evolution of the fast magnetoacoustic wave at the X-point is accompanied by occurrence of dramatic variations of the electric current density induced by the wave. These current variations can, in turn, periodically induce various plasma micro-instabilities which are known to produce anomalous resistivity in the region. Oscillatory behaviour of the anomalous resistivity causes periodic triggering of the magnetic reconnection. Consequently, the periodic reconnection then accelerates particles periodically which follow field lines and precipitate in the dense atmosphere, causing QPPs in the microwave and X-ray bands. QPPs in soft X-ray and EUV could then be a manifestation of plasma that is periodically heated by the modulated X-ray emission, and hence can also be simultaneously explained in this scenario.

An important feature of this model is that the driving MHD wave is not required to have a large amplitude, and hence there is no limitation on the modulation depth of the observed QPP signatures. The periods of the observed QPPs detected in this regime would be prescribed by the properties of the external loop, and hence are not determined by the geometrical size of the flaring region itself.

A similar model is also described in (Chen & Priest, 2006), in which it is shown that a compressive wave can induce periodic reconnection by variation in the plasma density in the vicinity of the reconnection site. Specifically it was

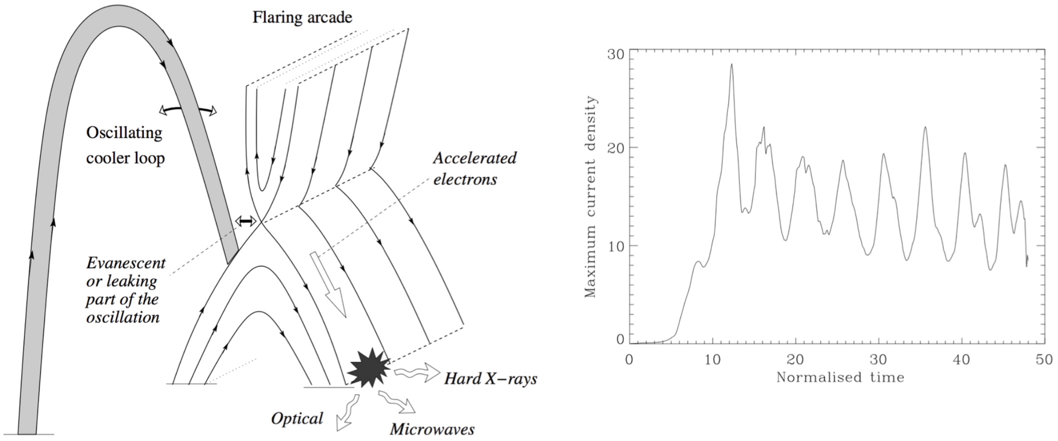

Figure 2.8: *Left*: A schematic sketch of an external periodic wave triggering reconnection. The external loop (shaded in grey) hosts the transverse oscillation, and a leaky part of this oscillation travels towards the magnetic X point of the flaring region. This leads periodic variations in the anomalous resistivity driven by the current density variations, resulting in periodic reconnection. *Right*: The current density variations as a function of time at the X-point. Both figures are from Nakariakov *et al.* (2006).

found that density variations in the vicinity of the reconnection site result in the periodic variation in the electron drift speed, which switches on and off anomalous resistivity and thus accelerates the process of reconnection periodically.

In the case of two-ribbon flares, Nakariakov & Zimovets (2011) demonstrated that slow magnetoacoustic waves propagating along a flaring arcade could trigger multiple episodes of reconnection along the arcade as it propagates. In this model, a slow magnetoacoustic wave excited by an initial energy release at the top of the arcade propagates at an angle to the magnetic field (rather than directly along it), towards the footpoints. At the footpoints (chromosphere), the wave experiences reflection due to the sharp gradient in the sound speed and returns to the top of the arcade. At the top of the arcade, the wave approaches the X-point and triggers reconnection through the perturbation of the current density (Nakariakov *et al.*, 2006) or plasma density Chen & Priest (2006). Moreover, this excites a new slow magnetoacoustic wave, which then repeats the process. In this way, this mechanism can be thought of as an autowave process (McLaughlin *et al.*, 2018). The most efficient angle of propagation is shown to be 25°-28°, allowing the slow waves to propagate along the arcade and trigger energy release at different locations along the arcade. The period of the generated QPPs is determined by the speed and propagation path of the triggering slow wave. This mechanism is also consistent with the observed progression hard X-ray and footpoints and UV brightenings along a magnetic neutral line. However, as shown by Inglis & Dennis (2012), this model may not be suitable to explain short QPP signatures < 60 s as shorter periods would require ribbons to be extremely close together or very fast motion that is not observed.

It remains a challenge however to explain QPPs purely in terms of MHD wave modes given the complex evolution and motion of flaring plasma, such as flare footpoint motions.

2.3.2 QPPs as signatures of the flare reconnection process

The mechanisms described above suggest that QPPs are a result of variations of the flaring plasma driven by oscillatory MHD wave modes. In the self-oscillatory case, the QPP are connected to the dynamics of magnetic reconnection and energy release which may be time-dependent. Within the framework of flaring energy release, it has been demonstrated that magnetic reconnection does not proceed in a quasi-steady fashion (such as Sweet-Parker or Petschek reconnection models), but instead exhibits fundamental ‘bursty’ behaviour and oscillatory regimes. In this way, QPP signatures may be directly related to the driving force of energy release from flares, and the observed timescales manifested as timescales of dynamic reconnection. Such regimes of magnetic reconnection are termed ‘load/unload’ (Nakariakov & Melnikov, 2009) or ‘magnetic dripping’ (Nakariakov *et al.*, 2010) models, which represent the gradual accumulation, and rapid release of magnetic energy when some threshold is achieved. Theoretically, periodic regimes of magnetic reconnection can be achieved in several different ways.

Oscillatory regimes of reconnection

Time-dependent MHD simulations have shown evidence of regimes of repetitive reconnection, termed *oscillatory reconnection*, that naturally produces periodic outputs from an aperiodic driver. This process was first reported in Craig & McClymont (1991), in which the relaxation of a 2D X-point (null point) following an initial perturbation was considered. It was found that an inertial overshoot of the plasma carries too much flux through the X point than is required for equilibrium, and the plasma goes through a series of oscillations through the X-point. This results in a damped oscillatory regime of magnetic reconnection in which the angle between X-point lines changes periodically. McLaughlin *et al.* (2009) extended this work to investigate the effect of an incoming nonlinear fast MHD wave near a 2D X-point. It was found that the incoming wave deforms the X-point into a cusp-shape which in turn collapsed to a current sheet. The system similarly developed into an oscillatory regime, evolving through a series

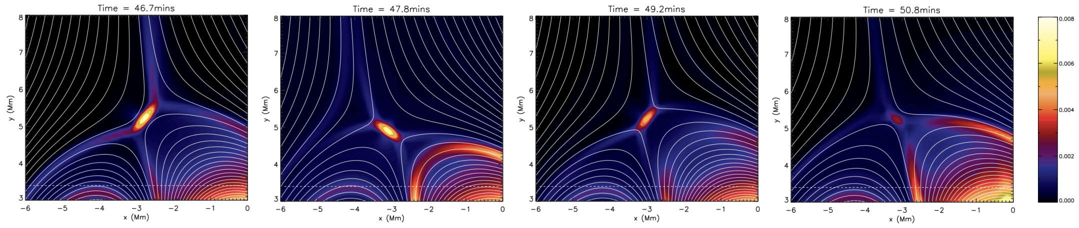

Figure 2.9: Figure from McLaughlin *et al.* (2012b) demonstrating the temporal evolution of the current sheet. The four panels show contours of current density and a selection of field lines for four different times.

of different current sheet orientations. In this model outflow reconnection jets heat the plasma at the ends of the newly formed current sheet causing it to expand, resulting in the current sheet to be squashed and forcing the separatrics apart. The system then attempts to restore to equilibrium, overshoots and forms a second current sheet in another orientation, and this evolution periodically proceeds. Together with this oscillatory behaviour, evidence for reconnection was also found during this time through the change in field line connectivity and vector potential, hence oscillatory reconnection. An example of oscillatory reconnection shown as the current sheet evolution is shown in Figure 2.9 from numerical simulations of McLaughlin *et al.* (2012b).

Another important example of oscillatory reconnection is presented in the 2.5D MHD simulations of the emergence of a magnetic flux rope into the solar atmosphere (Murray *et al.*, 2009). It was found that a series of 'reconnection-reversals' took place, whereby reconnection occurred in distinct bursts and the inflow and outflow magnetic fields of one burst become the outflow and inflow fields in the following burst. This arises as a consequence of growing gas pressure in the bounded outflow region which pulls the inflow regions apart (due to the pressure gradient across the boundaries of the outflow and inflow regions), causing the current burst of reconnection to slow and stop, bringing the outflow fields together such that reconnection commences. This work was generalized by McLaughlin *et al.* (2012b), and it was found that the physical mechanism of oscillatory reconnection naturally generates quasi-periodic vertical outflows. The periodicities generated by oscillatory reconnection are promising in terms of explaining observed QPP - around a null point they are found to be 56.3 - 78.9 s (McLaughlin *et al.*, 2012a), and via flux emergence to be 105-212.5 s (McLaughlin *et al.*, 2012b). To note however, oscillatory reconnection itself is generated with an exponentially decaying signature. This means that this mechanism will struggle to explain decayless oscillations, particularly in the case of some QPPs where the pulsations are observed to systematically grow in intensity. Recently Thurgood *et al.* (2017) extended this work to a realistic 3D null point, and found that reconnection naturally proceeded in a time-dependent and oscillatory fashion. They also found that the reconnection itself produced periodically excited propagating MHD waves. The identification of inherent periodicity in 3D reconnection provides prospects for oscillatory reconnection to play a role in explaining the observed quasi-periodicity observed in flares. Further parametric studies are now required to test the range of periodicities possible and how plasmoid generation modifies the system.

Dynamics current sheet and bursty reconnection

Another possible mechanism consistent with regimes of ‘bursty’ energy release is related to instability dynamics in reconnecting current sheets. The formation of long current sheets, for example in the case following a solar eruption, are subject to the tearing instability (Furth *et al.*, 1963). As a result of this instability, the current sheet fragments forming a series of magnetic islands or plasmoids (regions of magnetically confined plasma). These magnetic islands can then enter the coalescence instability (Finn & Kaw, 1977) in which they interact and merge together, and releasing a main part of the free energy within the current sheet (Leboeuf *et al.*, 1982). The process of the tearing instability and subsequent coalescence instability occur iteratively leading to a scenario termed impulsive bursty reconnection (Leboeuf *et al.*, 1982; Priest, 1985).

Early simulations of nonlinear coalescence found that coalescing plasmoids display periodic oscillations in field and other particle quantities (Pritchett & Wu, 1979; Tajima *et al.*, 1987). Since particle acceleration is expected during coalescence, either via secondary magnetic reconnection at the merging points, and through the contraction of merging plasmoids (Drake *et al.*, 2006b), QPPs in the emission associated with accelerated electrons may be a manifestation of the timescales of this process.

Kliem *et al.* (2000) numerically simulated the evolution of a long 2D current sheet above a flaring loop. In their model, the dynamic phase of magnetic reconnection involved the repeated generation of magnetic islands and their coalescence. The coalescing (merging) plasmoids formed one or more larger plasmoids, which were rapidly ejected upwards and downwards along the current sheet. The inability of the plasma to carry sufficient flux into the diffusion region to support the Alfvénic outflow of the plasmoids in steady Petschek state caused the system to keep switching between a fast Petschek regime to a slow Sweet-Parker regime of reconnection. The formation of a new island was suggested to be accompanied with a burst of accelerated particles, and hence a pulsation in the observed emission in the bands associated with non-thermal electrons. It was found that for flaring coronal conditions, the time between pulsations could be in the 0.4-20 s range. In this scenario, particles are presumably accelerated by DC electric fields near reconnection X-points.

Recently Guidoni *et al.* (2016) extended the approach of Drake *et al.* (2006b) to investigate electron acceleration in Sun-ward moving magnetic islands formed in a current sheet in a 2.5D simulation of an eruptive flare. In this scenario, magnetic islands trap and accelerate electrons, increasing their energy by two orders of magnitude (Drake *et al.*, 2006b). As the islands descent Sun-ward they interact with the flare arcade, and the electrons escape, streaming to footpoints to result in hard X-ray emission. The authors find that this mechanism is capable of explaining the electron energies observed in flares, and the intermittent emission is due to the discrete acceleration episodes associated with the formation and contraction of the islands during the plasmoid-dominated reconnection.

2.4 D-region Electron Density

The D-region of the ionosphere is created and maintained by a dynamic equilibrium between the production of free electrons and ions and their subsequent recombination. The variation of the electron density N_e can hence be expressed as a combination of electron production, q, and loss processes, L, given by the continuity equation,

$$\frac{dN_e}{dt} = q - L \tag{2.38}$$

The effects of transport processes can be ignored in this continuity equation since charged particle motion in the D-region corresponds to that of the neutral density. Recombination here is rapid due to the fact that the neutral density in the D-region is relatively large (Davies, 1990). The production rate, q, depends on ionizing radiation (i.e. X-ray flux) and the density of the neutral constituents. The loss rates depends on the electron and ion densities and the rate coefficients of the recombination processes. In the D-region, recombination can occur in several ways, mainly through electron-ion recombination, ion-ion recombination and three-body combination. For the condition of quasi-neutrality ($N^+ = N^- + N_e$), this continuity equation can be written as (Rowe *et al.*, 1970; Whitten & Poppoff, 1961; Žigman *et al.*, 2007)

$$\frac{dN_e}{dt} = \frac{q}{1+\lambda} - \frac{N_e}{1+\lambda}\frac{d\lambda}{dt} - \alpha_{eff} N_e^2 \tag{2.39}$$

Here λ is the ratio of the negative ions and electron density, and α_{eff} is termed the *effective recombination coefficient* and embodies several of the electron loss processes mentioned above. The λ term is slowly varying as a function of time (Mitra, 1974; Rowe *et al.*, 1970), and during times of increased ionization (such as during the day, and particularly during flares) the negative ion density is small, and is assumed to be <0.1 at altitudes above 70 km (Mitra, 1974; Žigman *et al.*, 2007). In this way, Equation 2.39 can be simplified to describe the behaviour of the electron density at a particular height during a flare, with both q and N_e a function of time,

$$\frac{dN_e}{dt} = q - \alpha_{eff} N_e^2 \tag{2.40}$$

Despite the fact that this equation is relatively simple, it has been readily exploited in many studies of the disruption of the ionosphere to ionizing disturbances. This equation is used in Chapter 6 to estimate α_{eff} as a function of flux in an ionizing flare event.

2.5 VLF propagation in the Earth-Ionosphere Waveguide

As discussed in the Introduction, the measurements of the propagation conditions of VLF radio waves can be used to probe the D-region electron density. VLF radio waves propagate in the waveguide formed between the Earth and the lower ionosphere (Figure 2.10) and this propagation in the Earth-ionosphere waveguide can be effectively represented in terms of waveguide mode theory (Budden, 1961). Waveguide mode theory assumes that the energy within the Earth-ionospheric waveguide is distributed among a series of modes. In the case of relatively long propagation paths (over several hundred km) the propagation can be conveniently described in terms of a relatively small number of modes, as the higher order modes will attenuate over the long distances. The minimum cut-off frequency f_c of the waveguide, or mode order n is given by (Davies, 1990)

$$f_c = \frac{nc}{2h} \tag{2.41}$$

For daytime conditions (h ∼74 km) the cut-off frequency for the first order mode is ∼2 kHz. VLF frequencies greater than this cut-off will propagate, whereas for frequencies less than this, the mode is evanescent and strongly attenuates.

The mathematical formulation for VLF waves in terms of waveguide mode theory was extensively developed in the 1960's and 1970's (e.g. Budden, 1961; Galejs, 1972; Wait & Spies, 1964a; Wait, 1974). See also Cummer (2000). Today these theoretical models are used in computational solutions to describe the

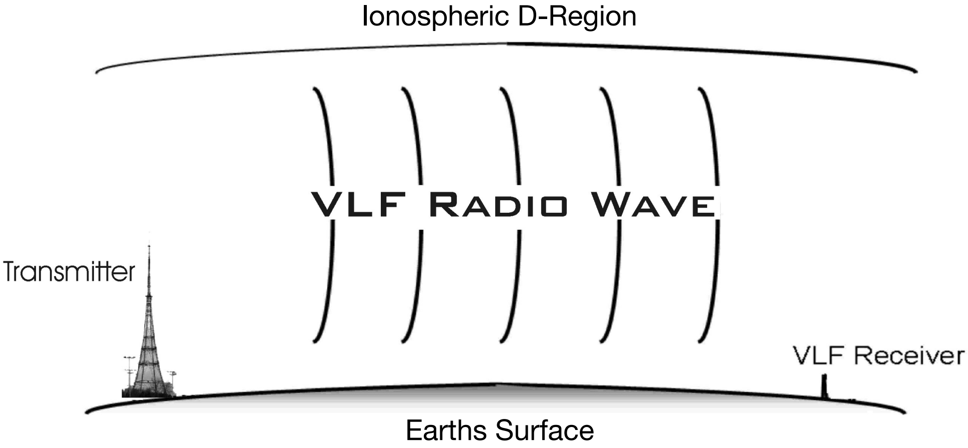

Figure 2.10: An illustration of the VLF propagation Earth-ionospheric waveguide. Figure adapted from Clilverd *et al.* (2009)

propagation of VLF radio waves in the Earth-ionospheric waveguide in order to estimate electron density variations of the upper waveguide boundary of the D-region. For example, the Long Waveguide Propagation Capability (LWPC) code, developed by the Space and Naval Warfare Systems, can model the propagation of VLF radio waves in the Earth-ionosphere waveguide in order to relate the received amplitude and phases of a VLF signal to the D-region electron density (Ferguson, 1998).

The LWPC programs employ full waveguide solutions to the anisotropic Earth-ionosphere waveguide problem. The program works by calculating a set of complex modal solutions for a specified Earth ionosphere waveguide (i.e. from a transmitter to a receiver). These modes are then summed at selected distances from the transmitter to calculate the VLF signal at a given distance. The program divides the propagation paths into a series of horizontally homogeneous segments and the parameters and distributions of the segments are determined by changes in the ionosphere, ground conductivity and geomagnetic field. The LWPC calculates the mode solutions for each horizontally homogeneous segment. The modal solutions are determined by the mode searching algorithm of Morfitt & Shellman (1976) and then a conversion model (Ferguson & Snyder, 1980) is used to connect the series of segments along the propagation path.

The propagation model implemented in LWPC treats the ground and lower ionosphere as waveguide boundaries, characterized by a defined conductivity profile. The lower boundary (surface of the Earth) has adjustable permittivity and conductivity values and is set to the default values provided by LWPC, which are based upon Westinghouse Geophysical Laboratory conductivity map (Ferguson, 1998; Morgan, 1968). The upper boundary of the waveguide, the D-region of the ionosphere, is characterized by an electron density/conductivity profile that can be specified by the user. As mentioned in the Introduction, the D-region chemistry and dynamics is complex and not well enough understood to provide sufficiently accurate profiles. However, it has been found that the extraction of ionospheric electron densities at the D-region can be made using a simplified ionospheric model based on the work of Wait & Spies (1964a). Under this framework, a height dependent conductivity parameter is defined as $\omega_r(z)$ given by

$$\omega_r(z) = \frac{\omega_0^2(z)}{\nu(z)} = 2.5 \times 10^5 e^{[\beta(z-H')]} \tag{2.42}$$

Here ω_0 is the plasma frequency which depends on the electron density profile, and ν is the effective electron-neutral collision frequency, both functions of height, z. The conductivity term is assumed to have an exponential profile with height, and is characterized by the two Wait parameters, β and H'. β, given in units of km^{-1} is often termed the 'sharpness' of the ionospheric boundary layer, describing the relative slope of the conductivity exponential profile. The parameter H' (in km) is the effective height of the ionosphere. The collision frequency, ν depends on the neutral air density which is known to decrease exponentially with height, approximated to be 0.15 km^{-1} at D-region altitudes. A general expression for the collision frequency is given in Morfitt & Shellman (1976),

$$\nu(z) = 1.82 \times 10^{11} e^{(-0.15z)} \text{ collisions/sec.} \tag{2.43}$$

The plasma frequency is related to the electron density expressed as

$$\omega_o^2 = \frac{N_e e^2}{\epsilon_0 m} \tag{2.44}$$

The Equations 2.42, 2.43 and the expression for the plasma frequency Equation 2.44 can then be rearranged to describe an exponentially varying electron density profile of the ionospheric D-region as a function of height z, in terms of the two Wait parameters H' and β as

$$N_e(z, H', \beta) = 1.43 \times 10^{13} e^{-0.15H'} e^{(\beta-\beta_0)(z-H')} \text{ m}^{-3} \tag{2.45}$$

This expression is plotted for different typical daytime Wait parameters (e.g. Ferguson, 1998) as a function of height in Figure 2.11. As shown, this expression for the electron density in the D-region increases exponentially with height. To demonstrate the dependence of the Wait parameters, H' and β, different combinations of the two-parameter system are plotted. The dashed lines denote the same values of β and the lines plotted with the same color denote the same H'

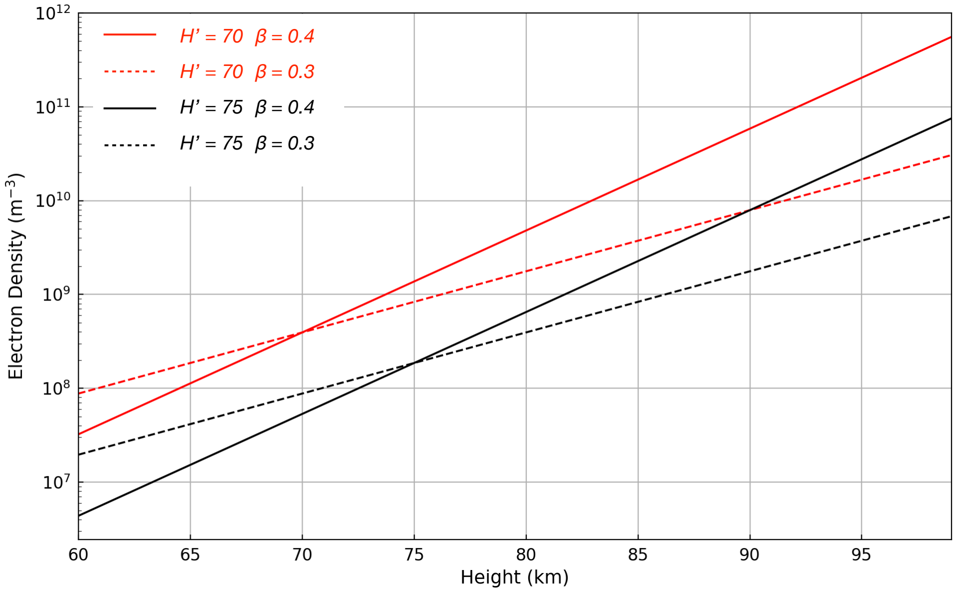

Figure 2.11: The electron density as a function of height in the D-region from Equation 2.45. The exponentially increasing electron density profile here depends on the two-parameter system of H' and β. To show how N_e depends on these parameters Equation 2.45 is plotted for different variations of H' and β. The dashed markings denote where the β value is the same and the coloured lines donate when H' is the same value. As shown, the β parameter acts as the relative slope of the exponential profile and the H' parameter acts as the intercept.

values. As described above, and shown in Figure 2.11, the β parameter describes the slope of the exponentially defined electron density, and H' varies the starting reference value (or intercept).

The modelling of the electron density increasing exponentially with height in the lower D-region is of course an approximation and the true conditions of the ionosphere are not exactly described by this simple expression. However, both experimental electron density profile gained from rocket experiments and modelling have shown that this is a reasonable approximation to make (Friedrich & Torkar, 1998; Mechtly *et al.*, 1972). The merit in this approach is that the ionosphere can be successfully described in terms of two parameters, H' and β and has proved useful for VLF propagation prediction. This is used in Chapter 6, together with the LWPC software[1] and VLF measurements to determine the electron density variations in the D-region in response to flaring activity.

---

[1] https://github.com/hayesla/LWPC

3

Instrumentation

The Sun is constantly observed in multiple wavelengths from both space- and ground- based observatories. The availability of these simultaneous datasets provides the necessary multi-wavelength information required for the study of QPPs in solar flares. This Chapter provides a detailed discussion of the instruments used in this thesis to observe the features of quasi-periodic processes in solar flares, and the detection of solar flares in our terrestrial ionosphere. In order to place our observations into a physical context, a comprehensive understanding of how these instruments observe is required.

3.1 The Ramaty High Energy Solar Spectroscopic Imager (RHESSI)

The *Ramaty High Energy Solar Spectroscopic Imager* (RHESSI) (Lin *et al.*, 2002) is a NASA Small Explorer mission launched in February 2002. The primary objective of RHESSI is to explore the physics of particle acceleration and explosive energy release in solar flares through the examination of high energy X-ray and γ ray emissions. This is achieved through RHESSIs capabilities to perform both imaging and spectroscopy in the energy range of 3 keV to 17 MeV, spanning both thermal and non-thermal X-ray and γ ray energies. RHESSI provides high spatial resolution of up to 2.3" with a full-disk field of view and spectral resolution of 1 keV at 3 keV, increasing up to 5 keV at 5 MeV (FWHM). RHESSI has played a central role in the study of QPPs and observations have been employed in this thesis in Chapters 4 and 5.

As of the 16th August 2018, RHESSI has been decommissioned following difficulties with detectors and the on-board receiver. For over 16 years, RHESSI provided unparalleled X-ray observations of the Sun allowing for studies that have changed the way we understand solar flares, and although RHESSI is no longer taking observations, a wealth of historic data spanning two solar cycles exists to be further explored.

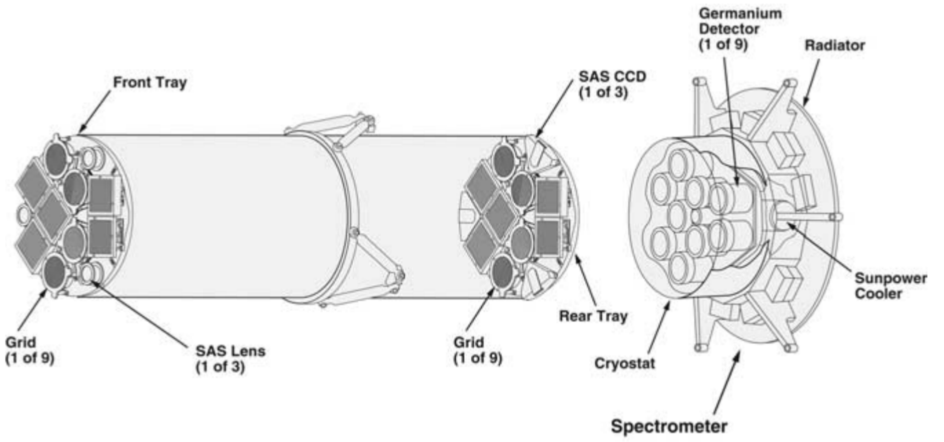

Figure 3.1: Schematic of RHESSIs imaging system. The key components are the dual grid rotating modulation collimators, as well as the set of nine cooled germanium detectors mounted behind the grids. Figure from Hurford *et al.* (2002).

3.1.1 Imaging

X-ray photons above a few keV are energetic enough to scatter or penetrate through a reflective coating or incidence mirror, and hence it proves a challenge to perform direct imaging observations. Recent missions such as *NuStar* (Harrison *et al.*, 2013), and rocket experiments such as *FOXSI* (Glesener *et al.*, 2016; Krucker *et al.*, 2011), have made significant developments in this regard, providing the new technologies required for future X-ray instruments. RHESSI, however, instead of using focusing optics, creates X-ray images via an indirect Fourier imaging technique (Hurford *et al.*, 2002), described below.

A schematic of the RHESSI instrument is shown in Figure 3.1. The single instrument consists of nine rotating modulation collimators (RMCs) each containing a pair of widely separated grids at a distance of 1.5 m. Behind the RMCs are nine cooled Germanium detectors placed at the rear of the spacecraft which make up the spectrometer. Each detector is cryogenically cooled to $\sim$75 K and

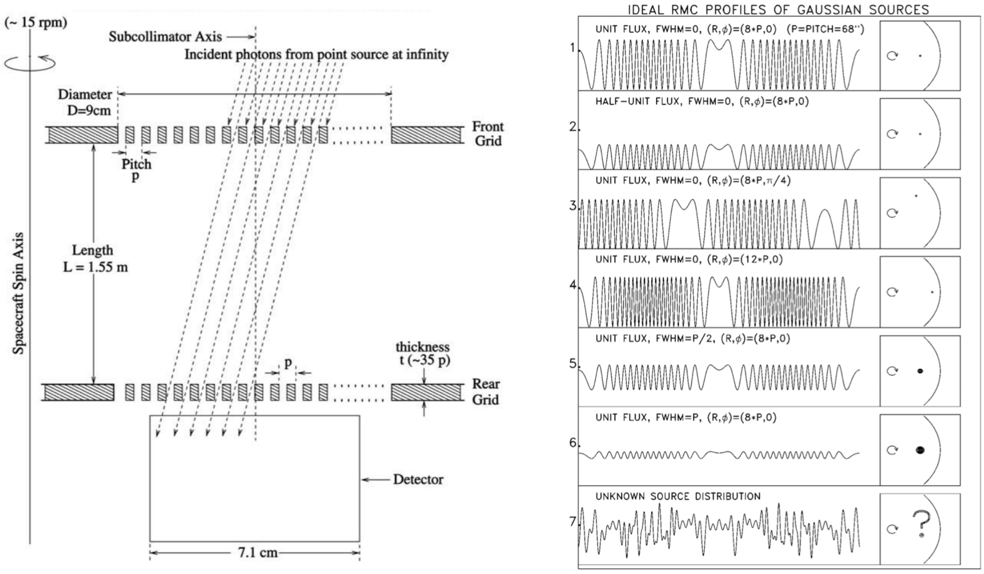

Figure 3.2: The RHESSI imaging concept. *Left*: A schematic geometry of how incident photons enter the RHESSI subcollimators. *Right*: An example of the the modulation profiles for various configurations of an emitting source on the solar disk. Both figures are from Hurford *et al.* (2002).

has no inherent imaging capability, but instead records counts of incoming photons. Each grid pair in the RMCs is made up of an array of X-ray opaque slats (made of Tungsten, or Molybdenum in case of grid set 1) separated by transparent slits. The slits of the two grids in each RMC are parallel and their pitches are identical. RHESSI rotates continuously around its axis pointing at the Sun at a rate of 15 rpm (every 4 s). The rotation of the spacecraft causes incident X-ray photons passing through the RMCs to be periodically blocked, resulting in a recorded time modulation profile at each of the detectors. This modulation pattern encodes spatial information about the X-ray source origin, and with knowledge of the spacecraft spin times and grid geometries, can be used to reconstruct an X-ray image. An illustration of this is shown in Figure 3.2. Incoming solar X-rays either fall upon a slit or slat of the front and rear grids of one of the RMCs before reaching the detector (left panel of 3.2). The resulting modulated time profile at the detector is demonstrated in the right hand panel of 3.2. Each profile provides an example of a different configuration of an off-axis source, demonstrating that modulation profile amplitude, phase and frequency encode the geometry of the source.

The time modulated signal can be stacked per fraction of the spacecraft rotation (or roll bin), over many rotations to create X-ray visibilities. These X-ray visibilities, V, are two-dimensional Fourier components of the X-ray source given by

$$V(u, v; \epsilon) = \int_x \int_y I(x, y; \epsilon) e^{2\pi i(ux+vy)} dxdy. \tag{3.1}$$

Here, (u, v) are the coordinates in Fourier space, determined by the RMCs grid pitch and current angle of the grid slats. The inverse Fourier transform of equation 3.1 results in an X-ray image I in the real (x, y) plane at a given energy ϵ.

The grids in each of the RMCs are numbered 1-9, and offer varying grid pitches that logarithmically increase (by a factor of $\sqrt{3}$) from the finest FWHM angular resolution of 2.3" for grid 1, up to the coarsest 183.2" for grid 9. Each RMC measures visibilities that are represented by circles of constant radius in the (u, v) plane (Massone *et al.*, 2009). Image reconstruction from measured visibilities has a long history from radio astronomy and similar techniques can be utilized to also produce RHESSI images. RHESSI X-ray images can be constructed for a defined time and energy range with a combination of detectors that optimizes the resolution of the source.

Various image reconstruction algorithms have been developed to produce maps from RHESSIs visibilities. The most basic approach is that of back-projection which corresponds to performing a two-dimensional Fourier transform of Equation 3.1, producing a so-called 'dirty-map'. However, this results in a map of poor image quality and tends to exhibit strong sidelobes, or rings of intensity around the primary source. To improve image quality a variety of techniques are available such as CLEAN (Högbom, 1974; Hurford *et al.*, 2002), Maximum Entropy Methods (MEM), Pixon and visibility forward fitting (VisFwdFit) to name but a few. In this thesis, the CLEAN algorithm was used to produce RHESSI images and is detailed briefly below.

The CLEAN algorithm was originally developed for the field of radio astronomy (Högbom, 1974), but was adapted for use in RHESSI imaging analysis (Hurford *et al.*, 2002) to remove sidelobes from a 'dirty map'. The CLEAN algorithm is an iterative process that is based upon the assumption that the X-ray image consists of a superposition of many X-ray point sources. Beginning with a 'dirty' back-projected map, the pixel of highest intensity is located and some chosen fraction of the flux value, known as the gain (default 10%), is taken to produce a point source of flux of that given value. This point source is then convolved with the CLEAN Point Spread Function (PSF), or 'beam width factor', which has a Gaussian profile intended to reflect the effective resolution off the subcollimators used to produce the 'dirty map'. This CLEAN component source is then subtracted from the image, and the process is repeated until a certain number of iterations is achieved, or until the peak flux in the image is negative. The resulting CLEANed map consists of the positions and amplitudes of each of the CLEAN components.

3.1.2 Spectroscopy

The RHESSI spectrometer is made up of the nine Germanium detectors located at the rear of the instrument (Smith *et al.*, 2003). An X-ray or γ ray photon that reaches the detectors creates an electron/hole pair which are then attracted to the cathode/anode resulting in a small current which is registered as a time-tagged count. This results in RHESSI producing a count spectrum. This count spectrum does not have a one-to-one relationship with the emitted photon spectrum. An expression relating the observed count spectrum (C) to the incident photon spectrum (I) is given by

$$C = B + DRM + I. \tag{3.2}$$

Here B refers to the background count rate, and DRM is the detector response matrix. The background count rate comes from a combination of instrumental noise, together with both solar and non-solar emissions. The DRM relates the incident photon energies to that of the observed count detected, taking into account the many effects that could modify the input count spectrum such as Compton scattering by various components of the spacecraft, Compton scattering by the Earth's atmosphere, noise in the electronics, radiation damage to detectors resolution etc. Once the RHESSI spectrum is obtained, it can be analyzed using the Objective Spectral Executive (OSPEX) (Schwartz *et al.*, 2002). OSPEX offers the ability to fit a background spectrum (often determined when RHESSI is in night-time), and a choice of model spectra to fit to the data in order to infer specific properties about the observed spectrum.

To accommodate the large dynamic range of soft X-ray emission from solar flares, RHESSIs detectors are mounted with attenuators (aluminum shutters) that are moved in front of the detectors during times of high photon counts to prevent saturation of the detectors. There are three attenuator states; A0 - no shutter, A1 - thin shutter, and A3 - thick shutter. The attenuator state of RHESSI must be taken into account when performing analysis. Similar care needs to be taken given the fact that some RHESSIs gyroscopic motions can, in some cases, produce artificial oscillations in the RHESSI lightcurves (Inglis *et al.*, 2011).

RHESSI is in a low Earth orbit, and experiences regular night-time intervals from which it is obscured from the Sun. In this way, continuous observations with RHESSI are not available, and some flaring events are missed. RHESSIs observational windows include a 75 minutes 'daytime' followed by 35 minutes of 'nighttime'.

3.2 FERMI Gamma Ray Burst (GBM) monitor

The Fermi Gamma-Ray Burst Monitor (GBM) (Meegan *et al.*, 2009) is one of the instruments on board the Fermi Gamma-Ray Space Telescope, an X-ray and γ ray astrophysics mission launched in June, 2008. The primary objective of Fermi GBM is to observe both time-history and spectra of gamma-ray bursts (GRBs) through observations of the entire sky over an energy range of $\sim$ 8 keV to 40 MeV. The instrument consists of 12 thallium-activated sodium iodide (NaI (Tl)) scintillation detectors which are sensitive to the energy range from 8 keV to 1 MeV and two bismuth germanate (BGO) detectors, sensitive to energies between 150 keV and 40 MeV. Although the focus of GBM is the study of GRBs, it also provides quality high energy solar flare observations, conveniently overlapping with the RHESSI energy range. At any one time, six NaI detectors are sun-ward facing, and provide nominal time cadence of 1 s in normal mode, and up to 0.28 s when triggered into burst mode. Fermi GBM observations are an excellent resource to study oscillatory signals in flaring time-series, particularly due to the high time cadence, and the fact that it doesn't share the time-series discontinuities that RHESSI experiences due to its attenuator state changes. In this way, the FERMI time-series observations can be used to perform detailed hard X-rays lightcurve investigations, and RHESSI can provide the complementary X-ray imaging. Similar to RHESSI, Fermi also has a low Earth orbit which results in regular occultations of the Sun. An important caveat of Fermi GBM is that during large solar flares, the lightcurves can exhibit non-linear responses due to pile-up effects. In order to mitigate this, often the most sunward facing detector is avoided.

3.3 Geostationary Operational Environmental Satellite (GOES)

The *Geostationary Operational Environmental Satellites (GOES)* are a series of satellites launched and maintained by the National Oceanographic and Atmospheric Association (NOAA). GOES-1 was initially deployed in 1975, and since then at least one GOES satellite has been in operation, with GOES-16 the latest in line (November 2016). GOES is primarily used to monitor terrestrial weather, however each satellite is fitted with two X-ray Sensors (XRS) which provide continuous spatially integrated solar X-ray flux for the wavelength bands 0.5–4 Å (3–24 keV) and 1–8 Å (1.5–12 keV) with 3 s cadence (2 s since December 2009).

3.3.1 The X-ray Sensor (XRS)

The X-ray measurements from GOES/XRS are obtained from dual ion chamber detectors with beryllium windows, one for each wavelength band. Chamber A (0.5–4 Å) is filled with Xenon gas and has a beryllium window thickness of 20mm, whereas Chamber B (1–8 Å) is filled with Argon gas and has a beryllium window of 2mm thickness. The detailed description of the design of GOES-8 is outlined in Hanser & Sellers (1996). The raw measured quantities are currents induced in the ion chambers by incident X-ray flux. The measured response is described by the transfer function $G(\lambda)$ which represents the amount of current produced per unit of incident X-ray flux. Each detector is calibrated before launch. In Figure 3.3 the transfer functions for the first 12 GOES satellites are shown. As can be seen there are very small differences between detectors on different satellites. Techniques have been developed that allow thermal properties of the soft X-ray emitting plasma to be estimated. In this way, temperature and emission measures estimates can also be provided by the GOES/XRS sensor. Details on how this is achieved are discussed in Appendix A.1. The GOES/XRS has become a vital tool in solar physics providing a largely uninterrupted record of solar activity over the last 40 years. Observations in the 1–8 Å channel provide the primary measurements used as the standard to classify the magnitude and duration of solar flares. These observations provides a valuable resource to study the past solar flare activity, and aid in building predictive flaring forecasts which is an important aspect of space weather.

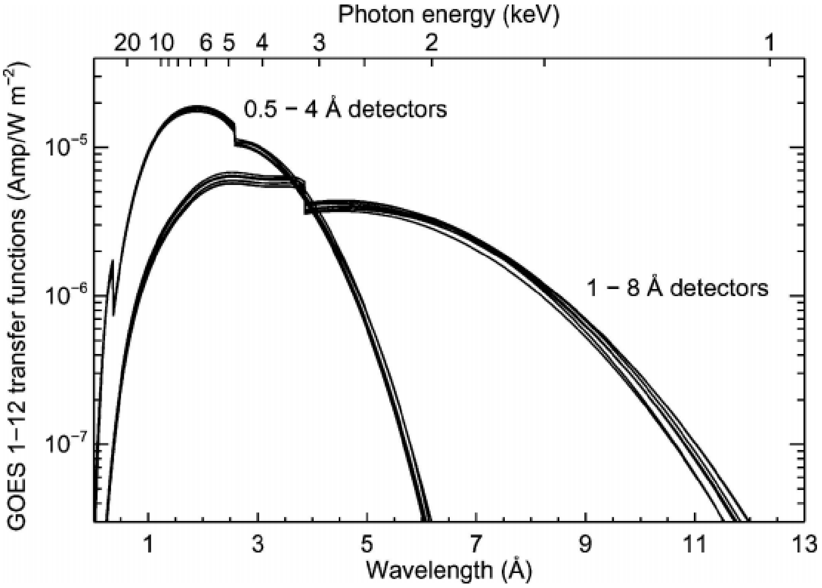

Figure 3.3: Response function of GOES XRS instruments from GOES satellites 1-12. As shown there has been relatively very small differences between the detectors on the different instruments. Figure from (White *et al.*, 2005)

3.3.2 Temporal Fine Structure in GOES XRS Lightcurves

For many years the GOES/XRS lightcurves were thought be rather uninformative with a typical lightcurve during a flare rising relatively slowly during the impulsive phase followed by a prolonged roughly exponential fall back to pre-flare levels. However with upgrades of GOES 13, 14 and 15 improved measurements of soft X-ray flux now provide 2 s time resolution and finer digitization. With these new observations made available since 2010, more extensive small amplitude temporal fine scale structure and pulsations have become evident in soft X-ray emission. We take advantage of these improved high signal-to-noise measurements to investigate the prevalence of these pulsations in a QPP context. An example of the temporal fine structure evident in the GOES time derivatives is shown in Figure 3.4.

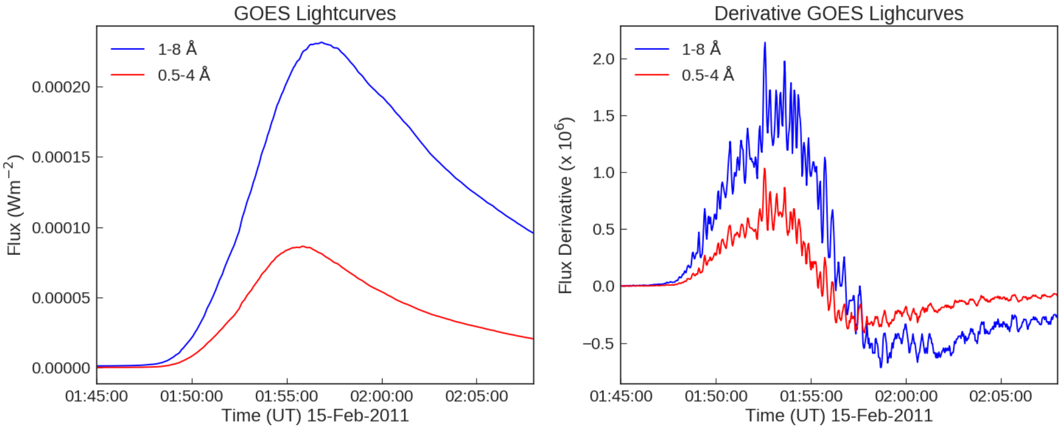

Figure 3.4: An example of the fine structure evident in the GOES derivative from an X2.2 solar flare from February 15 2011. The left panel shows the GOES lightcurves in both the 0.5–4 Å and 1–8 Å channels. The right hand panels shows their respective derivatives, highlighting the fine scale structure of the emission

3.4 Large Yield Radiometer (LYRA) on board PROBA2

The Large Yield Radiometer (LYRA), on board the *PRoject for On-Board Autonomy (PROBA2)* spacecraft launched in 2009, provides solar irradiance measurements in the soft X-ray and EUV passbands (Dominique *et al.*, 2013; Hochedez *et al.*, 2006). LYRA observes the Sun in four channels with nominal cadence of 0.05s. In this thesis we focus on the Zirconium (Zr) ($<$ 2 nm + 6-20 nm) and Aluminum ($<$ 5 nm + 17-80 nm) channels, both of which include contributions of soft X-ray and EUV. These provide complementary data sets to that of GOES/XRS and EVE/ESP and assist in the detection of QPPs signatures at these wavelengths.

3.5 Nobeyama Radioheliograph and Radiopolarimeters

The Nobeyama Radioheliograph (NoRH) (Nakajima *et al.*, 1994; Takano *et al.*, 1997) is a ground-based radio interferometer dedicated to observing the Sun in the microwave frequency range. NoRH was built in 1992 at the Nobeyama Solar Observatory in Japan. The array consists of 84 0.8 m parabolic antenna arranged in an equally spaced T-shaped configuration., extending 220 meters in the north-south direction and 489 m in the east west direction. A view of NoRH is shown in Figure 3.5. This baseline configuration is designed to yield full-disk observations of the Sun with a field of view of 40'. Each pair of antenna measures a complex Fourier component of the brightness distribution of the Sun, which can be used to produce images of the full-disk of the Sun via a Fourier reconstruction process, similar to RHESSI. NoRH provides observations at two frequencies of 17 and 34 GHz at a maximum spatial resolution of 10" and 5" respectively. Measurements of polarization are also available at 17 GHz.

NoRH takes measurements every 1 s, but this can be reduced to 0.1 s in event mode, providing excellent temporal resolution for the study of solar flares. Given the nominal temporal resolution and ability to image flaring regions, NoRH has played a key role in many studies of QPPs. The observations at GHz frequencies at 17 and 34 GHz is attributed to non-thermal gyrosynchrotron emission from flare accelerated electrons. Observations of microwave emission hence provide another diagnostic in addition to hard X-rays to understand the flaring energy release process, and help constrain what mechanisms cause QPPs.

Figure 3.5: A view of the Nobeyama RadioHeliograph array. Image from *https://solar.nro.nao.ac.jp/norh/*

The Nobeyama RadioPolarimeters (NoRP) observe the Sun at multiple frequencies in the microwave range, namely 1, 2, 3.75, 9.4, 17, 35 and 80 GHz. NoRP does not have imaging capabilities but can record spatially integrated flux and circular-polarization at each frequency at a high time resolution (1 s). The range of frequencies observed with NoRP provides a microwave spectrum from which we can determine if a source is optically think/thin, and provide spectral information to infer properties of the emitting plasma. The disadvantage of NoRH and NoRP however is that observations can only be made during hours of daylight, which can be as little as 8 hours during some parts of the year.

3.6 The Solar Dynamics Observatory (SDO)

The Solar Dynamics Observatory (SDO) (Pesnell, 2015) is a NASA mission launched in February 2010. It was designed to study the solar atmosphere in multiple wavelengths with high spatial and temporal resolution. SDO is the first mission to be launched as part of NASA's *Living With a Star* (LWS) program, a program with a primary objective to aid our understanding of the different aspects of the connected Sun-Earth system. The observatory consists of three scientific instruments, namely the Atmospheric Imaging Assembly (AIA; Lemen *et al.* (2011)), the Helioseismic and Magnetic Imager (HMI; Scherrer *et al.* (2012)) and the Extreme Ultraviolet Experiment (EVE; Woods *et al.* (2010)). AIA and the Extreme Ultraviolet Spectrometer (ESP) which is part of EVE are the instruments from SDO that are used in this thesis, and are described in detail in this section.

3.6.1 Atmospheric Imaging Assembly (AIA)

The Atmospheric Imaging Assembly (AIA) on-board SDO provides continuous high-resolution full-disk images of the solar atmosphere in 10 EUV and UV passbands (94, 131, 171, 193, 211, 304, 335, 1600, 1700 and 4500 Å). The field of view of AIA is 41' (up to 0.5 $R_\odot$ above the limb) and has a spatial and temporal resolution of 0.6" and 12 s respectively.

The AIA instrument comprises of four 20 cm Cassegrain telescopes which record images onto a 4096×4096 back-illuminated CCD. Entrance filters at the telescope aperture block unwanted visible and infrared radiation, and filters in a filter wheel mechanism located in front of the CCD are used to select the wavelength of interest. Each telescope has two sets of multi-layer filters that are optimized for the desired central wavelength. The filters are designed to observe solar emissions in a range of temperatures spanning the transition region to the hot flaring corona. These provide imaging in seven EUV passbands centered on specific lines - Fe XVII (94 Å), Fe VII, XXI (131 Å), Fe IX (171 Å), Fe XII,

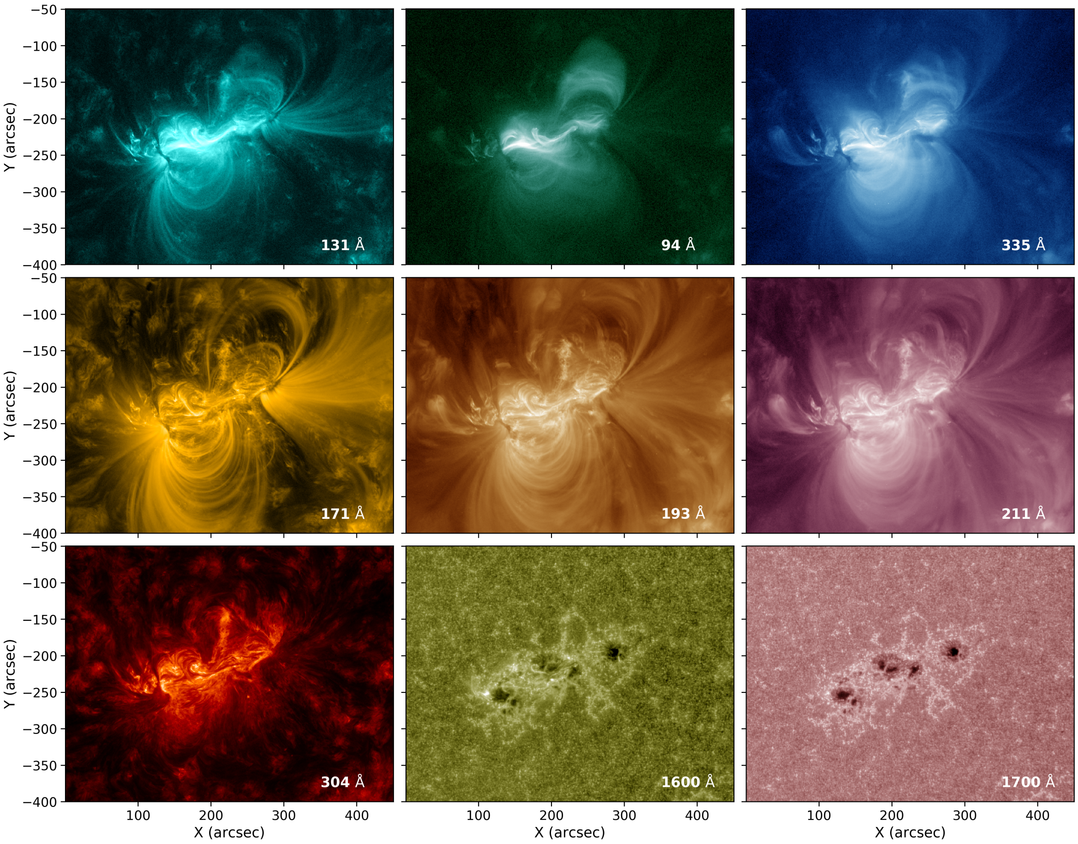

Figure 3.6: An active region observed on February 15 2011 with the different AIA EUV and UV passbands. This image illustrates the different temperature-dependent structures that AIA can observe.

XXIV (193 Å), Fe XIV(211 Å), He II (304 Å), and Fe XVI (335 Å). There are also two UV filters that observe continuum emission (1700 Å) and also contributions from the C IV line (1600 Å). One filter also provides observations in the visible 4500 Å passband. An example observation of an active region from the different AIA channels is shown in Figure 3.6, demonstrating how different passbands are sensitive to different features.

Each telescope is dual channel, consisting of two sets of multi-layer filters on each half of the telescope. The exception to this is telescope 3, in which

Channel	**Primary ions**	**Regions of atmosphere**	**log T (K)**
4500 Å	continuum	photosphere	3.7
1700 Å	continuum	temperature minimum, photosphere	3.7
304 Å	He II	chromosphere, transition region	4.7
1600 Å	CIV + cont	transition region, upper photosphere	5.0
171 Å	Fe IX	quiet corona, upper transition region	5.8
193 Å	Fe XII, XXIV	corona, hot flare plasma	6.2, 7.3
211 Å	Fe XIV	active region corona	6.3
335 Å	Fe XVI	active region corona	6.4
94 Å	Fe XVIII	flaring corona	6.8
131 Å	Fe VIII, XXI	transition region, flaring corona	5.6, 7.0

Table 3.1: An overview of the AIA channel details, including the wavelength, primary ions responsible for the emission, targeted region of the solar atmosphere and peak characteristic temperature. From Lemen *et al.* (2011)

one half caters for the 171 Å channel and the other provides the broadband UV and visible coverage for 1600, 1700 and 4500 Å. A mechanical shutter is used to regulate the exposure time of the image. This exposure time varies with passbands but is usually on the order of 2 s. During events when the intensity of emission can increase by orders of magnitude (i.e. during a flare) this exposure time can be reduced to 0.2 s to mitigate the effects of saturation on the CCD. The EUV passbands have a nominal observational cadence of 12 s whereas the UV passbands have a typical cadence of 24 s. The UV channels have a reduced cadence as telescope 3 provides the optics for four different channels. The 4500 Å channel has a cadence of 1 hour. This is not particularly useful in the study of solar flares, but is used for the co-alignment with observations from other telescopes.

These wavelengths are chosen for the specific purpose to probe different regions of the solar atmosphere depending on their temperature. Table 3.1 provides

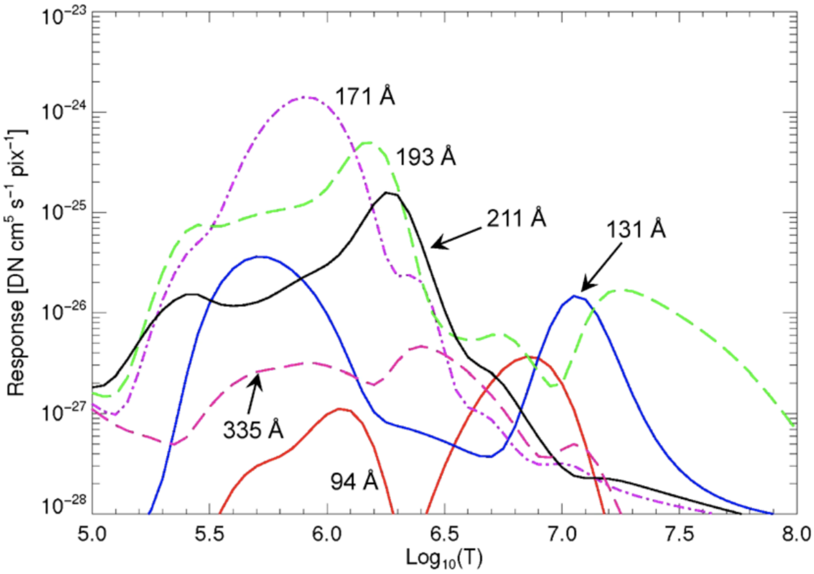

Figure 3.7: The AIA temperature response function for each of the 6 EUV passbands. Figure from Lemen *et al.* (2011).

an overview of the different AIA channels, the primary ions, regions of the atmosphere the channel probes and the peak temperatures response. The filters themselves are quite broad and have a complex temperature response due to contributions from different spectral lines in addition to the primary ion. The temperature response function of 6 coronal EUV channels is shown in Figure 3.7 (Lemen *et al.*, 2011). It demonstrates that some of the channels have quite a wide temperature response, whereas others have a double peak.

3.6.2 EUV Variability Experiment (EVE/ESP)

The Extreme ultraviolet Variability Experiment (EVE) instrument suite (Woods *et al.*, 2010) on-board SDO consists of several irradiance instruments, namely the Multiple EUV Grating Spectrographs (MEGS - A and B), and the EUV SpectroPhotometer (ESP) (Didkovsky *et al.*, 2009). ESP provides high time cadence

(0.25 s) irradiance observations in five channels, one soft X-ray (0.1-7 nm) and four EUV (17.1, 25.7, 30.4 and 36.6 nm). The instrument consists of silicon photo-diode detectors that are located behind a filter wheel and a transmission grating. An aluminum foil filter is placed in front of the aperture to limit visible light into the detector, and transmits soft X-ray and EUV radiation to the detectors. The four first order bands of the diffraction grating are centered around the EUV wavelengths. An additional filter consisting of a titanium layer between two carbon layers in front of the zeroth order grating isolates the 0.1-7 nm bandpass to provide soft X-ray measurements.

The research outlined in this thesis makes use of the 0.1-7 nm measurements provided by ESP to study the detail of fine structure QPPs in the thermal emission from solar flares. The bandpass of ESP (1–70 Å) conveniently overlaps with that of GOES (1–8 Å and 0.5–4 Å), and hence provides independent measurements of the fine structure variability detected in soft X-ray emission. In this way, complementary observations of ESP 0.1–7 nm lightcurves are used to clarify that the small scale structure observed in the GOES lightcurves is not an instrumental artefact, but indeed of solar flare origin.

3.7 Sudden Ionospheric Disturbance (SID) Monitor

The D-region of the ionosphere can be thought of as a giant X-ray detector. As a partially ionized plasma, it characteristically responds to ionizing disturbances such as enhanced X-ray emission during a solar flare. The measurements of VLF

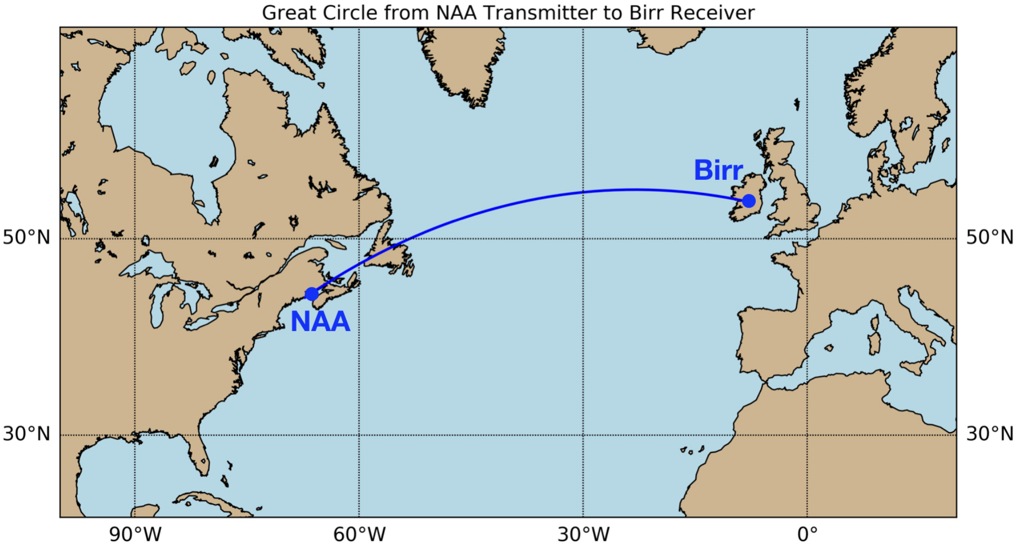

Figure 3.8: A map of the VLF propagation path from the transmitter (NAA) to the receiver (Birr). Measurements of a VLF signal at Birr provide information about the ionospheric D-region over the propagation path.

signals, generated by large communication/navigational transmitters has emerged as one of the most reliable tools for the remote sensing of these ionizing disturbances in the D-region. This research makes use of VLF signal measurements from the Stanford Sudden Ionospheric Disturbance (SID) Monitor (Scherrer *et al.*, 2008) that is located at the Rosse Solar-Terrestrial Observatory (RSTO) in Birr, Co. Offaly, Ireland. The SID monitor is tuned to the US Naval communications transmitter (call-sign NAA) located in Cutler, Maine, USA, that operates at a frequency of 24 kHz. The propagation path of the VLF signal from NAA to Birr has a great circle distance of 5320 km and is largely over the Atlantic ocean, as illustrated in Figure 3.8.

3.7.1 SID Monitor

The VLF recording system consists of a Stanford SID monitor and a receiving antenna, both of which are shown in Figure 3.9. The SID monitor used was developed and distributed by Stanford University's Solar Center, and provides an inexpensive VLF receiving system. Used together with a wire-loop antenna, the SID monitor has the capability to record the amplitude of narrowband VLF signals of a particular frequency, in this case tuned to 24 kHz. The receiving antenna is a magnetic loop antenna that simply consists of a diamond shaped frame (1.42 m side length) that holds a series of wire loops (23 turns), as shown in the left hand panel of Figure 3.9. The signal from the antenna is fed into the SID monitor where it is then filtered, amplified, rectified, and integrated to provide a measure of the detected VLF signal strength.

3.7.2 VLF Transmitter

The US Navy operates a number of VLF transmitters located around the world as part of the submarine broadcast system. VLF radio waves have the ability to penetrate into the sea and hence provide a means for communications to submerged submarines. The need for navigation and communications with submarines, along with reliable global military communications was actually the indirect driving force to much of the developments of VLF propagation theory and experiment over the past century (Barr *et al.*, 2000). The VLF transmitter NAA located in Cutler, Maine, US, is one of the largest radio transmitters in the world operating with a radiative power of up to 1.8 MW at a frequency of 24 kHz. Given the long wavelength range of VLF radio waves and the high

Figure 3.9: The Stanford SID monitor (left) and the wire-loop antenna (right) that make up the VLF receiving system. This system is located at the Rosse Solar Terrestial Observatory in Birr, Co. Offaly Ireland and receives VLF signals at 24 kHz.

radiative power, the transmitter consists of an enormous antenna system. An aerial view and a plan view of the NAA VLF antenna is shown in Figure 7.12. It consists of two separate arrays, each composed of 13 towers connected at the top by a network of horizontal cables. The central tower in each array is 298 m high and is surrounded by six masts 266 m tall arranged on a 558 m radius circle, and a second ring of masts 243 m tall are located on a 935 m radius circle (Hansen, 1994; Watt, 1967). Both arrays are over 1.5 km across, and almost cover the entire peninsula. Although the primary function of the NAA VLF transmitter is to facilitate naval communications, it also provides a continuous VLF signal for which amplitude and phase measurements can be recorded and readily used in ionospheric research (e.g. Clilverd *et al.*, 1999, 2009; Kolarski *et al.*, 2011; Žigman

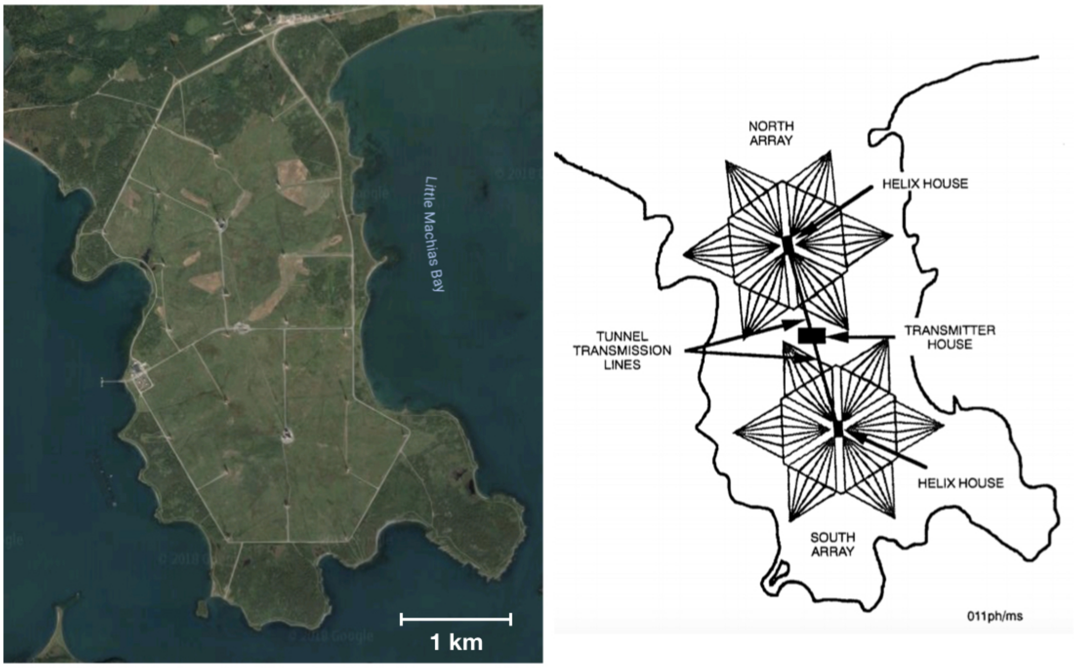

Figure 3.10: An aerial view and schematic plan of the NAA VLF transmitter located in Cutler, Maine. The left hand satellite view is from Google Maps, and the plan view (right) is from Hansen (1994). The large size of the antenna is clear, almost encompassing the entire peninsula.

et al., 2007).

4

Quasi-Periodic Pulsations during the Impulsive and Decay phases of an X-class flare

In this Chapter a multi-instrument investigation into the nature of QPPs observed during the impulsive and decay phases of the X1.0 solar flare of October 28 2013 is presented. This work focuses on the characteristics of the fine structure pulsations evident in the soft X-ray time derivative, and compares this variability with structure across multiple wavelengths including hard X-ray and microwave emissions. It is found that during the impulsive phase of the flare, high correlations between QPPs observed in both the thermal and non-thermal emissions are found. A characteristic timescale of ~20 s is observed across all channels investigated, and a second period of ~55 s is observed in the non-thermal emissions. Soft X-ray pulsations are observed to persist into the decay phase, up to 20 minutes after the non-thermal emissions have ceased. The decay phase thermal QPPs have a small amplitude and demonstrate an increase in their characteristic timescale from ~40 s to ~70 s. The impulsive phase co-existing multi-wavelength QPPs are interpreted in terms of episodic particle acceleration and plasma heating. The persistent decay phase thermal QPPs are most likely connected with MHD processes of post flare loops such as the fast sausage mode or vertical kink mode. This research is published in *Astrophysics Journal Letters* Hayes *et al.* (2016).

4.1 Introduction

The temporal evolution of a solar flare is often divided into two phases, an impulsive phase that is dominated by explosive energy release in the form of particle acceleration and prominent heating, and a decay phase that is dominated by cooling processes as the reconfigured coronal structures relax back to their original state. A key observational feature of the impulsive phase is the common presence of QPPs observed in the non-thermal emission associated with flare accelerated electrons, such as hard X-ray bremsstrahlung and microwave gyrosynchrotron emissions. The observations of such QPPs places constraints on the physical mechanisms responsible for solar flaring energy release and their study can help provide clues about the flaring site itself. Despite the fact that QPPs have been an important research topic in solar flare studies over the past 40 years, the exact nature and underlying mechanism for their appearance in flaring emissions remain a subject of debate.

The majority of QPP investigations have focused on observations at hard X-ray and microwave wavelengths (e.g. Fleishman *et al.*, 2008; Inglis & Dennis, 2012; Nakariakov & Melnikov, 2009; Parks & Winckler, 1969). This is due in part by the large amplitude pulsations often observed in this type of emission, reflecting the impulsive energy release. Recently it has become clear that similar QPPs can also exist in the emission associated with flare heated plasma, such as the soft X-ray observations from the GOES X-ray sensors (1–8 Å and 0.5–4 Å). The pulsations from these emissions are much less pronounced than their non-thermal counter parts, and hence require some data processing to be visually identified. It has been found that the soft X-ray QPPs can be highlighted upon the removal of the large scale trend of the overall emission, achieved either by detrending (Dolla *et al.*, 2012) or in the numerical time derivative of the flaring lightcurves (Simões *et al.*, 2015). These observations provide new insight into QPPs in flaring emission, and suggest that QPPs are indeed a multi-wavelength phenomena.

In a recent statistical study by Simões *et al.* (2015) it was found that 80 % of X-class solar flares from solar cycle 24 demonstrate QPPs in the GOES soft X-ray measurements during the impulsive phase. The exact nature of the fine structure soft X-ray QPPs associated with thermal flaring emissions remains to be studied in detail, and comparisons across multiple wavelengths are required to improve our understanding of the QPP phenomena. In this Chapter a particular event was chosen to perform a detailed study, namely the X1.0 solar flare from October 28 2013. This flare was selected following a screening of all X-class flares that demonstrate QPP signatures and that had observations across multiple wavelengths. The X1.0 flare presented here had available observations throughout the entire flaring event (in particular both hard X-ray and microwave), and provided one of the most prominent examples of large modulated QPPs from the sample of X-class flares.

4.2 Observations

We investigate the presence of QPPs detected in the GOES X1.0 solar flare on October 28 2013 (SOL2013-10-28) from NOAA active region 11875 located at N07W77. The observations used in this study focus on multiple datasets that consist of high cadence ($\geq$2 s) X-ray (both soft and hard) and microwave emissions, from both space-borne and ground-based instruments. QPPs in soft X-ray emissions were observed using both channels of the GOES X-ray sensor (1–8 Å and 0.5–4 Å), the Zirconium channel (< 2 nm + 6-20 nm) of LYRA, and the soft X-ray (1-70 Å) channel from ESP. These channels have overlapping passbands and observe the thermal contribution from the flaring emission. Fermi GBM provided X-ray observations in the 8-100 keV energy range, spanning both soft and hard X-ray regimes. Observations at 17 GHz and 34 GHz from the Nobeyama Radioheliograph were also used to investigate the microwave emission associated with accelerated electrons. These observations provide information on both the non-thermal and thermal emissions from the flare, allowing us to probe the different aspects of the observed QPPs in the flaring energy release.

For the analysis in this chapter, we concentrate on the GOES observations as they are uniquely capable of revealing the smallest pulsations in the 1-10 keV energy range, isolating the hot flaring plasma. The sampling precision and excellent signal-to-noise ratio of the GOES-15 instrument allows the time-derivative or detrended flaring timeseries to be studied in detail, revealing a wealth of pulsations and fine structure (Simões *et al.*, 2015). It is now certain that this small-scale variability is real and of solar origin based on simultaneous observations of different events made with both GOES 13 and 15 (Dennis & Tolbert, 2016), and with the comparison with other independent instruments (Dolla *et al.*, 2012). In this Chapter we also make use of both ESP and LYRA to investigate the thermal pulsations.

An overview of the soft X-ray lightcurves under investigation is shown in Figure 4.1 for GOES, ESP and LYRA, with their respective fluxes normalized to between 0 and 1. These lightcurves seem not to show an impulsive phase

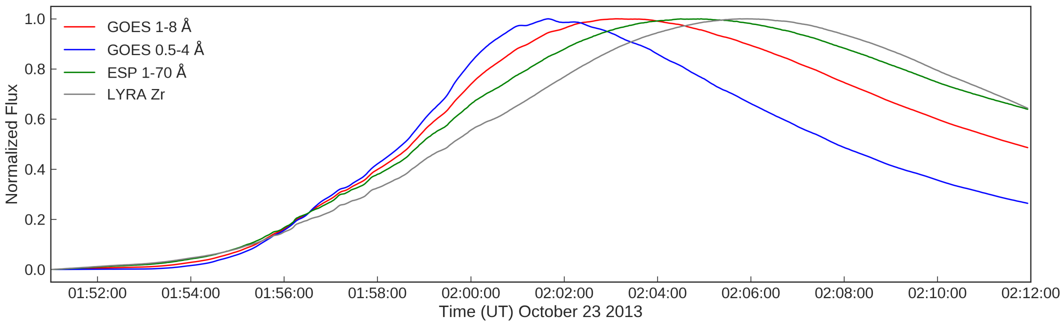

Figure 4.1: Normalized soft X-ray lightcurves. The different lightcurves peak at different times depending on the instrument temperature response. The GOES 0.5-4 Å channel peaks first, observing the hottest plasma, with the other channels peaking as the plasma cools through their respective passbands. Some variability is evident in the raw lightcurves, however it is very small compared to the overall emission. To enhance the fine structure QPPs, the time derivatives of these lightcurves are investigated and presented in Figure 4.2.

signature, with a rise and decay profile that looks relatively smooth with each channel peaking at different times depending on their associated temperature response. As expected, the higher energy emission peaks first (GOES 0.5–4 Å), a signature of the hottest plasma. This is then followed by the GOES 1–8 Å channel, ESP 1-70 Å and the LYRA Zr respectively as the plasma cools through their respective passbands.

The impulsive nature of the flare and quasi-periodic signatures are clearly demonstrated in the emissions associated with non-thermal electrons, such as the hard X-ray Fermi GBM observations in the 25-100 keV energy range and the microwave 17 and 34 GHz shown in Figure 4.2 (a). The impulsive behaviour begins at 01:55:00 UT, and continues with 8 distinctive pulsations of growing intensity until 02:00:30 UT (this region is shaded in blue). The time derivative of the soft X-ray lightcurves is shown in Figure 4.2 (b), highlighting fine structure QPPs associated with the thermal emission. The lightcurves are multiplied by an exponential cooling constant function before the derivative is taken to allow for the derivative curves to stay above 0 in the plot. This has no effect on the identification of the pulsations, and is only applied for visual purposes.

The fine scale structure is correlated across the different instruments, confirming again that these pulsations are indeed real. The impulsive phase pulsations in the non-thermal emission clearly have counter parts in the thermal soft X-rays. The non-thermal hard X-ray and microwave impulsive emission cease at approximately 02:00:30 UT. After this time, the soft X-ray derivatives have a different character. The correlation between GOES, ESP and LYRA becomes less evident, and pulsations continue well into the decay phase in both GOES channels. To further investigate this, the flaring time series are divided into two regimes - the impulsive between 01:55:00 UT and 02:00:30 UT, and the decay regime: 02:00:30-02:20:00 UT, and the characteristics of these two intervals are studied with cross correlation and wavelet techniques.

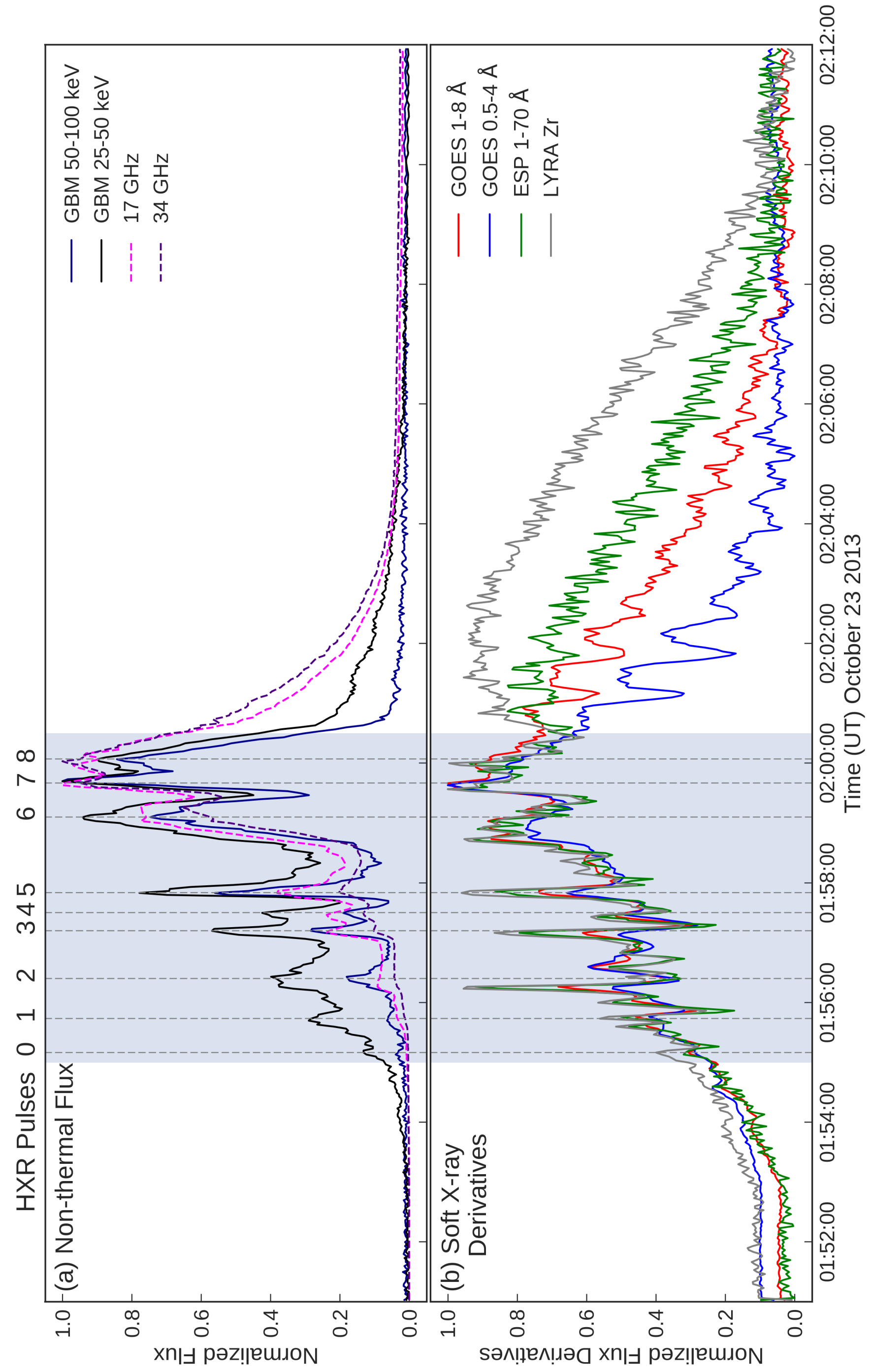

Figure 4.2: (a) Normalized lightcurves from the Fermi GBM 25-50 keV and 50-100 keV channels and from NoRH 17 and 34 GHz. (b) Derivatives of the soft X-ray channels from Figure 4.1. The blue shaded region denotes the impulsive phase regime of the flare, and the vertical grey dashed lines mark the peaks in the hard X-ray pulsations, numbered 0-8.

4.3 Impulsive Phase QPPs

The impulsive phase of the flare is marked within the blue shaded region in Figure 4.1. It is characterized by a ‘bursty’ regime of quasi-periodic signatures, clearly evident in the non-thermal emissions that demonstrate a large modulation depth, up-to 80% in the 50-100 keV channel. The modulation depth is calculated as the ratio of the amplitude of the pulsations to the overall trend given by $F_m = (F(t) - F_s)/F_s$, where F is the lightcurve timeseries and F_s is the slowly varying component that represents the overall trend (Reznikova & Shibasaki, 2011). Here the smoothly varying signal is calculated as the smoothed average of the signal (using a 60 s boxcar window). Different window sizes were tested here, and 60 s was chosen here as it was found to highlight the large pulsations of interest evident by eye. The modulation depth for the soft X-ray lightcurves is on the order of 1%, whereas higher energy wavebands demonstrate larger modulation depths. The maximum modulation depth is given for all channels in Table 4.1.

High correlations are observed across multiple wavelengths in both the non-thermal and time derivative of the thermal channels, with peaks in the derivative corresponding well with the hard X-ray peaks, both reflecting impulsive energy release during this phase. Each peak of a non-thermal pulsation is numbered for reference in Figure 4.2 to aid with comparison with the soft X-ray derivative. Notably, some of the pulsations in the soft X-ray derivative appear to peak before the pulsation in hard X-ray, such as peak 2, 3, 6 and 7. To examine this further and to compare the short time-scale variability, the gradual trend of the lightcurves is removed. This is achieved by subtracting a boxcar average of the time-series using a full width window of 30 s. This width is chosen to highlight the small scale fluctuations. This window size was found most appropriate following testing of several different window widths extending from 10 s to 1 minute. Different choices of window sizes did not change the results here in searching for time delays once the same window size is used on all the wavelengths of interest. Care however has to be taken when searching for a periodic signature as the size of the window in that case can effect results. We discuss this in more detail below. The original soft X-ray lightcurves, rather than their respective derivatives were used. Subsampling to the GOES cadence of 2 s (the longest cadence), cross correlation coefficients of each waveband were calculated with respect to the GOES 1-8 Å channel and their values are presented in Table 4.1. On these short time scales it is found that there is a minimal delay ($\leq$ 2 s) between the wavebands during the impulsive phase. This minimal time delay is inconsistent with the idea that the soft X-ray emitting plasma is coming from the plasma that has evaporated into the loop following heating by the accelerated electrons (that produce the hard X-rays) for which a time delay would be expected. It instead suggests that the soft X-ray and hard X-ray pulsations are occurring simultaneously such that the soft X-ray emitting plasma is a result of direct heating, either at the footpoints, or indeed potentially from the thermalisation of the accelerated electrons as they travel along the loop - the so called ‘warm-target’ model (e.g. Kontar *et al.*, 2015).

To search for the characteristic period of the QPPs during the impulsive phase, wavelet analysis was employed using a Morlet wavelet. When searching for a periodic signal in a time-series, care must be taken and an understanding of the methods used is required, a description of wavelet analysis is given in the Appendix A.2. In recent years it has come to light that some detection methods used to analyse QPPs may lead to a false detection of a significant period in a solar flare time series. For example, solar flare time series have an intrinsic power-law shape in the Fourier domain, meaning that the spectral power is related to the frequency ($P \propto f^{-\alpha}$), with a power law index $\alpha > 0$. In this way, the power-law component should be taken into account when assessing the significance of a dominant frequency (i.e. period). Recent work has demonstrated that by assuming a flat power spectrum when performing analysis on a detrended signal, the period found may readily be misinterpreted, with no explicit oscillation required to describe the observation (Gruber *et al.*, 2011; Inglis *et al.*, 2015). Following this, detrending here is avoided. For the soft X-ray lightcurves however, the variability needs to be highlighted against the overall trends, so the derivative is used, as in Figure 4.2 (b). This preserves the power-law shape in the Fourier domain, and so can be taken into account when searching for periodicity. The significance of enhanced power is tested for by assuming a power-law background, estimated for each individual time series using an auto-regressive AR(1) model as detailed in Torrence & Compo (1998). The power-law index that resulted from this was approximately -2 for all channels, a representation of 'red-noise'. The values are given in Table 4.1 for each time-series investigated.

The results of the wavelet analysis for the ESP 0.1-7 nm, GOES 1-8 Å and the GBM 50-100 keV time series, spanning thermal and non-thermal emissions, are shown in Figure 4.3 (a), (b) and (c) respectively. Each panel shows the time series under investigation, the wavelet power spectrum, and the corresponding global wavelet spectrum. The dotted line in the global wavelet spectrum signifies the 99.7% significance level above the power-law background model. During the impulsive phase it is found that the enhanced power is broadband with no narrow feature of a single timescale present. In all channels, a characteristic timescale of $\sim$ 20 s is found to be significant. A second peak at $\sim$ 55 s is also found, but only reaches above the 99.7% significance level in the non-thermal channels. The range of periods for each channel that are found above the significance level are listed in Table 4.1.

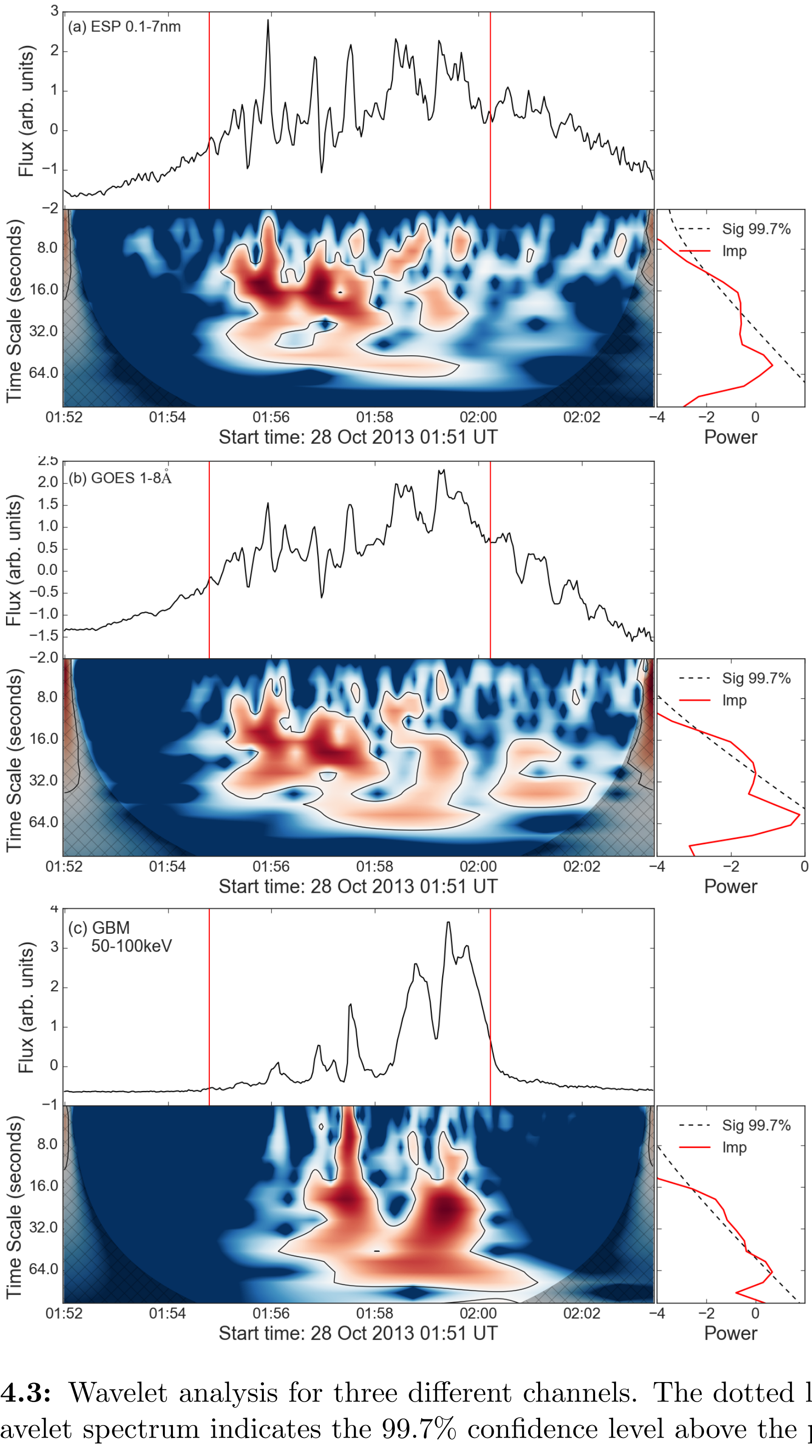

Figure 4.3: Wavelet analysis for three different channels. The dotted line in the global wavelet spectrum indicates the 99.7% confidence level above the power law background model. The red line is the global wavelet spectrum which demonstrates the summed power over the impulsive phase. (a) Derivative of ESP 0.1-7 nm channel, (b) derivative of GOES 1–8 Å and (c) GBM 50-100 keV.

Instrument	Corr.Coef	Modulation (%)	Power-law Index	Significant Timescale Range(s)
GOES 1–8 Å	1	0.9	-2.3	14-27 s
GOES 0.5–4 Å	0.92	1.2	-2.3	17-29 s
LYRA Zr	0.85	0.7	-2.2	13-24 s
ESP 1–70 Å	0.90	1.2	-2.3	12-25 s
GBM 8–15 keV	0.81	2.1	-2.2	18-32 s
GBM 15–25 keV	0.78	6.5	-2.1	14-33 s
GBM 25–50 keV	0.64	51.2	-2.3	16-26, 34-64 s
GBM 50–100 keV	0.56	80.1	-2.3	17-40, 49-68 s
NoRH 17 GHz	0.51	35.6	-2.3	15-27, 48-70 s
NoRH 34 GHz	0.48	16.2	-2.3	17-30, 54-56 s

Table 4.1: Summary of characteristics of pulsations across multiple wavelengths during the impulsive phase. The cross correlation coefficients are shown compared to GOES 1-8 Å. The 'significant timescale' column gives the range of timescales for which the summed power exceeds the 99.7% significance level above the power-law background model during impulsive phase.

4.4 Decay Phase QPPs

The decay phase of the flare has a different nature to the highly correlated ‘bursty’ features observed during the impulsive phase. The highly modulated pulsations associated with the non-thermal emission features cease at around 02:00:30 UT and the correlated nature of the multi-wavelength emissions breaks away. QPPs in the GOES derivative however persist well into the decay phase, even though the non-thermal emission is no longer evident. Some of the extended variability is observed in the ESP 1-70 Å just much less pronounced, and almost nothing can be detected above the noise in LYRA Zr. The wavebands of both ESP and LYRA are very broad, and it may be that the fine structure pulsations are smeared out. Moreover, these wavebands are also sensitive to a lower temperature plasma, and it may be that the QPPs only exist in the hottest plasma (as observed with GOES).

To investigate the extent of the pulsations in the decay phase, the GOES emission is studied in further detail, focusing on the time range from 02:00:30 - 02:20:00 UT. The derivative and detrended derivative of the GOES 1–8 Å lightcurve is shown in Figure 4.4, with the time range of interest plotted in black. The extended nature of the pulsations is clearly demonstrated. These fine structure features appear to have a less chaotic nature compared to the impulsive phase, with the amplitude of the QPPs subject to damping.

To investigate the timescale of these decay phase QPPs, wavelet analysis is again employed. Wavelet power is dependent on the amplitude of the pulsations, and hence to account for the amplitude damping observed, the pulsations are normalized to have a constant amplitude, see Figure 4.4 (c). This normalization is achieved by dividing the time series in Figure 4.4 (b) by an appropriate envelope, marked in red. This envelope is calculated as the absolute value of the lightcurve smoothed with a boxcar window of 200 s. A wavelet power spectrum is shown in Figure 4.4 (d). Interestingly, the wavelet power is not constant, and varies with time. The QPPs here demonstrate longer periods than detected in the impulsive phase. Enhanced power is observed at ∼40 s just after the impulsive phase, which then extends to ∼70 s over a duration of approximately 2 minutes from 02:06:30 to 02:08:30 UT. The vertical black lines in Figure 4.4 (d) highlight the time when this increase occurs. The period of ∼70 s then stays constant until approximately 02:15:00 UT, when the signal-to-noise level becomes comparable to the amplitude of the pulsations.

4.4.1 Decay Phase Loop Evolution

The increase in timescale into the decay phase is likely to be connected with longer loop lengths at later stages of the flare. To investigate this, RHESSI observations are used to produce soft X-ray source images in the 6-12 keV range which overlaps with the GOES passbands. Images were produced using the CLEAN algorithm (Hurford *et al.*, 2002). Figure 4.5 shows the contours of the soft X-ray source overlaid on 94 Å EUV images from AIA at two select times during the decay phase of the flare, just after the impulsive phase at 02:00 UT and then at the end of the observed QPPs at 02:20 UT. It is found that the soft X-ray source height readily increases as the time progresses, presumable a signature of continued magnetic reconnection resulting in newly formed loops at higher altitudes.

The loop length of the flare can be estimated from the RHESSI soft X-ray

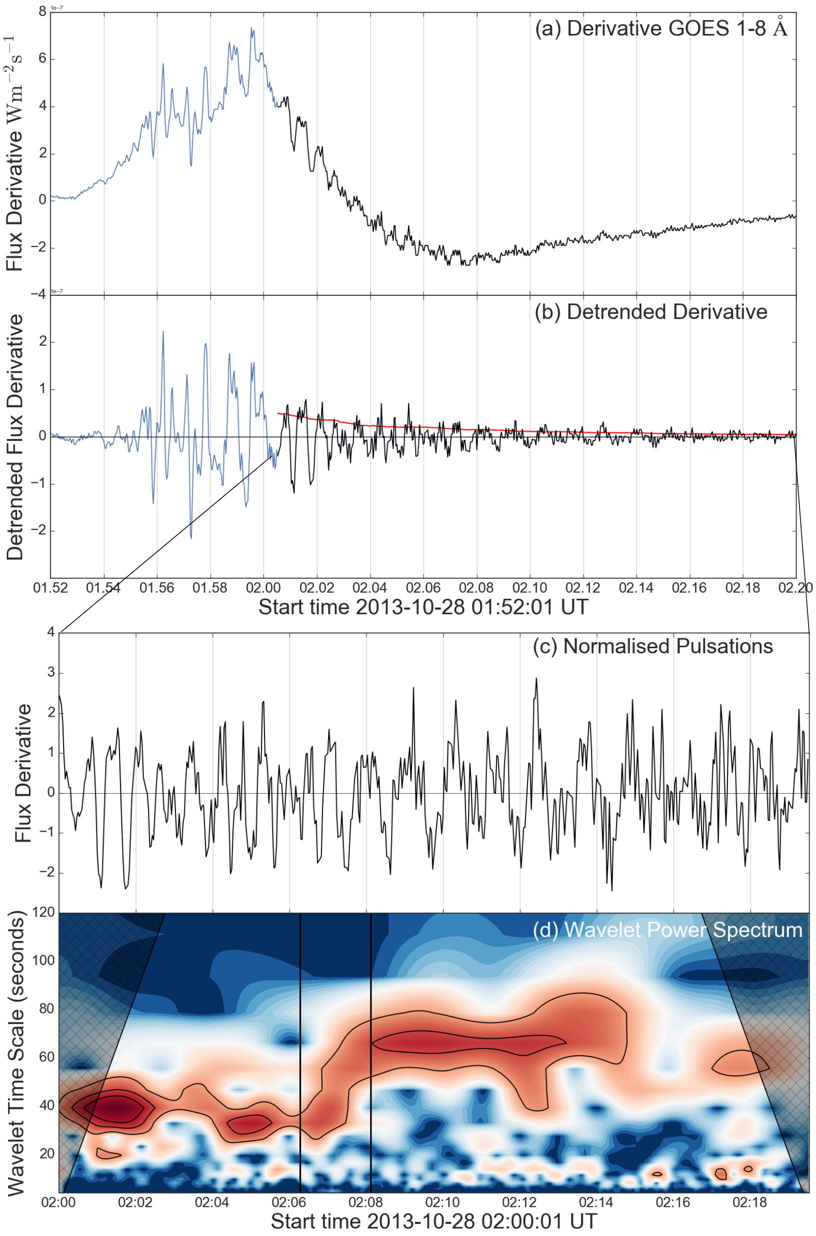

Figure 4.4: Decay phase QPPs observed by GOES 1-8 Å. The black marked part of the lightcurve indicates the decay phase under investigation. (a) Derivative of the GOES 1-8 Å lighcurve. (b) Detrended GOES derivative. (c) Pulsations observed in (b) but with the amplitude of the pulsations normalized. (d) Wavelet power spectrum of (c). The vertical black lines at 02:06:20 and 02:08:30 UT highlight the region in time for which the period increases from ~40 s to ~70 s.

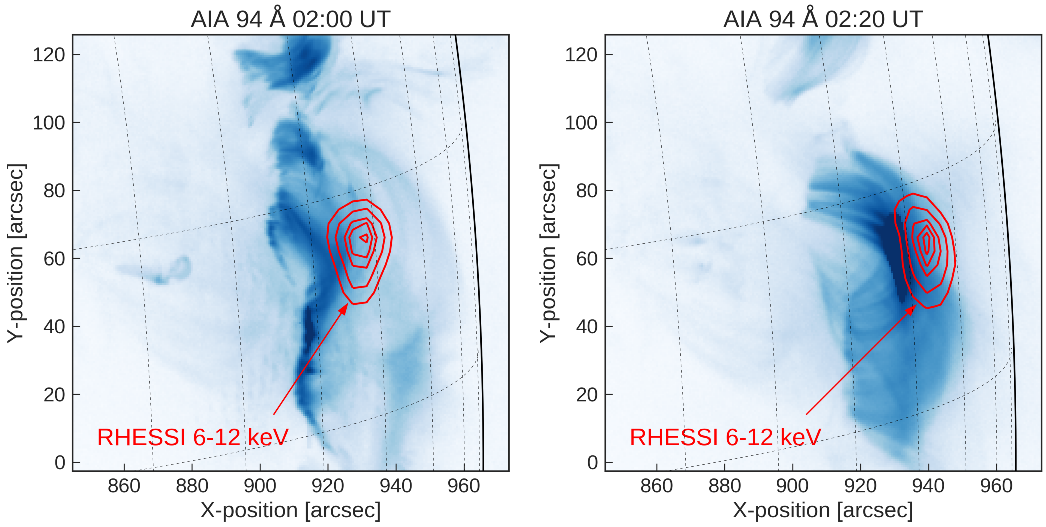

Figure 4.5: RHESSI contours of the 6-12 keV energy range overlaid on AIA 94 Å images during the decay phase of the solar flare at 02:01 UT and 02:20 UT respectively. The contours are at 30, 50, 70 and 90% of peak value.

sources by assuming that the loops have a semicircular shape and are vertical as observed in the plane of sky. The altitude of the soft X-ray source is taken to be the radius of the semicircle. To find this altitude, a sequence of RHESSI images were made and the centroids of the sources in the sequence were determined. The footpoints observed in AIA were used to estimate the base of the flare, and the position halfway between them was used to find the height of the centroid source. To account for projection effects given that the flare was approximately 20° inside the limb, the estimated height of the source is divided by cos(20°). The calculated heights can then be used to estimate the loop length ($L = \pi h$) as a function of time and this is shown in Figure 4.6. The loop length is observed to systematically increase from approximately 38 Mm at 02:00 UT to 59 Mm at 02:20 UT. Notably, during the increase in timescale from ~40 s to ~70 s (marked by the black vertical lines, the same time as marked in Figure 4.5), the loop

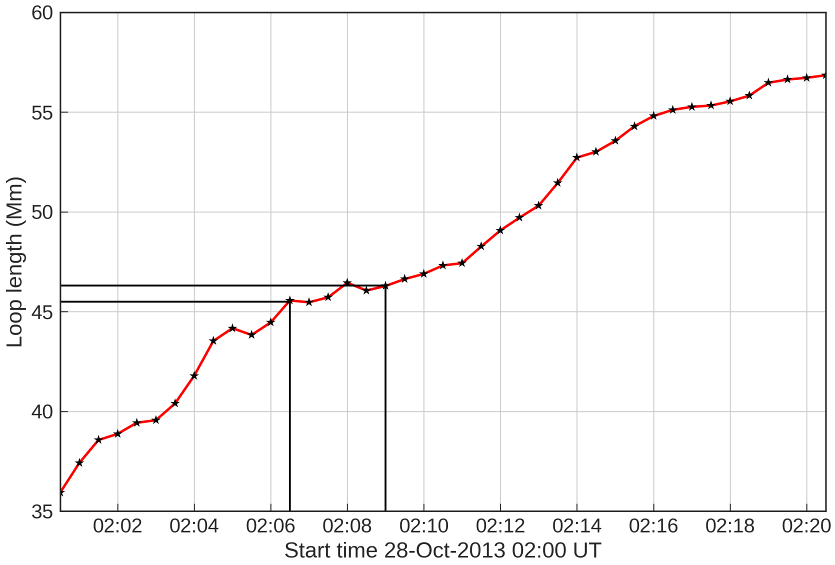

Figure 4.6: Estimates of the loop length (in Mm) as a function of time calculated from the RHESSI soft X-ray source heights. The region noted with the black vertical lines is the time in which the period detected in the wavelet power spectra changes from ∼40 s to ∼70 s.

length only increases by 2 Mm, which is small compared to the large increase in period. The loop length then continues to grow even when the timescale of the observed pulsations remains constant at 70 s until 02:15 UT.

4.5 Discussion

Throughout the impulsive phase of the flare, highly correlated common features are observed at all wavebands including hard X-ray, soft X-ray and microwave emission with minimal time delay between peaks. Wavelet analysis of this impulsive phase shows broadband features in the wavelet spectrum, with similar enhanced power across all channels. Testing above a power-law background model, characteristic peaks in the global spectrum at ∼20 s are detected in all wavebands.

Enhanced power is also seen at approximately ∼50 s in all wavebands, but only with a significance above 99.7% in the non-thermal emissions. These characteristic timescales are consistent with previous QPP investigation of different events (e.g. Kupriyanova *et al.*, 2010; Simões *et al.*, 2015).

It is of particular interest that some peaks in the soft X-ray time derivative occur before the peaks in hard X-ray, especially peak 2, 3, 6 and 7 in Figure 4.2. These observations suggest that for some pulsations, the heating comes before the collisions of the accelerated electrons into the chromosphere that produce the 25 keV X-rays (and above). This perhaps implies that the heating is by some other means, presumably by direct heating in the corona, or by lower energy electrons or ions.

Following the highly correlated 'bursty' impulsive phase, the emission in the non-thermal channels is no longer present. However, distinct QPPs are evident in the high temperature plasma, as observed by GOES, to persist into the decay phase. The timescales of these pulsations are observed to increase from ∼40 s at the end of the impulsive phase at 02:00 UT to ∼70 s at 02:15 UT. These thermal pulsations could be a manifestation of continued weak particle acceleration (MacCombie & Rust, 1979), or some other heating mechanism that persists into the decay phase of the flare. This would support the idea that continuous heating is required to describe the long decay times observed in many flares compared with estimated conduction and radiation cooling timescales (Cargill *et al.*, 1995; Ryan *et al.*, 2013).

But what causes the periods and timescale of the observed QPPs? The observed period of the QPPs in the flare are consistent with the expected characteristic timescale of MHD modes in the coronal plasmas (e.g. Macnamara &

Roberts, 2011; McEwan *et al.*, 2008; Pascoe *et al.*, 2007, 2009). However, given the complex restructuring of coronal plasma structures that occurs during the impulsive phase, the identification of the specific MHD waves of oscillation producing QPPs is unlikely. This is supported by the large modulation depths observed in the emission, which suggest that the QPPs are a result of episodic reconnection. The timescale would then be determined by either dynamic or periodic variations of the magnetic reconnection process such as multi-island reconnection in coronal current sheets (Drake *et al.*, 2006a; Guidoni *et al.*, 2016).

During the decay phase however, the increase in timescale and small amplitude of the thermal soft X-ray pulsations is consistent with MHD processes within the flaring loop/s. Compressive MHD wave modes cause plasma density variations within the flaring loop and cause a modulation in the emission. Recent work has attributed QPPs to that of the fast sausage mode (Tian *et al.*, 2016) and the vertical kink mode (Dennis *et al.*, 2017). The damped nature of the decay phase QPPs observed here, identified in Figure 4.4 (b), suggest that they could be a manifestation of the global sausage mode in the leaky regime. In the leaky regime, sausage modes are subject to damping and demonstrate a decaying oscillatory behaviour. The period of the sausage mode is determined by the ratio of the wavelength (twice the loop length) to the external Alfvén speed, $P = 2L/c_{Ve}$ (Pascoe *et al.*, 2007). This dependence of L decreases in the leaky regime, and the period becomes indepenent of the loop length of the oscillating loop, and is determined by the transverse travel time across the loop, $P^{leaky} \approx \pi a/V_{Ai}$, where a is the loop width and V_{Ai} the internal Alfvén speed (Nakariakov *et al.*, 2012). This may explain why the period of ~70 s stays constant even when the loop lengths of the flare continue to grow. Taking the period of 70 s, together with a in the range of ≈ 2”-10”, this interpretation yields an estimation of $V_{Ai} \approx 65 - 350$ km s^{-1}. This is considerably low for coronal loop Alfvén speeds (Aschwanden *et al.*, 1999b), perhaps suggesting that the loops are not sufficiently long enough to be in the long-wavelength limit and so this interpretation cannot fully explain the observations. MHD wave mode oscillations may be also be present in the impulsive regime of this flare, but the modulation would be small compared to the overall rapid release processes.

4.6 Conclusion

QPPs have been detected and analyzed at multiple wavelengths during the X1.0 flare of October 28 2013. The novelty of this research is the identification of extended thermal soft X-ray QPPs that exist during both the impulsive and decay phases of the X-class solar flare. The majority of QPP investigations have focused on impulsive phase events and decay phase QPPs have rarely been reported in the literature. Future work is now required to study other events with persistent QPPs and newly proposed QPP mechanisms should take decay phase QPPs into account.

Although the underpinning mechanism of the QPPs observed in this flare cannot be conclusively determined, the correlations between the non-thermal emissions during the impulsive phase, and the extended damped QPP signatures in the decay phase, together with the evolution of QPP periods, suggest a change in the dominant driver of QPPs during different stages of the flare. If this were the case, the QPPs during the impulsive phase could be interpreted in terms of the energy release process which may have a characteristic timescale such as periodic electron acceleration. This would naturally explain the large modulation depths and similarity of QPPs observed across multiple wavelengths given that the emission modulation would be directly related the modulation of the accelerated electrons. The decay phase QPPs could then be attributed to MHD wave processes in the post-flare loops which can then explain the prolonged thermal pulsations when no non-thermal emission modulation is observed.

Furthermore, the existence of the fine structure soft X-rays QPPs across multiple channels and their correlations between different energies provides a new diagnostic tool. When correlations between different energies are high, especially soft X-rays and hard X-rays (as with most peaks in the impulsive phase of this flare), we can argue that the soft X-ray emitting plasma is heated by the electron beams at that time. When pulsations in soft X-rays are seen to occur before the hard X-ray emission peak, and persist late into the decay phase after the hard X-ray emission has stopped, some other heating mechanism must be taking place. Thus, detailed comparisons between thermal and non-thermal structures can potential assist in the understanding of the distribution of the different heating processes that occur during a solar flare.

It has now become apparent that the fine structure QPPs, like observed here, are a common (Simões *et al.*, 2015), if not intrinsic feature of flaring emissions. The investigation of the thermal QPPs and their relation to other wavelengths provide a clearer insight into the origin of QPPs, and indeed require further investigation to test the relationship between the impulsive and decay phases of solar flares. Their presence needs to be taken into account when searching for QPP models. These QPPs also provide information about the flaring conditions, and their appearance needs to be better explained if we are to work towards a unified view of the solar flaring process.

5

Long Duration Quasi-Periodic Pulsations during the September 10 2017 X8.2 Solar Flare

QPPs are typically identified during the impulsive phase of flares, yet in some cases, their presence is detected late into the decay phase. In this Chapter, we report extensive fine structure QPPs that are detected throughout the large solar eruptive X8.2 solar flare from September 10 2017. Following the analysis of the thermal pulsations observed in the GOES X-ray sensor channels and the 131 Å channel of SDO/AIA, we find a pulsation period of ∼65 s during the impulsive phase followed by lower amplitude pulsations with a period of ∼150 s in the decay phase, up to three hours after the peak of the flare. Through spatially resolved RHESSI X-ray observations, it is found that during the time of the impulsive phase QPPs, the soft X-ray source rapidly rises at a velocity of approximately 17 km s^{-1} following the plasmoid/CME eruption. We relate the QPP signatures during this time to a manifestation of reconnection dynamics in the eruptive event. During the long-duration decay phase however, the source height evolution slows down and extended downward contractions of collapsing loops/plasmoids that impact the top of the arcade are observed in EUV. We note that the existence of persistent QPP into the decay phase of this flare are most likely related to these features. The QPPs during this time are discussed in terms of MHD wave modes triggered in the post-flaring loops. This work is currently in review in the *Astrophysical Journal* as Hayes *et al.* (2019).

5.1 Introduction

QPPs are a common feature of solar flare emission, and recent evidence has clearly demonstrated that the oscillatory signatures are a truly multi-wavelength phenomena (Van Doorsselaere *et al.*, 2016b). Of particular interest is the identification of fine structure small amplitude QPPs detected in the soft X-ray lightcurves, such as presented in Chapter 4. There is growing evidence that QPPs of this type are a common characteristic feature of solar flare emission, and the observed nature must be linked to some aspects of the flaring region and energy release.

Large solar flares are often observed to be associated with a CME, the ejection of plasma and magnetic field out of the corona. The eruption of a plasmoid is suggested in the standard flare model, and its existence is required to explain long duration solar flaring events and cusp-shaped post flare loops. It is presumed that reconnection continues in the current sheet that extends between the erupted CME and the underlying flaring loops, and that this continued reconnection is the source of continued heating and energy release after the impulsive energy release. QPPs that exist late into the decay phase may be related to such a process, and the relationship between the dynamics of solar eruptions and observed QPPs requires investigation.

In this Chapter, we investigate the extensive nature of QPPs detected in the soft X-ray emission from the well-observed X8.2 solar flare associated with a large CME that occurred on September 10 2017. By using a combination of high cadence soft X-ray measurements from GOES and ESP, together with spatially resolved observations from AIA and RHESSI, the characteristics of the detected QPPs are related to spatial features and length scales of the solar eruptive event.

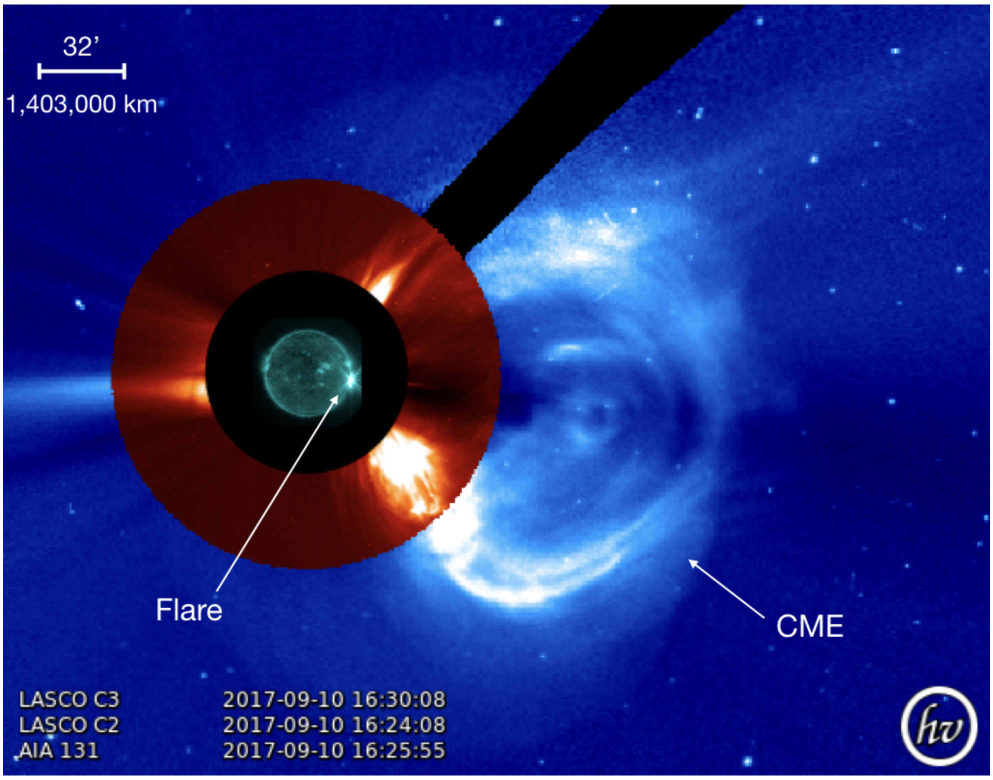

Figure 5.1: An extended view of the solar eruptive event that occurred on September 10 2017. The figure is a composite image with data from SDO/AIA in EUV, and the C2 and C3 coronagraphs of LASCO instrument on board SOHO. The brightening in EUV of the flare is seen and the associated large CME is observed to extend out to several solar radii. This was one of the fastest CMEs observed to date. Figure made with *helioviewer.org*.

5.2 Observations

The flare analyzed in this Chapter is the X8.2 solar flare that occurred on September 10 2017 from NOAA active region 12673. This event was the second largest flare of solar cycle 24, and was accompanied by one the fastest CMEs observed to date, on the order of ~3000 km s^{-1} (Gopalswamy *et al.*, 2018; Morosan *et al.*, 2019). The event was positioned on the western limb of the Sun, just as the prominent active region was rotating off-disk. The position and magnetic configuration of this solar eruptive event provided a unique observational perspective of the complete eruptive process, and displayed one of the best examples of the standard flare model configuration. An extended view of the solar flare and CME is shown in Figure 5.1. Here, the flare is observed as an intense EUV brightening in the corona, and the extended large CME is observed in white light observations from the LASCO C2 and C3 coronagraphs, an instrument on board the SOHO mission. The clear side-on view of the eruption has gained traction in the community, and recent studies of different aspects of the flaring event have been discussed in the literature (e.g. Gary *et al.*, 2018; Li *et al.*, 2018; Liu *et al.*, 2018; Omodei *et al.*, 2018).

The flare started at approximately 15:35 UT, reached a peak in the GOES 1-8 Å channel at 16:06 UT and did not return to pre-flare flux levels until the next day. The evolution of the flaring event, as observed in the 131 Å channel of AIA is shown in Figure 5.2. The pre-eruptive plasmoid is clearly seen in (a) followed by the flare and cusp-shaped post-flaring loops (b-d). The bright linear structure extending outwards is presumably related to the reconnecting current sheet following the eruption. This feature has been identified as a current sheet in recent works (Li *et al.*, 2018; Warren *et al.*, 2018), and turbulence is noted for it appearing wider than theoretically expected (Cheng *et al.*, 2018). Here, we will also refer to it as the current sheet, however it should be noted that the structure observed in EUV may not actually be the region where reconnection itself is taking place, but an emission structure perhaps associated with the reconnection outflow jets.

In this Chapter we focus on the fine structure of the QPPs detected in both channels (1–8 Å and 0.5–4 Å) of the GOES X-ray sensor, the 1-70 Å soft X-ray

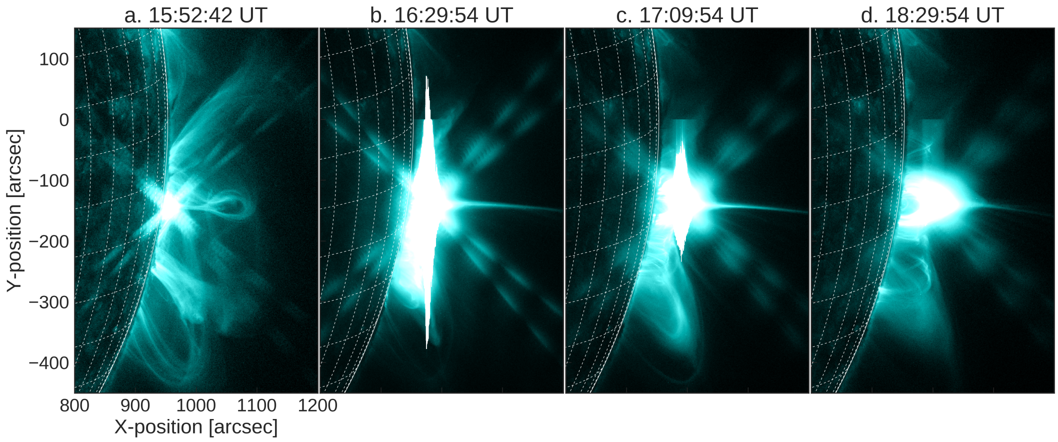

Figure 5.2: The evolution of the X8.2 solar flare as observed in EUV at 131 Å from AIA. The erupting plasmoid can clearly be observed in (a) followed by the impulsive flaring release (b,c) and the post-flare cusp-shaped loops (d). Saturation is clearly playing a role due to the large magnitude of the flare.

channel from ESP and the 131 Å channel of AIA. Both GOES and ESP provide soft X-ray high time cadence observations of 2 s and 0.25 s, respectively. In order to enhance the signal-to-noise ratio of ESP, the signal is rebinned to 2 s to match GOES. The lightcurves of both the GOES and ESP channels is shown in Figure 5.3 (a). The shaded blue region marks the defined GOES start and end times, and the vertical line marks the time of the flare peak in the GOES 1–8 Å channel.

In comparison to non-thermal emission in which QPPs are usually clearly evident as large modulation depths, QPPs in soft X-rays constitute a small fraction ($\lesssim 1\%$) of the total emission in this energy range and are difficult to visually identify in the raw lightcurves. In order to enhance the variability, the lightcurves are detrended by subtracting a background trend that is calculated using a Savitzky-Golay smoothing filter (Press & Teukolsky, 1990; Savitzky & Golay, 1964). The idea behind the Savitzky-Golay filter is to approximate the underlying function within a moving window by a low degree polynomial. A boxcar or moving average smoothing filter is appropriate when the underlying trend is constant or changing linearly with time as it works by replacing each data value within a window with a constant average. However if the underlying data has a non-zero second derivative, a boxcar smoothing filter can introduce errors, especially around a local maximum. The flaring lightcurve in this Chapter demonstrates a sharp rise followed by a long decay and hence a Savitsky-Golay filter is used to approximate the (non-linear) background trend. The Savitzky-Golay filter works by using the method of least squares to fit a polynomial to all points within a moving window. The inputs into the filter are a polynomial degree and a window size. A polynomial of degree 1 would hence allow the Savitzky-Golay filter to perform as a boxcar smoothing filter. For the flaring event in this Chapter a Savitzky-Golay filter of degree 3 and window size of 200 s was used. This window size and degree were chosen as they were found to appropriately approximate the background trend which was then subtracted to visually highlight the pulsations of interest. Other window sizes can be chosen and were tested on this flare and these similarly highlighted the QPP signatures of interest. The QPPs can also be enhanced by taking the numerical derivative of the raw lightcurve as demonstrated in Chapter 4. The detrended lightcurves of both the GOES and ESP channels are shown in Figure 5.3 (b, c) respectively. Here, QPPs can be clearly identified, both during the impulsive and late into the decay phase. The similarity of the GOES and ESP QPPs confirms that these pulsations are of solar origin and not an instrumental feature.

It should be noted that both GOES and ESP lightcurves are Sun-as-a-star observations and so their lightcurves contain full disk-integrated flux. To confirm

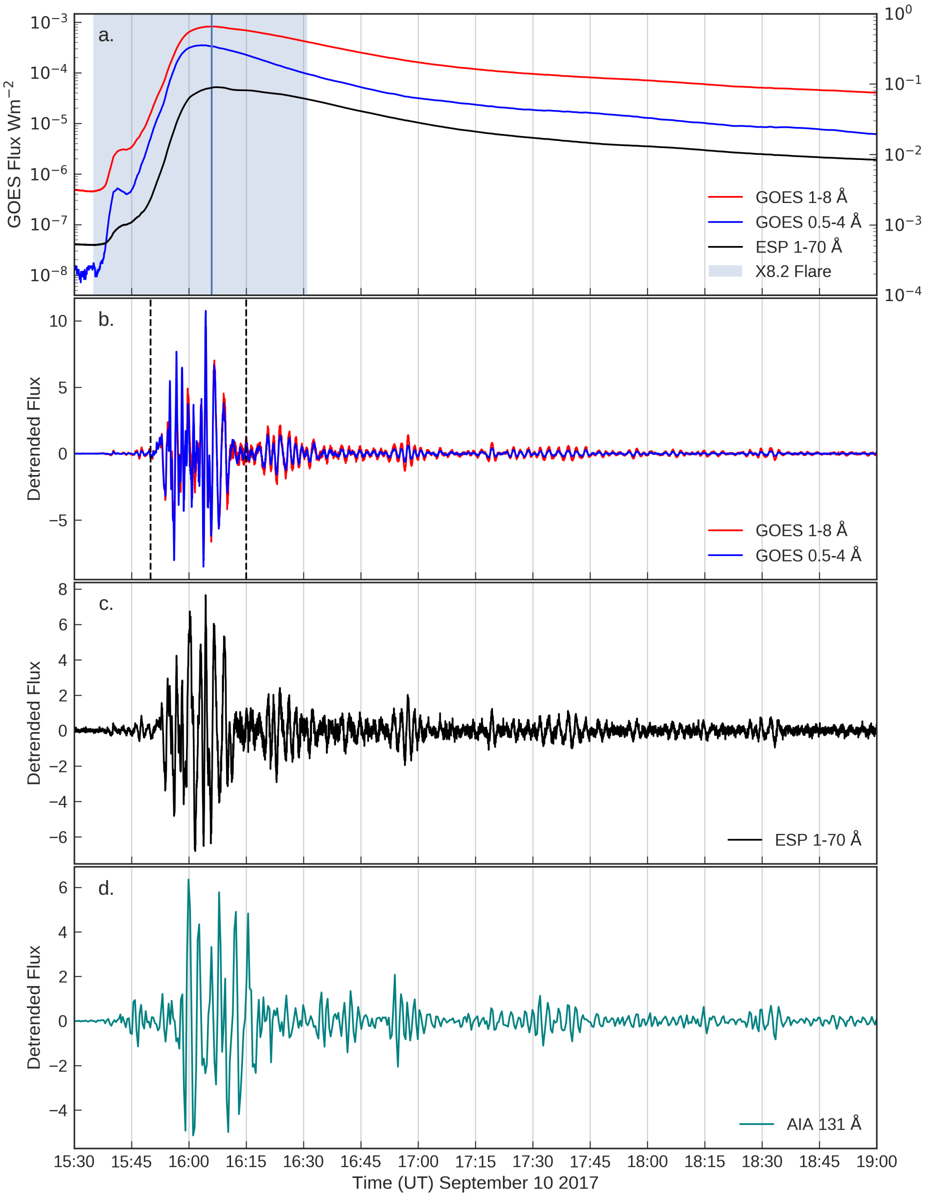

Figure 5.3: The soft X-ray lightcurves of GOES 1–8 Å 0.5–4 Å and ESP 1–70 Å are shown in (a). The shaded region denotes the GOES start and end defined times and the blue vertical line is the peak of the 1–8 Å channel. (c, d) are the detrended lightcurves of the (a). (d) is the detrended AIA 131 Å lightcurve integrated over the field of view in Figure 5.2. The detrended lightcurves are normalized by dividing by their respective standard deviations. Long duration small amplitude QPPs are detected in each channel.

that the observed long duration QPPs are associated with emission from the flaring region of interest, an integrated AIA 131 Å lightcurve is created over the field of view in Figure 5.2. This is achieved by summing over all the pixels in each image timestep. Given the extent of the flare, the detectors suffer from saturation (observed as the bright extended features in Figure 5.2). To take this into account when making the lightcurve, all saturated pixels are included in the field of view for which the lightcurve is made. The 131 Å channel of AIA has a response to the hot Fe XXI (10 MK) line, and hence is sensitive to the soft X-ray emitting plasma that is observed by GOES. The detrended lightcurve of the 131 Å channel is shown in Figure 5.3 (d). Signatures of QPPs are also clearly evident, particularly extending late into the decay phase, confirming that these long duration persistent QPPs are associated with this flaring region. The AIA 131 Å detrended lightcurve also display two extra large amplitude pulsations during the impulsive phase at approximately 16:12-16:16 UT which are not observed in GOES or ESP. These are also observed in AIA 193 Å channel shown in Figure A.1 in Appendix A.4, confirming that they are real. It may be possible that these are associated with a lower temperature plasma that the 131 Å (0.4 MK) and 193 Å (1.2 MK) channels are sensitive to.

During the rise of soft X-ray flux in the impulsive phase, the associated QPPs are bursty features with a larger observed amplitude than in the decay phase. The amplitude of the pulsations in all channels is small; on the order of $\sim$1% of the overall emission during the impulsive phase and $\sim$0.3% during the decay phase. What is noteworthy in this event is that QPPs continue for over 3 hours after the GOES peak of the flare. We are not aware of any other observation that reports this type of behaviour. Furthermore, the long-duration pulsations that extend into the decay phase are observed to have a 'beat' signature, with wavepackets of larger amplitude pulsations. To investigate the QPPs in more detail, both the impulsive phase from 15:50–16:15 UT (between the vertical dashed lines in Figure 5.3 (b)), and the decay phase from 16:15-19:00 UT, are studied with a focus on the characteristics of the QPPs and their relation to spatial features observed with AIA and RHESSI.

5.3 Methods and Results

5.3.1 Periodicity

The presence of QPPs is confirmed by periodogram analysis using the Automated Flare Inference of Oscillations (AFINO) method detailed in Inglis *et al.* (2015, 2016). As discussed in Chapter 4, flaring time series have an intrinsic power-law shape in the Fourier domain which must be taken into account when assessing the significance of a peak in a periodogram. If a signal is detrended before analysis the spectral components get suppressed, which can lead to a false detection of a periodic signal (e.g. Gruber *et al.*, 2011; Inglis *et al.*, 2015). The advantage of using AFINO here is that it avoids detrending the data beforehand, and the analysis is performed on the raw lightcurves.

AFINO is outlined in detail in Inglis *et al.* (2016) and in the Appendix A.3 but is summarized here. First the raw, undetrended, lightcurve is normalized and a window function is applied to account for the finite duration of the time-series. The Fourier power spectrum is then calculated and a model fit and comparison test is performed. There are three models considered to represent the power spectrum - a single power law, a broken power law, and a power law with a Gaussian bump. The latter represents a situation where excess power exists at a localized frequency range - i.e. a QPP model. The maximum likelihood of the models to fit the power spectra are calculated and then tested against each other to find which model most likely represents the data. The comparison is done via the Bayesian Information Criterion (BIC). A smaller value of BIC indicates that a model is preferred to others, and hence the ΔBIC between model fits represent a way to determine which model is most appropriate. A $\Delta\mathrm{BIC}_{modelA-modelB} > 10$ suggests a model B is strongly preferred over model A. AFINO offers a robust QPP detection analysis technique which minimizes the chance of a false detection of a periodic signature which may be introduced to a lightcurve when a signal is detrended by an arbitrarily chosen boxcar or smoothing function.

AFINO is applied to both the impulsive and decay phases of the lightcurves separately, and the results are shown in Figures 5.4 and 5.5, respectively. Each panel shows the input time-series and the three model fits to the power spectra. For the QPP model, the 2.5% and 97.5% quantiles relative to the power-law component are plotted in gray. If the QPP model is preferred, a red dashed line is plotted to denote the peak position of the Gaussian bump, f_0, which is the frequency of the QPP oscillation detected.

It is found that during the impulsive phase, the QPP model is preferred for both the GOES channels and the ESP channel. The QPP component is found to peak at ∼65 s ($f_0 = 0.015$ Hz) in both these channels. The impulsive phase of the AIA 131 Å lightcurve however shows no significant enhanced power in the Fourier spectrum in Figure 5.4 (c). This does not mean that the peaks in Figure 5.3 (d) are not real in the impulsive phase, just that they do not have a periodic component. It should be noted that the time cadence of the AIA 131 Å lightcurve is 24 s here, rather than the 12 s cadence that can usually be achieved with AIA. This is to ensure normal exposure time, as during the large event, the exposure time repeatedly switches to less than the normal 2 s to reduce saturation effects. In this way, it is possible that with a cadence of 24 s there are just not enough data points to detect the 65 s periodicity over the short time in which it is present.

In the decay phase all channels show significant enhanced power in the Fourier power spectrum, and the QPP model is found to fit best for all three instruments. The QPP Gaussian bump is broad and is centered at ∼150-160 s. This confirms the visual identification of the long duration, low amplitude QPP observed in the decay phase of Figure 5.3. It is notable that there is a much longer period (150 s vs 65 s) in the decay phase than the impulsive phase. Longer timescales during the decay phase have been seen before (Dennis *et al.*, 2017; Hayes *et al.*, 2016; Simões *et al.*, 2015), and may be attributed to the increase in height of emitting hot plasma in longer loops at the later stages of the flare, or perhaps a different underpinning mechanism, as suggested in Chapter 4.

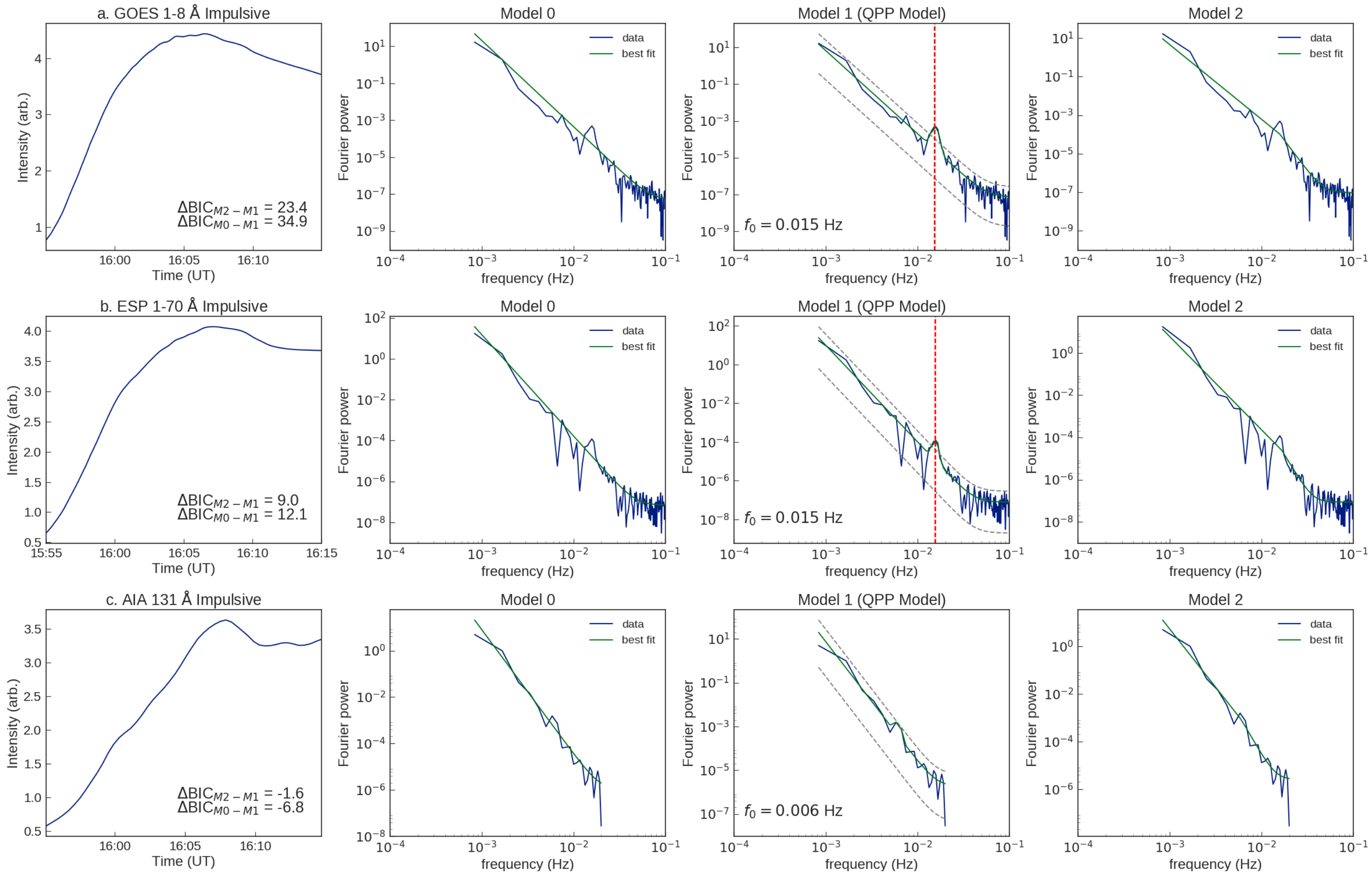

Figure 5.4: Impulsive phase lightcurves, their Fourier power spectrum and the AFINO model fits. (a), (b) and (c) correspond to the GOES 1-8 Å, ESP 1-70 Å, and AIA 131 Å respectively. For each, the original time-series is shown on the left panel and the subsequent panels show different model fits to the associated time-series power spectra. If the QPP model is preferred, a red dashed line is shown, as in (a) and (b).

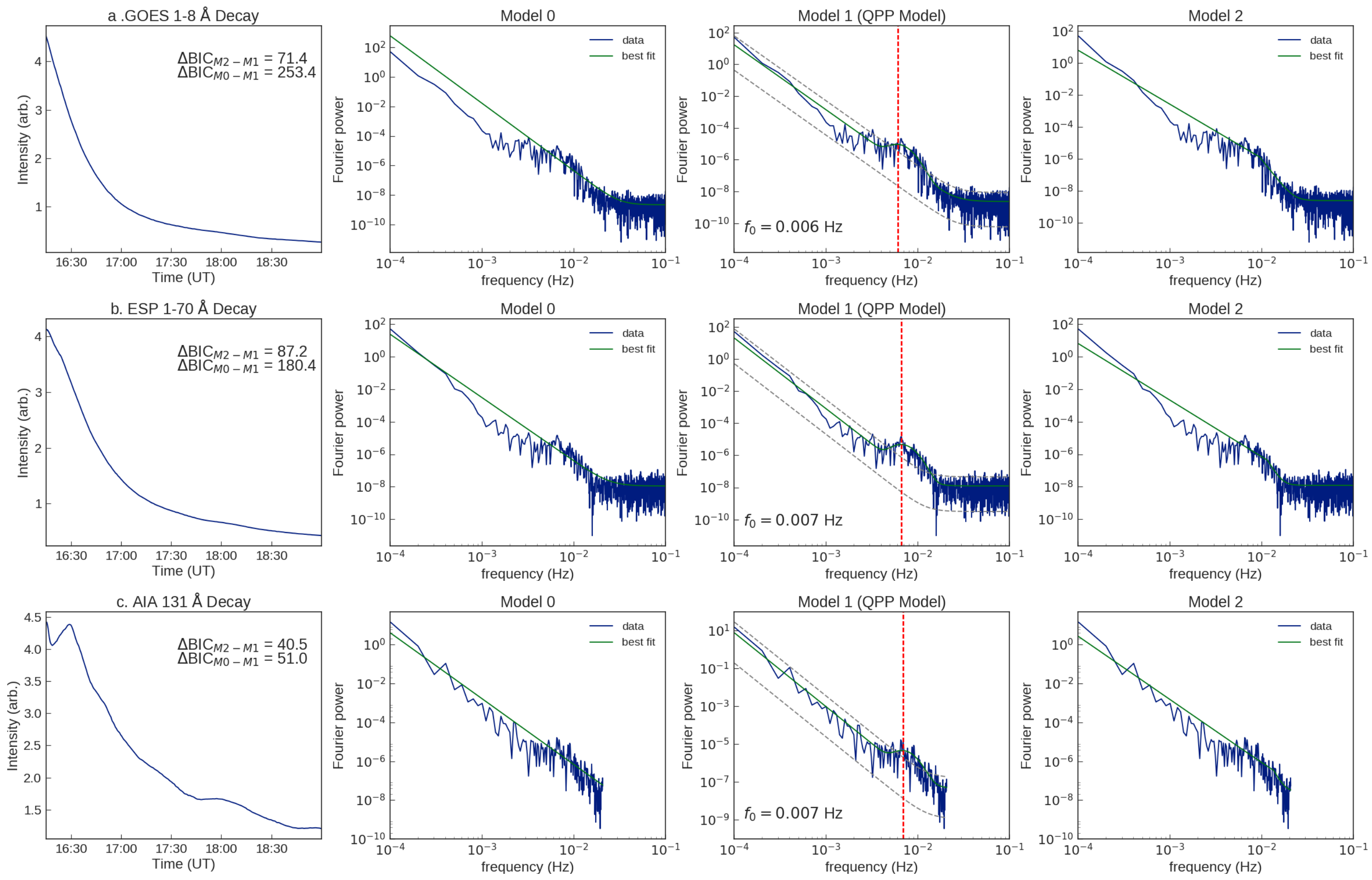

Figure 5.5: Decay phase lightcurves with AFINO analysis. The same as Figure 5.4 but for the decay phase portion of the time-series. Here all three lightcurves are best descrIbed by the QPP model with a period of 165s.

5.3.2 X-ray Source Evolution

The magnetic configuration of this solar eruptive event and its position on the limb provide an excellent view of the flare and an opportunity to observe the post-flare loops edge on (see Figure 5.2 a–d). The flare was well observed by RHESSI, and the on-limb location allows the soft X-ray sources to be imaged and their altitudes (and hence loop length) resolved. To determine the locations of the soft X-ray emitting plasma, a sequence of RHESSI X-ray images in the 6–12 keV and 12–25 keV energy bands was made and analyzed. The images were reconstructed using the CLEAN algorithm (Hurford *et al.*, 2002) with detectors 3, 6 and 8, a beam-width-factor of 1, and an integration time of 20 s.

The 6–12 keV RHESSI soft X-ray contours over-plotted on the AIA 131 Å images are shown in Figure 5.6 at four times during the flare. The soft X-ray sources are located at the top of the loop, presumably under the reconnection region. The loop top source is observed to increase in altitude as the flare evolves, following the evolution of the EUV arcade structure. To track the height evolution, the centroid value inside the contour of each image in the sequence is determined. The computed height of the centroids above the solar limb in the plane of sky is shown in Figure 5.6. The gaps in the data represent periods when RHESSI is at night and unavailable to take observations. The red and green markers are of the 6–12 keV and 12–25 keV energy ranges, respectively. It should be noted that the 12–25 keV source is invariably above the 6–12 keV source. This energy dispersion is consistent with previous works (Gallagher *et al.*, 2002; Liu *et al.*, 2013), and can be be attributed to the fact that higher loops are newly energized and thus hotter, whereas lower loops are cooling into the 6–12 keV bandpass.

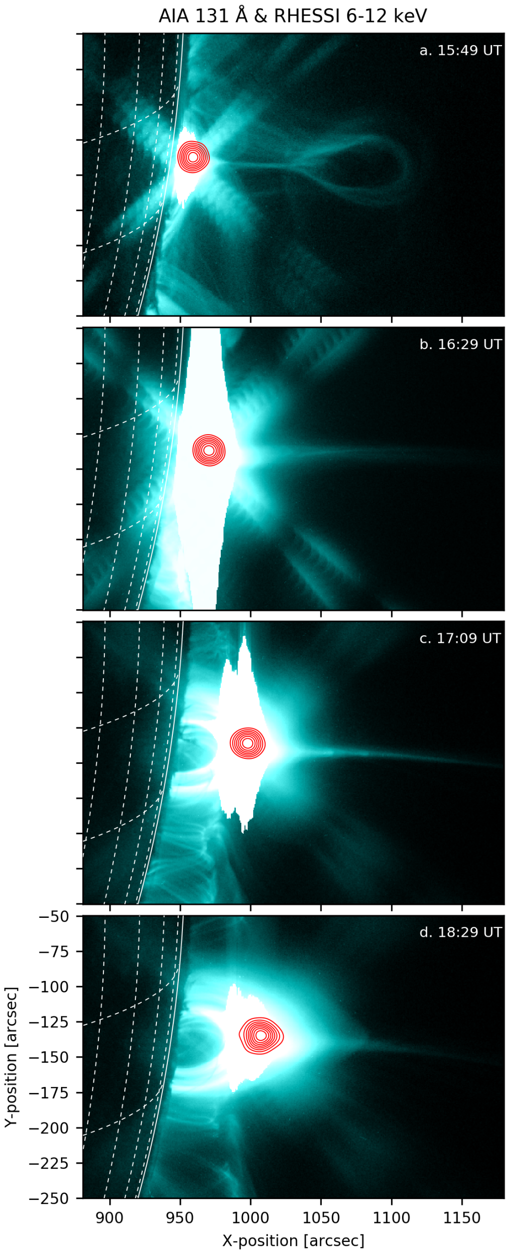

Figure 5.6: RHESSI contours of the 6–12 keV source overplotted on 131 Å images at four stages during the flaring evolution. As in Figure 5.2, the pre-eruption plasmoid is clearly observed in (a). Following this, the evolution of the EUV arcade is accompanied by the ascension of the soft X-ray source to higher altitudes (c–d). The 12–25 keV source is not shown here as it shows similar evolution, demonstrated in Figure 5.7

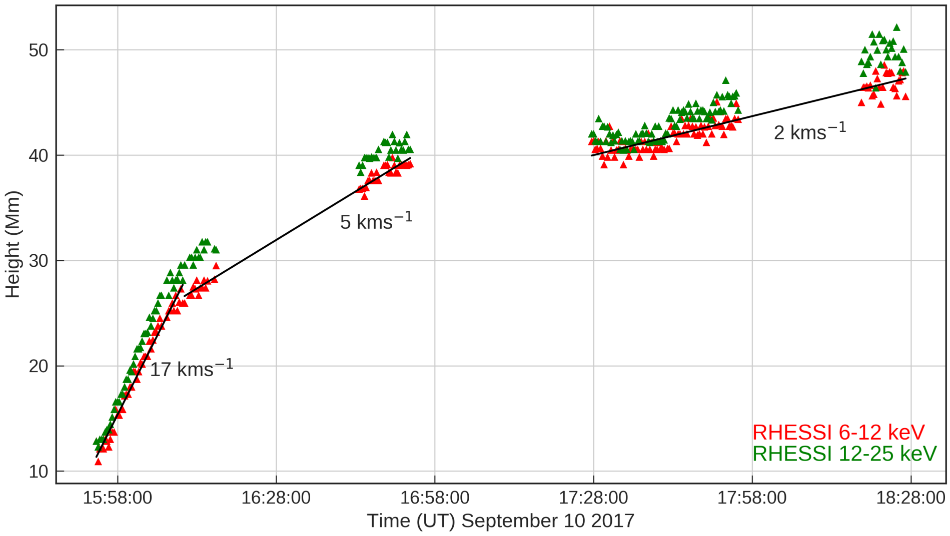

Figure 5.7: The centroids of the 6–12 keV and 12–25 keV RHESSI sources shown in red and green respectively, plotted as a function of projected height (in the plane of sky). The velocities of the sources were determined by the linear fits illustrated as the black lines.

The soft X-ray source rises throughout the flare, evolving rapidly during the impulsive phase with a velocity of 17 km s^{-1}. The velocity is estimated by fitting a linear function to the centroids. The source slows down to $\sim$ 5 km s^{-1} just after the impulsive phase and then decreases to 2 km s^{-1} into the decay phase. This motion is similar to that found in Gallagher *et al.* (2002). However, here the impulsive phase velocity of 17 km s^{-1} is much faster, but the decay phase linear speed is comparable. The higher velocity during the impulsive phase is presumably attributed to the extremely fast associated CME that is on the order of 3000 km s^{-1} (Gopalswamy *et al.*, 2018; Morosan *et al.*, 2019).

It is interesting to note that the bursty larger-amplitude QPPs associated with the impulsive phase occur during a time that the soft X-ray source is rapidly rising. The decay phase pulsations, on the other hand occur when the evolution slows down, and perhaps may explain the more coherent nature observed.

5.3.3 AIA Loop Contractions and Downflows

We now turn our attention to the EUV observations from AIA 131 Å. To enhanced the flaring features, a sequence of running difference images was produced. A running difference image is one in which a preceding image is subtracted from the image of interest, hence highlighting evolution of features as an intensity increase/decrease. This allows us to investigate and track loop features and motions throughout the flare and relate them to the QPPs. The running difference movie (Movie 5.1) shows the plasmoid eruption clearly, followed by the flare. In the early stages of the flare, and during the impulsive phase, the saturated pixels dominate the running difference images and it is difficult to distinguish any features of interest. Later in the event during the decay phase there is clear evidence of downward retracting loops/blobs that follow a sunward direction along the current sheet that hit the top of the newly formed cusp-shaped loops. Not only is material moving downwards towards the cusp-top of the flare, but also material is observed to be moving down the legs of the loops below the saturated pixels in the flare arcade.

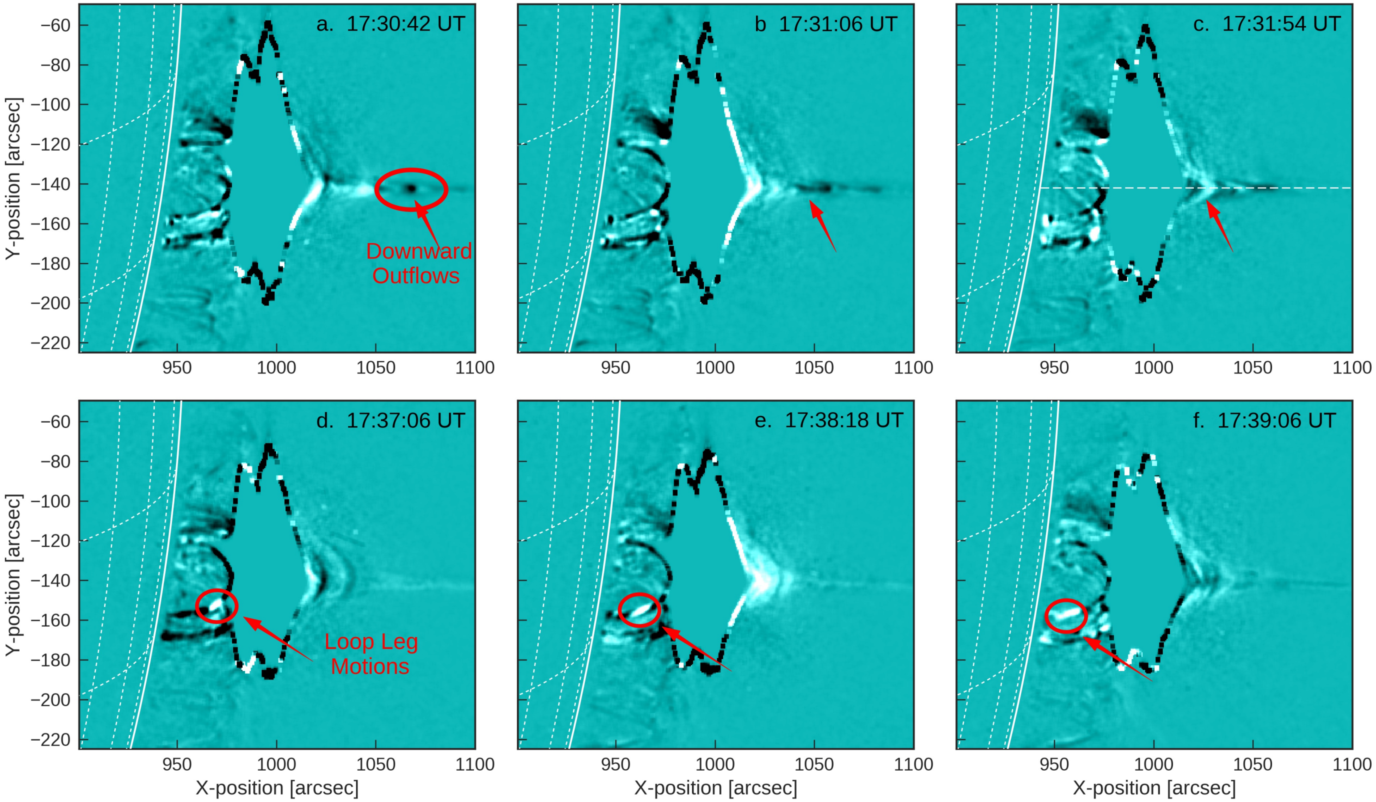

Figure 5.8: Snapshots from Movie 5.1 of the AIA 131 Å running difference images. (a-c) show three consecutive images to highlight the downward contracting loops/plasmoids that travel along the current sheet and impact the underlying arcade to form new post-flare loops. (d-f) show the other interesting feature noted in the movie. Loop leg motions are seen throughout the decay phase, once the saturation in the AIA pixels have subsided.

Figure 5.8 (a–c) and (d–f) display three consecutive running difference images at two separate times to demonstrate motions observed in the movie and described above. In (a–c) the current sheet and downward moving outflows are highlighted. The red oval and arrow in (a) points to a feature that is observed to move down towards the arcade structure (see (b)) and then form cusp-shaped loops (c). This downward moving feature is likely to be associated with supra-arcade downflowing loops (Savage & McKenzie, 2011) originating from the newly reconnected field lines higher up along current sheet that propagate towards the flare arcade apex. In Figure 5.8 (d–f), the downward motions in the loop legs are demonstrated. The red circle and arrows points to a bright feature of interest. The brightening is observed to propagate down the legs of the loop, starting at the top in (d) just below the saturation region and then travels down along the southern leg of the loop towards the southern loop footpoint. These loop leg motions are found to have an approximate 80 s travel time from the loop top to the footpoint.

To track the downward contracting motions observed above the flare apex in Figure 5.8 (a–c), a slit is placed along the current sheet marked as a white dashed line in (c). The slit is taken to be 10” wide, and the pixels are averaged over the region. The averaged pixels from this slit are then stacked for each image in the sequence and a new space-time plot is made. This is shown in Figure 5.9, with moving feature from the AIA images observed now as a dark intensity track. The intensity tracks were manually identified and overplotted with red/blue markings. Similar to Liu *et al.* (2013), each feature is fit with a simple expression for the projected height as a function of time. The plasmoid eruption is clearly identified in the space-time plot at the beginning of the event, marked in red. The eruption is found to have an initial velocity of 120 kms^{-1} and

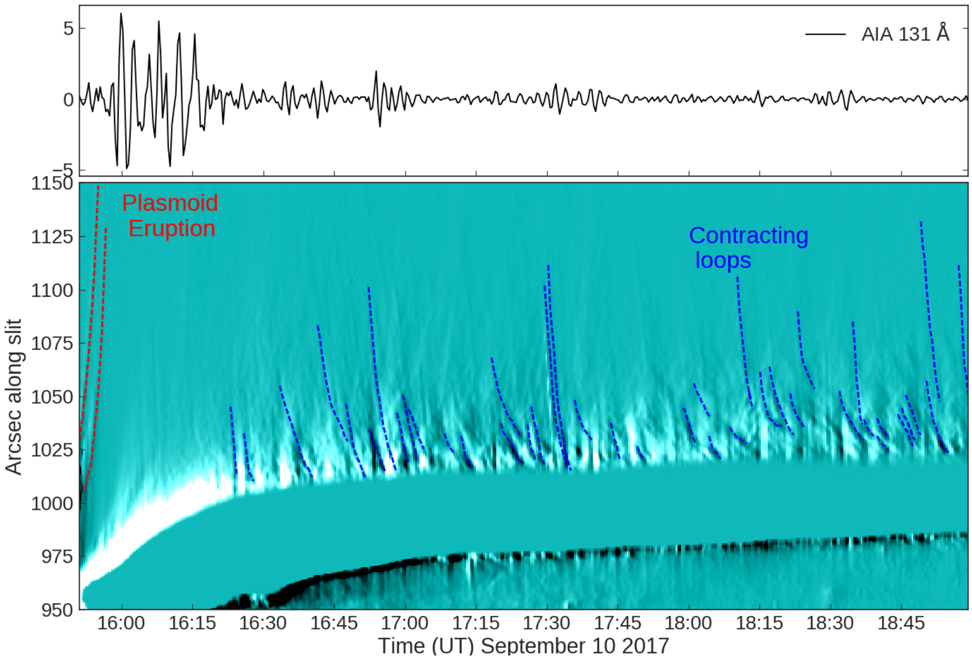

Figure 5.9: The top panel shows the AIA 131 Å detrended lightcurve. The bottom panel displays the space-time plot produced from the slit placed along the presumed current sheet shown in Figure 5.8 (c). The dark tracks were manually detected and have been fit with either red (motions away from loop top) or blue (motions towards the loop top) markings to highlight them.

an acceleration of approximately 2 km s^{-2}. These values are consistent with the CME velocity observed following the eruption (Morosan *et al.*, 2019).

The large gap between 950-1000 arcsecs tracks the area of saturated pixels. The problem with the saturation here is that it is difficult to determine the loop top observed in AIA 131 Å. The saturated pixels, however, are clearly seen to rise in altitude during the impulsive phase followed by a more stable increase in the decay phase, similar to the RHESSI source heights from Figure 5.7. The downward contracting loops above the cusp shaped flare loops are identified as blue tracks in the space-time plot. The velocities of these downward contracting loops have values of 100-200 km s^{-1} at higher altitudes, followed by a deceleration once they arrive at the flare cusp top, where an average velocity of approximately 5-20 km s^{-1} is found. These estimated velocity values are consistent to those discussed in Savage & McKenzie (2011) and Liu *et al.* (2013).

The detrended AIA 131 Å lightcurve is plotted on top of the space-time figure to compare to the observed timing of the QPPs to that of the observed EUV motions along the current sheet. During the impulsive phase (from 15:50 UT to approximately 16:15 UT) the large amplitude QPPs are observed at the same time as the rapid rise of the emitting source as new flaring loops are formed following reconnection. After this time, the altitude increase slows down and downward contracting loops/plasmoids are observed. These are clearly also identified in the movie 5.1. The motion of the soft X-ray source to higher altitudes in Figure 5.7 and the observed motions of the saturated pixels here suggests that the reconnection site moves higher into the corona along the current sheet and continues to release energy. The sunward moving blobs are presumably a result of this continued magnetic reconnection that is occurring higher up in the corona. These downward-moving blobs hit the top of the flaring arcade and form new loops. The fact that they are seen persistent into the decay phase suggests that they are related to the decay phase QPPs, with each downward moving feature perhaps resulting in bursts of larger amplitude 'beat' packets of QPPs that is observed.

5.4 Discussion

We have identified extensive QPP in the thermal emissions from the X8.2 flare from September 10 2017. The pulsations persist for up to three hours after the peak of the flare, providing one of the best examples of long duration QPP observed in a flaring event. Similar to Chapter 4, the analyzed lightcurves demonstrate two regimes of QPP signatures; bursty, larger amplitude, pulsations in the impulsive phase with a shorter period of 65 s, and decay phase coherent pulsations that extend late after the impulsive phase has ended, with a longer characteristic timescale of 150-160 s. During a solar flare, the impulsive and decay phases are dominated by physically different processes, and it is quite likely that perhaps two distinct mechanisms are underpinning the observations of QPP here.

5.4.1 Impulsive Phase QPPs

The impulsive phase of the solar flare is dominated by rapid energy release and particle acceleration due to the rapid reconfiguration of the magnetic field following the plasmoid/CME eruption. The prompt ascension of the soft X-ray source during this time suggests that the reconnection site moves quickly ($\sim$17 kms^{-1}) to higher altitudes along the current sheet. In this way, it is difficult to interpret the impulsive phase QPPs in terms of standing MHD wave modes as it is unlikely that they be could supported in the flaring loops during this rapid evolution. It is most likely that the QPPs during this time are related to the dominant processes of energy release and particle acceleration that have some associated characteristic timescale.

For example, the recent work of Thurgood *et al.* (2017) has shown that reconnection at a 3D null point can proceed in an time-dependent periodic fashion and also periodically excite propagating MHD waves. This inherent property of oscillatory reconnection may play a role in producing the observed QPPs. Other works have suggested that QPPs are related to the formation and dynamics of plasmoids in flaring current sheets (e.g. Kliem *et al.*, 2000). Moreover, Guidoni *et al.* (2016) built on the work of Drake *et al.* (2006a) and investigated sunward moving plasmoids formed during reconnection in the simulation of an eruptive flare. They demonstrated that the magnetic islands could trap and accelerate electrons which then interact with the flare arcade to produce emission. The discrete acceleration episodes associated with the generation and interaction of magnetic islands in a flaring current sheet could result in the observed pulsations in emission.

Another possible scenario is that the QPPs are a manifestation of reconnection jets (the fast downflows associated with magnetic reconnection) that collide with the ambient plasma above the loop top and excite local oscillations. Takasao & Shibata (2016) performed a set of 2D MHD simulations of a solar flare and studied these oscillations excited by the reconnection outflows. They found that the above-loop-top region was full of shocks and oscillations and the region generated quasi-periodic propagating fast magnetoacoutsic waves (QPFs). The oscillations were controlled by multiple shocks in the region produced as a result of the collision of the reconnection outflows with the reconnected flaring loops piled up below. Their study also found quasi-periodic oscillations of the termination shock strength. It has been noted that termination shocks could be a possible site for particle acceleration (e.g. Chen *et al.*, 2015), and hence a quasi-periodic oscillation of the termination shock at the top of the flare loop could accelerate non-thermal electrons quasi-periodically. The accelerated electrons could then proceed to precipitate in the chromosphere leading to the observed QPPs in the hot soft X-ray emitting plasma (similar to the Neupert effect, Neupert, 1968)

More recently Takahashi *et al.* (2017) performed 2D simulations of magnetic reconnection that occurs below an erupting CME, and similarly found oscillations in the above-the-loop-top region, even in the case of plasmoid driven reconnection. In this scenario it was found during a solar eruptive event, the QPPs take place during the impulsive phase when the CME acceleration is peaking, which is the case for the impulsive phase QPPs observed in this flare.

5.4.2 Long Duration Decay Phase QPPs

Unlike the impulsive phase, where reconnection processes and magnetic configuration evolution dominate, the decay phase is characterized by a more stable configuration of post-flare loops. In this way, it is possible the QPPs at this time are a manifestation of MHD wave modes supported in the post-flare loops. The AIA running difference movie shows extended downward contractions of plasmoids/loops which hit the top of the post-flare arcade and presumably form new loops. The downward contractions could excite MHD wave oscillations in the underlying arcade, resulting in density perturbations of the post-flare loops. The density perturbations would then be observed in the hottest thermal plasmas of the newly formed loops and hence are detectable in the soft X-ray and 131 Å wavebands.

Recent numerical simulations by Jelínek *et al.* (2017) supports this idea, as their simulation of magnetic reconnection in a current sheet found that plasmoids formed by the tearing mode instability could interact with the underlying flaring arcade and generate standing transverse MHD waves of the slow magnetoacoustic type. Slow magnetoacoustic waves can perturb the plasma density of a flaring loop and produce the observed modulation in the thermal emissions (e.g. Wang, 2011). Moreover, it has been shown that an energy deposition at a flaring loop apex preferably excites the second spatial harmonic of the mode in a hot flaring loop (Nakariakov *et al.*, 2004; Selwa *et al.*, 2005; Tsiklauri *et al.*, 2004), with periods in the range of 10-300 s. The period observed in this flare (∼150-160 s during the decay phase) lies within this range and hence slow magnetoacoustic waves may be a reasonable explanation. The period, P, of the second harmonic of the slow magentoacoutic wave is given by $P = 6.7L/\sqrt{T}$, where L is the loop length in Mm, and T is the average temperature in the loop (in MK). The loop length can be readily estimated if we assume that the loops have a semicircular shape, $L = \pi h$, where h is the soft X-ray source altitude height which can be taken from Figure 5.7. During the decay phase the loop lengths are in the range of 125-150 Mm, and with a period of 150 s, the assumption of a slow magnetoacoutsic wave suggests a plasma temperature of 35-40 K. This temperature estimate is much higher than what is found in the GOES temperature measurements for the flaring event, shown in Figure 5.10, in which ∼15 MK temperature plasma is observed during the decay phase. Hence it questions the validity of the slow magnetoacoustic interpretation.

Indeed, other MHD wave modes can perturb the flaring plasma, such as discussed in Chapter 2 and Chapter 4. The global sausage mode is often discussed in terms of thermal QPPs, given that it is a compressive wave mode and can cause density variations within the loop to produce observed soft X-ray and EUV modulation (Tian *et al.*, 2016; Van Doorsselaere *et al.*, 2011). However the sausage mode has a wavenumber cutoff, and can not support long period oscillations (Nakariakov *et al.*, 2012). The period here of ∼150 s is too long to be interpreted

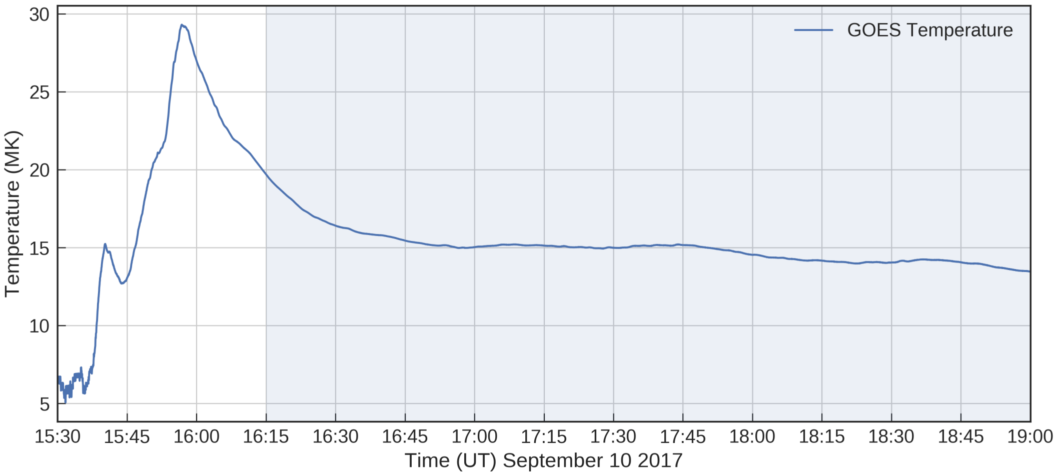

Figure 5.10: Plot of the GOES temperature measurements throughout the flaring event. This temperature is estimated from the ratio of the two channels of the GOES X-ray sensor (0.5–4 Å and 1–8 Å). This ratio is a function of the colour temperature of the emitting plasma, and details on how the temperature is calculated is given in White *et al.* (2005) and discussed further in Appendix A.1. The temperature reaches a peak of ∼29 K during the impulsive phase at the maximum flux of the GOES X-ray flux. The decay phase, shaded in blue, has an approximate temperature of ∼15 MK, much lower than the estimated temperature from the slow magnetoacoutic interpretation.

as sausage mode oscillations of the flaring loops.

The kink mode can also cause density perturbations when it oscillates in the vertical polarization - i.e. up and down in the same direction of the plane of the loop rather than in the transverse horizontal motion often observed (Aschwanden & Schrijver, 2011). In the vertical polarization, the loop length can vary, moving up and down during the oscillations. This stretching and shrinking of the loop is likely to cause a density modulation of the central loop cross section, hence producing a sausage-like cross sectional and density oscillation in the loop (Aschwanden & Schrijver, 2011). For the kink-mode to move in this way, an initial excitation in the plane of the loop is required. For this event, the downward contracting loops at the top of the flare cusp could be a viable exciter in this way. The expected changes of the soft X-ray emission in this case would be expected to be small, a fraction of the overall emission, which is consistent with the observations. The period of the kink mode is given by $P = 2L/c_k$, where L is the loop length, and c_k is the phase speed of the kink mode. The phase speed of the kink mode in coronal flaring loops can be approximated to be $\sqrt{2}v_{Ai}$, where v_{Ai} is the internal Alfvén speed of the loop (Aschwanden, 2006). Using the period values of 150 s, and a loop length of 125–150 Mm (Figure 5.7), an interpretation of the QPPs in terms of the kink mode oscillations suggests an Alfvén speed of $\sim$ 1178 - 1414 kms^{-1}. These are reasonable velocities for coronal loops (e.g. Aschwanden, 2006), and perhaps suggests that the prolonged soft X-rays QPPs are a manifestation of vertical kink mode oscillations in the post-flare loops.

It is also possible that MHD wave mode oscillations are present during the impulsive phase. In this case however, it could be expected that the overall energy release and particle acceleration dominates and their specific oscillations cannot be identified.

5.5 Conclusions

In this Chapter, long duration QPPs have been detected and investigated from the large X8.2 solar flare from September 10 2017. Soft X-ray thermal QPPs are observed throughout both phases of the flare, during the impulsive and in particular, late into the decay phase. Similar to Chapter 4 a shorter associated period of the QPPs is detected in the impulsive phase ($\sim$65 s) compared to the decay phase ($\sim$150-160 s). The decay phase pulsations are of particular interest, persisting up to 3 hours after the peak in the GOES X-ray flux. The extensive nature detected in this Chapter is one of the longest duration consistent examples of QPPs of these timescales reported in the literature.

A key finding in this work is that the decay phase pulsations co-exist with observations of extended downward moving motions along the current sheet that impact the top of the flaring arcade to result in enhanced amplitude of the pulsations, possibly causing the ‘beat-like’ signatures observed in the detrended lightcurves (see Figure 5.3 and 5.9). The co-existent QPPs and observed downward contractions suggest that the dynamical structure of the current sheet formation and the associated CME eruption play an important role for the existence of decay phase QPP signatures.

Furthermore, this study may help explain why no correlations were found between detected QPP periods and global active region properties such as active region size, average magnetic field strength or dipole separation in the recent statistical study performed by Pugh *et al.* (2017). The results here instead suggest that QPP signatures are most likely related to the loop length scales of the flare and the magnetic configuration. Future work is now required to perform a similar statistical study investigating the relationship between QPP signatures, throughout both the impulsive and decay phases, to flaring eruption dynamics and loop length scales.

This September flare event offered an excellent observational opportunity to study these QPPs in detail and relate their characteristics to the flaring evolution. Perhaps the decay phases of all eruptive flares have associated QPPs, but the amplitudes of the oscillations are too small to compete with the resolution of the instruments we use to observe them. The magnitude of this flare was exceptionally high, and hence the flux was still above a GOES M level late into the decay phase. This may be the reason why they are observed for such a long period of time after the initial impulsive energy release.

6

Pulsations in the Earth's Lower Ionosphere Synchronized With Solar Flare Emission

Solar flare emission at X-ray and EUV energies can cause substantial enhancements in the electron density in the lowest regions of the Earth's ionosphere, namely the D-region. It has now become clear that quasi-periodic signatures are a common feature of this flaring emission with timescales ranging from seconds to several minutes. To date, it has not been known if these oscillatory signatures could be detected in the terrestrial ionosphere. In this Chapter, the combined measurements of the D-region electron density from VLF monitoring at 24 kHz, together with space based X-ray and EUV observations, synchronized QPPs are reported in both the D-region electron density and a set of pulsating flaring loops. Through the modelling of the VLF propagation, it is found that the electron density varies by up to an order of magnitude over the timescale of the pulsations ($\sim$ 20 mins). This is the first detection of solar flare QPPs synchronized with an ionospheric response. This work has been published in *Journal of Geophysical Research: Space Physics*, Hayes *et al.* (2017).

6.1 Introduction

Solar flare activity affects all planetary atmospheres (Witasse *et al.*, 2008). On Earth, the terrestrial ionosphere characteristically responds to the increased ionization from flaring radiation and results in a so-called sudden ionospheric disturbance (SID), as discussed in Chapter 1. It is the lowest lying D-region where solar flare effects are most appreciable. X-ray photons of wavelengths $\lambda < 10$ Å penetrate down to D-region altitudes and dominate photoionization of all neutral constituents to extents that significantly increases the local electron density (Davies, 1990; Mitra, 1974). In this way, the D-region is the ultimate depository of flaring emission in the Earth's ionized environment and one of the final links in the solar-terrestrial connection.

Observations of the propagation characteristics of VLF radio waves provide one of the best available probes for establishing the behaviour of the lower ionospheric D-region in response to solar flares. There has been a wealth of studies that focus on D-region solar flare effects using VLF remote sensing (Grubor *et al.*, 2005; Kumar & Kumar, 2014; Mitra, 1974; Thomson *et al.*, 2004). In particular, numerical models are often used in conjunction with VLF observations to infer the variation of the D-region electron density, a measurement that is not readily available by any other means (Thomson & Clilverd, 2001; Thomson *et al.*, 2005; Žigman *et al.*, 2007). Much work has been expanded in detailed statistical studies to understand the relationship of the ionospheric response to solar flares magnitudes (Selvakumaran *et al.*, 2015; Thomson *et al.*, 2005), solar cycle variations (Pacini & Raulin, 2006), and also both seasonal and diurnal effects (Basak & Chakrabarti, 2013; McRae & Thomson, 2000). This research is timely and important given the role the D-region dynamics plays on other radio wave propagation such as HF communications. However, studies rarely focus on the particular details of a flaring event, and no such research has been employed to search for correlations of the ionospheric response to associated dynamic flaring activity such as QPPs.

It has now become clear that QPPs are a common, if not intrinsic, feature of solar flare emission. In this Chapter we embark on an investigative study for the detection of quasi-periodic signatures in the terrestrial ionosphere that correspond to solar flare QPPs. In Chapters 4 and 5, the QPPs investigated were of small amplitude and short timescale, on the order of tens of seconds. However a different branch of longer period pulsations are also observed in associated flaring emission. Long period QPPs, with timescales on the order of tens of minutes, have been reported in the X-ray emission from solar flares (e.g. Foullon *et al.*, 2010; Harrison, 1987; Li & Gan, 2008; Švestka *et al.*, 1982). These long period pulsations are often discussed in terms of slow-mode oscillations of large scale coronal loops (Švestka, 1994), or by the periodic modulation by an external MHD oscillation of a nearby loop (Foullon *et al.*, 2005). Similar timescale pulsations have also been extensively studied in EUV, so-called SUMER oscillations, and interpreted as standing slow-mode waves in hot coronal loops (Wang, 2011).

Of particular interest is a recent study by Tan *et al.* (2016) in which QPPs with periods in the range of 8–30 min were found to be a common feature of the GOES 1-8 Å channel, particularly observed before the onset of a flare. The question now arises as to whether these oscillatory signatures of soft X-ray pulsations can appear in the terrestrial observable of the ionosphere. To the best of our knowledge there has been no reports in the literature of QPPs observed in both a solar flare and responding ionospheric variations. In this Chapter, through the measurements of VLF signals to probe the D-region of the ionosphere, together with EUV imaging from AIA and X-ray measurements from GOES, previously unseen characteristics of the relationship between dynamic oscillatory signatures in both the solar atmosphere and the Earth's ionosphere is revealed.

6.2 Observations

On July 24 2016, an active region located on the western limb of the Sun began to flare (NOAA active region 12567, N05W91). This active region and flaring loops of interest were imaged using EUV observations of the hot 131 Å passband (peak response ∼10 MK) of AIA and are shown in Figure 6.1 (a–c). Beginning at 11:00 UT and lasting for four hours until 15:00 UT, a series of X-ray pulsations of GOES class B9.2–C6.8 were observed in the 1-8 Å channel of the GOES X-ray sensor. The EUV observations similarly demonstrate quasi-periodic brightness variations (see Movie 6.1). The evolution of the X-ray emission together with the AIA 131 Å lightcurve, integrated over the field of view in Figure 6.1, is shown in Figure 6.2 (a). These time-profiles clearly demonstrate a sequence of QPPs of growing amplitude intensity. Periodogram analysis of the flux profiles find a characteristic timescale of ∼20 min between peaks of the pulsations. The coherent pulsations in both the X-ray and the spatially resolved EUV emission confirm that these QPPs are associated with this set of flaring loops.

To examine the lower ionospheric response to the X-ray QPPs, VLF signal amplitude measurements were analyzed. As discussed in Chapter 3, VLF observations in this work were taken using a Stanford University SID monitor that is

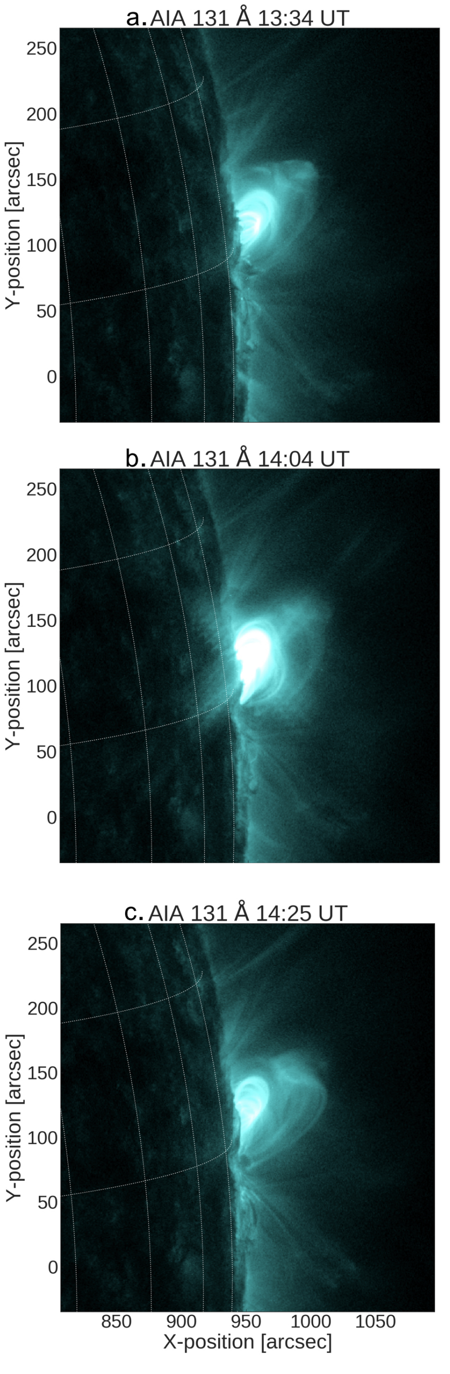

Figure 6.1: Flaring loops of interest observed in 131 Å from AIA. The EUV loop brightness variation also clearly demonstrate QPPs. The lightcurve integrated over this field of view is shown in Figure 6.2 (a). See also accompanying Movie 6.1

located at the Rosse Solar Terrestrial Observatory in Birr, Co. Offaly, Ireland. The monitor is tuned to receive VLF radio signals transmitted at 24 kHz from the communications transmitter NAA, located in Cutler, Maine, US. This propagation path has a great circle distance of ∼5320 km across the Atlantic Ocean, and provided a continuous sunlit path during this event to remotely measure the conditions of the lower ionosphere as the Sun traverses the ocean.

The VLF signal measurements of the flaring event are shown in Figure 6.2 (b), and the influence of the QPPs on the lower ionosphere can be clearly identified. The enhancement in amplitude of the VLF signal strength results from the increased electron density in the D-region, which lowers the effective reflective height and sharpens the conductivity profile of the upper waveguide boundary through which the signal reflects. This allows the VLF wave to reflect at a sharper boundary with less attenuation (Grubor *et al.*, 2005; Thomson & Clilverd, 2001). In this way, the VLF amplitude measurement can be considered as a parameter in tune with the electron density variations.

Notably, the amplitude of the VLF signal demonstrates QPPs with observed pulsations that systematically track the pulsations observed in X-ray. A Pearson correlation coefficient of 0.92 is found between the GOES 1-8 Å lightcurve time profile and the VLF signal amplitude. To take into account the diurnal solar zenith angle variation of the electron density in response to the daily solar Lyman α emission, the differential VLF amplitude is computed and also compared to the X-ray QPPs. This is achieved by subtracting the mean values of quiet day curve of VLF measurements for a few days close to the event. The correlation coefficient of the differential VLF and the X-ray flux is then found to be 0.94. In Figure 6.2 the pulsation peaks are numbered 0-9 for comparison. The VLF

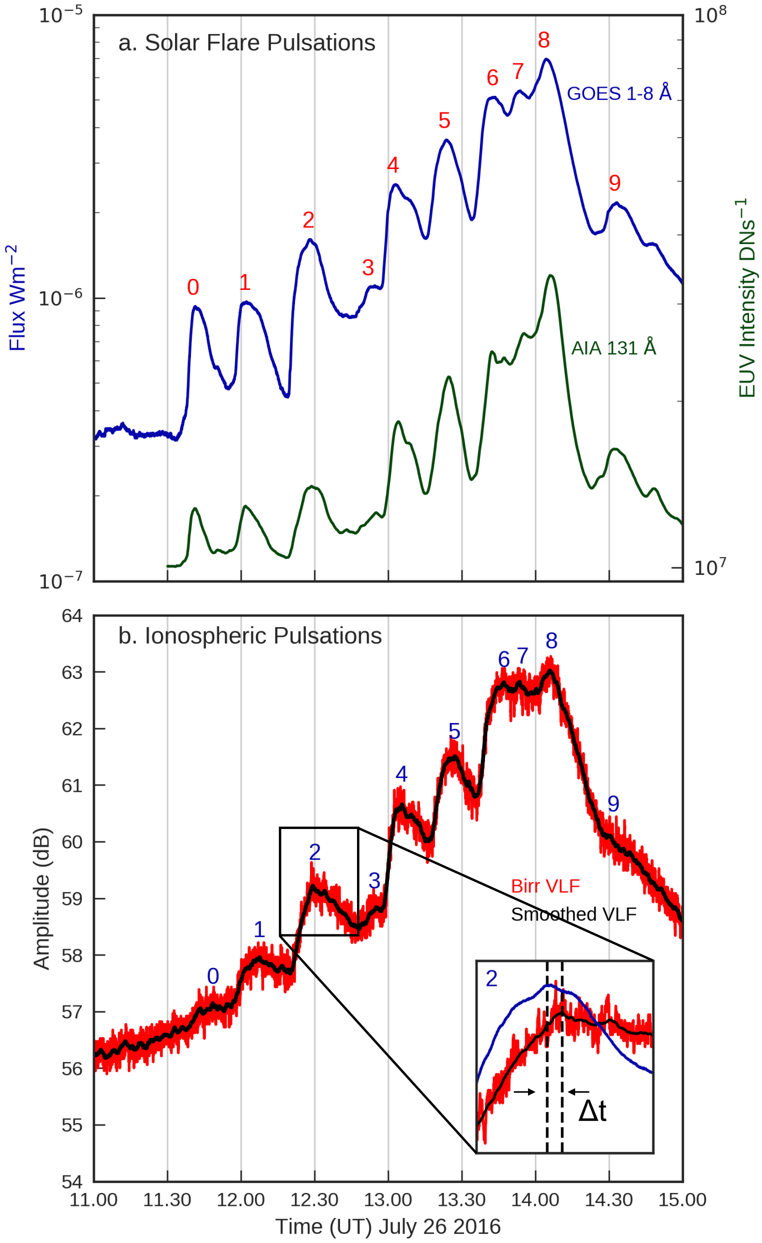

Figure 6.2: QPPs observed in both solar flaring emission and the ionospheric response. The GOES X-ray pulsations and the AIA lightcurve integrated over the field of view in Figure 6.1 is shown in (a). The corresponding VLF measurements of the ionospheric response is shown in (b). The subplot in (b) is a zoomed-in plot of pulsations number 2 to highlight the time delay between the X-ray and VLF response (~90 s).

amplitude response to the X-ray flux is more prominent with each pulsation, attributed to the increasing X-ray flux of the later pulsations. The electron density production rate (q) is directly proportional to the flux (F_s) of the ionizing X-ray emission (Budden, 1988; Ratcliffe *et al.*, 1972), and hence larger amplitude responses are observed during times of higher X-ray flux. The fact that the X-ray QPPs produce synchronized pulsations in the D-region electron density (as monitored by the VLF) indicate a close coupling of the solar-terrestrial relationship, with X-ray QPPs essentially acting as an external quasi-periodic driver to the D-region electron density.

A common feature of the observed pulsations is a time delay (Δt) between the peak of a pulsation in the X-ray flux and the corresponding peak in the VLF amplitude ionospheric response. This time delay is highlighted in the sub-panel of Figure 6.2 (b), in which a zoomed-in view of both the GOES 1-8 Å lightcurve and VLF amplitude is shown for pulsation 2. Cross-correlation analysis between the two profiles finds a delay of ~90 s. The GOES satellite that measures the X-ray emission operates in a geostationary orbit[1] and so there should only be a 0.1 s delay between the signals if the delay was attributed to the light-travel time. The time delay instead represents a characteristic feature of the ionospheric response to ionizing disturbances and is commonly termed the 'sluggishness' (Appleton, 1953) or 'relaxation time' (Mitra, 1974) of the lower ionosphere. In the D-region, the electron production rate is dominated by photoionization, while electron losses result from various recombination processes (Mitra, 1974; Nina *et al.*, 2012; Žigman *et al.*, 2007). The physical effect of the electron loss processes is to delay the response of changes to electron density (N_e) to changes in

---

[1] the orbit is ~35790 km in altitude above the Earth

the ionizing flux (F_s). Hence there is an inherent time delay between the ionizing X-ray flux peak and that of the VLF response, signifying the time taken for the D-region photoionization-recombination processes to recover balance after increased ionization (Appleton, 1953; Basak & Chakrabarti, 2013; Žigman *et al.*, 2007).

6.3 D-Region Absorption Prediction (D-RAP) Model

The D-Region Absorption Prediction (D-RAP) model is a product provided by the NOAA Space Weather Prediction Center to address the operational impact of solar X-ray flux on high frequency radio communications. In this way it provides additional insights into the effects of the X-ray pulsations on the terrestrial ionosphere. As introduced in Chapter 1, the excess ionization during a flare has significant effects on the propagation conditions for radio wave frequencies across a broad spectrum. While improving signal strength in VLF, increased ionization has deleterious impacts on higher frequency sub-ionospheric radio waves, such as those employed in HF radio communications (Davies, 1990). HF radio waves (3–30 MHz) facilitate long range communications as they reflect in the upper ionosphere, typically at the F2 region ($\sim$300 km in altitude), passing through the D-region as they propagate. During a significant ionizing disturbance, such as a solar flare, HF radio signals suffer attenuation due to absorption by the increased electron density and collisional frequency in the D-region. In extreme cases, these signals can fade out before and after they undergo reflection.

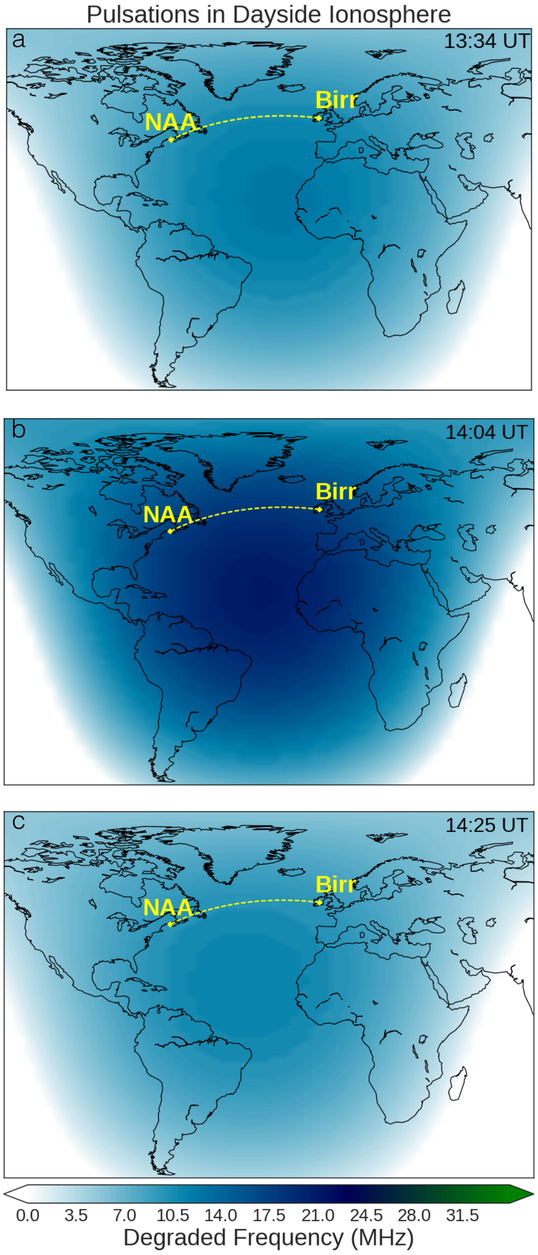

Figure 6.3: D-RAP model of HF radio absorption as a result of increased ionization in the ionospheric D-region. The locations of the VLF transmitter (NAA) and receiver (Birr) are shown along with the great circle path of propagation. The D-RAP model illustrates that the day-side ionosphere over the Atlantic Ocean suffering increased ionization as a result of the flaring QPPs. The three panels correspond to the times (a, b, and c) from Figure 6.1.

D-RAP models the impact on HF wave attenuation attributed to X-ray ionization of the lower ionospheric D-region, and is used here to illustrate the HF propagation effects over the path travelled by the VLF (from Maine, US to Birr, Ireland). The D-RAP model is driven by the GOES X-ray and proton fluxes, and relies on empirically derived relationships between X-ray flux and frequency degradation (Akmaev *et al.*, 2010). Data from the global D-RAP model for the event is shown in Figure 6.3 at three intervals that correspond to the same three intervals as the EUV images in Figure 6.1. The NAA transmitter and SID monitor locations are highlighted and the great circle between them plotted. The color map denotes the highest frequency radio wave affected by an absorption of 1 dB, with higher values indicating increased electron density. Throughout the flaring event, ionizing perturbations take place in the D-region along this path, illustrating that the NAA-Birr propagation path is an appropriate path to use for VLF remote diagnostics in relation to this event. See also Movie 6.2.

6.4 Modeling D-region Electron Density

To infer the electron density from the VLF measurements, full waveguide solutions to the propagation of the VLF signal during the perturbed conditions are utilized. The analysis undertaken is based on the Wait & Spies (1964b) model, which uses two parameters of a reference height H' (km) and an electron density e-folding or 'sharpness' β (km^{-1}) parameter to describe the electron density height profile of the ionospheric D-region. This two parameter system provides a model of a vertically stratified ionosphere with an electron density profile N_e

that exponentially increases with altitude, h given by

$$N_e(h, H', \beta) = 1.43 \times 10^{13} e^{-0.15H'} e^{(\beta-\beta_0)(h-H')} \text{ m}^{-3} \tag{6.1}$$

Here β_0 is equal to 0.15 km^{-1}. Though simplified, this is a useful expression for the estimation of D-region electron density profile as discussed in Chapter 2.

The changes to this electron density profile in response to ionizing disturbances can be achieved through the use of the Long Waveguide Propagation Capability (LWPC) software (Ferguson, 1998). LWPC enables the simulation of VLF signal propagation based on the waveguide mode theory (see Chapter 2). The input variables into the LWPC code are the VLF path parameters, such as transmitter and receiver locations, time of day, and H' and β values. Based on these inputs LWPC then calculates full waveguide solutions to the VLF propagation along the defined path and calculates the expected amplitude and phase measurements for the given input parameters. By varying the two independent H' and β parameters, a range of VLF signal amplitudes were simulated, and the resulting agreement between the modelled and observed signals provided the most likely height profile of the ionosphere.

The reference values for the parameters of the H' and β during daytime quiet solar condition by 74±1 km^{-1} and 0.31±0.1 km^{-1}, respectively (Thomson & Clilverd, 2001). During increased ionization during a flare, the effective height H' is readily lowered and the sharpness parameter β is increased. The quiet time values are used as a starting set of values for the LWPC, and then are varied to produce a set of (H', β) parameters and calculated amplitude values. The temporal variation of the calculated H' and β values for this flare are marked as

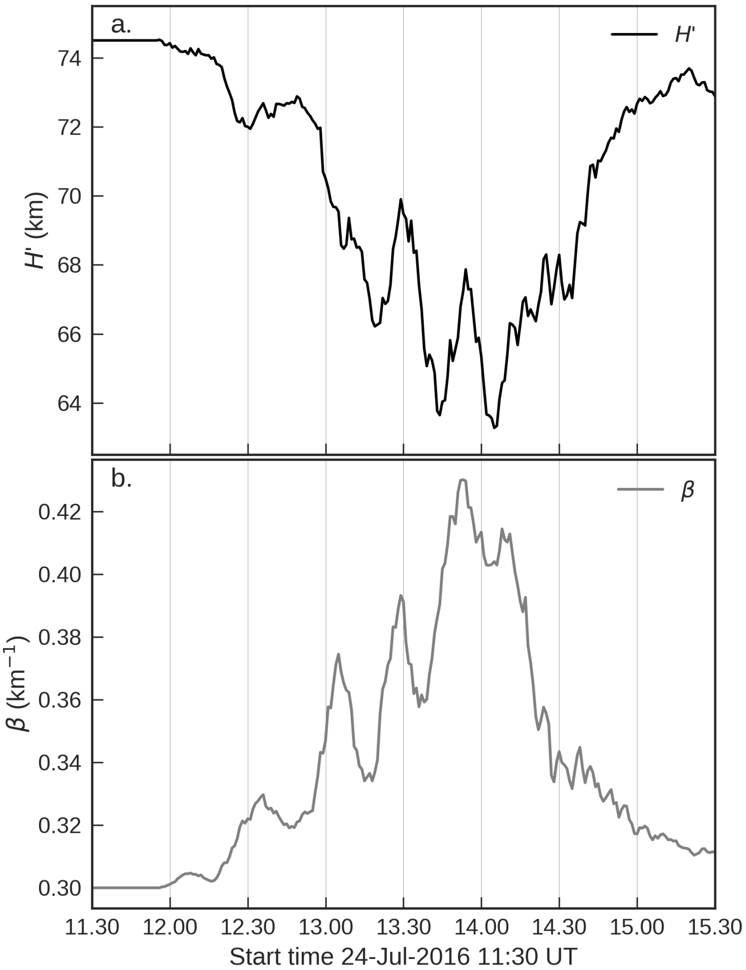

Figure 6.4: Calculated Wait parameters from LWPC as a function of time throughout the flaring event. (a) the effective reflection height, H', and (b) the 'sharpness' parameter, β. The parameters are obtained from the best fits between the simulated LWPC and the observed VLF amplitude.

black and grey respectively in Figure 6.4. As shown, these parameters similarly follow the pulsating signatures. At the peak of the maximum X-ray flux (at ~14:05 UT), it is found that the H' decreases from 74 km to 63 km, and β increases from 0.31 km^{-1} to 0.42 km^{-1}.

These estimated parameter values are then used with Equation 6.1 to calculate the resulting electron density profile as a function of time. This is shown as a

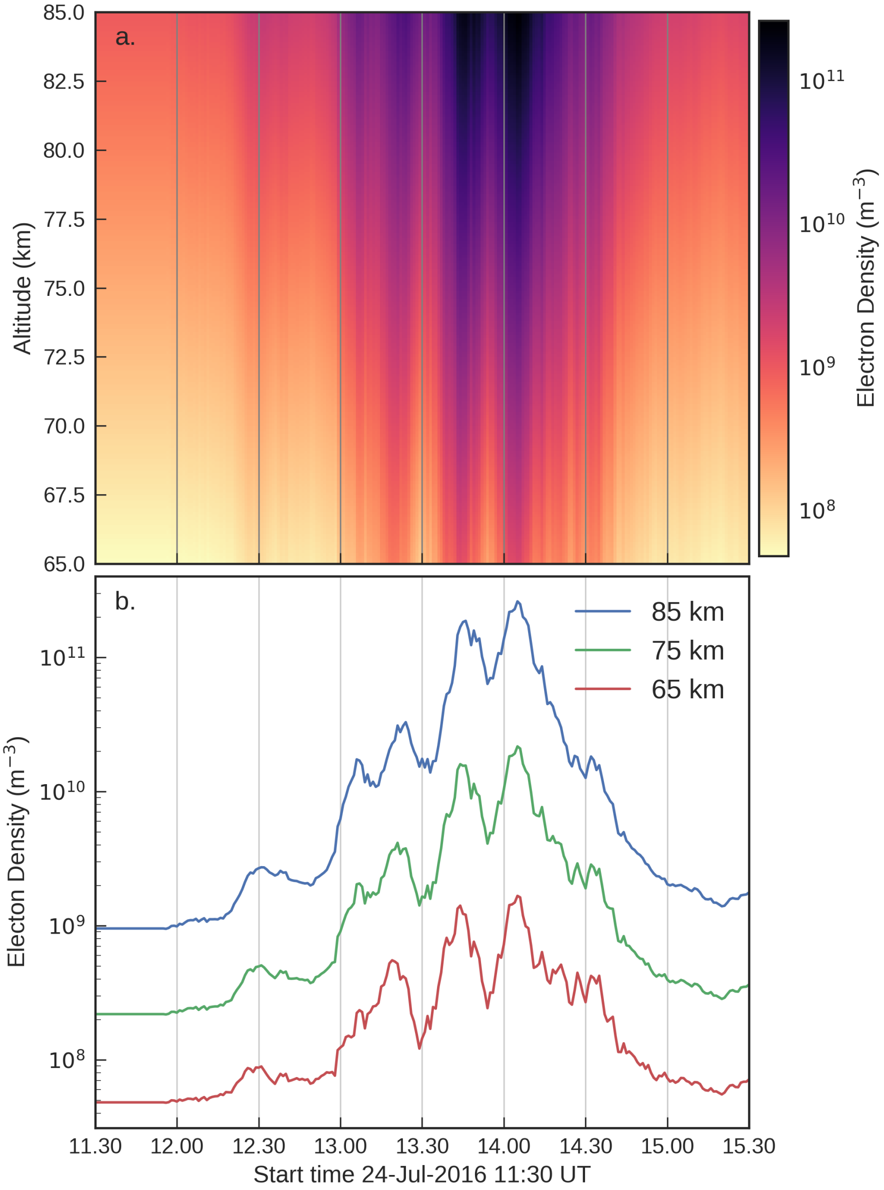

Figure 6.5: The electron density N_e estimated from the calculated Wait parameters from Figure 6.4 and Equation 6.5 as a function of both altitude and time is shown in (a). The color table is in a log scale, and the associated colorbar denotes electron density in m^{-3}. To demonstrate the variability of the electron density, the values at three altitudes of 65, 70 and 85, are extracted from (a) and plotted as a function of time in (b).

contour plot in Figure 6.5 (a). To further demonstrate the variation, time-slices are taken at three altitudes; 65, 75 and 85 km and are plotted in Figure 6.5 (b). During the flaring event, especially for pulsations 2–8, the variation in electron density closely matches the soft X-ray QPPs, similarly displaying pulsating signatures. It can also be noted that the influence of the ionizing radiation is more pronounced at higher altitudes, and during times of higher X-ray flux values. For example, pulsation peaks 0 and 1 do show some temporal variation, more so at higher altitudes, however the magnitude of the variations is much smaller. At 74 km, the electron density varies from $\sim 2\times10^{8}$ m^{-3} from the pre-flare quiet daytime conditions, to $\sim 1.6\times10^{10}$ m^{-3} during the largest flaring pulsation. These estimated values are in accordance with solar flare induced electron density variations reported in the literature (e.g Grubor *et al.*, 2005; Selvakumaran *et al.*, 2015). The novelty here is that the electron density is demonstrating a clear quasi-periodic variation on a 20 min timescale that corresponds to the solar flare QPPs.

6.4.1 Estimating the Effective Recombination Coefficient

The electron density in the D-region is controlled by the balance between photoionization and electron loss processes. The intrinsic time delay that is noted between the VLF amplitude (electron density) and the X-ray flux is the inherent chemical reaction timescale of the D-region which results from recombination (electron loss) processes. At D-region altitudes, the dominant loss processes are electron-ion, ion-ion and three body recombination. These processes together can be quantified in terms of the *effective recombination* coefficient, α_{eff} that embodies the combined effect.

Here we formulate an expression for the effective recombination coefficient following the works of Appleton (1953); Basak & Chakrabarti (2013); Žigman *et al.* (2007). The fundamental assumption for this calculation is that the VLF amplitude reflects the instantaneous variations of the electron density in response to ionizing disturbances, such that $t_{VLF} = t_{N_e}$. We have seen from Chapter 2 that the electron continuity equation can be written in the form,

$$\frac{dN_e}{dt} = q(t) - \alpha_{eff} N_e^2 \tag{6.2}$$

This equation can be utilized to understand the time delay between the X-ray emission and VLF amplitude, and to estimate α_{eff}. At the peak of an X-ray pulsation, a maximum in the electron production rate (q) is inferred. For conditions at the maximum q at time t_q, the derivative of Equation 6.2 at this time (i.e. $dq/dt = 0$) can be written as

$$\left(\frac{d^2N_e}{dt^2}\right)_{t_q} = -2\alpha_{eff} N_e \left(\frac{dN_e}{dt}\right)_{t_q} \tag{6.3}$$

Equation 6.2 describes the general expression for the behaviour of the D-region electron density, however at the time of the maximum production rate (i.e. at t_q), the rate of change of the electron density can be expressed as the Taylor expansion of dN_e/dt up to the second order term;

$$\frac{dN_e(t)}{dt} = \left(\frac{dN_e}{dt}\right)_{t_q} + (t - t_q)\left(\frac{d^2N_e}{dt^2}\right)_{t_q} \tag{6.4}$$

During the time for a peak in the VLF amplitude measurements, the value of N_e

is a maximum and so $dN_e/dt = 0$ and hence Equation 6.4 becomes

$$0 = \left(\frac{dN}{dt}\right)_{t_q} + (t_{N_e} - t_q)\left(\frac{d^2N_e}{dt^2}\right)_{t_q} \tag{6.5}$$

Here, t_{N_e} represents the time of the maximum VLF peak (i.e. maximum electron density). Equating Equation 6.3 and 6.5, and rearranging for α_{eff}, we arrive at an expression that relates the effective recombination coefficient to the time delay (Δt) and the electron density at the time of t_q,

$$\alpha_{eff} = \frac{1}{2(t_{N_e} - t_q)N_e(t_q)} = \frac{1}{2\Delta t N_e(t_q)} \tag{6.6}$$

This expression was originally derived for the diurnal maximum delay (Appleton, 1953), but has been revisited and employed in the study of solar flares in recent years (Žigman *et al.*, 2007). The expression is valid at a maximum in ionizing flux, so is often employed in statistical studies where a number of different flaring peaks from different classes of flares can be investigated. However, in this study the QPPs offer a number of local maxima, and hence α_{eff} can be estimated as a function of flux for the *same* flaring event.

The values of N_e, estimated from LWPC in Figure 6.5, are used together with the observed time delay of ∼90 s to calculate α_{eff} for each QPP peak numbered 0–9. These calculated values are plotted as a function of X-ray flux for different altitudes in Figure 6.6. The coefficient is calculated for each peak 0–9 and a log-linear fit to the points are determined for the different altitudes plotted. The shaded regions are the 95% confidence intervals of each fit. Unlike the electron density, the values of α_{eff} decrease with increasing flux and altitude.

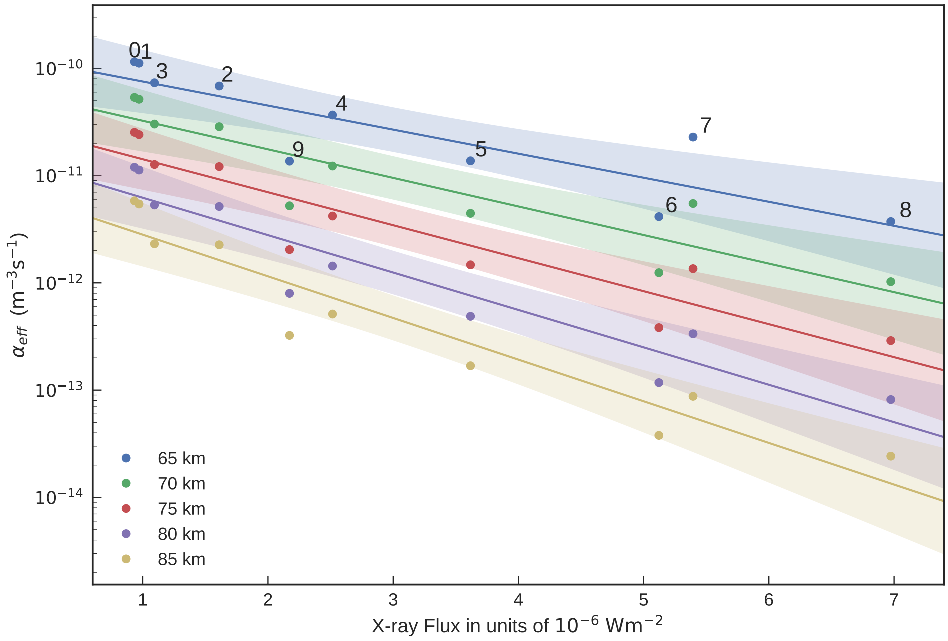

Figure 6.6: Estimated values of the effective recombination coefficient (α_{eff}) as a function of X-ray flux and altitude. The coefficient is calculated for each pulsations peak, numbered 0-9. The shaded regions are the 95% confidence interval of least squares fit.

The range of values determined here are in the range of 10^{-10}–10^{-13} ms^{-1}. These values are consistent with both which are in accordance with other works in the literature (e.g. Basak & Chakrabarti, 2013; Gledhill, 1986; Žigman *et al.*, 2007). The decrease of α_{eff} with increased flux has been evidenced in a number of studies, and is attributed to the fact that the increased ionization reduces the population of hydrated ions and clusters in the D-region. The advantage of the analysis here is that we can estimate multiple values of the α_{eff} during the same flaring event.

6.5 Discussion and Conclusions

The work outlined in this Chapter reveals that the Earth's lower ionosphere is sensitive to dynamic solar activity such as QPPs in solar flares. This is the first observation of its kind, exposing a coupling of oscillatory signatures in solar X-ray emission and the Earth's ionized environment on short timescales. The detection of solar flare QPPs in the Earth's ionospheric response has interesting implications for the study of the geoeffectiveness of solar flares. The quasi-periodic electron density variations driven by the X-ray QPPs could result in further triggering of processes in the Earth's atmosphere. The electron density variations may constitute a periodic driver for dynamic atmospheric phenomena, such as acoustic gravity waves (Nina & Čadež, 2013). These effects could have the potential to be greatly enhanced if a resonance occurred between the periodicity of the incoming X-ray flux and the natural frequencies of the ionosphere (Nakariakov *et al.*, 2016).

The comparative nature of solar X-ray flares and the ionospheric response (without pulsating signatures) has been widely discussed in the literature (e.g. Mitra, 1974; Selvakumaran *et al.*, 2015; Thomson *et al.*, 2005). VLF provides a powerful tool to probe the D-region electron density in response to ionizing disturbances such as solar flares. The Earth's ionosphere essentially acts as a giant X-ray detector, characteristically responding to the enhanced ionization of X-ray flux. Subsequently, the D-region has responded to the QPPs present in the flaring emission from this event. Global VLF networks, such as the Global Ionospheric Flare Detection System (GIFDS) (Wenzel *et al.*, 2016), will allow for the continuous monitoring of the D-region in response to solar flare activity, and indeed will allow us to further explore the relationship of dynamic QPP events and their ionospheric response.

Other planetary atmospheres are similarly affected by solar flares. For example, Mendillo *et al.* (2006) showed that an enhancement of up to 200% in electron density can occur in the lower ionosphere of Mars in response to a large X-ray flare. Similar reports have also shown evidence for solar flare effects on the atmosphere of Venus (Kar *et al.*, 1986). The question now arises as to whether oscillatory signatures can be observed in other planetary atmospheres, and how coupled these atmospheres are to solar activity. Finally given the recent evidence of QPPs in stellar flare emission (e.g. Cho *et al.*, 2016; Mitra-Kraev *et al.*, 2005; Pugh *et al.*, 2016), this observation implies the presence of oscillatory responses in exoplanetary atmospheres.

7

Conclusions and Future Work

The research outlined in this thesis has aimed to further the current understanding of the QPP phenomenon, both in solar flare energy release and into the investigation of the geophysical impacts of solar flare QPPs on the Earth's terrestrial ionosphere. In this Chapter, we summarize and conclude the principal results of the research presented in this thesis and outline how this work can be expanded upon in future studies. Some promising preliminary results of these future work directions are also discussed.

7.1 Principal Thesis Results

The research carried out in this thesis has contributed to our understanding of the nature of QPPs in solar flares and has provided the first observational evidence for the geophysical effects of QPPs on the Earth's ionosphere. We present two detailed observational investigations into the temporal fine structure QPPs that are observed in the soft X-ray emission from solar flares. The results from these two studies have furthered our understanding into the characteristics of soft X-ray QPPs, exposing the extended variability that exists from this emission and provides suggestive evidence that perhaps a different dominant QPP driver is at play in the different phases of a solar flare. We also present a study of synchronized QPPs observed in both soft X-ray flaring emission and in the corresponding electron density variations in the Earth's lower ionosphere, shedding light on the intricate solar-terrestrial relationship and indeed on the geoeffectiveness of flaring QPPs. These studies provide new insights into the physical nature and characteristics of solar flaring energy release and the relationship with the Earth's ionized environment. In this section we review and summarize the principal results from the three research Chapters of this thesis.

7.1.1 QPPs during the Impulsive and Decay Phases of an X-class Solar Flare

In Chapter 4, a multi-wavelength investigation of solar flaring QPPs detected in an X1.0 flare from October 28 2013 is presented. In this study we pay particular attention to the temporal fine structure pulsations evident in the soft X-ray time derivative, and compare this variability to the QPPs observed at other wavelengths including hard X-ray and microwave observations. This research was published in Hayes *et al.* (2016) and the main results of this study are as follows:

- During the impulsive phase of the flare, co-existing QPPs are detected across multiple wavelengths including the thermal emissions from the soft X-ray time derivative observations and the non-thermal emissions from both hard X-ray and microwave observations. These QPPs reflect impulsive energy release, and an underpinning cause of the QPPs must be able to explain the modulation of the physically different emission mechanisms.

- Testing against a power law background model, wavelet analysis shows broadband features in the wavelet spectrum with a characteristic period of $\sim$20 s observed across all channels and a second significant period of $\sim$55 s found in the non-thermal emissions.

- Decay phase QPPs are observed to persist in the thermal soft X-ray emissions as observed by GOES, even after the non-thermal emission has ceased. The extended QPPs demonstrate a decaying amplitude and tend towards longer timescales, increasing from $\sim$40 s just after the impulsive phase to $\sim$70 s later into the decay phase. The loop lengths of the flare, estimated from RHESSI observations, are found to systematically increase throughout the decay phase, a potential explanation of the longer periods in this phase of the flare.

- We interpret the co-existing highly correlated QPPs during the impulsive phase of the flare in terms of periodic injection/acceleration of electrons into the flaring loop as this can simultaneously explain the multi-wavelength QPPs. In the decay phase however, we interpret the thermal damped QPPs in terms of standing compressive MHD wave modes that exist in the post-flare loops.

Future work to test the interpretation presented here could include detailed forward modelling used in conjunction with the observations to test if the density perturbations produced by a standing MHD wave mode (such as sausage or vertical kink) could produce the observed soft X-ray emission modulation from this flaring event. Recently, new forward modelling tools have become available to simulate emission from solar flares (e.g. Nita *et al.*, 2018; Van Doorsselaere *et al.*, 2016a). These offer an important and exciting new avenue to pursue in the study of solar flaring QPPs.

7.1.2 Long Duration QPPs detected during a Large X-class Solar Flare

In Chapter 5 we present an investigation into the extended QPPs observed in the soft X-ray thermal emissions from an X8.2 solar flare that occurred on September 10 2017, the second largest flare of solar cycle 24. This study focuses on the the relationship between the observed QPPs to the length scales and eruption dynamics of the flaring event through spatially resolved observations from AIA and RHESSI. The research presented in this Chapter is currently in review as Hayes *et al.* (2019) and the principal results are as follows:

- Long duration soft X-ray QPPs are detected throughout the entire solar eruptive flaring event, from the beginning of the impulsive phase to late into the decay phase, up-to three hours after the peak of the flare. These QPPs are clearly identified in the detrended lightcurves and, to the best of our knowledge, provide the most extended detection of consistent QPPs of this type from a flaring event.

- The analyzed lightcurves demonstrate two regimes of QPP signatures, 'bursty', relatively larger amplitude QPPs in the impulsive phase with characteristic periods of ∼65 s, followed by more coherent lower amplitude QPPs in the extended decay phase that have periods of ∼150-160 s. These results complement those in Chapter 4 and Dennis *et al.* (2017), providing further evidence of multiple periods in the different phases of a flare. The decay phase QPPs are also detected in the hot 131 Å channel of AIA, and demonstrate beat-like signatures in the pulsation amplitudes (see Figure 5.3).

- During the time of the impulsive QPPs, the soft X-ray source, observed by RHESSI, is found to rapidly rise at a velocity of 17 km s^{-1} following the CME eruption. This source evolution then slows down to 2-5 km s^{-1} in the decay phase. EUV observations in the 131 Å channel of AIA demonstrate extended downward moving features that travel along the current sheet and impact the top of the flaring arcade. These structures are clearly identified throughout the decay phase of the flaring event (see movie 5.1), suggesting that they are related to the extended QPP signatures observed in soft X-ray and EUV emissions.

- The QPPs observed during the impulsive phase are interpreted in terms of the dominant processes that are occurring during this time, namely impulsive energy release and particle acceleration. The period of ∼65 s is most likely related to the timescales of the reconnection dynamics. The extended decay phase QPPs are instead interpreted in terms of MHD wave modes in the post-flare loops, triggered by the observed downward moving features that impact the top of the arcade. We infer that the vertical kink mode is the most likely candidate given the timescale of the pulsations, and the reasonable estimate for the Alfvén speed ($\sim$ 1178-1414 km s^{-1}) found when interpreted in this way.

7.1.3 Pulsations in the Earth's Lower Ionosphere Synchronized With Solar Flare Emission

In Chapter 6 a detailed investigation into the relationship between long period solar flare X-ray QPPs and the Earth's lower ionospheric response is presented. This study focuses on VLF remote sensing measurements of the D-region electron density in response to solar flare emission, and for the first time, reports synchronized QPPs in both the D-region electron density and the X-ray emission from a solar flare. This is the first study of its kind and provides the first observational evidence for the geoeffectiveness of solar flare QPPs. This work is published in Hayes *et al.* (2017) and the main points of this study are summarized below:

- We detect QPPs with periods of 20 mins in both the VLF radio wave amplitude measurements the represents the state of the ionospheric D-region and in the observations of solar flare soft X-ray and EUV measurements from a localized active region.
- The VLF amplitude measurements are used together with the Long Waveg-

uide Propagation Capability (LWPC) code to estimate the electron density variation in the D-region during the flaring event. It is found that the electron density profile similarly demonstrates quasi-periodic variations, with increase of up to one order of magnitude over the timescales of the pulsations.

- An associated time delay of ∼90 s is observed between the X-ray flux measurement and the VLF amplitude response, indicating an intrinsic finite time of the complex electron gain and loss processes in the ionospheric D-region. This measured time delay can be used together with the electron density values determined from LWPC to estimate the effective recombination coefficient, α_{eff}, at each peak of the pulsations. The values of α_{eff} are found to be in agreement with several other studies. The novelty here is that it can be measured as a function of flux for the same flaring event given the number of pulsation peaks observed.

7.2 Future Work

The results presented in this thesis provide important new insights into the nature and evolution of flaring QPPs and indeed into the geophysical effects of solar flaring QPPs on the Earth's atmosphere. There are, however, still many open questions regarding the properties and underlying mechanism of quasi-periodic signatures in flaring lightcurves, and much work can be expanded upon the results in this thesis to further our understanding of the QPP phenomena. In this section we present details of future work directions and preliminary new results that build upon the QPP investigations in this thesis.

7.2.1 Temporal, Spectral and Spatially-Resolved Investigations of QPPs

From Chapter 4 it is clear that QPPs can co-exist across multiple wavelengths associated with physically different emission mechanisms. For example, QPPs observed at hard X-ray wavelengths are associated with non-thermal bremmstahlung emission from accelerated electrons that precipitate into the dense chromosphere, whereas microwave observations are associated with gyrosynchrotron emission of accelerated electrons that are magnetically confined to the flaring loops. QPPs at soft X-ray and EUV wavelengths on the other hand are associated with thermal plasma properties and heating mechanisms. In this way it is difficult to conclusively identify an underpinning mechanism as a complete theory would have to be able to describe the variations of electron acceleration, plasma parameters, heating processes and reconnection itself. While the detailed temporal relationships between the different wavebands prove useful in detecting and providing some interpretation of QPPs, the observed spectral and spatial properties of the emitting sources will help to further constrain the emission modulation mechanisms. Furthermore, the results from Chapter 5 demonstrate that the eruption dynamics of a flaring event can play a role in the observed QPP properties and further investigation into this relationship is required.

To build upon this, we present here a flaring event for which a rich data-set of observations exists to perform such an in-depth future study of the temporal, spectral and spatial features of detected QPPs, and to relate them to an accompanying CME eruption. The event of interest is an X1.2 solar flare that occurred on May 15 2013 from NOAA AR 11748. The reason for choosing this flare for a future study is that it is an eruptive two-ribbon solar flare which was well observed by many different instruments. The UV ribbons can be clearly observed in 1600 and 1700 Å channels of AIA, and double hard X-ray footpoints can be readily resolved in the RHESSI hard X-ray observations. We have excellent NoRH spatially resolved observations throughout the flare in both 17 and 34 GHz [1]. The CME eruption can also be clearly identified in the EUV observations from AIA in multiple passbands. Finally the flare was also well observed by FERMI, the Nobeyama RadioPolarimeters (NoRP) and GOES. In this way, this flare provides detailed observations from which we can probe all aspects of the solar eruptive event and perform an in-depth analysis of the observed QPPs. In this section we demonstrate some of the preliminary data analysis and outline the future work that will be performed on this QPPs observed in this flare.

7.2.1.1 Event Overview

An overview of the X1.2 solar eruptive event is shown in Figure 7.1. QPPs can be clearly identified in the soft X-ray time derivative of the GOES 1–8 Å channel in Figure 7.1 (a), the hard X-ray observations from FERMI in (b) and in the microwave observations at 3.75, 9.4 and 17 GHz from NoRP in (c). The QPPs observed by RHESSI are not shown here, but demonstrate the same time profile as the FERMI observations in (b). The CME eruption that accompanied the solar flare is observed in the AIA 171 Å channel shown in Figure 7.1 (d-f). The red arrow in (d) points the coronal loop structure that begins to rise up in (e) and (f) to finally erupt out of the corona as a CME. The QPPs are observed to

---

[1] This data was provided by Stephen White who pre-processed and co-aligned the NoRH images.

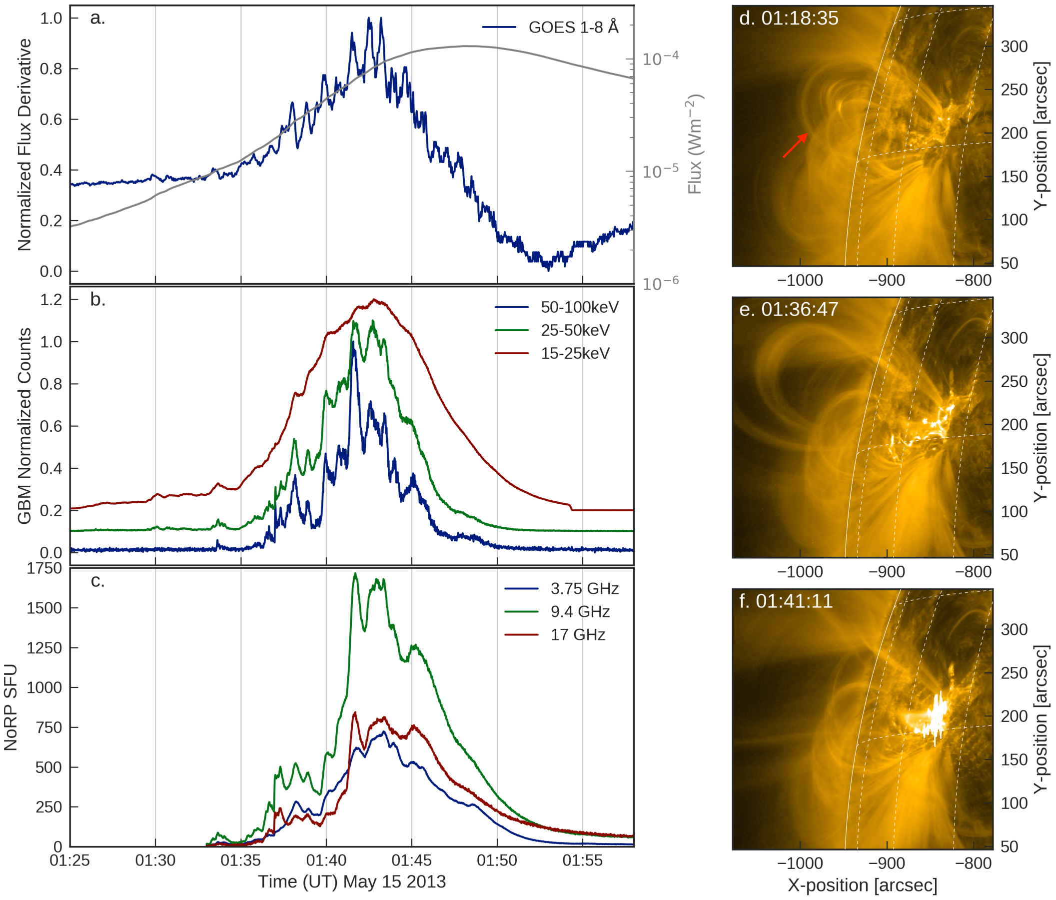

Figure 7.1: An overview of the X1.2 solar flare from May 15 2013. The lightcurve and lightcurve time derivative of the GOES 1–8 Å channel is shown in (a) in the grey and blue colors respectively. The FERMI X-ray observations are shown in (b) in three wavelengths bands; 50-100 keV, 25-50 keV and 15-25 keV. Microwave observations at 3.75, 9.4 and 17 GHz from the Nobeyama RadioPolarimeters (NoRP) are shown in (c). It should be noted that the 17 GHz observations from the NoRH observations shows the same time profile as the 17 GHz NoRP lightcurve. The eruption can be identified in the AIA 171 Å observations in (d-f). The red arrow in (d) points to the coronal loop structure that is observed to erupt out of the corona.

co-exist across the multiple wavebands, and are found to have a period of ∼50 s in all channels, spanning both thermal and non-thermal emissions.

The NoRP observations provide both total and circularly polarized intensity at several microwave frequencies. The NoRP microwave spectrum is shown in Figure 7.2, and is fit with a functional form of a gyrosynchrotron spectrum (Dulk, 1985). The measurement at 1 GHz is not included in the fit as it is probably associated with plasma emission rather than gyrosynchrotron emission. The turnover frequency from this spectrum is found to be ∼10 GHz, such that frequencies below 10 GHz are associated with optically thick gyrosynchrotron and frequencies above 10 GHz are that of optically thin emission. In this way we can investigate the relationship between optically thick (2 GHz, 3.75 GHz, 9.4 GHz) and the optically thin (17 GHz, 34 GHz) QPPs from this flare which have the potential to confirm or rule out the role of MHD waves modulating the observed emission. This spectra will be investigated in more detail, and both the optically thick and optically thin spectral indices and polarization will be related to the observed QPPs in emission. Furthermore, flaring hard X-ray spectra from RHESSI will also be studied. The non-thermal spectral index as a function of time will be determined and compared to the microwave observations.

7.2.1.2 Preliminary Spatial Observations

A snapshot multi-wavelength view of the spatially-resolved observations of this flare as observed in UV, hard X-ray and microwave emissions in shown in Figure 7.3. The extended bright UV two-ribbon structures are observed in the 1600 Å channel of AIA. The RHESSI hard X-ray footpoints in the 35-100 keV range are shown in blue, representing non-thermal bremsstrahlung sources. The NoRH 17 GHz observations are plotted as red contours and trace out the trapped population of accelerated electrons in the flaring loops. The goal of the future work for this event will be to understand the relationship between the QPPs observed in the flaring lightcurves to the associated spatial feature observed here.

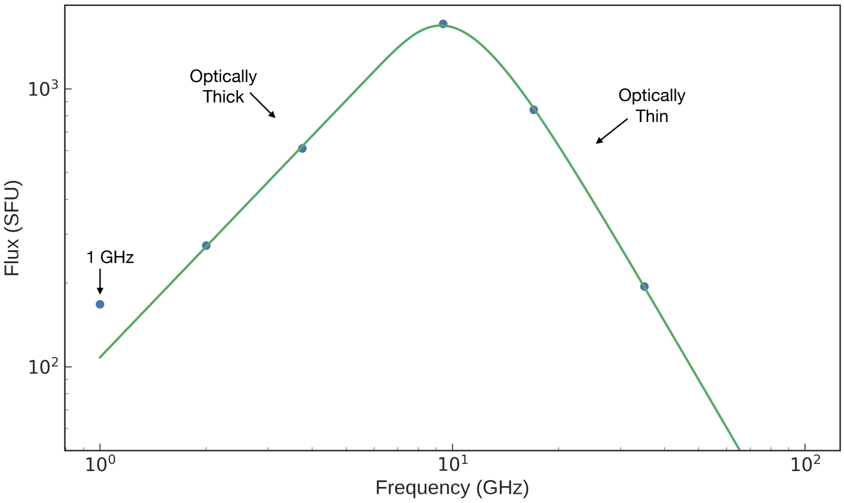

Figure 7.2: The observed NoRP radio spectrum at 01:41:36 UT. Here, the spectrum with a gyrosynchrotron spectrum (Dulk, 1985). The 1 GHz frequency is not included in the fit as this is probably related to plasma emission rather than gyrosynchrotron. The fit is of the form $F(f) \propto f^{-\alpha}$, where α is the spectral index. For optically thin emissions, i.e. for frequencies greater than the turn-over frequency f_{peak}, $\alpha_{thin} > 0$, whereas for optically thick emissions at frequencies less than f_{peak}, $\alpha_{thick} < 0$. The turnover frequency of this fit is at ~10 GHz.

The flaring ribbons themselves are of particular interest, and as QPPs are observed in the hard X-ray emission associated with precipitating electrons into the chromosphere, it is reasonable to assume that the UV brightenings of heated chromospheric plasma should also demonstrate QPP variability. To preliminary investigate this, we focus on each ribbon individually as shown in Figure 7.4. Two boxes are drawn to isolate each ribbon in (a) and an associated lightcurve for each is produced by summing over the pixels in each box, and plotted in (b). The cadence of the 1600 Å channel is 24 s and so it is difficult to resolve the QPPs with periods of 50 s, however the lightcurves do exhibit variability and it can be seen that this variability co-exists in both ribbons. It is also interesting to note that while the variability is synchronous in both ribbons there is stronger

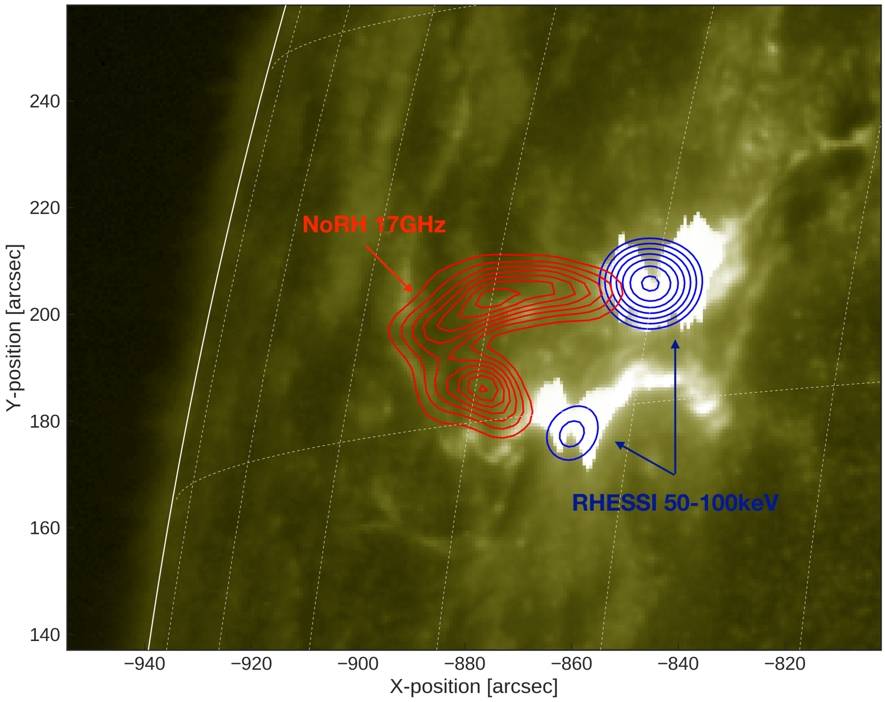

Figure 7.3: An overview of the spatially resolved observations that will be utilized in this investigation at 01:43 UT. Here the AIA 1600 Å wavelength band is plotted where two bright ribbon structures can be identified. Overplotted in blue are the RHESSI hard X-ray footpoint sources in the energy range of 35-100 keV. It can be seen that these footpoints appear at the same locations of the ribbons. The NoRH 17 GHz contours are plotted in red, and demonstrate a loop-like structure connecting the two footpoints.

emission associated with the top ribbon, similar to the stronger X-ray footpoint as observed in Figure 7.3.

The preliminary spatial investigations of the NoRH 17 GHz microwave emissions is demonstrated in Figure 7.5. Here, the 17 GHz observation is plotted as an intensity map in (a), and three boxes of interest are placed on the image, chosen to isolate the different parts of the flaring loop (loop legs and loop top) to search for the sources of modulated emission. Lightcurves from these boxes are then produced, taken as the maximum brightness pixel in each box, and plotted as a

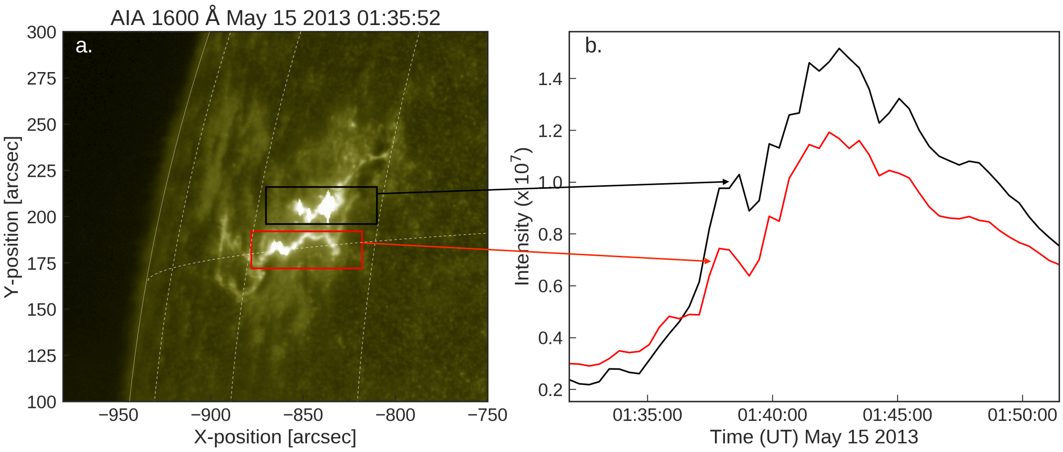

Figure 7.4: Preliminary analysis on the UV ribbon structures observed in AIA 1600 Å. In (a) the extended two ribbon structure can be clearly identified. To search for pulsating features in both ribbons, boxes are placed on each, and a lightcurves created by summing over the pixels in a sequence of images. The associated lightcurves from each box is shown in (b).

function of time in Figure 7.5 (b). The colours of the lightcurves correspond to the coloured boxes in (a). The QPPs observed in microwave emission seem to be dominated by the southern leg of the loop. Of particular interest is that the adjacent footpoint is demonstrating stronger emission in both X-ray and in UV. Perhaps this is suggesting that this flaring scenario fits into the trap-plus-precipitation model (Melrose & Brown, 1976) and requires detailed further investigation, with particular focus on the hard X-ray footpoint emission as observed by RHESSI.

7.2.1.3 Relation to Eruption

A key feature of the future investigations of this flaring event is to focus on the relationship between the CME eruption and the observed QPPs. As a first step to investigate the timing relationship between the two, a slit is placed along the axis of the rising loop structure and a space-time plot is produced to inspect the

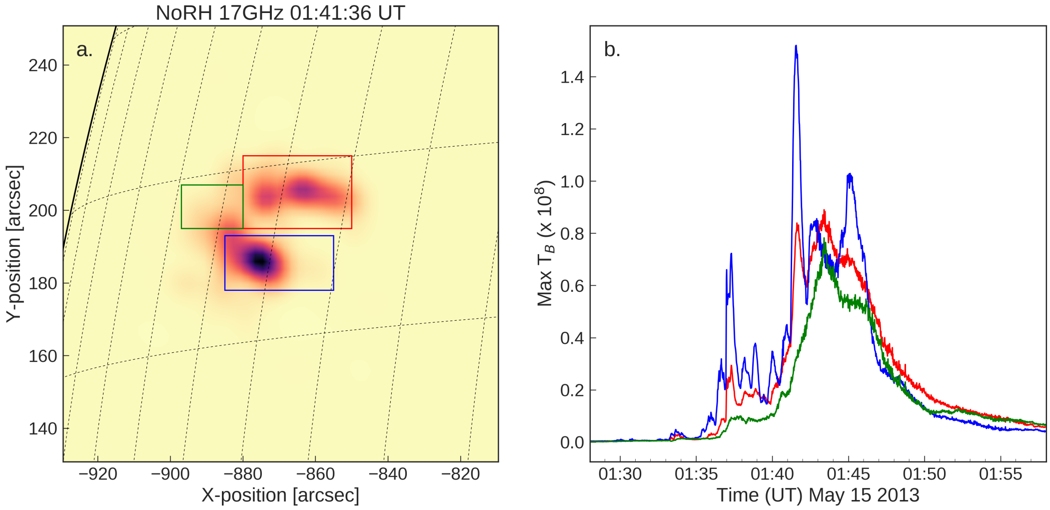

Figure 7.5: An intensity image of the NoRH 17 GHz observations of the flaring loops is shown in (a). To perform a preliminary spatial analysis of the observed 17 GHz loops, three boxes are placed at the loop legs and presumed loop top. Lightcurves from inside each of these boxes are created (taken as the maximum brightness temperature) and plotted in (b). The colors of the plotted lightcurves correspond to the color of the associated boxes.

dynamics of the evolution. The chosen slit is shown as the white dashed line in Figure 7.6 (c). The associated space-time plot is shown in Figure 7.6 (a) and the QPPs observed in GBM 50-100 keV are plotted in (b) for comparison. The vertical lines in (a) and (b) are plotted to highlight the time range over which the QPPs are present in the emission. In the space-time plot in (a) two arrows are plotted to denote two apparent stages in the eruption evolution. The arrow of stage 1 points to a time in which the eruption rises with an approximate constant velocity, whereas at stage 2 the eruption seems to accelerate as it reaches greater heights above the corona. What is interesting to note here is that the QPPs are observed during a time of relatively constant motion upward of the coronal loop structures, and the apparent acceleration occurs at the end of the observed pulsations. The intricate details of this require further investigation, but provide

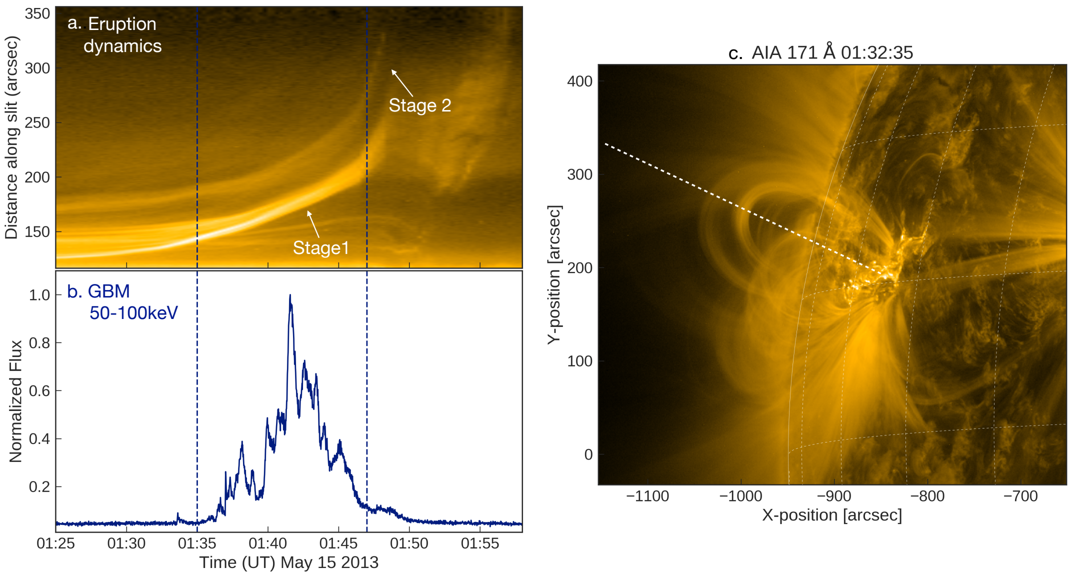

Figure 7.6: Preliminary analysis on the relationship between the observed QPPs and the CME eruption. (a) is the space-time plot along the white dashed line marked in the AIA 171 Å image in (c). The normalized GBM 50-100 keV lightcurve is plotted in (b) for time comparison. The vertical dashed lines are placed to highlight the times of the pulsations.

suggestive evidence of the relationship between QPPs and the eruptive dynamics for this event.

7.2.1.4 Future directions of this investigation

The preliminary data analysis of the observations from this event demonstrate some very interesting perspectives that require further investigations. In particular, the following questions will be addressed:

- Are there associated time delays between the QPPs observed across multiple wavebands?
- What is the relationship between the optically thick and optically thin mi-

crowave emissions? Are there in-phase correlations between the polarization and spectral indices of the emissions?

- What is the relationship between the hard X-ray spectral index and the observed QPPs? Does it demonstrate a soft-hard-soft evolution as you would expect for an injection of electrons into the flaring loops?
- Are there hard X-ray footpoint motions? If so, are they random or in a certain direction? Do they relate to kernal brightenings in the UV ribbons?
- How are the hard X-ray and microwave spatially resolved QPPs related? Is it some sort of trap-plus-precipitation model with the periodic injection of accelerated electrons in to the flaring loops?
- What is the direct relationship between the eruption dynamics and the observed QPPs? Do we observe a soft X-ray loop top source that follows the eruption?
- Do the extended low amplitude soft X-ray QPPs have a longer period than the impulsive phase? Are they related to the eruption dynamics?

7.2.2 Statistical Analysis of QPPs

While event-focused research is important to understand the detailed physical processes that occur in flaring QPPs, large-scale statistical studies are also required to determine the true prevalence of such signals and to help constrain the important parameters that are related to QPPs. The two flaring events reported in Chapter 4 and 5, and indeed in the section above, are all large X-class flares. The study of larger solar flares is motivated by the fact that the non-thermal emission from these flares is much easier to detect. However it has been shown that smaller flares do exhibit QPPs (e.g. Nakariakov *et al.*, 2018a). The question arises as to what conditions are necessary for a flare to host QPPs. Are larger flares more likely to exhibit QPPs? Do smaller flares have shorter periods? Do the conditions for QPPs depend on the flaring site itself? Indeed, some of the proposed QPP mechanisms suggest that the periods of the QPPs should be related to a spatial scale of the host flare. For example, the period of a MHD oscillation should relate to the length of a coronal loop. On the other hand, if the QPPs are associated with dynamic reconnection it might be expected that larger flares would have longer period QPPs. Furthermore, the results outlined in this thesis also suggests that perhaps decay phase QPPs have longer timescales than their associated impulsive phases. Is this true for all flares? Are there different dominant mechanisms in the different flare phases? In this section, some preliminary statistical analysis results, discussions and future directions are presented in regards to the questions listed above.

7.2.2.1 Extended Analysis of Inglis et al. 2016

The largest statistical study of QPPs to date is reported in Inglis *et al.* (2016). In this study, QPPs were searched for in the Fourier power spectra of lightcurves from 675 M- and X- class flares observed by the GOES 1–8 Å channel. The Automated Flare Inference of Oscillations (AFINO) method was utilized, which, as described in Chapter 5 and in A.3, involves a model comparison approach for determining if there is evidence of QPP signals in the flare power spectra. The focus of the statistical analysis was to determine the prevalence of QPPs in the 4-300 s period range, such as the QPPs reported in Chapters 4 and 5. The start and end times of the flares were determined from the GOES flare catalogue and the analysis was fully automated. It was found that ∼30 % of the solar flares from this sample showed significant signs of QPP-like events, and these events had a preferred timescale of 10-30 s.

The results from this study is a conservative estimate of the prevalence of QPPs in solar flares, and 30% can be thought of as a lower detection limit. The AFINO method employed is a global technique as the Fourier power spectrum is analyzed for the entire duration of the event. Hence if a QPP signal is present for a relatively small fraction of the flare, the overall strength in the Fourier power spectrum may be too small to be detected. Additionally, if the period or phase of the QPPs changes over the course of the flare, the QPP signature may also not be detected. The events that are detected however are flares that show *stationary* QPPs and a significant stable periodic signature. Even though the AFINO methodology is conservative, it is a powerful tool to obtain statistically robust, consistent results and has the ability to correctly find stationary QPP events.

The robustness of this methodology means that it can be easily extended to include all C-class flares in addition to the M- and X- class flares analyzed. As a further step to answer some of the questions proposed in Section 7.2.2, we extend the work of Inglis *et al.* (2016) with an aim to determine if smaller flares in fact do show prevalent QPP signals and indeed if there is any correlation between the period detected and GOES class (size of flare). We make use of the Heliophysics Event Knowledgebase (HEK) to access the GOES flaring catalogue and search for all X-, M- and C-class flares between the period of January 1 2011 to December 31 2017, a slightly longer extension of the Inglis *et al.* (2016) work.

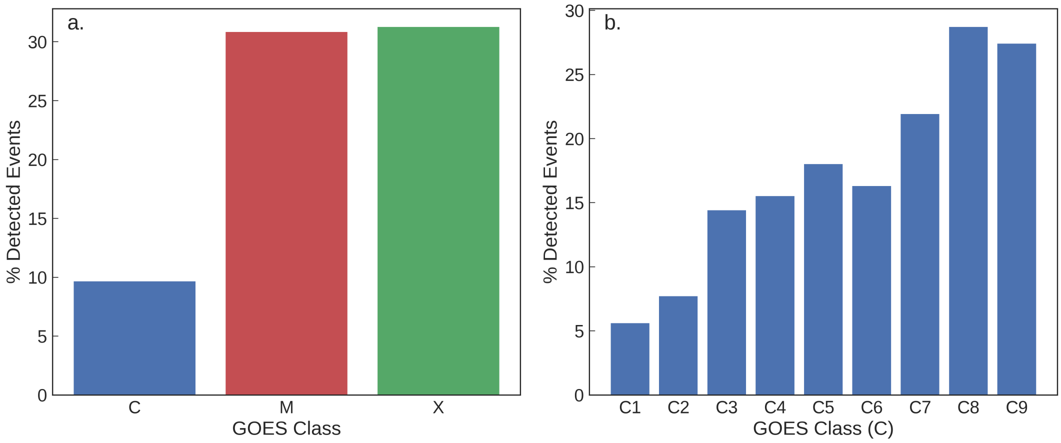

Figure 7.7: The percentage of detected events shown for the different associated GOES classes. (a) The percentage of flares in each class that were found to show evidence of stationary QPP signatures. (b) A breakdown of the different C classes to further understand the detection distribution.

We exclude events that had a shorter duration than 400 s, similar to Inglis *et al.* (2016), and identified a total of 7491 flares to analyze. The following constraints were also employed; that the period range searched for was restricted between $4 < P < 300$ s, and that the width of the Gaussian bump in the QPP model was between $0.05 < \sigma < 0.25$, in log-frequency space. This was chosen again to have the same conditions as Inglis *et al.* (2016). Indeed for an event to be classified as a QPP event, the QPP model had to be strongly favored over the other two model fits (with a $\Delta \mathrm{BIC} > 10$), and finally we also require that if the QPP model is found to be preferred over the other two, it has to fit the power spectra reasonably ($p > 0.01$).

The AFINO methodology was applied to these flares and Figure 7.7 presents the results of the QPP detection rates for the different GOES classes. In Figure 7.7 (a) the percentage of flares with detected QPP signatures to the number of overall flares of that class is shown. The prevalence for both the M- and X-

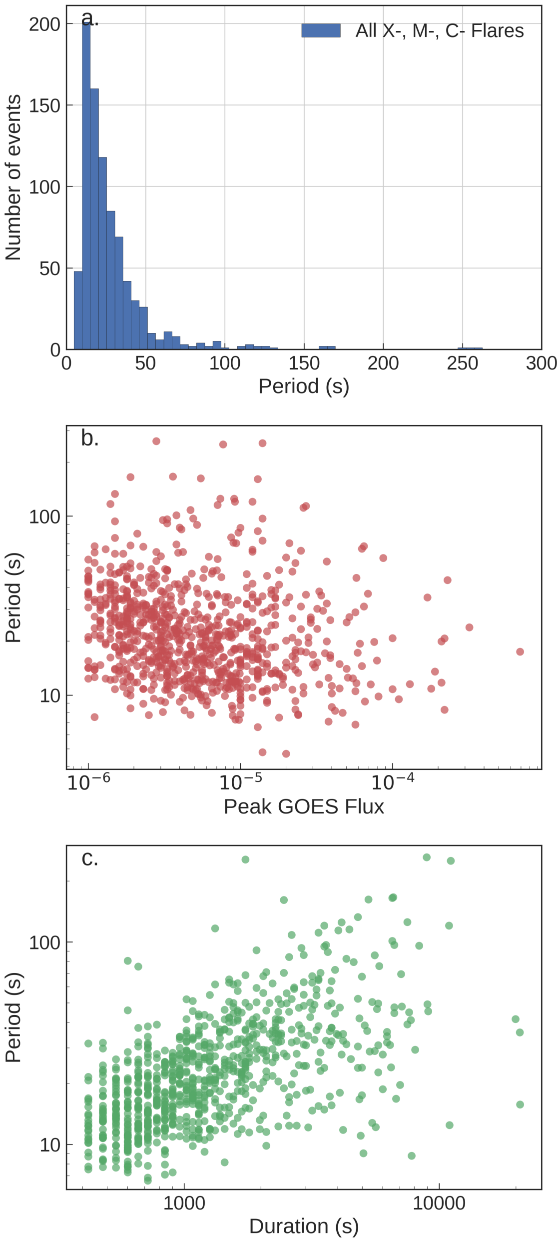

Figure 7.8: Results from the statistical survey all all X-, M- and C- class flares. (a) The distribution of the periods detected from the QPP events. (b) The detected QPP periods plotted as a function of the their associated peak GOES 1–8 Å values. (c) The detected periods plotted as function of duration of the flare.

class flares is $\sim$ 30 %, suchlike the results of Inglis *et al.* (2016). However a new finding here is that the percentage of detected QPPs in C class flares is much lower, $\sim$9.5 %. To further investigate this, a breakdown of the different classifications within the C class is shown in Figure 7.7 (b). Evidently, the larger C-class flares (C8, C9) show the 30 % prevalence rate of QPPs as the M- and X-class flares. The detection reduces for smaller flaring events, with the smallest C1 showing only a 5.6% prevalence of QPP signatures. It should be noted that this is still a large number of events (185 flares out of 3828). Perhaps it suggests that smaller flares are indeed less likely to exhibit QPPs. However the results could also reflect the detection limits of the GOES measurements, such that GOES cannot identify the small amplitude QPPs that would accompany small flares. This requires further investigation but is an interesting preliminary result.

Primarily exploration of the results of this extended statistical study is shown in Figure 7.8. The distribution of the detected periods is shown in Figure 7.8 (a). These results are consistent with Inglis *et al.* (2016), even with the C- class flares included, suggesting a preferred timescale of QPPs to be in the range of $\sim$10-50 s. A scatter plot of the periods of the detected QPPs as a function of their size (estimated as the peak of the 1–8 Å flux) is shown in Figure 7.8 (b). There is no apparent correlation between the detected period and the size of a flare. A Spearman correlation coefficient of 0.24 is found between the two. This suggests that perhaps the size of the period of QPPs does not depend on the size of the flare, and is it is interesting to note that QPPs detected in a small C class flare can have the same period as QPPs detected in a large X-class flare. Furthermore, a scatter plot of the period against the duration of the associated flare is shown in Figure 7.8 (c), where a positive correlation seems evident. The duration here is defined as the time between the defined start and end times of the flare from the GOES catalogue. A Spearman correlation coefficient of 0.62 is found between the two. This suggests that longer duration events have longer period QPPs. Similar results have recently been reported in (Pugh *et al.*, 2017), in which a statistical analysis was performed on 181 flares from a single active region. This correlation has some observational bias such that to detect longer periods, longer duration events are required. However this does not account for the fact that shorter period QPPs are not as equally detected in longer events, which one would expect if there were no correlation.

Recent results by Toriumi *et al.* (2017) may shed some light on this apparent correlation. In their work a positive correlation between flare duration and flare ribbon separation was found. This suggests that in longer duration events have greater ribbon separations, and hence larger loop arcades. If interpreted in this way, this could suggest that if QPPs were a manifestation of MHD wave modes, longer duration flares would have longer flaring loops and hence longer periods producing the observed correlation. This apparent correlation clearly needs more analysis, but provides an interesting avenue for investigation, particularly focusing on spatially resolved statistical analysis to relate ribbon properties (such as those observed in AIA 1600 Å and 1700 Å) to the detected periods.

7.2.2.2 Impulsive Vs Decay QPPs

The results from Chapter 4 and Chapter 5 suggest that the decay phases of solar flares demonstrate longer period timescales than their associated impulsive phases. There is growing evidence that this is perhaps an inherent feature of flaring emissions with similar results reported in recent studies (e.g. Dennis *et al.*,

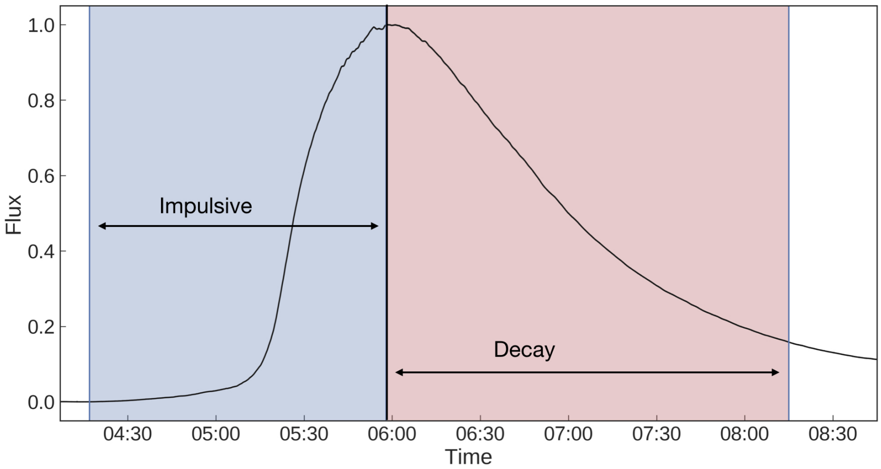

Figure 7.9: An example of a solar flare from the X- and M- class sample with the defined impulsive and decay phases used in the preliminary statistical analysis.

2017; Kolotkov *et al.*, 2018; Simões *et al.*, 2015). What is required now is a detailed statistical study on the differences between QPP signatures during the impulsive and decay phases to determine if this is in fact a common feature.

As a preliminary first step towards a statistical study of this kind, we report some early results that makes use of the AFINO methodology to search for differences in the detected periods between the impulsive and decay phases of all the X- and M- class solar flares observed in the 1–8 Å channel of GOES from solar cycle 24. To be statistically robust, the same selection criteria for the impulsive and decay phase is used for all flares. We define the impulsive phase as the time between the GOES catalogue start time and the peak flux in the GOES 1–8 Å channel. The decay phase of a flare is often found to extend out longer than the end time defined in the GOES catalogue (see also Chapter 5). To take this into account and to define a decay phase criteria, extra time is added on to the GOES defined end times. This extra time is chosen to be half the duration of the defined start to end times. The decay phase is then defined between the GOES

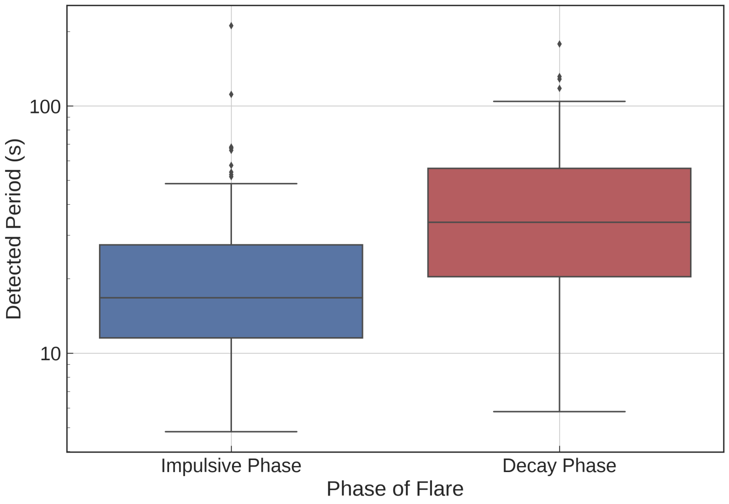

Figure 7.10: A box plot demonstrating the distributions of detected periods in the different phases of solar flares from a sample of all X- and M- class flares from solar cycle 24. The mean period for the QPPs detected in the impulsive phase is 23.7 s, whereas the mean period of the decay phase is 43.5 s.

flux peak and this new end time. An example of a flare from this sample with these defined phases is shown in Figure 7.9. The Fourier power spectrum of each phase of the flare is analyzed using AFINO. A box plot of the determined periods found from this analysis is shown in Figure 7.10. These preliminary results clearly demonstrate a longer period distribution in the decay phase in comparison to the impulsive phase.

Moreover, events in which a significant QPP signature was detected in both the original full flare analyzed, and independently in impulsive and decay phases were further investigated (∼10% of sample), and it is found that 86% of these events had a longer period in the decay phase that in the impulsive phase. These preliminary results provide evidence that decay phase QPPs have longer periods. Indeed, the fact that longer periods are detected in the decay phase of flares may also be suggestive as to why there is an apparent correlation between the duration of a flare and the detected QPP periods in Figure 7.8 (c). If it is the case that the period of QPPs evolve throughout flares then it would be expected that longer duration events would demonstrate longer periods.

The preliminary results outlined in this section open up a number of important questions that require further investigation:

- Is the low detection rate of C-class flares a symptom of the GOES measurements or is it in fact an inherent feature of flaring emission - that smaller flares are less likely to host QPPs?

- Does the correlation in Figure 7.8 (c) have a physical meaning? And if so do the longer duration flares also exhibit shorter periods during the impulsive phase and is the period detected by AFINO the evolved timescale later in the flare?

- It is clear now that there are different timescales in the different phases of solar flares. Is there an average growth rate of QPP periods from the impulsive and decay phases?

- Is there a relation between the flaring length scales, such as ribbon separation or soft X-ray source height increase, and the detected QPP periods?

- Are QPPs associated with both compact and two-ribbon flares? And is an eruption required for the appearance of decay phase QPPs?

These questions will be investigated in a more detailed statistical analysis using wavelet analysis and windowed AFINO techniques to search for evolving periods. To determine the physical conditions of the flaring site itself and to relate the

QPPs to the site properties such the length scales of the flaring loops, EUV imaging from AIA and soft X-ray source sizes will also be investigated. In particular, AIA 1700 Å and 1600 Å images can be used to estimate flaring ribbon properties (Toriumi *et al.*, 2017), which can be used as a proxy of the loop lengths for flares that occur on disk. A starting sample of flaring events to begin this investigation will be the 25 flares that showed significant signs of QPP signatures in all phases of the flare.

7.2.3 QPPs detected in the Terrestrial Ionosphere

The work outlined in Chapter 6 serves as the first reported detection of solar flaring QPPs in the Earth's ionosphere and provides a proof of concept that oscillatory flaring signatures have the potential to be detected in the terrestrial ionosphere. Future research expanding upon the first detection presented in this thesis will be extremely beneficial in furthering our understanding of the solar-terrestrial connection. A natural extension of this research is to search for more events with this type of behaviour.

A select number of further potential flaring pulsation candidates have been identified in the data available from the SID monitor in Birr. One such example is shown in Figure 7.11. The identified event is a compact M1.8 solar flare that occurred from NOAA AR 12497 on February 13 2016. The normalized lightcurves from the GOES channels (1–8 Å and 0.5–4 Å) are shown in Figure 7.11 (a). Three large amplitude pulsations can be identified with a period of ∼4 mins between each. The corresponding VLF amplitude measurements is shown in Figure 7.11 (b). The VLF measurements similarly demonstrate pulsating signatures, just much less pronounced. Vertical dashed lines are plotted at the peak times of the GOES 1–8 Å pulsations to aid with the visual comparison between the observed X-ray pulsations and the ionospheric response. A time delay can also be identified between the X-ray peaks and the ionospheric response, suchlike the pulsations discussed in Chapter 6. It is interesting to note that the ionospheric QPPs here are not as responsive as those observed in Chapter 6. The first large X-ray pulsation has a much greater amplitude that the two subsequent pulsations, yet the ionospheric pulsations do not show this to the same extent. This is most likely due to the fact that the ionosphere was strongly ionized by the first pulsation and did not have enough time to recombine back to pre-ionizing conditions before the second pulsation occurred, although further investigation is required. The detection of QPPs reported in Chapter 6 was from an event that has a period of ∼20 mins with reasonably large amplitude modulations. The flaring event shown in Figure 7.11 has a period of ∼4 min.

Building upon this, a number of important questions in regards to QPPs detection in the Earth's ionosphere require further investigations, for example:

- What is the shortest timescale QPP signature detectable in the ionosphere?
- What is the smallest detectable pulsation amplitude?
- Do the quasi-periodic density variations in the ionosphere constitute a periodic driver for other dynamic atmospheric phenomena such as atmospheric gravity waves?
- Can QPP be detected in the ionospheres of other planets such as Mars?

While the database of VLF measurements from Birr has proved extremely

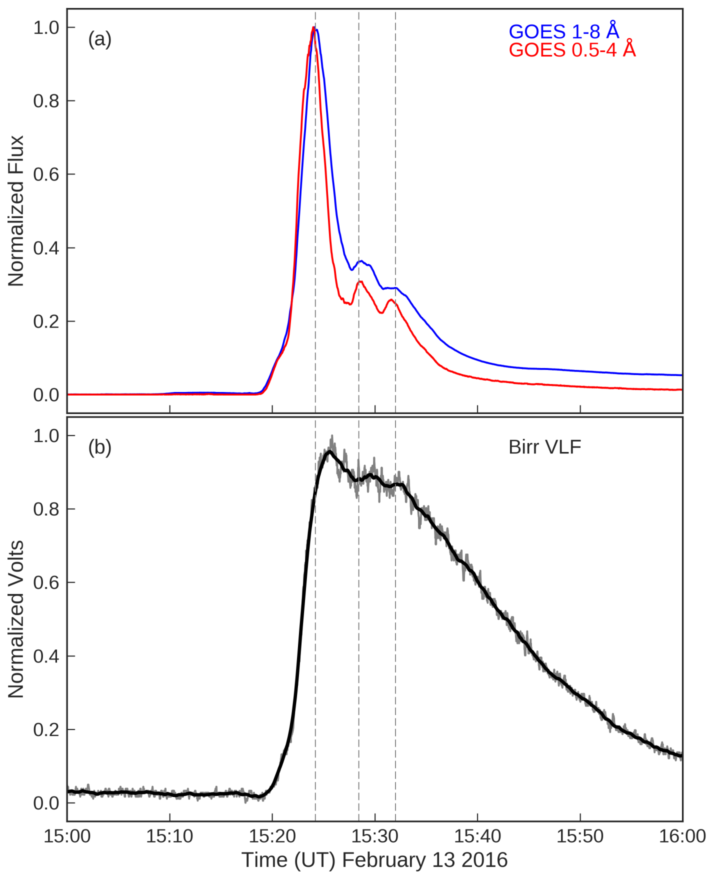

Figure 7.11: An example of a further detection of synchronized pulsations in solar flaring emission and the ionospheric response. (a) Normalized GOES X-ray channels, both 1–8 Å and 0.5–4 Å. The lightcurves clearly demonstrate 3 pulsations peaks with a period of ∼4 mins. (b) Normalized VLF amplitude measurements of both the raw data and the data smoothed with a 60 s window to reduce the noise and highlight the corresponding pulsations. The vertical dashed lines in both (a) and (b) mark the pulsation peak times of the X-ray pulsations in the 1–8 Å channel. A time delay, similar to Chapter 6, between the X-ray pulsations and the ionospheric VLF response can also be identified.

useful in this thesis, the database contains a limited number of flare detections. This limitation is due to the fact that flaring events can only be detected during daylight hours when the Sun is high in the sky, and hence many flaring events are missed, especially during the winter months. There are also extended periods of time for which the SID monitor was not taking measurements. In order to answer some of the important questions listed above and to further the investigation of synchronized flaring QPPs in the ionosphere, data from worldwide VLF receiving networks can be utilized. For example, both the South American VLF network (SAVNET, Raulin *et al.*, 2010) and the Global Ionospheric Flare Detection System (GIFDS, Wenzel *et al.*, 2016) networks provide large databases of VLF measurements, particularly over the last solar cycle, which can be used to perform a statistical study of QPP signatures in the Earths ionosphere, and indeed use the number of local maxima identified in QPP events to probe the effective recombination coefficient.

7.2.3.1 SuperSID installment

The SID monitor used for the work outlined in Chapter 6 was the original design of the Stanford University Solar Center SID monitor program. The low-cost instrument has the ability to monitor one particular frequency, and provides measurements of the ionospheric region over the Atlantic between its location in Birr, Ireland and the transmitter NAA in Maine, US. The Stanford SID program has continued in its effort to provide low-cost ionospheric measurement instruments and we have recently received one of their SuperSID monitors. The SuperSID monitor is a more powerful, upgraded VLF receiver and has the ability to record a spectrum of VLF frequencies, allowing several VLF stations to be monitored at once. A map of worldwide VLF transmitters is shown in Figure 7.12. The measurements from a number of different transmitters from both an eastern and western direction will provide longer daytime coverage for which flares can be detected. Indeed, the monitoring from a number of different transmitters will also

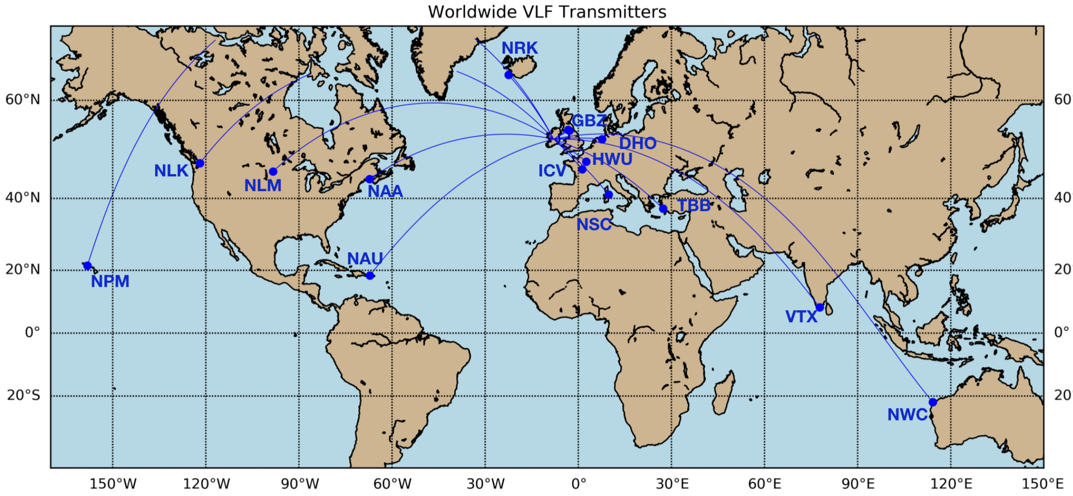

Figure 7.12: A Map of VLF transmitters located around the world. The station call-sign identifications are plotted together with the great circle distance from the transmitters to Ireland. We will primarily determine which transmitter stations provide the best signals and then use these frequencies to continuously monitor the ionospheric conditions.

allow us to probe different geographical regions of the ionosphere. Undergraduate students from Trinity are currently in the process of building an antenna receiving system and the receiver and the monitoring system will be located in Dunsink observatory, Dublin. The monitoring system located in Birr will continue to operate and we will then have two independent VLF measurements from which to analyze. This will prove useful for the detection of low amplitude QPPs as to rule out instrumental effects and to determine what signatures are real. Although we are now entering a time of solar minimum, we expect a number of small C-class flares to occur. The detection of small flares will also aid in a study of the detection limits of the VLF monitoring systems.

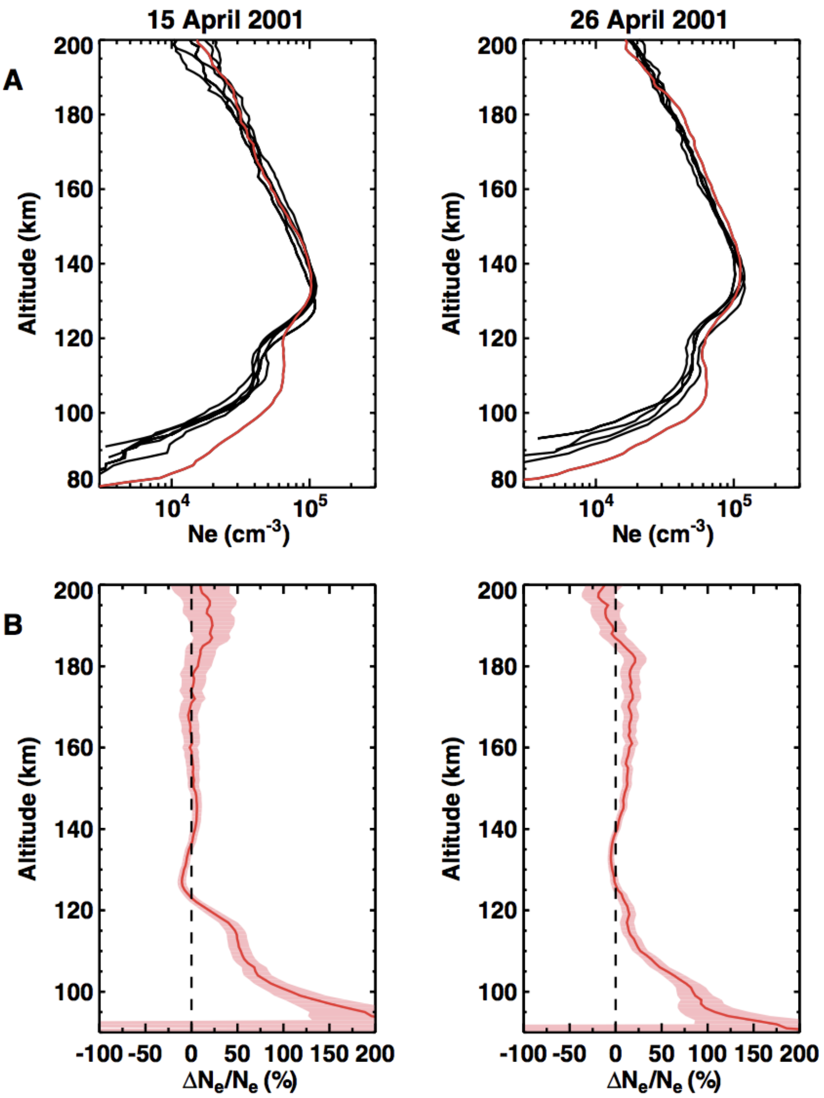

Figure 7.13: (a) Electron density altitude profiles of the Martian upper atmosphere for two days for which solar flares occurred, April 15, April 16 2001. The red lines demonstrate the enhancements in the profiles at low altitudes in response to solar flare effects. (b) Percentage difference between the flare affected profiles and the average profiles for each day. Notably, the electron density can increase up to 200% in the lower Martian ionosphere. Figure from Mendillo *et al.* (2006).

7.2.3.2 Ionospheric Effects on Other Planets

Similar to Earth, ionospheres of other planets are also significantly affected by the enhanced radiation during a solar flare. The Martian ionosphere has a very similar electron density profile to Earth (Witasse *et al.*, 2008), and observations of solar flare effects on the lower ionosphere of Mars have been reported in the literature. Radio sounding measurements from the Mars Global Surveyor (MGS) of the Martian atmosphere in response to two solar flares is shown in Figure 7.13. It is found that during two separate flaring events, a 200 % increase in the peak electron density at ~100 km can occur in response to the enhanced X-ray emission from a flare (Mendillo *et al.*, 2006). It is interesting to note that it is the lower Martian ionosphere that is affected the most, similar to the D-region on the Earth.

Furthermore, the Mars Atmosphere and Volatile EvolutioN (MAVEN) mission can perform *in-situ* measurements of the atmospheric conditions of Mars and has also observed enhancements in the electron density profile of the Martian lower ionosphere in response to solar flares. For example, the large solar flare discussed in Chapter 5 was observed by MAVEN, and it was found that the ionospheric conditions in the lower Martian ionosphere was significantly disturbed during this time (Thiemann *et al.*, 2018; Xu *et al.*, 2018). Given that the Martian lower ionosphere can be readily observed in response to the X-ray emission from solar flares, and now that we know QPP signatures can be detected in our own terrestrial ionosphere, it would be a very interesting scientific investigation to search for QPP signatures in the Martian ionospheric response. Data from MAVEN could provide the in-situ measurements required to perform such a study.

7.3 Concluding Remarks

The research in this thesis has examined the presence of QPPs in solar flares with a particular focus on the soft X-ray emissions and the terrestrial ionospheric response. The results of this research has improved our understanding of the nature and characteristics of soft X-ray QPPs, and has provided the first observational evidence of solar flaring QPPs in the response of the terrestrial ionosphere. In this Chapter we have detailed new promising avenues of investigations that build upon the results of this thesis. The rich data-set of observations presented in Section 7.2.1 will allow us to study the temporal, spectral, and spatial evolution of the observed QPPs from this flare, together with the observed eruption dynamics of the associated CME. The future study of this flare encompassing all aspects of the solar eruptive event will offer new perspectives into the QPP phenomena in solar flares. The preliminary results of the statistical analysis presented in Section 7.2.2 are particularly promising, and further research into these results is now required. Finally, there is much to do in regards to the solar-terrestrial relationship of QPPs in the future, and making use of the large available networks of VLF observations shall open new perspectives into the geophysical effects of solar flare QPPs and the coupled solar-terrestrial relationship.

The work in this thesis also looks towards the next generation of observational instruments on the horizon. For example, the capability to perform detailed multi-wavelength observations of accelerated electrons and their QPP signatures has been greatly improved now that the Expanded Owens Valley Solar Array (EOVSA) is fully operational (as of January 2017). EOVSA is the first solar interferometer array with the ability to produce high quality images over hundreds of frequencies in the broad spectral band (1-18 GHz). These observations will allow us to characterize all aspects of flare-accelerated QPP signatures, and provide the relevant constraints to QPP mechanisms. Future X-ray missions used in conjunction with EOVSA observations, such as the planned Spectrometer/Telescope for Imaging X-rays (STIX) (Krucker *et al.*, 2016) mission on-board Solar Orbiter and the proposed Focusing Optics X-ray Solar Imager (FOXSI) Small Explorer (Shih *et al.*, 2016) mission, will provide the next generation of QPP observations that will build upon the legacy of RHESSI and reshape our understanding of flaring dynamics and QPP processes.

A

Appendix

A.1 Estimation of Temperature and Emission Measure from GOES.

The two-channel measurements of GOES/XRS not only provide us with flux measurements, but the temperature and emission measure of the emitting flare plasma can also be readily estimated (Thomas *et al.*, 1985; White *et al.*, 2005).

This is achieved through the assumption that the emitting plasma has coronal abundances and is isothermal. Outlined here is the technique of Thomas *et al.* (1985), which developed expressions that give the effective color temperature, T, and corresponding emission measure, EM. The effective color temperature is defined here as the temperature of an isothermal plasma that would produce the observed ratio of responses in the two GOES/XRS detectors.

The incident flux $f(EM, T, \lambda)$ in each detector i will produce an output current in each detector given by A$_i$;

$$A_i = C_i \int_0^\infty G_i(\lambda) f(EM, T, \lambda) d\lambda \tag{A.1}$$

Here $G_i(\lambda)$ is the transfer function, and C_i is a detector dependent constant ($\sim$1) that represents the entrance collimator attenuation factor. The reported X-ray fluxes are derived by assuming that a wavelength-averaged response function $\bar{G}_i$ is appropriate for each detector. The reported X-ray values B_i are expressed as

$$B_i = A_i / (C_i \bar{G}_i) \tag{A.2}$$

If the emitting plasma is assumed to be isothermal the incident flux can be rewritten as

$$f(EM, T, \lambda) = EM \times f(T, \lambda) \tag{A.3}$$

The reported X-ray flux in each channel i can then be written as

$$B_i = EM \int_0^\infty G_i(\lambda) f(T, \lambda) d\lambda / \bar{G}_i = EM \times b_i, \tag{A.4}$$

here b_i is the temperature dependent part of the detectors response defined as

$$b_i(T) = \int_0^\infty G_i(\lambda) f(T, \lambda) d\lambda / \bar{G}_i \tag{A.5}$$

Thus the ratio of the two channels, $R(T)$, only depends on temperature. By letting the X-ray flux in the 0.5–4 Å channel be written as B_4 and the 1–8 Å channel as B_8, the ratio is given by

$$R(T) = \frac{B_4}{B_8} = \frac{b_4(T)}{b_8(T)} \tag{A.6}$$

Once the effective color temperature is found, the emission measure can be readily found by then inverting Equation A.4;

$$EM = B_i / b_i(T) \tag{A.7}$$

To find the scaling between R and T, and $B(T)$ and EM, the responses in the two channels to isothermal model spectra need to be calculated. Thomas *et al.* (1985) used model X-ray spectra of an isothermal plasma at various temperatures and folded this model through the GOES 1 response function. With this the flux ratio and the temperature dependent part of the XRS response were found as a function of temperature. From this, simple monotonic polynomial fits were determined to relate the ratio of flux to the temperature and emission measure. White *et al.* (2005) used coronal abundance estimates to determine the model spectra. The model spectra are convolved with the XRS response functions of the first 12 GOES satellites to find the scaling relationships. To estimate the temperature response of the GOES/XRS X-ray measurements, White *et al.* (2005) used spectral models calculated by CHIANTI for a range of temperatures of both coronal and photospheric abundances to determine the response of the GOES/XRS detectors as a function of temperature. These responses are then used to determine the temperature and emissions measure under isothermal assumption. The model of White *et al.* (2005) is now the standard used to calculate the temperature and emission measure and is integrated into the SolarSoft package.

A.2 Wavelet Analysis

Wavelet analysis is a popular tool used for the analysis of time-series when searching for characteristic variations and periodic signatures. A detailed description of the technique is outlined in Torrence & Compo (1998) (see also De Moortel & Hood (2000)). Unlike Fourier analysis which is inherently a global technique, wavelet analysis offers local information providing a 2D spectrum of both frequency and time. In this way, wavelet analysis offers a powerful tool to assess quasi-periodic signature which may vary in time.

The idea of wavelet analysis is to convolve a chosen wavelet function, $\psi(\eta)$, that depends on a time parameter η, with a time-series of interest. The wavelet function must be localized in time and frequency space and have mean of zero. The Morlet wavelet is a commonly used wavelet function in the study of oscillatory signals as its defined as a plane wave modulated with a Gaussian described by

$$\psi_0(\eta) = \pi^{-1/4} \exp(i\omega_0\eta) \exp(-\frac{\eta^2}{2}) \tag{A.8}$$

Here, ω_0 is the non-dimensional associated frequency. The wavelet transform of an equally spaced time-series, x_n, is then expressed as the convolution of a scaled and translated wavelet function $\psi(\eta)$ with x_n,

$$W_n(s) = \sum_{n'=0}^{N-1} x_{n'} \psi * \left[\frac{(n' - n)\delta t}{s} \right], \tag{A.9}$$

where $\psi*$ represents the complex conjugate of the wavelet function, and s is the wavelet scale. To then perform wavelet analysis, the scale s is varied and translated along the localized time index n to produce an array of complex wavelet transforms. The wavelet power spectrum is then determined by $|W_n(s)|^2$ which informs us on the amount of power that is present at a certain scale s, and hence provides information on the dominant timescale present in the time series.

To determine the significance of wavelet power, an appropriate background model must be chosen. For the analysis outlined in this thesis, the significance was tested using a red-noise (power-law) background model, estimated by an auto-regressive process (Gilman *et al.*, 1963; Torrence & Compo, 1998). This simple model is expressed as

$$x_n = \alpha x_{n-1} + z_n, \tag{A.10}$$

where α represents the lag-1 auto-correlation, $x_0 = 0$, and z_n represents white noise.

A.3 Automated Flare Inference of Oscillations (AFINO)

The Automated Flare Inference of Oscillations (AFINO) (Inglis *et al.*, 2015, 2016) method is designed to take into account the power-law shape in the Fourier domain of flaring lightcurves when searching for global QPP signatures. The main idea behind AFINO is to perform a model comparison test on the Fourier power spectrum of a flaring timeseries to determine whether there is evidence for a discrete enhancement in the Fourier power that would be consistent with a QPP signature. AFINO is outlined in detail in Inglis *et al.* (2015, 2016), and the main features are discussed here.

The advantage of AFINO is that it avoids detrending the data and the analysis can be performed on the raw lightcurves. The initial step of AFINO is to normalize the input data (lightcurve timeseries, F) by the mean

$$F_{norm} = \frac{F - \bar{F}}{\bar{F}}, \tag{A.11}$$

where $\bar{F}$ is the mean of the signal. A windowing function is then applied to the normalized data to account for the effects of the finite duration timeseries, and the Fourier power spectrum is found.

The next main step of AFINO is then to perform a model comparison on the Fourier power spectrum of the input flare data. AFINO tests three functional forms of the Fourier power spectrum, including a power-law model, a broken power law model, and a power law model with an additional Gaussian bump located at a particular frequency. The latter model is designed to represent a localized enhancement in Fourier power - i.e. a QPP model. These power-law models are chosen based on the observation that power-law Fourier power spectra are a common property of both solar flares (Gruber *et al.*, 2011; Inglis *et al.*, 2015; McAteer *et al.*, 2007) and other solar phenomena (e.g. Ireland *et al.*, 2014; Threlfall *et al.*, 2017). The inclusion of a broken power law is motivated by the idea that a single power law may be too restrictive. Formally these models can be written, respectively, as

$$M_0(f) = A_0 f^{-\alpha_0} + C_0 \tag{A.12}$$

$$M_1(f) = A_1 f^{-\alpha_1} + B\mathrm{exp}\left(\frac{-(lnf - lnf_p)^2}{2\sigma^2}\right) + C_1 \tag{A.13}$$

$$M_2(f) = \begin{cases} A_2 f^{-\alpha_b} + C_2 & \mathrm{if} f < f_{break} \\ A_2 f^{-\alpha_b - \alpha_a} f^{-\alpha_a} + C_2 & \mathrm{if} f > f_{break} \end{cases} \tag{A.14}$$

In each model M_i, f is frequency, α_i is the power law exponent, constants A_i are the slopes of the respective power-laws and constants C_i are to account for the transition from the power-law shape to constant white noise. Model M_1 is equivalent to M_0, but includes a Gaussian bump at a frequency f_p with a width σ, intended to account for excess power in a localized frequency range.

These models are then fit to the Fourier power spectrum of the input data. To determine the best fit to each model, the maximum likelihood L of each model with respect to the data is calculated. The maximum likelihood can be written as (Inglis *et al.*, 2016; Vaughan, 2005, 2010),

$$L = \prod_{j=1}^{N/2} \frac{1}{m_j} \exp\left(-\frac{i_j}{s_j}\right), \tag{A.15}$$

where $I = (i_1, ..., i_{N/2})$ represents the Fourier power at a frequency f_j for a time series of length N. $M = m_1, ..., m_{N/2}$ represents the model of the Fourier power spectra. To then compare which model is most representative of the data, a comparison between the model fits is performed by using the Bayesian Information Criterion (BIC). This criterion is given by

$$BIC = -2\ln(L) + k\ln(n), \tag{A.16}$$

where L is the maximum likelihood, k is the number of free parameters in the model and $n = N/2$, the number of data points in the Fourier power spectrum. BIC is used here given that it penalizes for adding complexity to the model - i.e. more free parameters, and hence determines if adding the complexity to model M_1, the QPP model, is justified. By comparing the BIC values of two models, the extent to which a model is preferred over another can be sought. To perform the comparison, the ΔBIC $= BIC_j - BIC_1$, for $j = 0, 2$ is calculated. Since lower values of BIC are preferred, a positive value for ΔBIC implies the QPP model, M_1 best represents the Fourier power spectra and hence evidence of QPP signatures in the flaring time series is found. In general, a ΔBIC value > 10 is considered strong evidence in favor of one model over another (Burnham & Anderson, 2004).

A.4 Supplementary plot for Chapter 5

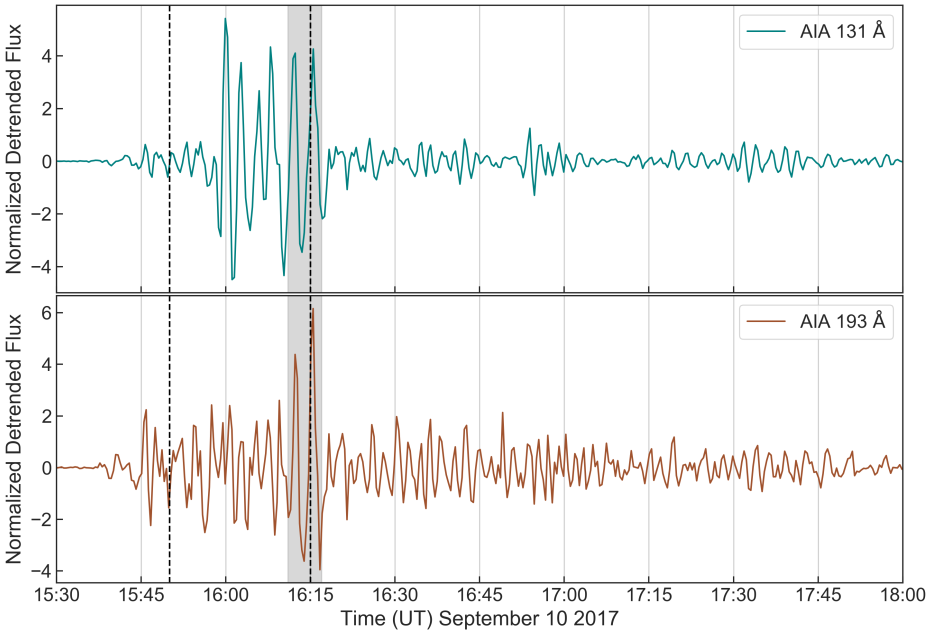

Figure A.1: Detrended AIA 131 Å and 193 Å lightcurves. The top panel shows the same as Figure 5.3 (h), and the bottom panel shows the detrended lightcurve of AIA 193 Å channel. The vertical dashed lines denote the impulsive phase as in Figure 5.3. The grey shaded region highlight the extra two pulsations that are observed in both EUV channels but not in GOES or ESP. They are shown to demonstrate that these pulsations are real as they are observed in both channels.

References

AKMAEV, R., NEWMAN, A., CODRESCU, M., SCHULZ, C. & NERNEY, E. (2010). D-rap model validation: I. scientific report. (Cited on page 168.)

ALFVÉN, H. (1942). Existence of electromagnetic-hydrodynamic waves. *Nature*, **150**, 405. (Cited on page 45.)

ANFINOGENTOV, S., NAKARIAKOV, V., MATHIOUDAKIS, M., VAN DOORSSELAERE, T. & KOWALSKI, A. (2013). The decaying long-period oscillation of a stellar megaflare. *The Astrophysical Journal*, **773**, 156. (Cited on pages xv, 23 and 25.)

ANFINOGENTOV, S., NAKARIAKOV, V. & NISTICÒ, G. (2015). Decayless low-amplitude kink oscillations: a common phenomenon in the solar corona? *Astronomy & Astrophysics*, **583**, A136. (Cited on page 54.)

APPLETON, E.V. (1953). A note on the" sluggishness" of the ionosphere. *Journal of Atmospheric and Terrestrial Physics*, **3**, 282–284. (Cited on pages 165, 166, 173 and 174.)

APPLETON, E.V. & BARNETT, M. (1925). Local reflection of wireless waves from the upper atmosphere. *Nature*, **115**, 333. (Cited on page 29.)

ASAI, A., SHIMOJO, M., ISOBE, H., MORIMOTO, T., YOKOYAMA, T., SHIBASAKI, K. & NAKAJIMA, H. (2001). Periodic Acceleration of Electrons in the 1998 November 10 Solar Flare. *Astrophysical Journal Letters*, **562**, L103–L106. (Cited on page 24.)

REFERENCES

Aschwanden, M. (2006). *Physics of the solar corona: an introduction with problems and solutions*. Springer Science & Business Media. (Cited on pages xiv, 9, 20, 58 and 154.)

Aschwanden, M.J. & Schrijver, C.J. (2011). Coronal loop oscillations observed with atmospheric imaging assembly—kink mode with cross-sectional and density oscillations. *The Astrophysical Journal*, **736**, 102. (Cited on pages 60 and 153.)

Aschwanden, M.J., Fletcher, L., Schrijver, C.J. & Alexander, D. (1999a). Coronal loop oscillations observed with the transition region and coronal explorer. *The Astrophysical Journal*, **520**, 880. (Cited on page 54.)

Aschwanden, M.J., Newmark, J.S., Delaboudinière, J.P., Neupert, W.M., Klimchuk, J., Gary, G.A., Portier-Fozzani, F. & Zucker, A. (1999b). Three-dimensional stereoscopic analysis of solar active region loops. i. soho/eit observations at temperatures of (1.0-.5) 106 k. *The Astrophysical Journal*, **515**, 842. (Cited on page 124.)

Babcock, H. (1961). The topology of the sun's magnetic field and the 22-year cycle. *The Astrophysical Journal*, **133**, 572. (Cited on page 11.)

Barr, R., Jones, D.L. & Rodger, C. (2000). Elf and vlf radio waves. *Journal of Atmospheric and Solar-Terrestrial Physics*, **62**, 1689–1718. (Cited on page 99.)

Basak, T. & Chakrabarti, S.K. (2013). Effective recombination coefficient and solar zenith angle effects on low-latitude d-region ionosphere evaluated from vlf signal amplitude and its time delay during x-ray solar flares. *Astrophysics and Space Science*, **348**, 315–326. (Cited on pages 159, 166, 173 and 175.)

Benz, A.O. (2017). Flare observations. *Living Reviews in Solar Physics*, **14**, 2. (Cited on page 16.)

Biskamp, D. (1986). Magnetic reconnection via current sheets. *The Physics of fluids*, **29**, 1520–1531. (Cited on page 58.)

BROSIUS, J.W. & DAW, A.N. (2015). Quasi-periodic Fluctuations and Chromospheric Evaporation in a Solar Flare Ribbon Observed by IRIS. *Astrophysical Journal*, **810**, 45. (Cited on page 25.)

BROWN, J.C. (1971). The deduction of energy spectra of non-thermal electrons in flares from the observed dynamic spectra of hard x-ray bursts. *Solar Physics*, **18**, 489–502. (Cited on page 14.)

BUDDEN, K.G. (1961). *The wave-guide mode theory of wave propagation*. Logos Press. (Cited on page 73.)

BUDDEN, K.G. (1988). *The propagation of radio waves: the theory of radio waves of low power in the ionosphere and magnetosphere*. Cambridge University Press. (Cited on page 165.)

BURNHAM, K.P. & ANDERSON, D.R. (2004). Multimodel inference: understanding aic and bic in model selection. *Sociological methods & research*, **33**, 261–304. (Cited on page 222.)

CARGILL, P.J., MARISKA, J.T. & ANTIOCHOS, S.K. (1995). Cooling of solar flares plasmas. 1: Theoretical considerations. *The Astrophysical Journal*, **439**, 1034–1043. (Cited on pages 21 and 122.)

CARMICHAEL, H. (1964). A Process for Flares. *NASA Special Publication*, **50**, 451. (Cited on page 14.)

CARRINGTON, R.C. (1859). Description of a singular appearance seen in the sun on september 1, 1859. *Monthly Notices of the Royal Astronomical Society*, **20**, 13–15. (Cited on page 2.)

CHARBONNEAU, P. (2010). Dynamo models of the solar cycle. *Living Reviews in Solar Physics*, **7**, 3. (Cited on page 11.)

CHEN, B., BASTIAN, T.S., SHEN, C., GARY, D.E., KRUCKER, S. & GLESENER, L. (2015). Particle acceleration by a solar flare termination shock. *Science*, **350**, 1238–1242. (Cited on page 150.)

Chen, P. & Priest, E. (2006). Transition-region explosive events: reconnection modulated by p-mode waves. *Solar Physics*, **238**, 313–327. (Cited on pages 64 and 66.)

Cheng, X., Li, Y., Wan, L., Ding, M., Chen, P., Zhang, J. & Liu, J. (2018). Observations of turbulent magnetic reconnection within a solar current sheet. *The Astrophysical Journal*, **866**, 64. (Cited on page 131.)

Chiu, Y. (1970). Theory of solar radio pulsation. *Solar Physics*, **13**, 420–443. (Cited on page 24.)

Cho, I.H., Cho, K.S., Nakariakov, V., Kim, S. & Kumar, P. (2016). Comparison of damped oscillations in solar and stellar x-ray flares. *The Astrophysical Journal*, **830**, 110. (Cited on pages 23 and 177.)

Clilverd, M.A., Thomson, N.R. & Rodger, C.J. (1999). Sunrise effects on vlf signals propagating over a long north-south path. *Radio Science*, **34**, 939–948. (Cited on page 100.)

Clilverd, M.A., Rodger, C.J., Thomson, N.R., Brundell, J.B., Ulich, T., Lichtenberger, J., Cobbett, N., Collier, A.B., Menk, F.W., Seppälä, A. *et al.* (2009). Remote sensing space weather events: Antarctic-arctic radiation-belt (dynamic) deposition-vlf atmospheric research konsortium network. *Space Weather*, **7**, 1–15. (Cited on pages xvii, 74 and 100.)

Cliver, E.W. & Dietrich, W.F. (2013). The 1859 space weather event revisited: limits of extreme activity. *Journal of Space Weather and Space Climate*, **3**, A31. (Cited on page 13.)

Craig, I.J.D. & McClymont, A.N. (1991). Dynamic magnetic reconnection at an X-type neutral point. *Astrophysical Journal Letters*, **371**, L41–L44. (Cited on page 67.)

Culhane, J., Vesecky, J. & Phillips, K. (1970). The cooling of flare produced plasmas in the solar corona. *Solar Physics*, **15**, 394–413. (Cited on page 21.)

Cummer, S.A. (2000). Modeling electromagnetic propagation in the earth-ionosphere waveguide. *IEEE Transactions on Antennas and Propagation*, **48**, 1420–1429. (Cited on page 73.)

Davies, K. (1990). *Ionospheric radio*. 31, IET. (Cited on pages 29, 32, 33, 72, 73, 159 and 166.)

De Moortel, I. & Browning, P. (2015). Recent advances in coronal heating. *Philosophical Transactions of the Royal Society of London Series A*, **373**, 20140269–20140269. (Cited on page 7.)

De Moortel, I. & Hood, A. (2000). Wavelet analysis and the determination of coronal plasma properties. *Astronomy and Astrophysics*, **363**, 269–278. (Cited on page 218.)

De Moortel, I. & Nakariakov, V.M. (2012). Magnetohydrodynamic waves and coronal seismology: an overview of recent results. *Philosophical Transactions of the Royal Society of London Series A*, **370**, 3193–3216. (Cited on pages 26 and 46.)

Dennis, B.R. & Tolbert, K. (2016). Rhessi nugget 262 fine structure in flare soft x-ray light curves. (Cited on page 107.)

Dennis, B.R. & Zarro, D.M. (1993). The neupert effect: what can it tell us about the impulsive and gradual phases of solar flares? *Solar Physics*, **146**, 177–190. (Cited on pages xiv, 19 and 21.)

Dennis, B.R., Tolbert, A.K., Inglis, A., Ireland, J., Wang, T., Holman, G.D., Hayes, L.A. & Gallagher, P.T. (2017). Detection and interpretation of long-lived x-ray quasi-periodic pulsations in the x class solar flare on 2013 may 14. *The Astrophysical Journal*, **836**, 84. (Cited on pages 26, 123, 138, 183 and 201.)

Didkovsky, L., Judge, D., Wieman, S., Woods, T. & Jones, A. (2009). Euv spectrophotometer (esp) in extreme ultraviolet variability experiment (eve): algorithms and calibrations. In *The Solar Dynamics Observatory*, 179–205, Springer. (Cited on page 96.)

Dikpati, M. & Gilman, P.A. (2009). Flux-transport solar dynamos. *Space science reviews*, **144**, 67–75. (Cited on pages xiv, 11 and 12.)

Dolla, L., Marqué, C., Seaton, D., Van Doorsselaere, T., Dominique, M., Berghmans, D., Cabanas, C., De Groof, A., Schmutz, W., Verdini, A. *et al.* (2012). Time delays in quasi-periodic pulsations observed during the x2. 2 solar flare on 2011 february 15. *The Astrophysical Journal Letters*, **749**, L16. (Cited on pages xv, 25, 27, 106 and 107.)

Dominique, M., Hochedez, J.F., Schmutz, W., Dammasch, I., Shapiro, A., Kretzschmar, M., Zhukov, A., Gillotay, D., Stockman, Y. & BenMoussa, A. (2013). The lyra instrument onboard proba2: description and in-flight performance. *Solar Physics*, **286**, 21–42. (Cited on page 90.)

Doyle, J.G., Shetye, J., Antonova, A.E., Kolotkov, D.Y., Srivastava, A.K., Stangalini, M., Gupta, G.R., Avramova, A. & Mathioudakis, M. (2018). Stellar flare oscillations: evidence for oscillatory reconnection and evolution of MHD modes. *Monthly Notices of the Royal Astronomical Society*, **475**, 2842–2851. (Cited on page 23.)

Drake, J., Swisdak, M., Che, H. & Shay, M. (2006a). Electron acceleration from contracting magnetic islands during reconnection. *Nature*, **443**, 553. (Cited on pages 123 and 150.)

Drake, J., Swisdak, M., Schoeffler, K., Rogers, B. & Kobayashi, S. (2006b). Formation of secondary islands during magnetic reconnection. *Geophysical research letters*, **33**. (Cited on pages 70 and 71.)

Dulk, G.A. (1985). Radio emission from the sun and stars. *Annual review of astronomy and astrophysics*, **23**, 169–224. (Cited on pages xxiv, 60, 61, 189 and 190.)

Edwin, P. & Roberts, B. (1983). Wave propagation in a magnetic cylinder. *Solar Physics*, **88**, 179–191. (Cited on pages xvi, 49, 50 and 52.)

Emslie, A., Kucharek, H., Dennis, B., Gopalswamy, N., Holman, G., Share, G., Vourlidas, A., Forbes, T., Gallagher, P., Mason, G. *et al.* (2004). Energy partition in two solar flare/cme events. *Journal of Geophysical Research: Space Physics*, **109**. (Cited on page 13.)

Emslie, A., Dennis, B., Shih, A., Chamberlin, P., Mewaldt, R., Moore, C., Share, G., Vourlidas, A. & Welsch, B. (2012). Global energetics of thirty-eight large solar eruptive events. *The Astrophysical Journal*, **759**, 71. (Cited on page 13.)

FAN, Y. (2009). The emergence of a twisted flux tube into the solar atmosphere: sunspot rotations and the formation of a coronal flux rope. *The Astrophysical Journal*, **697**, 1529. (Cited on page 11.)

FERGUSON, J. (1998). Computer programs for assessment of long-wavelength radio communications, version 2.0: User's guide and source files. Tech. rep., SPACE AND NAVAL WARFARE SYSTEMS CENTER SAN DIEGO CA. (Cited on pages 74, 75, 76 and 169.)

FERGUSON, J. & SNYDER, F. (1980). Approximate vlf/lf waveguide mode conversion model. computer applications: Fastmc and bump. Tech. rep., NAVAL OCEAN SYSTEMS CENTER SAN DIEGO CA. (Cited on page 75.)

FINN, J.M. & KAW, P. (1977). Coalescence instability of magnetic islands. *The Physics of Fluids*, **20**, 72–78. (Cited on page 70.)

FLEISHMAN, G.D., BASTIAN, T. & GARY, D.E. (2008). Broadband quasi-periodic radio and x-ray pulsations in a solar flare. *The Astrophysical Journal*, **684**, 1433. (Cited on pages 24 and 105.)

FLETCHER, L., DENNIS, B.R., HUDSON, H.S., KRUCKER, S., PHILLIPS, K., VERONIG, A., BATTAGLIA, M., BONE, L., CASPI, A., CHEN, Q. *et al.* (2011). An observational overview of solar flares. *Space science reviews*, **159**, 19. (Cited on pages 13, 16 and 22.)

FOULLON, C., VERWICHTE, E., NAKARIAKOV, V. & FLETCHER, L. (2005). X-ray quasi-periodic pulsations in solar flares as magnetohydrodynamic oscillations. *Astronomy & Astrophysics*, **440**, L59–L62. (Cited on pages 63 and 160.)

FOULLON, C., FLETCHER, L., HANNAH, I.G., VERWICHTE, E., CECCONI, B., NAKARIAKOV, V., PHILLIPS, K. & TAN, B. (2010). From large-scale loops to the sites of dense flaring loops: preferential conditions for long-period pulsations in solar flares. *The Astrophysical Journal*, **719**, 151. (Cited on pages 23 and 160.)

FRIEDRICH, M. & TORKAR, K. (1998). Empirical d-region modelling, a progress report. *Advances in space research*, **22**, 757–766. (Cited on page 77.)

REFERENCES

Furth, H.P., Killeen, J. & Rosenbluth, M.N. (1963). Finite-Resistivity Instabilities of a Sheet Pinch. *Physics of Fluids*, **6**, 459–484. (Cited on page 69.)

Galejs, J. (1972). Stable solutions of ionospheric fields in the propagation of elf and vlf waves. *Radio Science*, **7**, 549–561. (Cited on page 73.)

Gallagher, P.T., Dennis, B.R., Krucker, S., Schwartz, R.A. & Tolbert, A.K. (2002). Rhessi and trace observations of the 21 april 2002 x1. 5 flare. *Solar Physics*, **210**, 341–356. (Cited on pages 21, 141 and 143.)

Gary, D.E., Chen, B., Dennis, B.R., Fleishman, G.D., Hurford, G.J., Krucker, S., McTiernan, J.M., Nita, G.M., Shih, A.Y., White, S.M. *et al.* (2018). Microwave and hard x-ray observations of the 2017 september 10 solar limb flare. *The Astrophysical Journal*, **863**, 83. (Cited on page 131.)

Gary, G.A. (2001). Plasma beta above a solar active region: Rethinking the paradigm. *Solar Physics*, **203**, 71–86. (Cited on pages xv and 43.)

Gilman, D.L., Fuglister, F.J. & Mitchell Jr, J.M. (1963). On the power spectrum of 'red noise'. *Journal of the Atmospheric Sciences*, **20**, 182–184. (Cited on page 219.)

Gledhill, J. (1986). The effective recombination coefficient of electrons in the ionosphere between 50 and 150 km. *Radio Science*, **21**, 399–408. (Cited on page 175.)

Glesener, L., Krucker, S., Christe, S., Ishikawa, S.n., Buitrago-Casas, J.C., Ramsey, B., Gubarev, M., Takahashi, T., Watanabe, S., Takeda, S. *et al.* (2016). The foxsi solar sounding rocket campaigns. In *Space Telescopes and Instrumentation 2016: Ultraviolet to Gamma Ray*, vol. 9905, 99050E, International Society for Optics and Photonics. (Cited on page 81.)

Gopalswamy, N., Yashiro, S., Mäkelä, P., Xie, H., Akiyama, S. & Monstein, C. (2018). Extreme kinematics of the 2017 september 10 solar eruption and the spectral characteristics of the associated energetic particles. *The Astrophysical Journal Letters*, **863**, L39. (Cited on pages 130 and 143.)

Gruber, D., Lachowicz, P., Bissaldi, E., Briggs, M., Connaughton, V., Greiner, J., van der Horst, A., Kanbach, G., Rau, A., Bhat, P. *et al.* (2011). Quasi-periodic pulsations in solar flares: new clues from the fermi gamma-ray burst monitor. *Astronomy & Astrophysics*, **533**, A61. (Cited on pages 113, 136 and 221.)

Grubor, D., Šulić, D. & Žigman, V. (2005). Influence of solar x-ray flares on the earth-ionosphere waveguide. *Serbian Astronomical Journal*, 29–35. (Cited on pages 159, 163 and 172.)

Grubor, D., Šulić, D. & Žigman, V. (2008). Classification of x-ray solar flares regarding their effects on the lower ionosphere electron density profile. In *Annales Geophysicae*, vol. 26, 1731–1740, Copernicus GmbH. (Cited on pages 30 and 35.)

Guidoni, S., DeVore, C., Karpen, J. & Lynch, B. (2016). Magnetic-island contraction and particle acceleration in simulated eruptive solar flares. *The Astrophysical Journal*, **820**, 60. (Cited on pages 71, 123 and 150.)

Hansen, P. (1994). Vlf cutler hollow core cable repair/replacement. Tech. rep., NAVAL COMMAND CONTROL AND OCEAN SURVEILLANCE CENTER RDT AND E DIV SAN DIEGO CA. (Cited on pages xviii, 100 and 101.)

Hanser, F.A. & Sellers, F.B. (1996). Design and calibration of the goes-8 solar x-ray sensor: the xrs. In *GOES-8 and Beyond*, vol. 2812, 344–353, International Society for Optics and Photonics. (Cited on page 88.)

Hargreaves, J.K. (1992). *The solar-terrestrial environment: an introduction to geospace-the science of the terrestrial upper atmosphere, ionosphere, and magnetosphere*. Cambridge University Press. (Cited on pages 30 and 31.)

Harrison, F.A., Craig, W.W., Christensen, F.E., Hailey, C.J., Zhang, W.W., Boggs, S.E., Stern, D., Cook, W.R., Forster, K., Giommi, P. *et al.* (2013). The nuclear spectroscopic telescope array (nustar) high-energy x-ray mission. *The Astrophysical Journal*, **770**, 103. (Cited on page 81.)

REFERENCES

Harrison, R. (1987). Solar soft x-ray pulsations. *Astronomy and Astrophysics*, **182**, 337–347. (Cited on page 160.)

Hayakawa, H., Tamazawa, H., Uchiyama, Y., Ebihara, Y., Miyahara, H., Kosaka, S., Iwahashi, K. & Isobe, H. (2017). Historical auroras in the 990s: Evidence of great magnetic storms. *Solar Physics*, **292**, 12. (Cited on page 2.)

Hayes, L.A., Gallagher, P.T., Dennis, B.R., Ireland, J., Inglis, A.R. & Ryan, D.F. (2016). Quasi-periodic pulsations during the impulsive and decay phases of an x-class flare. *The Astrophysical Journal Letters*, **827**, L30. (Cited on pages 37, 104, 138 and 181.)

Hayes, L.A., Gallagher, P.T., McCauley, J., Dennis, B.R., Ireland, J. & Inglis, A. (2017). Pulsations in the earth's lower ionosphere synchronized with solar flare emission. *Journal of Geophysical Research: Space Physics*, **122**, 9841–9847. (Cited on pages 38, 158 and 184.)

Hayes, L.A., Gallagher, P.T., Dennis, B.R., Ireland, J., Inglis, A. & Morosan, D. (2019). Persistent quasi-periodic pulsations during a large x-class solar flare. *in review Astrophysical Journal*. (Cited on pages 38, 128 and 182.)

Hirayama, T. (1974). Theoretical Model of Flares and Prominences. I: Evaporating Flare Model. *Solar Physics*, **34**, 323–338. (Cited on page 14.)

Hochedez, J.F., Schmutz, W., Stockman, Y., Schühle, U., Benmoussa, A., Koller, S., Haenen, K., Berghmans, D., Defise, J.M., Halain, J.P. *et al.* (2006). Lyra, a solar uv radiometer on proba2. *Advances in Space Research*, **37**, 303–312. (Cited on page 90.)

Hodgson, R. (1859). On a curious appearance seen in the sun. *Monthly Notices of the Royal Astronomical Society*, **20**, 15–16. (Cited on page 2.)

Högbom, J. (1974). Aperture synthesis with a non-regular distribution of interferometer baselines. *Astronomy and Astrophysics Supplement Series*, **15**, 417. (Cited on page 84.)

Hurford, G.c., Schmahl, E., Schwartz, R., Conway, A., Aschwanden, M., Csillaghy, A., Dennis, B., Johns-Krull, C., Krucker, S., Lin, R. *et al.* (2002). The rhessi imaging concept. In *The Reuven Ramaty High-Energy Solar Spectroscopic Imager (RHESSI)*, 61–86, Springer. (Cited on pages xvii, 81, 82, 84, 118 and 141.)

Inan, U.S., Lehtinen, N.G., Lev-Tov, S., Johnson, M., Bell, T. & Hurley, K. (1999). Ionization of the lower ionosphere by -rays from a magnetar: Detection of a low energy (3–10 kev) component. *Geophysical Research Letters*, **26**, 3357–3360. (Cited on page 35.)

Inglis, A. & Dennis, B. (2012). The relationship between hard x-ray pulse timings and the locations of footpoint sources during solar flares. *The Astrophysical Journal*, **748**, 139. (Cited on pages 66 and 105.)

Inglis, A., Van Doorsselaere, T., Brady, C. & Nakariakov, V. (2009). Characteristics of magnetoacoustic sausage modes. *Astronomy & Astrophysics*, **503**, 569–575. (Cited on page 59.)

Inglis, A., Zimovets, I., Dennis, B., Kontar, E., Nakariakov, V., Struminsky, A. & Tolbert, A. (2011). Instrumental oscillations in rhessi count rates during solar flares. *Astronomy & Astrophysics*, **530**, A47. (Cited on page 86.)

Inglis, A., Ireland, J. & Dominique, M. (2015). Quasi-periodic pulsations in solar and stellar flares: re-evaluating their nature in the context of power-law flare fourier spectra. *The Astrophysical Journal*, **798**, 108. (Cited on pages 113, 136, 220 and 221.)

Inglis, A., Ireland, J., Dennis, B., Hayes, L. & Gallagher, P. (2016). A large-scale search for evidence of quasi-periodic pulsations in solar flares. *The Astrophysical Journal*, **833**, 284. (Cited on pages 136, 196, 197, 198, 200, 220 and 222.)

Inglis, A.R. & Nakariakov, V.M. (2009). A multi-periodic oscillatory event in a solar flare. *Astronomy & Astrophysics*, **493**, 259–266. (Cited on page 26.)

Inglis, A.R., Nakariakov, V.M. & Melnikov, V.F. (2008). Multi-wavelength spatially resolved analysis of quasi-periodic pulsations in a solar flare. *Astronomy & Astrophysics*, **487**, 1147–1153. (Cited on page 24.)

REFERENCES

Ireland, J., McAteer, R.J. & Inglis, A.R. (2014). Coronal fourier power spectra: Implications for coronal seismology and coronal heating. *The Astrophysical Journal*, **798**, 1. (Cited on page 221.)

Janvier, M. (2017). Three-dimensional magnetic reconnection and its application to solar flares. *Journal of Plasma Physics*, **83**, 535830101. (Cited on page 58.)

Jelínek, P., Karlickỳ, M., Van Doorsselaere, T. & Bárta, M. (2017). Oscillations excited by plasmoids formed during magnetic reconnection in a vertical gravitationally stratified current sheet. *The Astrophysical Journal*, **847**, 98. (Cited on page 151.)

Kane, S.R., Kai, K., Kosugi, T., Enome, S., Landecker, P.B. & McKenzie, D.L. (1983). Acceleration and confinement of energetic particles in the 1980 June 7 solar flare. *Astrophysical Journal*, **271**, 376–387. (Cited on pages xv, 23 and 24.)

Kar, J., Mahajan, K., Srilakshmi, M. & Kohli, R. (1986). Possible effects of solar flares on the ionosphere of venus from pioneer venus orbiter measurements. *Journal of Geophysical Research: Space Physics*, **91**, 8986–8992. (Cited on page 177.)

Kaufmann, P., Kuntz, V., Leme, N.P., Piazza, L., Boas, J.V., Brecher, K. & Crouchley, J. (1989). Effects of the large june 1975 meteoroid storm on earth's ionosphere. *Science*, **246**, 787–790. (Cited on page 35.)

Kliem, B., Karlicky, M. & Benz, A.O. (2000). Solar flare radio pulsations as a signature of dynamic magnetic reconnection. *arXiv preprint astro-ph/0006324*. (Cited on pages 58, 70 and 150.)

Klimchuk, J.A. (2006). On solving the coronal heating problem. *Solar Physics*, **234**, 41–77. (Cited on page 7.)

Kolarski, A., Grubor, D. & Šulić, D. (2011). Diagnostics of the solar x-flare impact on lower ionosphere through the vlf-naa signal recordings. *Open Astronomy*, **20**, 591–595. (Cited on page 100.)

Kolotkov, D.Y., Nakariakov, V.M., Kupriyanova, E.G., Ratcliffe, H. & Shibasaki, K. (2015). Multi-mode quasi-periodic pulsations in a solar flare. *Astronomy & Astrophysics*, **574**, A53. (Cited on page 26.)

Kolotkov, D.Y., Pugh, C.E., Broomhall, A.M. & Nakariakov, V.M. (2018). Quasi-periodic pulsations in the most powerful solar flare of cycle 24. *The Astrophysical Journal Letters*, **858**, L3. (Cited on page 202.)

Kontar, E.P., Jeffrey, N.L., Emslie, A.G. & Bian, N. (2015). Collisional relaxation of electrons in a warm plasma and accelerated nonthermal electron spectra in solar flares. *The Astrophysical Journal*, **809**, 35. (Cited on page 112.)

Kopp, R.A. & Pneuman, G.W. (1976). Magnetic reconnection in the corona and the loop prominence phenomenon. *Solar Physics*, **50**, 85–98. (Cited on page 14.)

Kowalski, A.F., Hawley, S.L., Holtzman, J.A., Wisniewski, J.P. & Hilton, E.J. (2010). A white light megaflare on the dm4. 5e star yz cmi. *The Astrophysical Journal Letters*, **714**, L98. (Cited on page 23.)

Krucker, S. & Battaglia, M. (2013). Particle densities within the acceleration region of a solar flare. *The Astrophysical Journal*, **780**, 107. (Cited on pages xiv, 17 and 19.)

Krucker, S., Christe, S., Glesener, L., Ishikawa, S.n., McBride, S., Glaser, D., Turin, P., Lin, R., Gubarev, M., Ramsey, B. *et al.* (2011). The focusing optics x-ray solar imager (foxsi). In *Optics for EUV, X-Ray, and Gamma-Ray Astronomy V*, vol. 8147, 814705, International Society for Optics and Photonics. (Cited on page 81.)

Krucker, S., Bednarzik, M., Grimm, O., Hurford, G.J., Limousin, O., Meuris, A., Orleański, P., Seweryn, K. & Skup, K.R. (2016). The spectrometer/telescope for imaging x-rays on solar orbiter: Flight design, challenges and trade-offs. *Nuclear Instruments and Methods in Physics Research Section A: Accelerators, Spectrometers, Detectors and Associated Equipment*, **824**, 626–629. (Cited on page 213.)

Kumar, A. & Kumar, S. (2014). Space weather effects on the low latitude d-region ionosphere during solar minimum. *Earth, planets and space*, **66**, 76. (Cited on page 159.)

Kumar, S., Kumar, A., Maurya, A.K. & Singh, R. (2016). Changes in the d region associated with three recent solar eclipses in the south pacific region. *Journal of Geophysical Research: Space Physics*, **121**, 5930–5943. (Cited on page 35.)

Kupriyanova, E., Melnikov, V., Nakariakov, V. & Shibasaki, K. (2010). Types of microwave quasi-periodic pulsations in single flaring loops. *Solar Physics*, **267**, 329–342. (Cited on pages 23 and 122.)

Leboeuf, J., Tajima, T. & Dawson, J. (1982). Dynamic magnetic x points. *The Physics of Fluids*, **25**, 784–799. (Cited on page 70.)

Lemen, J.R., Akin, D.J., Boerner, P.F., Chou, C., Drake, J.F., Duncan, D.W., Edwards, C.G., Friedlaender, F.M., Heyman, G.F., Hurlburt, N.E. *et al.* (2011). The atmospheric imaging assembly (aia) on the solar dynamics observatory (sdo). In *The Solar Dynamics Observatory*, 17–40, Springer. (Cited on pages xviii, xxix, 5, 93, 95 and 96.)

Li, Y. & Gan, W. (2008). Observational studies of the x-ray quasi-periodic oscillations of a solar flare. *Solar Physics*, **247**, 77–85. (Cited on page 160.)

Li, Y., Xue, J., Ding, M., Cheng, X., Su, Y., Feng, L., Hong, J., Li, H. & Gan, W. (2018). Spectroscopic observations of a current sheet in a solar flare. *The Astrophysical Journal Letters*, **853**, L15. (Cited on page 131.)

Lin, R., Dennis, B., Hurford, G., Smith, D., Zehnder, A., Harvey, P., Curtis, D., Pankow, D., Turin, P., Bester, M. *et al.* (2002). The reuven ramaty high-energy solar spectroscopic imager (rhessi). In *The Reuven Ramaty High-Energy Solar Spectroscopic Imager (RHESSI)*, 3–32, Springer. (Cited on pages 17 and 80.)

Liu, W., Chen, Q. & Petrosian, V. (2013). Plasmoid ejections and loop contractions in an eruptive m7. 7 solar flare: Evidence of particle acceleration and heating in magnetic reconnection outflows. *The Astrophysical Journal*, **767**, 168. (Cited on pages 21, 141, 146 and 148.)

Liu, W., Jin, M., Downs, C., Ofman, L., Cheung, M.C. & Nitta, N.V. (2018). A truly global extreme ultraviolet wave from the sol2017-09-10 x8. 2+ solar flare-coronal mass ejection. *The Astrophysical Journal Letters*, **864**, L24. (Cited on page 131.)

MacCombie, W. & Rust, D. (1979). Physical parameters in long-decay coronal enhancements. *Solar Physics*, **61**, 69–88. (Cited on page 122.)

Macnamara, C. & Roberts, B. (2011). The period ratio for kink and sausage modes in a magnetic slab. *Astronomy & Astrophysics*, **526**, A75. (Cited on page 122.)

Mariska, J.T. (1992). *The solar transition region*, vol. 23. Cambridge University Press. (Cited on page 6.)

Massone, A.M., Emslie, A.G., Hurford, G., Prato, M., Kontar, E.P. & Piana, M. (2009). Hard x-ray imaging of solar flares using interpolated visibilities. *The Astrophysical Journal*, **703**, 2004. (Cited on page 83.)

Masuda, S., Kosugi, T., Hara, H., Tsuneta, S. & Ogawara, Y. (1994). A loop-top hard x-ray source in a compact solar flare as evidence for magnetic reconnection. *Nature*, **371**, 495. (Cited on page 17.)

McAteer, R.J., Young, C.A., Ireland, J. & Gallagher, P.T. (2007). The bursty nature of solar flare x-ray emission. *The Astrophysical Journal*, **662**, 691. (Cited on page 221.)

McEwan, M., Díaz, A. & Roberts, B. (2008). Analytical determination of coronal parameters using the period ratio p. *Astronomy & Astrophysics*, **481**, 819–825. (Cited on page 123.)

McKenzie, D. & Hudson, H. (2001). Downflows and structure above lde arcades: Possible signatures of reconnection? *Earth, planets and space*, **53**, 577–580. (Cited on page 22.)

McLaughlin, J. & Hood, A.W. (2004). Mhd wave propagation in the neighbourhood of a two-dimensional null point. *Astronomy & Astrophysics*, **420**, 1129–1140. (Cited on page 64.)

McLaughlin, J., Thurgood, J.O. & MacTaggart, D. (2012a). On the periodicity of oscillatory reconnection. *Astronomy & Astrophysics*, **548**, A98. (Cited on page 69.)

McLaughlin, J., Verth, G., Fedun, V. & Erdélyi, R. (2012b). Generation of quasi-periodic waves and flows in the solar atmosphere by oscillatory reconnection. *The Astrophysical Journal*, **749**, 30. (Cited on pages xvii, 68 and 69.)

McLaughlin, J., Nakariakov, V., Dominique, M., Jelínek, P. & Takasao, S. (2018). Modelling quasi-periodic pulsations in solar and stellar flares. *Space Science Reviews*, **214**, 45. (Cited on pages 26, 59 and 66.)

McLaughlin, J.A., De Moortel, I., Hood, A.W. & Brady, C.S. (2009). Nonlinear fast magnetoacoustic wave propagation in the neighbourhood of a 2d magnetic x-point: oscillatory reconnection. *Astronomy & Astrophysics*, **493**, 227–240. (Cited on page 67.)

McRae, W.M. & Thomson, N.R. (2000). Vlf phase and amplitude: Daytime ionospheric parameters. *Journal of Atmospheric and Solar-Terrestrial Physics*, **62**, 609–618. (Cited on page 159.)

McRae, W.M. & Thomson, N.R. (2004). Solar flare induced ionospheric d-region enhancements from vlf phase and amplitude observations. *Journal of Atmospheric and Solar-Terrestrial Physics*, **66**, 77–87. (Cited on page 35.)

Mechtly, E., Bowhill, S. & Smith, L. (1972). Changes of lower ionosphere electron concentrations with solar activity. *Journal of Atmospheric and Terrestrial Physics*, **34**, 1899–1907. (Cited on page 77.)

Meegan, C., Lichti, G., Bhat, P., Bissaldi, E., Briggs, M.S., Connaughton, V., Diehl, R., Fishman, G., Greiner, J., Hoover, A.S. *et al.* (2009). The fermi gamma-ray burst monitor. *The Astrophysical Journal*, **702**, 791. (Cited on page 86.)

Melrose, D. & Brown, J. (1976). Precipitation in trap models for solar hard x-ray bursts. *Monthly Notices of the Royal Astronomical Society*, **176**, 15–30. (Cited on page 192.)

Mendillo, M., Withers, P., Hinson, D., Rishbeth, H. & Reinisch, B. (2006). Effects of solar flares on the ionosphere of mars. *Science*, **311**, 1135–1138. (Cited on pages xxvi, 177, 210 and 211.)

Milligan, R.O. (2015). Extreme ultra-violet spectroscopy of the lower solar atmosphere during solar flares (invited review). *Solar Physics*, **290**, 3399–3423. (Cited on page 16.)

Milligan, R.O., Gallagher, P.T., Mathioudakis, M. & Keenan, F.P. (2006). Observational evidence of gentle chromospheric evaporation during the impulsive phase of a solar flare. *The Astrophysical Journal Letters*, **642**, L169. (Cited on page 16.)

Mitra, A.P., ed. (1974). *Ionospheric effects of solar flares*, vol. 46 of *Astrophysics and Space Science Library*. (Cited on pages 32, 33, 72, 159, 165 and 176.)

Mitra-Kraev, U., Harra, L., Williams, D. & Kraev, E. (2005). The first observed stellar x-ray flare oscillation: constraints on the flare loop length and the magnetic field. *Astronomy & Astrophysics*, **436**, 1041–1047. (Cited on page 177.)

Morfitt, D.G. & Shellman, C.H. (1976). 'modesrch', an improved computer program for obtaining elf/vlf/lf mode constants in an earth-ionosphere waveguide. Tech. rep., NAVAL ELECTRONICS LAB CENTER SAN DIEGO CA. (Cited on pages 75 and 76.)

Morgan, R.R. (1968). World-wide vlf effective-conductivity map. Tech. rep., WESTINGHOUSE ELECTRIC CORP BOULDER CO ENVIRONMENTAL SCIENCE AND TECHNOLOGY DEPT. (Cited on page 75.)

Morosan, D., Carley, E., Hayes, L., Murray, S., Zucca, P., Fallows, R., McCauley, J., Kilpua, E. & Gallagher, P. (2019). Multiple regions of shock accelerated particles in the solar corona. *Accepted Nature Astronomy*. (Cited on pages 130, 143 and 147.)

Morton, R.J., Verth, G., Jess, D.B., Kuridze, D., Ruderman, M.S., Mathioudakis, M. & Erdélyi, R. (2012). Observations of ubiquitous compressive waves in the sun's chromosphere. *Nature Communications*, **3**, 1315. (Cited on pages xvi and 51.)

Murray, M.J., van Driel-Gesztelyi, L. & Baker, D. (2009). Simulations of emerging flux in a coronal hole: oscillatory reconnection. *Astronomy & Astrophysics*, **494**, 329–337. (Cited on page 68.)

Nakajima, H., Nishio, M., Enome, S., Shibasaki, K., Takano, T., Hanaoka, Y., Torii, C., Sekiguchi, H., Bushimata, T., Kawashima, S. *et al.* (1994). The nobeyama radioheliograph. *Proceedings of the IEEE*, **82**, 705–713. (Cited on page 91.)

Nakariakov, V. & Melnikov, V. (2006). Modulation of gyrosynchrotron emission in solar and stellar flares by slow magnetoacoustic oscillations. *Astronomy & Astrophysics*, **446**, 1151–1156. (Cited on page 61.)

Nakariakov, V. & Melnikov, V. (2009). Quasi-periodic pulsations in solar flares. *Space Science Reviews*, **149**, 119–151. (Cited on pages 59, 67 and 105.)

Nakariakov, V. & Ofman, L. (2001). Determination of the coronal magnetic field by coronal loop oscillations. *Astronomy & Astrophysics*, **372**, L53–L56. (Cited on page 46.)

Nakariakov, V. & Zimovets, I. (2011). Slow magnetoacoustic waves in two-ribbon flares. *The Astrophysical Journal Letters*, **730**, L27. (Cited on page 65.)

Nakariakov, V., Ofman, L., DeLuca, E., Roberts, B. & Davila, J. (1999). Trace observation of damped coronal loop oscillations: Implications for coronal heating. *Science*, **285**, 862–864. (Cited on page 54.)

Nakariakov, V., Melnikov, V. & Reznikova, V. (2003). Global sausage modes of coronal loops. *Astronomy & Astrophysics*, **412**, L7–L10. (Cited on page 53.)

Nakariakov, V., Foullon, C., Verwichte, E. & Young, N. (2006). Quasi-periodic modulation of solar and stellar flaring emission by magnetohydrodynamic oscillations in a nearby loop. *Astronomy & Astrophysics*, **452**, 343–346. (Cited on pages xvii, 63, 65 and 66.)

Nakariakov, V., Inglis, A., Zimovets, I., Foullon, C., Verwichte, E., Sych, R. & Myagkova, I. (2010). Oscillatory processes in solar flares. *Plasma Physics and Controlled Fusion*, **52**, 124009. (Cited on page 67.)

Nakariakov, V., Hornsey, C. & Melnikov, V. (2012). Sausage oscillations of coronal plasma structures. *The Astrophysical Journal*, **761**, 134. (Cited on pages 123 and 152.)

Nakariakov, V., Pilipenko, V., Heilig, B., Jelínek, P., Karlickỳ, M., Klimushkin, D., Kolotkov, D., Lee, D.H., Nisticò, G., Van Doorsselaere, T. *et al.* (2016). Magnetohydrodynamic oscillations in the solar corona and earth's magnetosphere: towards consolidated understanding. *Space Science Reviews*, **200**, 75–203. (Cited on page 176.)

Nakariakov, V., Anfinogentov, S., Storozhenko, A., Kurochkin, E., Bogod, V., Sharykin, I. & Kaltman, T. (2018a). Quasi-periodic pulsations in a solar microflare. *The Astrophysical Journal*, **859**, 154. (Cited on page 196.)

Nakariakov, V.M. (2007). Mhd oscillations in solar and stellar coronae: Current results and perspectives. *Advances in Space Research*, **39**, 1804–1813. (Cited on pages 59 and 60.)

Nakariakov, V.M. & Melnikov, V.F. (2009). Quasi-Periodic Pulsations in Solar Flares. *Space Science Reviews*, **149**, 119–151. (Cited on page 24.)

Nakariakov, V.M. & Verwichte, E. (2005). Coronal waves and oscillations. *Living reviews in solar physics*, **2**, 3. (Cited on pages 50 and 53.)

Nakariakov, V.M., Tsiklauri, D., Kelly, A., Arber, T. & Aschwanden, M.J. (2004). Acoustic oscillations in solar and stellar flaring loops. *Astronomy & Astrophysics*, **414**, L25–L28. (Cited on page 152.)

Nakariakov, V.M., Foullon, C., Myagkova, I.N. & Inglis, A.R. (2010). Quasi-Periodic Pulsations in the Gamma-Ray Emission of a Solar Flare. *Astrophysical Journal Letters*, **708**, L47–L51. (Cited on page 25.)

Nakariakov, V.M., Kolotkov, D., Kupriyanova, E.G., Mehta, T., Pugh, C.E., Lee, D.H. & Broomhall, A.M. (2018b). Non-stationary quasi-periodic pulsations in solar and stellar flares. *Plasma Physics and Controlled Fusion*. (Cited on page 26.)

Neupert, W.M. (1968). Comparison of solar x-ray line emission with microwave emission during flares. *The Astrophysical Journal*, **153**, L59. (Cited on pages 19 and 150.)

REFERENCES

Nina, A. & Čadež, V. (2013). Detection of acoustic-gravity waves in lower ionosphere by vlf radio waves. *Geophysical Research Letters*, **40**, 4803–4807. (Cited on page 176.)

Nina, A., Čadež, V., Srećković, V. & Šulić, D. (2012). Altitude distribution of electron concentration in ionospheric d-region in presence of time-varying solar radiation flux. *Nuclear Instruments and Methods in Physics Research Section B: Beam Interactions with Materials and Atoms*, **279**, 110–113. (Cited on page 165.)

Nita, G.M., Viall, N.M., Klimchuk, J.A., Loukitcheva, M.A., Gary, D.E., Kuznetsov, A.A. & Fleishman, G.D. (2018). Dressing the Coronal Magnetic Extrapolations of Active Regions with a Parameterized Thermal Structure. *Astrophysical Journal*, **853**, 66. (Cited on page 182.)

Omodei, N., Pesce-Rollins, M., Longo, F., Allafort, A. & Krucker, S. (2018). Fermi-LAT Observations of the 2017 September 10 Solar Flare. *Astrophysical Journal Letters*, **865**, L7. (Cited on page 131.)

Pacini, A.A. & Raulin, J.P. (2006). Solar x-ray flares and ionospheric sudden phase anomalies relationship: A solar cycle phase dependence. *Journal of Geophysical Research: Space Physics*, **111**. (Cited on page 159.)

Palit, S., Basak, T., Mondal, S., Pal, S. & Chakrabarti, S. (2013). Modeling of very low frequency (vlf) radio wave signal profile due to solar flares using the geant4 monte carlo simulation coupled with ionospheric chemistry. *Atmospheric Chemistry and Physics*, **13**, 9159–9168. (Cited on page 35.)

Parker, E.N. (1963). The solar-flare phenomenon and the theory of reconnection and annihiliation of magnetic fields. *The Astrophysical Journal Supplement Series*, **8**, 177. (Cited on page 56.)

Parks, G. & Winckler, J. (1969). Sixteen-second periodic pulsations observed in the correlated microwave and energetic x-ray emission from a solar flare. *The Astrophysical Journal*, **155**, L117. (Cited on pages 24 and 105.)

PARNELL, C.E. & DE MOORTEL, I. (2012). A contemporary view of coronal heating. *Philosophical Transactions of the Royal Society A: Mathematical, Physical and Engineering Sciences*, **370**, 3217–3240. (Cited on page 7.)

PARROT, M. & MOGILEVSKY, M. (1989). Vlf emissions associated with earthquakes and observed in the ionosphere and the magnetosphere. *Physics of the Earth and Planetary Interiors*, **57**, 86–99. (Cited on page 35.)

PASCOE, D. & DE MOORTEL, I. (2014). Standing kink modes in three-dimensional coronal loops. *The Astrophysical Journal*, **784**, 101. (Cited on page 59.)

PASCOE, D., NAKARIAKOV, V. & ARBER, T. (2007). Sausage oscillations of coronal loops. *Astronomy & Astrophysics*, **461**, 1149–1154. (Cited on pages xvi, 62 and 123.)

PASCOE, D., DE MOORTEL, I. & MCLAUGHLIN, J. (2009). Impulsively generated oscillations in a 3d coronal loop. *Astronomy & Astrophysics*, **505**, 319–327. (Cited on pages 59 and 123.)

PESNELL, W.D. (2015). *Solar dynamics observatory (SDO)*. Springer. (Cited on page 92.)

PETSCHEK, H.E. (1964). Magnetic field annihilation. *NASA Special Publication*, **50**, 425. (Cited on page 57.)

PONTIN, D. (2011). Three-dimensional magnetic reconnection regimes: A review. *Advances in Space Research*, **47**, 1508–1522. (Cited on page 58.)

PRESS, W.H. & TEUKOLSKY, S.A. (1990). Savitzky-golay smoothing filters. *Computers in Physics*, **4**, 669–672. (Cited on page 132.)

PRIEST, E. (2014). *Magnetohydrodynamics of the Sun*. Cambridge University Press. (Cited on pages xiii and 4.)

PRIEST, E. & FORBES, T. (2000). Magnetic reconnection (cambridge. (Cited on page 45.)

PRIEST, E. & FORBES, T. (2002). The magnetic nature of solar flares. *The Astronomy and Astrophysics Review*, **10**, 313–377. (Cited on pages 13 and 58.)

Priest, E.R. (1985). The magnetohydrodynamics of current sheets. *Reports on Progress in Physics*, **48**, 955. (Cited on page 70.)

Pritchett, P. & Wu, C. (1979). Coalescence of magnetic islands. *The Physics of Fluids*, **22**, 2140–2146. (Cited on page 70.)

Pugh, C., Armstrong, D., Nakariakov, V. & Broomhall, A.M. (2016). Statistical properties of quasi-periodic pulsations in white-light flares observed with kepler. *Monthly Notices of the Royal Astronomical Society*, **459**, 3659–3676. (Cited on pages 23 and 177.)

Pugh, C.E., Nakariakov, V., Broomhall, A.M., Bogomolov, A. & Myagkova, I. (2017). Properties of quasi-periodic pulsations in solar flares from a single active region. *Astronomy & Astrophysics*, **608**, A101. (Cited on pages 155 and 201.)

Raftery, C.L., Gallagher, P.T., Milligan, R.O. & Klimchuk, J.A. (2009). Multi-wavelength observations and modelling of a canonical solar flare. *Astronomy & Astrophysics*, **494**, 1127–1136. (Cited on page 21.)

Ratcliffe, J.A. *et al.* (1972). *An introduction to ionosphere and magnetosphere*. CUP Archive. (Cited on page 165.)

Raulin, J.P., Bertoni, F.C., Gavilán, H.R., Guevara-Day, W., Rodriguez, R., Fernandez, G., Correia, E., Kaufmann, P., Pacini, A., Stekel, T.R. *et al.* (2010). Solar flare detection sensitivity using the south america vlf network (savnet). *Journal of Geophysical Research: Space Physics*, **115**. (Cited on page 208.)

Redmon, R., Seaton, D., Steenburgh, R., He, J. & Rodriguez, J. (2018). September 2017's geoeffective space weather and impacts to caribbean radio communications during hurricane response. *Space Weather*. (Cited on page 33.)

Reznikova, V. & Shibasaki, K. (2011). Flare quasi-periodic pulsations with growing periodicity. *Astronomy & Astrophysics*, **525**, A112. (Cited on pages 26 and 111.)

Rowe, J.N., Ferraro, A.J., Lee, H.S., Kreplin, R.W. & Mitra, A.P. (1970). Observations of electron density during a solar flare. *Journal of Atmospheric and Terrestrial Physics*, **32**, 1609–1614. (Cited on page 72.)

Ryan, D.F., Chamberlin, P.C., Milligan, R.O. & Gallagher, P.T. (2013). Decay-phase cooling and inferred heating of m-and x-class solar flares. *The Astrophysical Journal*, **778**, 68. (Cited on pages 21 and 122.)

Sabine, E. *et al.* (1852). Viii. on periodical laws discoverable in the mean effects of the larger magnetic disturbance.—no. ii. *Philosophical Transactions of the Royal Society of London*, **142**, 103–124. (Cited on page 2.)

Savage, S.L. & McKenzie, D.E. (2011). Quantitative examination of a large sample of supra-arcade downflows in eruptive solar flares. *The Astrophysical Journal*, **730**, 98. (Cited on pages 22, 146 and 148.)

Savitzky, A. & Golay, M.J. (1964). Smoothing and differentiation of data by simplified least squares procedures. *Analytical chemistry*, **36**, 1627–1639. (Cited on page 132.)

Scherrer, D., Cohen, M., Hoeksema, T., Inan, U., Mitchell, R. & Scherrer, P. (2008). Distributing space weather monitoring instruments and educational materials worldwide for ihy 2007: The awesome and sid project. *Advances in Space Research*, **42**, 1777–1785. (Cited on page 98.)

Scherrer, P.H., Schou, J., Bush, R., Kosovichev, A., Bogart, R., Hoeksema, J., Liu, Y., Duvall, T., Zhao, J., Schrijver, C. *et al.* (2012). The helioseismic and magnetic imager (hmi) investigation for the solar dynamics observatory (sdo). *Solar Physics*, **275**, 207–227. (Cited on page 93.)

Schwartz, R., Csillaghy, A., Tolbert, A., Hurford, G., Mc Tiernan, J. & Zarro, D. (2002). Rhessi data analysis software: rationale and methods. *Solar Physics*, **210**, 165–191. (Cited on page 85.)

Selvakumaran, R., Maurya, A.K., Gokani, S.A., Veenadhari, B., Kumar, S., Venkatesham, K., Phanikumar, D., Singh, A.K., Siingh, D. & Singh, R. (2015). Solar flares induced d-region ionospheric and geomagnetic perturbations. *Journal of Atmospheric and Solar-Terrestrial Physics*, **123**, 102–112. (Cited on pages 159, 172 and 176.)

Selwa, M., Murawski, K., Solanki, S., Wang, T. & Tóth, G. (2005). Numerical simulations of vertical oscillations of a solar coronal loop. *Astronomy & Astrophysics*, **440**, 385–390. (Cited on page 152.)

Severino, G. (2017). *The Structure and Evolution of the Sun, Chapter 3*. Springer. (Cited on page 5.)

Shao, X.M., Lay, E.H. & Jacobson, A.R. (2013). Reduction of electron density in the night-time lower ionosphere in response to a thunderstorm. *Nature Geoscience*, **6**, 29. (Cited on page 35.)

Shibata, K. & Magara, T. (2011). Solar flares: magnetohydrodynamic processes. *Living Reviews in Solar Physics*, **8**, 6. (Cited on page 57.)

Shih, A.Y., Christe, S., Shih, A.Y., Christe, S., Alaoui, M., Allred, J.C., Antiochos, S.K., Battaglia, M., Buitrago-Casas, J.C., Caspi, A. *et al.* (2016). Science objectives of the foxsi small explorer mission concept. In *AAS/Solar Physics Division Abstracts# 47*, vol. 47. (Cited on page 213.)

Simões, P.J.A., Hudson, H.S. & Fletcher, L. (2015). Soft X-Ray Pulsations in Solar Flares. *Solar Physics*, **290**, 3625–3639. (Cited on pages 23, 25, 26, 106, 107, 122, 125, 138 and 202.)

Smith, D.M., Lin, R., Turin, P., Curtis, D., Primbsch, J., Campbell, R., Abiad, R., Schroeder, P., Cork, C., Hull, E. *et al.* (2003). The rhessi spectrometer. In *The Reuven Ramaty High-Energy Solar Spectroscopic Imager (RHESSI)*, 33–60, Springer. (Cited on page 85.)

Stewart, B. (1861). Xxii. on the great magnetic disturbance which extended from august 28 to september 7, 1859, as recorded by photography at the kew observatory. *Philosophical Transactions of the Royal Society of London*, **151**, 423–430. (Cited on page 2.)

Sturrock, P.A. (1968). A Model of Solar Flares. In K.O. Kiepenheuer, ed., *Structure and Development of Solar Active Regions*, vol. 35 of *IAU Symposium*, 471. (Cited on page 14.)

Švestka, Z. (1994). Slow-mode oscillations of large-scale coronal loops. *Solar Physics*, **152**, 505–508. (Cited on page 160.)

Švestka, Z., Dennis, B., Pick, M., Raoult, A., Rapley, C., Stewart, R. & Woodgate, B. (1982). Unusual coronal activity following the flare of 6 november 1980. *Solar Physics*, **80**, 143–159. (Cited on page 160.)

Sweet, P.A. (1958). The neutral point theory of solar flares. In *Electromagnetic phenomena in cosmical physics*, vol. 6, 123. (Cited on page 56.)

Tajima, T., Sakai, J., Nakajima, H., Kosugi, T., Brunel, F. & Kundu, M. (1987). Current loop coalescence model of solar flares. *The Astrophysical Journal*, **321**, 1031–1048. (Cited on page 70.)

Takahashi, T., Qiu, J. & Shibata, K. (2017). Quasi-periodic oscillations in flares and coronal mass ejections associated with magnetic reconnection. *The Astrophysical Journal*, **848**, 102. (Cited on page 151.)

Takano, T., Nakajima, H., Enome, S., Shibasaki, K., Nishio, M., Hanaoka, Y., Shiomi, Y., Sekiguchi, H., Kawashima, S., Bushimata, T. *et al.* (1997). An upgrade of nobeyama radioheliograph to a dual-frequency (17 and 34 ghz) system. In *Coronal Physics from Radio and Space Observations*, 183–191, Springer. (Cited on page 91.)

Takasao, S. & Shibata, K. (2016). Above-the-loop-top oscillation and quasi-periodic coronal wave generation in solar flares. *The Astrophysical Journal*, **823**, 150. (Cited on page 150.)

Tan, B. & Tan, C. (2012). Microwave quasi-periodic pulsation with millisecond bursts in a solar flare on 2011 august 9. *The Astrophysical Journal*, **749**, 28. (Cited on page 23.)

Tan, B., Yu, Z., Huang, J., Tan, C. & Zhang, Y. (2016). Very long-period pulsations before the onset of solar flares. *The Astrophysical Journal*, **833**, 206. (Cited on pages 25 and 160.)

Thiemann, E., Andersson, L., Lillis, R., Withers, P., Xu, S., Elrod, M., Jain, S., Pilinski, M., Pawlowski, D., Chamberlin, P. *et al.* (2018). The mars topside ionosphere response to the x8. 2 solar flare of 10 september 2017. *Geophysical Research Letters*, **45**, 8005–8013. (Cited on page 211.)

Thomas, R.J., Crannell, C.J. & Starr, R. (1985). Expressions to determine temperatures and emission measures for solar X-ray events from GOES measurements. *Solar Physics*, **95**, 323–329. (Cited on pages 215, 216 and 217.)

Thomson, N.R. & Clilverd, M.A. (2001). Solar flare induced ionospheric d-region enhancements from vlf amplitude observations. *Journal of Atmospheric and Solar-Terrestrial Physics*, **63**, 1729–1737. (Cited on pages 159, 163 and 169.)

Thomson, N.R., Rodger, C.J. & Dowden, R.L. (2004). Ionosphere gives size of greatest solar flare. *Geophysical research letters*, **31**. (Cited on page 159.)

Thomson, N.R., Rodger, C.J. & Clilverd, M.A. (2005). Large solar flares and their ionospheric d region enhancements. *Journal of Geophysical Research: Space Physics*, **110**. (Cited on pages 35, 159 and 176.)

Threlfall, J., De Moortel, I. & Conlon, T. (2017). Above the noise: The search for periodicities in the inner heliosphere. *Solar Physics*, **292**, 165. (Cited on page 221.)

Thurgood, J.O., Pontin, D.I. & McLaughlin, J.A. (2017). Three-dimensional oscillatory magnetic reconnection. *The Astrophysical Journal*, **844**, 2. (Cited on pages 69 and 149.)

Tian, H., Young, P.R., Reeves, K.K., Wang, T., Antolin, P., Chen, B. & He, J. (2016). Global sausage oscillation of solar flare loops detected by the interface region imaging spectrograph. *The Astrophysical Journal Letters*, **823**, L16. (Cited on pages 123 and 152.)

Toriumi, S., Schrijver, C.J., Harra, L.K., Hudson, H. & Nagashima, K. (2017). Magnetic properties of solar active regions that govern large solar flares and eruptions. *The Astrophysical Journal*, **834**, 56. (Cited on pages 201 and 205.)

Torrence, C. & Compo, G.P. (1998). A practical guide to wavelet analysis. *Bulletin of the American Meteorological society*, **79**, 61–78. (Cited on pages 113, 218 and 219.)

Tsiklauri, D., Nakariakov, V., Arber, T. & Aschwanden, M. (2004). Flare-generated acoustic oscillations in solar and stellar coronal loops. *Astronomy & Astrophysics*, **422**, 351–355. (Cited on page 152.)

Tsurutani, B., Verkhoglyadova, O., Mannucci, A., Lakhina, G., Li, G. & Zank, G. (2009). A brief review of "solar flare effects" on the ionosphere. *Radio Science*, **44**. (Cited on page 32.)

Tsurutani, B.T., Gonzalez, W., Lakhina, G. & Alex, S. (2003). The extreme magnetic storm of 1–2 september 1859. *Journal of Geophysical Research: Space Physics*, **108**. (Cited on page 2.)

Van Doorsselaere, T., De Groof, A., Zender, J., Berghmans, D. & Goossens, M. (2011). Lyra observations of two oscillation modes in a single flare. *The Astrophysical Journal*, **740**, 90. (Cited on page 152.)

Van Doorsselaere, T., Antolin, P., Yuan, D., Reznikova, V. & Magyar, N. (2016a). Forward modeling of euv and gyrosynchrotron emission from coronal plasmas with fomo. *Frontiers in Astronomy and Space Sciences*, **3**, 4. (Cited on page 182.)

Van Doorsselaere, T., Kupriyanova, E.G. & Yuan, D. (2016b). Quasi-periodic pulsations in solar and stellar flares: an overview of recent results (invited review). *Solar Physics*, **291**, 3143–3164. (Cited on pages 24 and 129.)

Vaughan, S. (2005). A simple test for periodic signals in red noise. *Astronomy & Astrophysics*, **431**, 391–403. (Cited on page 222.)

Vaughan, S. (2010). A bayesian test for periodic signals in red noise. *Monthly Notices of the Royal Astronomical Society*, **402**, 307–320. (Cited on page 222.)

Vršnak, B., Temmer, M., Veronig, A., Karlickỳ, M. & Lin, J. (2006). Shrinking and cooling of flare loops in a two-ribbon flare. *Solar Physics*, **234**, 273–299. (Cited on page 21.)

Wait, J. & Spies, K. (1964a). Propagation of radio waves past a coast line with a gradual change of surface impedance. *IEEE Transactions on Antennas and Propagation*, **12**, 570–575. (Cited on pages 73 and 75.)

Wait, J.R. (1974). Theory of the terrestrial propagation of vlf electromagnetic waves. In *ELF-VLF Radio Wave Propagation*, 129–147, Springer. (Cited on page 73.)

Wait, J.R. & Spies, K.P. (1964b). *Characteristics of the Earth-ionosphere waveguide for VLF radio waves*. 300, US Dept. of Commerce, National Bureau of Standards: for sale by the Supt. of Doc., US Govt. Print. Off. (Cited on pages 35 and 168.)

Wang, T. (2011). Standing slow-mode waves in hot coronal loops: observations, modeling, and coronal seismology. *Space science reviews*, **158**, 397–419. (Cited on pages 152 and 160.)

Wang, T., Solanki, S., Curdt, W., Innes, D. & Dammasch, I. (2002). Doppler shift oscillations of hot solar coronal plasma seen by sumer: a signature of loop oscillations? *The Astrophysical Journal Letters*, **574**, L101. (Cited on page 54.)

Warren, H.P., Brooks, D.H., Ugarte-Urra, I., Reep, J.W., Crump, N.A. & Doschek, G.A. (2018). Spectroscopic observations of current sheet formation and evolution. *The Astrophysical Journal*, **854**, 122. (Cited on page 131.)

Watt, A. (1967). Vlf radio engineering, international series of monograph in electromagnetic waves. (Cited on page 100.)

Wenzel, D., Jakowski, N., Berdermann, J., Mayer, C., Valladares, C. & Heber, B. (2016). Global ionospheric flare detection system (gifds). *Journal of Atmospheric and Solar-Terrestrial Physics*, **138**, 233–242. (Cited on pages 176 and 208.)

White, S.M., Thomas, R.J. & Schwartz, R.A. (2005). Updated expressions for determining temperatures and emission measures from goes soft x-ray measurements. *Solar Physics*, **227**, 231–248. (Cited on pages xviii, xxii, 89, 153, 215, 217 and 218.)

White, S.M., Benz, A.O., Christe, S., Farnik, F., Kundu, M.R., Mann, G., Ning, Z., Raulin, J.P., Silva-Válio, A.V., Saint-Hilaire, P. *et al.* (2011). The relationship between solar radio and hard x-ray emission. *Space science reviews*, **159**, 225. (Cited on page 18.)

Whitten, R.C. & Poppoff, I.G. (1961). A Model of Solar-Flare-Induced Ionization in the D Region. *Journal of Geophysical Research*, **66**, 2779–2786. (Cited on page 72.)

Witasse, O., Cravens, T., Mendillo, M., Moses, J., Kliore, A., Nagy, A. & Breus, T. (2008). Solar system ionospheres. In *Comparative Aeronomy*, 235–265, Springer. (Cited on pages 159 and 211.)

Woods, T., Eparvier, F., Hock, R., Jones, A., Woodraska, D., Judge, D., Didkovsky, L., Lean, J., Mariska, J., Warren, H. *et al.* (2010). Extreme ultraviolet variability experiment (eve) on the solar dynamics observatory (sdo): Overview of science objectives, instrument design, data products, and model developments. In *The Solar Dynamics Observatory*, 115–143, Springer. (Cited on pages 93 and 96.)

Xu, S., Thiemann, E., Mitchell, D., Eparvier, F., Pawlowski, D., Benna, M., Andersson, L., Liemohn, M.W., Bougher, S. & Mazelle, C. (2018). Observations and modeling of the mars low-altitude ionospheric response to the 10 september 2017 x-class solar flare. *Geophysical Research Letters*, **45**, 7382–7390. (Cited on page 211.)

Zaitsev, V.V. & Stepanov, A.V. (2008). Coronal magnetic loops. *Physics-Uspekhi*, **51**, 1123–1160. (Cited on page 59.)

Zajtsev, V.V. & Stepanov, A.V. (1975). On the origin of pulsations of type IV solar radio emission. Plasma cylinder oscillations (I). *Issledovaniia Geomagnetizmu Aeronomii i Fizike Solntsa*, **37**, 3–10. (Cited on page 49.)

Žigman, V., Grubor, D. & Šulić, D. (2007). D-region electron density evaluated from vlf amplitude time delay during x-ray solar flares. *Journal of atmospheric and solar-terrestrial physics*, **69**, 775–792. (Cited on pages 35, 72, 100, 159, 165, 166, 173, 174 and 175.)

Zimovets, I. & Struminsky, A. (2010). Observations of double-periodic x-ray emission in interacting systems of solar flare loops. *Solar Physics*, **263**, 163–174. (Cited on page 26.)